SELF-EXCITED INSTABILITY REGIMES OF CONFINED TURBULENT PREMIXED JET FLAMES

A Dissertation

Submitted to the Faculty

of

Purdue University

by

Timo Buschhagen

In Partial Fulfillment of the

Requirements for the Degree

of

Doctor of Philosophy

May 2020

Purdue University

West Lafayette, Indiana

THE PURDUE UNIVERSITY GRADUATE SCHOOL
STATEMENT OF DISSERTATION APPROVAL

Dr. Carson D. Slabaugh, Chair

School of Aeronautics and Astronautics

Dr. William E. Anderson

School of Aeronautics and Astronautics

Dr. Rohan M. Gejji

School of Aeronautics and Astronautics

Dr. Robert P. Lucht

School of Mechanical Engineering

Dr. Carlo Scalo

School of Mechanical Engineering

Approved by:

Dr. Gregory A. Blaisdell

Head of Gambaro Program of Aeronautics and Astronautics

To my family.

ACKNOWLEDGMENTS

First and foremost, I would like to thank my advisor Prof. Carson D. Slabaugh for the opportunity to be part of his research group and work on this exciting topic. I am grateful for his academic support and advice throughout my time at Zucrow and will always be thankful for his guidance and trust that he extended towards my work. I would also like to thank Prof. Carlo Scalo for his support and advice on the numerical part of this work. His guidance and help accelerated my modelling progress significantly and helped me to produce results in a timely manner. I am also grateful for Prof. Robert P. Lucht who was willing to take me on initially as a PhD student and gave me the opportunity to gain insight in spray diagnostics and first experiences with the design, building and operation of high pressure fluid systems. I would like to thank Prof. William E. Anderson for serving on my advisory committee and providing valuable input on this work.

I would also like to thank Dr. Rohan M. Gejji, not just for serving on my advisory committee, but especially for his dedicated mentorship, guidance and friendship he was willing to extend to me during my time at Zucrow. I am thankful for the many discussions we had on the topic and his teaching on the design and operation of complex experimental systems as well as measurement techniques. I am also thankful for his help on testing days, often with long and odd hours.

Special thanks goes to John Philo for his support on this work and willingness to spent long days running VIPER with me from the very beginning. Similarly I'd like to thank Mark Frederick for his support on VIPER testing and emissions sampling. I'd also like to thank Andrew Pratt for his initial guidance on high speed imaging and crucial support during VIPERs commissioning in ZL3 and recommissioning in ZL8.

I would also like to thank the remaining students of the Slabaugh research group for their support on build-up and constructive feedback during presentation and talk preparations. Special thanks also go to Scott Meyer for his dedicated support and valuable guid-

ance throughout the design process as well as experiment build-up. I would also like to thank our Zucrow machinists Rob McGuire and Toby Lamb as well as Jerry Hardt for their fabrication expertise and guidance during the design process of VIPER.

Furthermore I'd like to thank the past and present students at Zucrow who I had the pleasure to work with, learn from and spent free time with, especially: Dr. Tristan Fuller, Dr. Dasheng Lim, Rufat Kulakhmetov, Dr. James Braun, Monique McClain, Ian Walters, Aaron Lemcherfi, Lalit Kishore, Dr. Vladlen Podolski, Gina Bishop, Dr. Steve Hunt and Dr. Brandon Kan.

Last but not least I am grateful for the support of my family and their trust in me, without whom I wouldn't have been able to undergo my studies abroad and conclude this journey.

The financial support for the project from Siemens Energy Inc. is acknowledged.

PREFACE

The subsections 3.3 and 4.3 of this document have been published in peer-reviewed journals. Chapter 7 is undergoing submission to the Journal of Fluid Mechanics.

Subsection 3.3:

Buschhagen, Timo, Rohan Gejji, John Philo, Lucky Tran, J. Enrique Portillo Bilbao, and Carson D. Slabaugh. "Experimental Investigation of Self-Excited Combustion Instabilities in a Lean, Premixed, Gas Turbine Combustor at High Pressure." Journal of Engineering for Gas Turbines and Power 140, no. 11 (2018).

Subsection 4.3:

Buschhagen, Timo, Rohan Gejji, John Philo, Lucky Tran, J. Enrique Portillo Bilbao, and Carson D. Slabaugh. "Self-excited transverse combustion instabilities in a high pressure lean premixed jet flame." Proceedings of the Combustion Institute 37, no. 4 (2019): 5181-5188.

TABLE OF CONTENTS

Page

LIST OF TABLES

LIST OF FIGURES

Figure Page

Figure Page

ABSTRACT

Buschhagen, Timo Ph.D., Purdue University, May 2020. Self-Excited Instability Regimes of Confined Turbulent Premixed Jet Flames. Major Professor: Carson D. Slabaugh.

The demand for more efficient and cleaner terrestrial gas turbine engines for energy generation has accelerated with stringent emission regulations. Most terrestrial gas turbine engine configurations utilize lean premixed jet stabilized flames for energy extraction. These highly turbulent flames provide the necessary thermal power densities and low NOx emissions but are prone to combustion instabilities. This work studies the stability of a canonical premixed turbulent jet flame to changes in operation condition at elevated pressure. The underlying coupling mechanisms leading to the excitation of different modes are of interest. Different fuel injection schemes are considered, to delineate the influence of system coupled excitation and flow field intrinsic mechanisms that lead to self-excitation of longitudinal and transverse modes in an axisymmetric jet flame.

The fundamental longitudinal mode sensitivity to operation conditions was investigated in a technically-premixed configuration, for which the fuel injector is exposed to the system dynamics. Global equivalence ratio fluctuations (ϕ') paired with flame-vortex interactions were observed to sustain the 1L mode, for which leaner operating conditions lead to an increase of the limit-cycle amplitude.

To solely focus on the shear layer dynamics involved in the feedback loop of the 1L instability a "fully-premixed" configuration (FPC) of the combustor was designed. The elimination of potential ϕ' lead to the excitation of longitudinal as well as transverse, and spinning modes, which can be associated with specific burner operation envelope regions. 1L mode coupled flame dynamics indicate axisymmetric emission patterns in OH^* emission imaging corresponding to axisymmetric instabilities in the shear layer. Transverse modes correlate with an asymmetric shear layer roll-up process and a flapping motion of

the flame. Spinning modes are characterized by high levels of limit-cycle amplitude and a single wave is observed that travels in the annulus of the recirculation zone. From the high speed imaging an azimuthal wave speed of up to 90% of the Chapman-Jouguet velocity for the natural gas - air mixture is computed.

The transverse mode is found to be sensitive to changes in chamber pressure and injector velocity. For a baseline injector velocity at which 1T mode excitation occurs, an increase in system pressure lead to an increase of the 1T mode amplitude. The 1T mode excitation is found to be sensitive to the injector velocity, where the highest amplitude are observed for a Strouhal number band of 1.6-1.7 based on the injector diameter.

A linear stability analysis (LSA) of the underlying base flow field is performed in order to assess if the underlying shear layer instability modes determine the selection of the instability regime for a given flame condition. Two flow perturbation modes are supported by the flow field, Mode 1 is associated with the recirculation zone domain, where preferred mode frequencies favors coupling with longitudinal acoustics chamber modes. Mode 2 resides in the mixture jet, for which preferred mode frequencies match local 1T acoustic eigenfrequencies of the chamber. It is found that for 1T mode dominated operation cases, the recirculation zone associated mode is stabilized leading to to the excitation of the 1T mode in the injector near field. For operation cases showing predominantly longitudinal combustion instability, the recirculation zone mode (Mode 1) shows elevated growth rates in the injector near field paired with preferred frequencies that are compatible with the longitudinal acoustic eigenmodes.

These observations indicate that the preferred shear layer perturbation modes impact the selection of the combustion instability regime for a given flame operation condition. These results can be utilized to build a model framework for the design of jet flame type burners, to avoid geometries and operation regions that show a high potential for transverse mode excitation by the underlying flow field.

1. INTRODUCTION

The demand for more efficient and cleaner terrestrial gas turbine engines for energy generation has accelerated with stringent emission regulations. While the goal is the complete transition to sustainable and renewable energy sources, fossil fuel based power generation will continue to serve as a buffer source during times of high energy demand. Natural-gas based gas turbine power plants are preferred over coal fired plants for that purpose, due to their relative lower emissions and shorter ramp-up times. Most terrestrial gas turbine engine configurations utilize lean premixed jet stabilized flames for energy extraction. These highly turbulent flames provide the necessary thermal power densities and low NOx emissions but are prone to combustion instabilities. Combustion instabilities emanate from the resonant coupling between heat release, acoustics, and hydrodynamics in the combustor resulting in high-amplitude pressure oscillations. The growth of these oscillations can eventually reach large enough amplitudes to cause significant hardware damage.

The identification of coupling mechanisms leading to these dynamics and their mitigation has been subject of intense research, in which most experimental work has been conducted in combustors operating close to atmospheric pressure. However, in order to investigate the coupling processes relevant for practical combustors, the experimental configuration needs to replicate the multi-scale characteristics of the reacting flow field present in actual engines. For this purpose an optically accessible, natural gas fueled, high pressure model combustor has been designed. The single element combustor VIPER-S operates at jet Reynolds numbers of $5{\cdot}10^5$ and thermal powers of about 1.4 MW. Strong fundamental longitudinal instability behavior was observed for a technically-premixed configuration (TPC) of the combustor, in which equivalence ratio fluctuations and flame-vortex interactions act to drive and sustain combustion instabilities in the combustor. A fully-premixed configuration (FPC) of the combustor was designed to eliminate potential equivalence ratio fluctuations in the system and restrict the study of instabilities in the combustor to flame-

vortex interactions. In this configuration, in addition to longitudinal mode instabilities, high frequency transverse modes were observed. The dominant chamber modes were observed to be a function of the mixture temperature and equivalence ratio. High amplitude transverse modes were excited at particularly lean conditions, whereas richer flame operation resulted in low amplitude longitudinal dynamics. A first study revealed a connection between hydrodynamic perturbation modes of the jet shear layer and the type of chamber instability mode.

1.1 Combustion Instability And Jet Flames

The broad range of spatiotemporal scales present in turbulent jet-stabilized premixed flames make them susceptible to combustion instabilities through resonance with chamber acoustic frequencies. Fundamental insight into transverse instabilities in gas turbine combustors has been primarily gained through studies in canonical atmospheric or moderate pressure combustors with low thermal power densities that are accessible to laboratory scale operation and detailed diagnostics [1, 2]. These canonical investigations have provided fundamental insight to thermoacoustic interactions under laboratory settings. Complex chamber geometry, high flame-power density, and pressure found in actual engines however alter the turbulent scales involved in driving combustion instabilities. Therefore an accurate reproduction and scaling of these conditions is beneficial to assess coupling mechanisms at realistic levels of turbulence that drive high frequency multi-kHz instability modes that often result of the interaction between the turbulent flame and hydrodynamic processes [3].

Transverse instabilities in air-breathing combustors are often encountered in multi-injector combustor configurations through inter-element flame interactions. These have also been reproduced in single-injector configurations through external excitation using acoustic drivers or periodic forcing of the fuel-supply [4]. Such studies aid both, further understanding of the problem as well as the development of predictive capabilities for combustion dynamics through detailed and low-order computational models. Hum-

mel and Berger characterized a traveling 1T mode in a swirl-stabilized atmospheric burner, in which flame displacement and reaction zone deformation is shown to couple with the acoustic field of the burner leading to a sustained limit cycle [5, 6]. Self-excited transverse combustion instability in a jet-stabilized flame was investigated by Buschhagen et al [7] in a natural gas fueled combustor at 7 bar. The presence of high frequency dynamics was observed to be correlated closely with an asymmetric vortex shedding mode near the combustor dump plane. Longitudinal instability modes were dominant in the absence of this asymmetry.

Elevated power densities of rocket-type combustors paired with the extended range of spatiotemporal scales found in these flows compared to gas turbine type combustors, lead to an increased range of acoustic modes that can be excited by hydrodynamics interacting with the reaction layer. Studies in a gaseous methane fueled single-element shear-coaxial injector combustors demonstrated the effect of the inlet length on the excited longitudinal dynamics [8, 9]. Computational studies of this experiment showed that the unstable operation is connected to a periodic interruption of the fuel supply, caused by compression waves reflected from the sonic boundaries of the combustor inlet and outlet. The resulting periodic flame detachment and reignition of reactants downstream of the dump plane where classified into a post coupled and vortex convection mode. A change in the inlet length hereby altered the longitudinal system mode shape, which leads to distinct reignition processes of the unburned fuel causing the instability [10]. A non-stationary fundamental transverse mode in a single element liquid oxygen/methane propelled rocket combustor has been investigated in studies conducted at DLR [11]. The behavior of the transverse mode was characterized based on the comparison of the experimental data with analytical solutions of acoustic modes in circular ducts. A preferred orientation of the transverse mode was found to be linked to a combustor asymmetry.

Jet-stabilized combustor configurations are characterized by a simple geometry, reliable scalability, high fuel flexibility and low levels of NO_x emissions at high process temperatures, thus providing a strong alternative to swirl-stabilized configurations for terrestrial power generation [12–17]. The minimization of low velocity regions reduce the potential

for flashback and the high velocity ($u_{jet} > 100$ m/s) fuel-air mixture jets inhibit high axial momentum that yield strong levels of combustion product recirculation and thus a reliable flame stabilization mechanism. Vortices shed from the backward-facing step of the combustor significantly affect the degree of mixing and transport of fresh reactants into the combustion zone, which in turn modulates the heat release rate. Large scale vortices lead to bulk modulation of the flame, such as flame-front stretching, whereas smaller scales influence the mixing processes between product gases, originating in the recirculation zone, and incoming reactants and thus promote ignition. These scales are strong functions of the reactant jet velocity, local temperature and density which in turn are coupled to local pressure oscillations, representing the complex feedback loop leading to the natural propensity of these flames to unstable behavior [1, 18].

1.2 Hydrodynamic Instabilities in Round Jets

Hydrodynamic instabilities within the complex flow fields found in practical combustors are a fundamental link between pressure and heat release perturbations, as velocity perturbations interact with the reaction layer and can induce local fluctuations in energy release through flame surface alteration. As a major part of the reaction zone is located in the shear layer that forms between the recirculating region and the jet potential core, the flame is subject to the inherent instabilities of the confined jet flow. Eddies and subsequent larger coherent structures forming in the shear layer downstream of the sudden expansion, modulate the transport of heat, mass, and momentum within the reaction zone and lead to fluctuations in the flame heat release. The interaction between these turbulent flame processes and the resonant acoustic field are often linked through hydrodynamic characteristics of the flow, which are strong functions of velocity, temperature, and density. Local pressure oscillations in turn influence the gas properties which closes the complex feedback loop leading to the natural propensity to unstable behavior of turbulent flames. An asymmetry in the flow field promotes spatial asymmetries in the distribution of local heat release, which has the potential to drive transverse instability modes [19–25].

Jets develop instabilities in the mixing or shear layer generated between the jet itself and its environment. The axial growing shear layer structure acts like a waveguide in which initial disturbances can evolve into different types of instability modes that travel around the potential core of the spreading jet. These jet modes are characterized by their azimuthal wavenumber m, that describes the periodicity in the azimuthal coordinate.

The most unstable modes are the fundamental axisymmetric ($m = 0$) and helical modes ($m = \pm 1$), from which only one dominates the shear layer in the jet near field. The spatial mode of disturbances inherent in the pressure field close to the nozzle lip dictate the initial jet mode selection. Planar disturbances evolve into an axisymmetric jet mode, whereas azimuthal disturbances generate asymmetric modes. Random mode switching is observed when stochastic disturbances are present. The counter-rotating helical modes ($m = +1$ and $m = -1$) show essentially identical stability behavior, such that the a superposition of these modes is more likely to observe than a single helical mode instability. If both helical modes occur at the same frequency and amplitude, a flapping mode results, which is also considered as a fundamental mode. Forcing and superposition of all three fundamental modes leads to a bifurcating, trifurcating or blooming jet, where the generated vortices travel on distinct branches leading to spreading angles of up to 80°. Mixing and entrainment behavior of the jet differ substantially between the fundamental modes, where helical modes disintegrate over a shorter streamwise distance and thus transfer energy towards smaller turbulent length scales more efficiently compared to axisymmetric modes [26].

A study of Worth [27] showed that the shear layer of a round jet centered at the nodal line of a forced transverse pressure field is dominated by a flapping motion in the nozzle near field. The pressure field phase change over the nodal line introduces an asymmetry in the velocity field at the nozzle plane that leads to a periodic asymmetric shear layer roll-up. This process generates two vortex rings for a forcing cycle that are inclined about the jet axis at opposed angles. While convected downstream by the mean flow, the vortex rings induce a velocity field upon each counterpart, forcing them to incline further towards the jet axis. This process leads to strong interaction between the vortex rings and rapid break down, causing an increased jet spreading rate compared to axisymmetric forcing.

Single mode characteristics can be assessed through linear stability analysis of the jet mixing layer [28]. In general the jet shear layer becomes more stable with growing axial distance from the ejection plane, as the shear layer growths in width and the flow gradients relax. For lower frequency regions the azimuthal instability ($m = 1$) shows consistently larger growth rates compared to the axisymmetric mode, whereas for the higher frequency the opposite is true. The critical frequency for which the dominant mode switch occurs is increasing in the streamwise direction. An increase in jet Mach number leads to a stabilization of both modes and mitigation of higher frequency oscillations, with the helical mode being less affected than the axisymmetric mode. A confined jet is subject to a coaxial flow generated by the recirculation zone, which can be estimated as $U_\infty = 0.22 * U_0$ [29]. Both modes are stabilized with increasing external flow magnitude, whereas the range of unstable frequencies is extended.

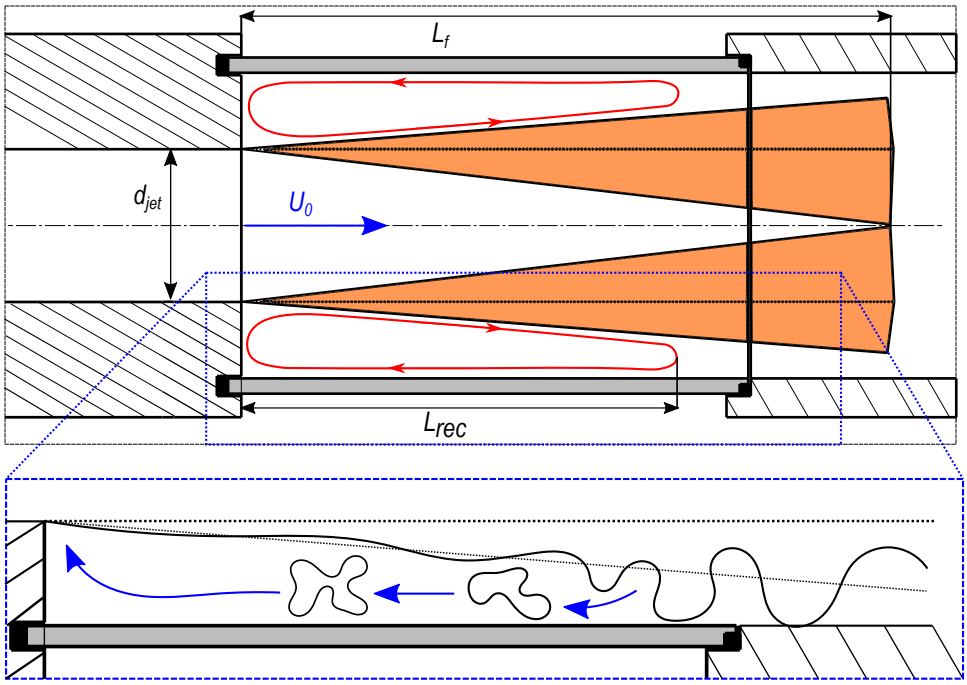

Figure 1.1. Recirculation zone schematic and convective transport of turbulent fluid pockets, adapted from [29]

The recirculation zone generated around the confined jet plays an important role in the flame stabilization process, as it transports hot products towards the reaction zone and thus

promotes the ignition of incoming reactants. The spreading angle of a fully turbulent jet ($Re = \rho U_0 D/\mu > 4000$) is constant and estimated at $\approx 20^\circ$ [29], thus the extent of the recirculation zone (L_{circ}) or the location of flow reattachment is only a function of the step height H. As the jet spreads in diameter in the streamwise direction a positive pressure gradient towards the jet nozzle is generated. Fluid particles located in the outer shear layer region are redirected at the stagnation or reattachment point and flows upstream due to that pressure gradient. Simultaneously the jet entrains fluid out of the created cavity, causing a pressure gradient towards the jet axis and ultimately the circular motion. Recirculation zones have been shown to undergo self-sustained oscillation, for which the actual reattachment location fluctuates. The observed oscillation frequency of this periodic motion is about two orders of magnitude lower than the preferred jet mode, which is usually found in the region of $St = fD/U_0 = 0.3...0.5$.

1.2.1 Linear Stability Analysis

Spatiotemporal linear stability analysis (LSA) has been successfully applied to determine the stability characteristics of complex flow fields, in which a distinction is made between convectively (CU) and absolutely (AU) unstable flows. CU flows feature perturbations that grow downstream of an initial impulse in space and time, but decay at the point of initial impulse. In contrast, AU modes do not decay in time at the point of impulse and have the potential to contaminate the whole flow field, if the absolutely unstable region is sufficiently large, yielding a global mode with a behavior comparable to a self-excited oscillator. [30, 31, 31, 32].

Juniper [33, 34] performed LSA of planar and round jet/wake flows and assessed the effect of flow confinement, velocity ratio Λ, and density ratio S between the inner and outer flows. Two instability modes in these type of flows are found, where the first mode is associated with the instability of the shear layer itself, characterizing the roll-up process due to the velocity difference between the inner and outer fluid layers with axial wave numbers that scale with the local shear layer width. The second mode is associated with

the bulk motion of the jet/wake at larger axial wavelength compared to mode 1, which leads to bulging ($m = 0$), spiraling ($m = \pm 1$) or flapping (combined $m = +1$ and $m = -1$) of the jet/wake body depending on the involved azimuthal wave numbers m. The shear layer instability (mode 1) in round jets is usually absolutely unstable for counter-flow configurations (except for $S > 2$), whereas for co-flow configurations this mode is never absolutely unstable. Mode 2 is more sensitive to changes in Λ and S leading to complex stability maps in this parameter space. The bulk motion of the jet/wake (mode 2) is seen to manifest as the fundamental mode (modes with zero group velocity, i.e. the wave behavior at a fixed location) of the inner flow and the contrary is found for strongly confined flows. At intermediate confinement levels, the fundamental modes of bulk motion of the inner and outer flow interact and are seen to generate combined modes due to resonance if their wave numbers are compatible, generating a standing wave. These flows are particularly unstable, whereas flows with larger wave number separation in the inner and outer regions are generally more stable.

LSA applied to combustion instability problems can help to elucidate the nature of the underlying coupling mechanisms, where the concepts of convective and absolute flow instabilities are employed [35–37]. Often instability modes are readily assigned to acoustic eigenfrequencies of the combustor geometry, for which the acoustic field of the enclosed flow field resonates due to the synchronization of acoustic perturbations and heat release fluctuations, which result from alterations of the reaction layer by hydrodynamic perturbations. The existence of modes with frequencies that are non-acoustic points to the presence of an AU global mode of the flow, for which the flow field itself acts as a resonator. Both scenarios can be achieved by convective and absolute flow instabilities. AU modes are self-sustained hydrodynamic oscillations that in turn yield heat release fluctuations due to flame-flow interaction, which result in pressure oscillations at the global mode characteristic frequency, given that the acoustic field does not provide sufficient damping at that frequency. AU flows with characteristic frequencies similar to combustor acoustic eigenmodes generate high amplitude limit-cycle behavior. CU flows readily amplify flow perturbations over a wide range of frequencies, though a preferred frequency exists for which

the downstream amplification is maximum. If the preferred frequency is similar to natural acoustic resonance of the combustor, the flow-acoustic coupling sustains the convective instability, yielding synchronized heat release fluctuations that in turn provide energy to the acoustic field.

Ghoniem *et al.* summarized evidence for the existence of AU global modes in shear-stabilized premixed combustion systems [35]. Focusing on a backward-facing step configuration, a global mode was identified that characterizes the shedding of coherent vortices and the subsequent pairing of these in the region of recirculating flow, that exists for lean and near stoichiometric operation points. The frequency of this process is a function of the downstream distance of the sudden expansion, from where the Strouhal number decreases from $St = fH/U = 0.3$ to 0.083 halfway through the recirculation zone length. This transition in frequency is paired with a growth in amplitude of the corresponding hydrodynamic fluctuations, starting from the center of the recirculation zone to the point of flow reattachment, from where the amplitude decays in the downstream direction. An isothermal LSA at several axial locations of the base flow obtained from a numerical simulation for this configuration revealed that the most unstable mode, which is the wake/recirculation zone mode associated with the vortex shedding/pairing process described above, is AU from the center of the recirculation zone to the point of flow reattachment. The mode is CU downstream of the reattachment point and in the near field downstream of the sudden expansion. The frequency of the mode was found to be constant within the range of absolute instability, corresponding to the characteristic global mode frequency $St = 0.083$. A subsequently performed LSA with analytical velocity and temperature profiles, allowed to assess the mode sensitivity to the magnitude of back-flow, the shear layer thickness, temperature ratio and offset between maximum shear stress and temperature inflection point. High back-flow magnitudes paired with small shear layer thicknesses were found to support a CU to AU transition of the global mode. Small flame-shear offsets, the distance between the maximum of shear stress and the temperature inflection point, paired with low temperature ratios were found to support absolute instability, explaining the suppression of the AU mode for intermediate equivalence ratios. The flame-shear offset increases with down-

stream distance, as the center of the shear layer slopes towards the containment wall while the reaction layer moves towards the jet center while consuming the mixture. The flame-shear offset also increases with equivalence ratio, as the reaction layer is able to anchor in higher velocity regions due to the increased turbulent flame speed. Large flame-shear offsets paired with high temperature ratios also showed to support AU modes, where these parameter combinations are associated with locations downstream of the recirculation zone in stoichiometric mixtures, consistent with the experimental observations.

Manoharan *et al.* [37] performed a similar study on a modeled base flow for a backward-facing step configuration, yielding similar results for the affect of back-flow magnitude and shear layer thickness on the transition from CU to AU for the most unstable mode, which they associate with the Kelvin-Helmholtz instability in the shear layer. A collocation of the inflection points within the density and velocity profile was found to suppress an AU mode and a positive/negative displacement was found to decrease/increase the mode growth rate, representing the reaction layer moving towards the jet center or recirculation zone respectively. The interaction of the velocity perturbations and the base flow vorticity gradient was found to be responsible for the Kelvin-Helmholtz instability and the vorticity production due to baroclinc mechanisms either further amplifies or dampens the mode, depending on the location of the reaction layer relative to the shear layer center.

Oberleithner *et al.* [38] applied spatiotemporal LSA to an atmospheric swirl-stabilized flame and studied the influence of the flame shape on the existence or suppression of a precessing vortex core (PVC) located in the shear layer separating the inner recirculation zone from the annular swirling jet. Here the density profile associated with the different flame shapes studied was found to determine if the global flow field mode related to the presence of the PVC is AU or CU. An detached flame, leading to a more homogeneous density field close to the burner inlet allows for the AU mode and the PVC is present, for an attached flame the strong gradients in the density field dampens the mode and no PVC forms. Turbulence models used to close the viscous incompressible Navier-Stokes equation system used for the study were found to influence the growth rate predictions, although the frequency prediction was found to be independent of the closure method.

Paredes *et al.* [39] compared the predictive capabilities of local and global LSA, for which the LSA is formulated within the entire domain of interest, rather then at distinct axial locations for which the parallel flow assumption holds. A similar atmospheric swirl-stabilized flame at different conditions, some displaying a PVC, with drastically varying flame shapes were analyzed. The local LSA predicted global mode frequencies and growth rates were comparable to the global analysis for flame cases with lower swirl numbers, closer resembling a parallel flow, whereas a global analysis is necessary in cases where the flow is highly non-parallel and the local analysis yields overestimated growth rates.

1.3 Objectives

Combustion dynamics in model gas turbine combustors have been extensively studied at atmospheric conditions. While this work provides fundamental insight into the underlying mechanisms leading to coupling between hydrodynamics, heat-release and acoustics, the involved spatiotemporal scales of the reacting flow field change drastically with thermal power densities. The objective of this work is to study the stability of a canonical premixed turbulent jet flame to changes in operation condition. The underlying coupling mechanisms leading to the excitation of different modes at elevated pressure are of interest and this work aims to extend the knowledge gained from work performed at atmospheric pressure. Hereby different fuel injection schemes are considered, to delineate the influence of system coupled excitation and flow field intrinsic mechanisms that lead to self-excitation of longitudinal and transverse modes in an axisymmetric jet flame. The structure of the document that summarizes the efforts towards this objective is briefly outlined below.

1. A “technically-premixed” configuration (TPC) of the experimental combustor was used to study the fundamental longitudinal mode (1L) sensitivity to flame conditions and fuel injection position relative to the sudden-expansion. The experimental configuration is described in chapter 2.1 and the results from this study are laid out in chapter 3.

2. The dynamics observed in TPC indicated that the 1L mode is driven by a combination of global equivalence ratio fluctuations ϕ' and axisymmetric shear layer dynamics altering the flame structure. The focus on the following study laid in characterizing these hydrodynamics and a "fully-premixed" configuration (FPC) of the combustor was designed, which allowed to eliminate potential ϕ' as driving mechanism of the longitudinal dynamics. The FPC hardware is described in chapter 2.2 and the results are summarized in chapter 4.

3. Self-excitation of the 1L and fundamental transverse chamber mode (1T) was observed in the parametric study conducted in FPC. Corresponding flame dynamics indicated different types of shear layer coupling for these instabilities, where axisymmetric emission patterns observed in OH^* emission imaging correspond to axisymmetric instabilities in the shear layer, that effectively couple with longitudinal unstable modes in the chamber. Transverse modes in contrast were seen to couple with an asymmetric shear layer roll-up process and a flapping motion of the flame. These results suggested that shear layer hydrodynamics affect the instability mode selection in this flame configuration. A parametric study was carried out to test this hypothesis and investigate the 1T mode sensitivity to changes in system pressure and injector velocity. An inlet immersion was also tested for which resonators were added as an attempt to reduce the 1T limit-cycle amplitude. These results are detailed in chapter 5.

4. The observed dynamics in FPC lead to the hypothesis that shear layer instability modes determine the selection of the instability regime for a given flame condition. To test this hypothesis a linear stability analysis (LSA) of the underlying base flow field was performed. The model formulation and base flow reconstruction is laid out in chapter 6 and tested against analytic solutions of duct acoustics.

5. Chapter 7 describes the application of the linear stability model to a representative set of FPC test, that show distinct combustion instability regimes for changes in

operation condition. The temporal LSA results indicate that the preferred shear layer modes correlate well with the resulting instability mode.

Chapter 8 summarizes the findings of this work and its potential use in the design of high power-density gas turbine combustors.

2. EXPERIMENT DESIGN

The single element natural gas (NG) fueled model combustor, VIPER-S (Versatile Intermediate Power Experimental Rig- Single element) was designed to promote self-excited combustion instabilities in a canonical experiment operated at conditions typical of gas turbine combustors used for power-generation. The typical specific thermal power density was 37 $MW/m^2.bar$ (based on the burner surface area). The combustor was operated at a mean chamber pressure of 8 bar (maximum design pressure of 22 bar) with an air temperature of 600-923 K. Two distinct hardware configurations of the experiment were evaluated, with several geometrical and operating parameter variations for both. The "technically-premixed" configuration (TPC) comprised of an injector provided by Siemens Energy, Inc. that was installed in a premixing length. The length of the premixing duct along with the injector geometry resulted in 'technically' premixed injection of reactants into the combustor. The second configuration comprised of an external premixer where reactants were premixed. The combustor was isolated from the external premixer using a choked orifice plate which ensured an isolation of the reactant supply from the chamber dynamics. This configuration is identified as "fully-premixed" configuration (FPC) for the rest of the document. The geometrical details and experimental diagnostics of TPC and FPC are highlighted in the current chapter.

2.1 Technically-Premixed Configuration

2.1.1 Design

The TPC is designed to promote self-excited combustion dynamics at frequencies corresponding to the fundamental longitudinal (1L) chamber mode. The combustor is capable of operating at chamber pressures up to 22 bar, inlet air temperatures of up to 923 K and

mass flow rates of 1.3 kg/s, conditions typical for land based power generation gas turbine engines. A schematic diagram of the three TPC of the combustor is presented in Figure 2.1 and a detailed description of the supporting infrastructure has been reported previously [40]. The three configurations differ in their effective premixer duct length, varying the baseline length of $l_{inj} = 395$ mm for configuration 1 by $\pm$ 40 mm for configuration 2 and 3 respectively.

The experiment is divided into an air plenum, a premixer, and the combustion chamber. The plenum provides a large volume upstream of the premixer to dampen any response of the air supply to the dynamics in the combustion chamber. Air enters the plenum through a choked sonic nozzle to provide a well-defined acoustic and flow inlet boundary condition. The premixer supports the injector assembly and creates a cross-sectional area reduction from the plenum to the premixer duct. A backward-facing step stabilizes the flame downstream of the jet-exit into the combustor, which features a cylindrical optical access at its upstream end for optical diagnostics of the combustion zone. The chamber length is designed to obtain the desired fundamental longitudinal (1L) mode frequency of $\approx$ 330 Hz and can be varied in discrete increments to alter this frequency. A choked nozzle at the exit of the chamber provides a well-defined acoustic exit boundary condition and enables system pressurization. Table 2.1 along with Figure 2.1 provide geometry information to replicate the system for low order models and simulation purposes.

Table 2.1. Design Envelope for the VIPER-S TPC

Geometry	Dimension
Effective Premixer Duct Length	353 / 393 / 433 mm
Premixer Duct Diameter	40 mm
Combustion Chamber Diameter	80 mm
Combustion Chamber Length	1200 mm

The double-windowed configuration is used to provide optical access at the head-end of the combustion chamber, in order to ensure safe operation of the system in the presence

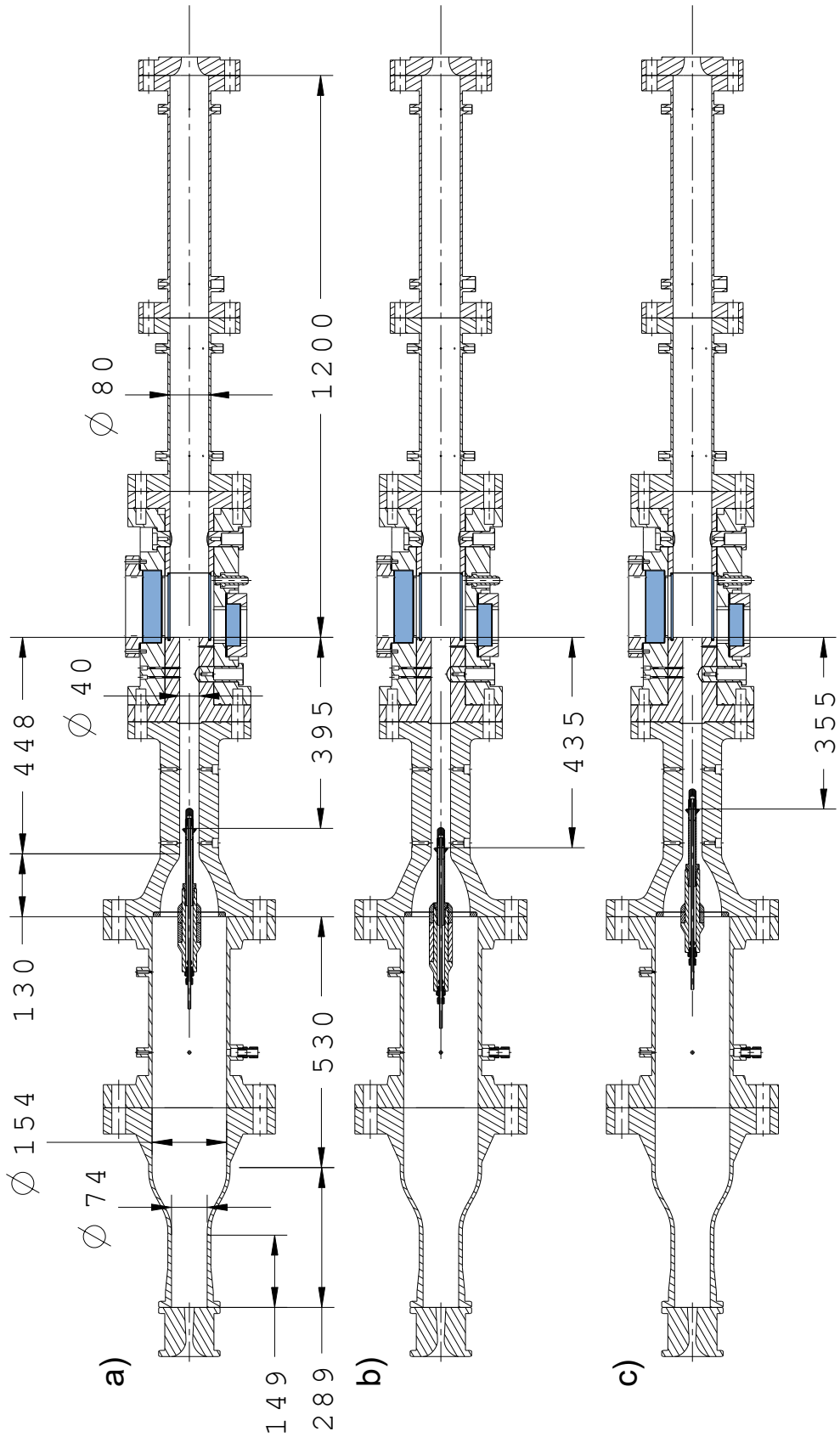

Figure 2.1. Technically-Premixed Configurations of VIPER-S: a) Config. 1, b) Config. 2 and c) Config. 3

of potential high amplitude pressure fluctuations. A quartz tube, supported by two interface flanges, provides the chamber geometry definition and is subjected to the thermal load from the flame. The thickness of the quartz tube is limited to 3.125 mm to limit optical distortion through the curved surfaces of the tube and minimize steep thermal gradients in its thickness. The quartz tube is surrounded by a pressurized cavity, which is connected to the plenum of the combustor. This interface allows the pressure differential over the quartz tube to be minimized during ignition events and the combustion period. The internal pressure of the cavity is contained by outer windows, which are relieved of strong temperature gradient changes due to the cavity volume and thus primarily support the pressure load during operation.

Combustion instabilities occur through a feedback mechanism between flow-field fluctuations (u'), heat release fluctuations (q') and acoustic pressure oscillations (p') in the combustor. To sustain self-excited instabilities, the pressure and velocity fluctuation amplitudes at the location of fuel injection and at the combustion zone and their phase relationship with heat release from the flame are critical. In the design phase, Linearized Euler Equations (LEE) were solved in the acoustic module of COMSOL® to determine the pressure and velocity mode-shapes of the combustor [41–43] at target instability frequencies. In order to mimic the flow properties throughout the combustor domain, gas property profiles are generated based on estimated gas properties. These profiles include pressure adjustments due to flow acceleration and deceleration as well as pressure losses. Temperature is adjusted corresponding to flow velocity changes throughout the domain, fuel injection and combustion occurring downstream of the dump plane. Changes in flow composition within the premixer due to fuel injection and downstream of the dump plane due to combustion are captured in the profile of specific heat for constant pressure c_p as well as in the profile for molecular weight. Density in the domain is then computed based on the ideal gas law. The highest Mach number between the choked inlet and outlet boundaries of the system occurs in the premixer with $M < 0.23$. The frequency shift associated with mean-flow is considered to be small and was neglected.

Figure 2.2 shows the acoustic pressure mode shape in the system, which corresponds to a 1L mode in the chamber at 330 Hz. The pressure field in the premixer establishes anti-nodes at the inlet and exit of the premixer, promoting a pressure coupled response between premixed duct and the combustion chamber.

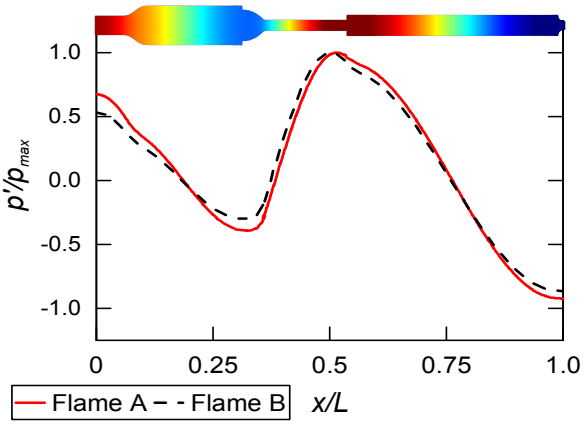

Figure 2.2. Computation results for 1L chamber pressure mode

2.1.2 Instrumentation and Diagnostics

Pressure and Temperature Measurements

The pressure and temperature instrumentation used in the TPC combustor is indicated with colored markers in Figure 2.3. An array of high frequency piezoresistive pressure transducers (Kulite WCT-312M-10/35BARA;0.1% FSO), is installed throughout the combustor (indicated in blue) and sampled at the standard facility rate of 180 kHz (DSPCon DataFlex-1000). The transducers are installed in a recessed cavity with a port resonance frequency ($>$ 9 kHz) significantly higher than frequencies of interest in this study. Table 2.2 specifies the axial location relative to the dump-plane and their respective azimuthal position as indicated in Figure 2.3. Low frequency pressure transducers (GE Sensing UNIK50E6) with an accuracy of 0.04% FSO (indicated in green), and Omega K-type thermocouples (indicated in red) are sampled at 100 Hz and located at multiple axial locations

throughout the combustor and in the fluid supply system. These measurements are used for condition monitoring during test operation.

Table 2.2. VIPER-S TPC HF probe locations

HF Probe	001	002	003	004	005	06A	06B
x (cm)	/	-70.0	-42.5	-27.5	-7.5	20	20
θ (°)	/	0	0	0	0	0	180
HF Probe	07A	07B	008	09A	09B	09C	010
x (cm)	68	68	104.5	54	54	54	-86.5
θ (°)	0	180	0	0	180	315	0

OH* Chemiluminescence Imaging

Chemiluminescence measurements are commonly used as a qualitative indicator of the spatio-temporal dynamics of the heat release rate from hydrocarbon flames. OH*, CH* and C_2 are the most common species used for chemiluuminescence detection. The OH radical luminescence mainly forms through the reaction: $CH + O_2 = CO + OH$ which occurs in the reaction zone of the flame. The OH* concentration then decays in the combustion products with emission peaks at 306.36, 306.76 and 309.04 nm [44, 45] wavelengths. The OH* chemiluminescence measurements in this work are performed at 10 kHz through the optically accessible section using a high-speed camera coupled to a UV image intensifier (Phantom V411 and LaVision HS-IRO, respectively). A mirror is placed in front of the combustor side window with a 45° angle with respect to the combustor axis. The reflection is then imaged through a 50 mm optical band-pass filter centered at 320 nm (Semrock 320/40 BrightLine® Bandpass) and UV-lens (Sodern 98 F/2.8 type CERCO® 2178) assembly with an image size of 800 by 456 pixels resulting in a final resolution of 0.175 mm/pixel.

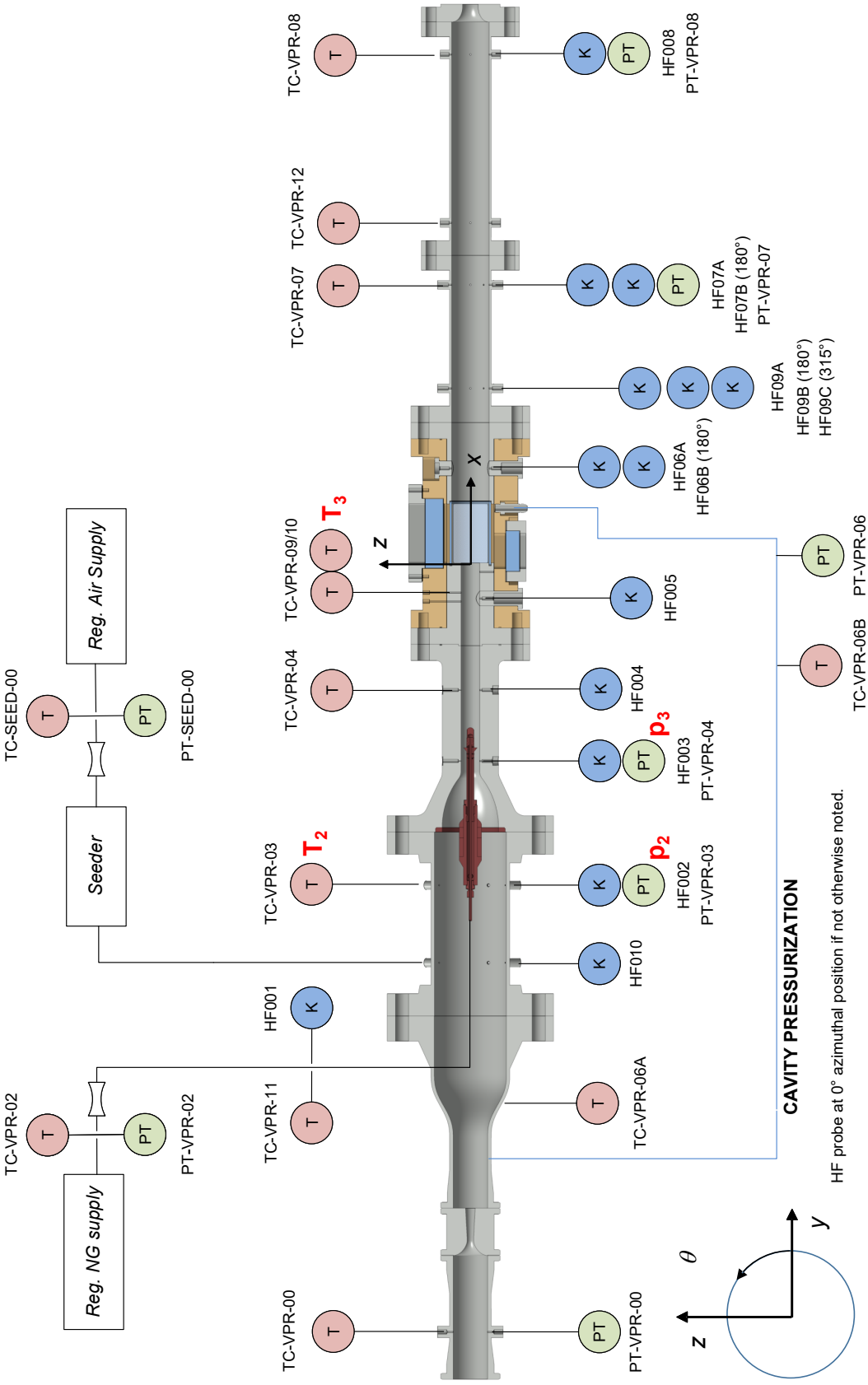

Figure 2.3. Instrumentation of VIPER-S TPC

Particle Image Velocimetry

Particle Image Velocimetry (PIV) measurements at the central axial plane of the TPC hardware were performed at a repetition rate of 10 kHz. The technical specifications of the laser system and the experimental configuration used for these measurements are summarized in Table 2.3 and Figure 2.4.

Table 2.3. DPSS based axial plane PIV system specifications

DPSS System		CMOS Camera		Seeding System	
Pulse Rate	10 kHz	Type	Phantom V411	Material	TiO_2
Pulse Power	6-8 W	fps	20k	$\bar{d}$	1.5 μm
Pulse Sep.	4-6 μs	Exposure	48.9 μs	$\dot{m}$	$0.05\dot{m}_{air}$
Pulse Len.	200 ns	Resolution	384 x 384 px	λ	85%

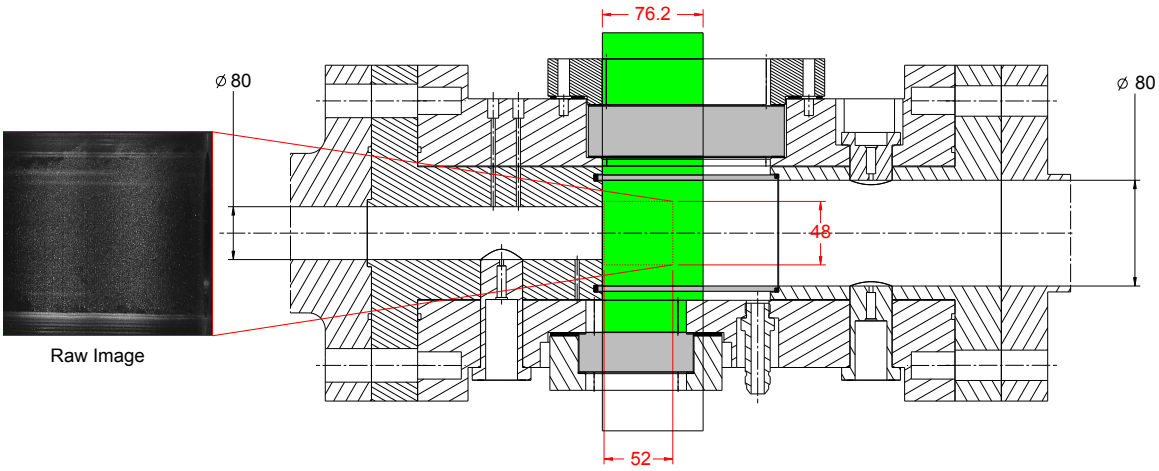

Figure 2.4. Axial plane PIV configuration for VIPER-S TPC, all dimensions in *mm*

2.2 Fully-Premixed Configuration

2.2.1 Design

The dynamics encountered in the technically-premixed configuration suggested that flame-vortex interactions amplify the equivalence fluctuation based feedback loop leading to the strong 1L instability. The fully-premixed configuration (FPC) was designed to replicate the frequency of dynamics observed in the TPC with the elimination of potential equivalence ratio fluctuations in the injection system. The simplified premixed injection scheme with premixed reactants helped study the flame-hydrodynamic interactions in the presence of the chamber acoustics in a canonical jet-stabilized flame at operating conditions and confinement typical of a practical gas turbine combustor. The sensitivity of the chamber instability mode on the mixture jet properties ϕ and T_3 are of interest.

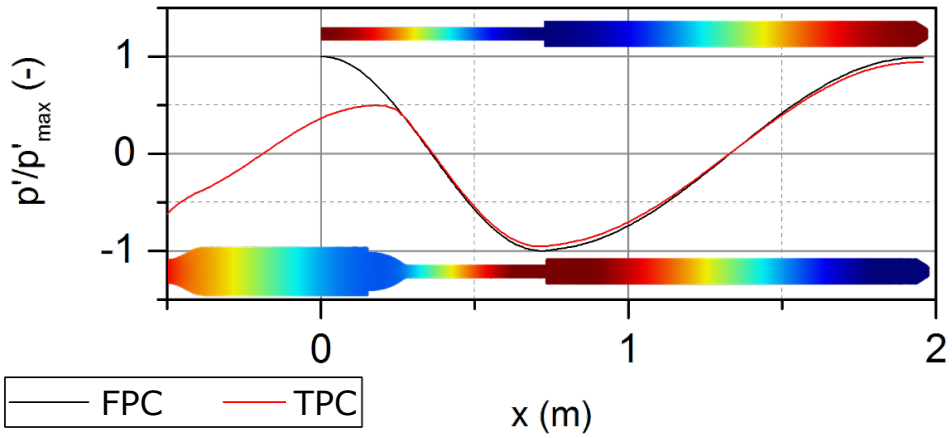

Figure 2.5. Computed 1L chamber pressure mode shape for TPC and FPC

Linearized Euler equations were again used for the design of premixed duct lengths in the FPC design. The length of the duct was scaled to replicate the acoustic mode-shape present in the TPC configuration. Using identical gas property profiles in the TPC geometry and the new combustor design, an Inlet duct length of 720 mm was determined. This length closely corresponds to a half-wave acoustic modeshape at the chamber 1L frequency. A

comparison of the computed pressure mode shape at the chamber 1L frequency is shown in Figure 2.5. To decouple the reactant supply completely from the combustor dynamics, the inlet duct needs to satisfy the acoustic boundary condition $u' = 0$, leading to a pressure anti-node at the upstream end of the inlet section. The final inlet duct length results in a system pressure mode shape that replicates the TPC configuration, allowing comparison of dynamics between the two configurations.

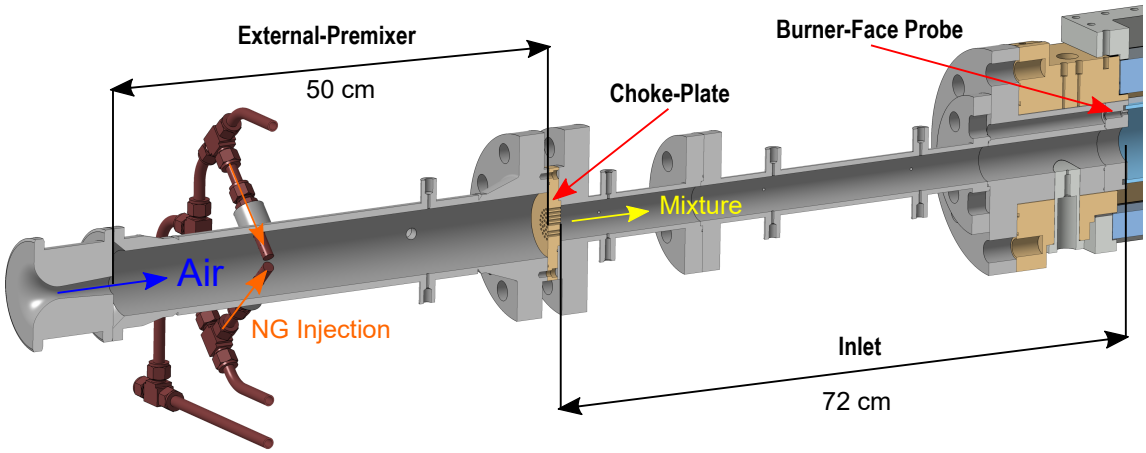

Figure 2.6. Isometric view of VIPER-S FPC Hardware

Figure 2.6 shows an isometric view of the FPC hardware, which is divided into an External-Premixer, Choke-Plate, two Inlet sections and a modified Inlet-Flame-Cube interface that connects the FPC hardware with the VIPER-S combustion chamber. The External-Premixer supplies the reactant mixture to the modified combustor. Preheated air is injected through a sonic metering nozzle in the 3" pipe body. Natural gas is injected through four 1/2" fuel lances, that each inject fuel in a counter-flow scheme through six 0.027" orifices.

The External-Premixer performance was assessed through an ANSYS simulation using the CFX module. The internal premixer geometry including the injection lances were modeled and, based on symmetry considerations, split along the XY-plane. The resulting mesh included the internal geometry of the air CFVN from the nozzle throat downstream, in order to simulate the high velocity jet exciting into the External-Premixer. The mesh

is comprised of tetrahedrons with an average cell size of 2 mm, resulting in $\approx$ 1 million elements. To solve a compressible flow problem with sonic/supersonic regions within the domain the heat transfer option "Total Energy" was chosen. The Shear-Stress-Transport (SST) turbulence model is used because of its suitability for flow fields with strong velocity gradients (strong shear flow). A summary of simulated operating parameters is tabulated in Table 2.4.

Table 2.4. CFX Simulation Parameters

$\dot{m}_{air}$	$\dot{m}_{NG}$	ϕ	T_{air}	T_{NG}	p_2	$p_{air,0}$	p_{air}	$T_{air,0}$
0.26	0.011	0.7	723	298	7.52	23.5	14.494	723
kg/s	kg/s	-	K	K	bar	bar	bar	K

The objective of this simulation was to determine the mixing efficiency of the dip-tube injection concept and determine the necessary External-Premixer length. The simulation domain fluid was defined as an ideal gas mixture of air and NG, where the NG properties $MW = 17.306$ g/mol, $c_p = 2.3$ kJ/kg/K, $\mu = 4.5 \cdot 10^{-6}$ Pa·s and $k = 1.43$ mW/m/K are prescribed. The air inlet was defined as pressure inlet, with a prescribed total ($p_{air,0}$) and static (p_{air}) pressure and total temperature $T_{air,0}$ in the supersonic flow regime. A zero NG mass fraction (x_{NG}) is set at the air inlet. The fuel lance inlet was defined as constant mass flow inlet with $x_{NG} = 1$. The domain outlet was defined as a constant mass flow outlet with a prescribed total mass flow rate of $\dot{m}_{tot} = \dot{m}_{air} + \dot{m}_{NG}$. The domain intersection with the XY-plane was defined as symmetry boundary and all walls were defined as smooth, no slip and adiabatic walls. The simulation was terminated once the RMS values for mass, momentum, turbulent kinetic energy (TKE), system enthalpy and NG mass fraction asymptotically converged.

To evaluate the mixing performance the "unmixedness" (UM) of the flow at XZ-plane downstream of the NG injection location was computed as:

$$UM = \frac{stdev(x_{NG})}{\overline{x_{NG}}} \tag{2.1}$$

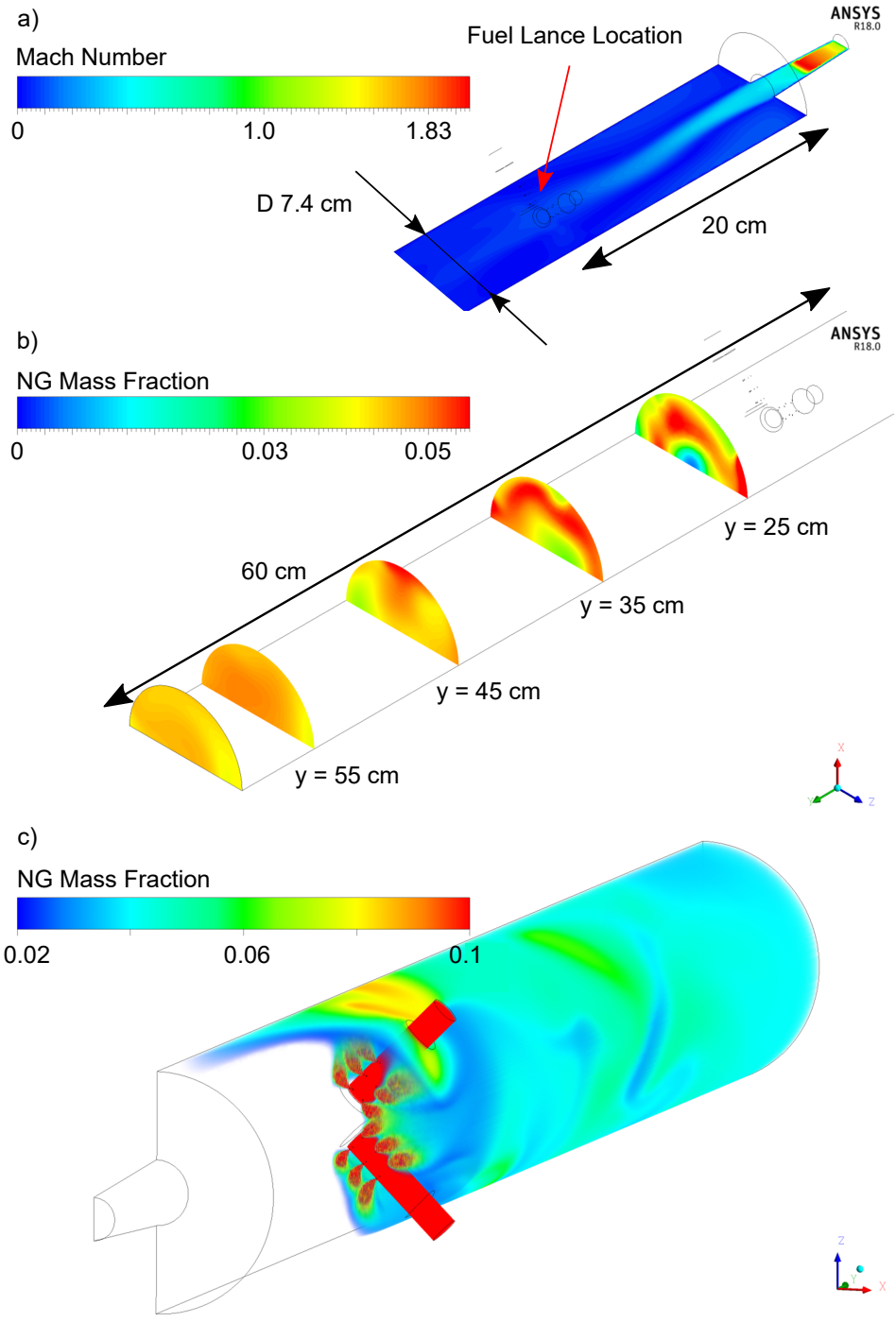

Figure 2.7. a) X-Y plane Mach Number contour b) X-Z cross-sections of the NG mass fraction and c) isometric view of the volumetric rendering of the NG mass fraction in the simulation domain

A Mach number contour plot, XZ cross-sections of the and a volumetric rendering of the NG mass fraction distribution in the simulation domain is given in Figure 2.7. From these results a premixer length of 0.5 m was presecribed, based on a $UM < 2\%$ value at an axial length of 0.55 m.

The orifice plate (Choke-Plate) downstream of the external premixer provides a sonic flow interface that decouples the reactant supply from the combustor dynamics, eliminating fluctuations in the equivalence ratio ϕ. The total pressure ratio of $p_{u,0}/p_{d,0} \approx 2$ over the Choke-Plate was chosen to ensure critical flow conditions throughout the combustor operation envelope. 53 holes with a diameter of 2.53 mm comprise the interface between Inlet and External-Premixer with an overall discharge coefficient of $C_d \approx 0.85$. The restricted flow area is 93.7% based on the External-Premixer duct area of $A = \pi/4 \cdot 0.074^2$ with $t/D = 0.628$, where t is the Choke-Plate thickness and D the orifice diameter.

The Inlet is comprised of two sections to allow discrete changes in the premixed duct length. The original fully-premixed hardware is sized to present half-wave acoustic mode-shape in the Inlet duct for a fundamental longitudinal mode (1L) in the combustion chamber with a total Inlet duct length of $\approx$ 720 mm (see Figure 2.5). Removal of the first Inlet section decreases the Inlet length by a factor of ≈ 2, which allows to study the effect of duct-chamber coupling on the chamber dynamics. The Inlet sections and the Choke-Plate were designed with metal o-ring sealed interfaces and centering features to smooth duct geometry and repeatable assembly.

Several modifications to improve ease of assembly and additional instrumentation were made in the combustor configurations over the period of the study. Hardware modifications were made to imporve following features of the experiment:

1. Pressure measurements at the burner-face
2. Increase spatial pressure resolution at chamber head-end
3. Provide additional optical access for introduction of laser induced spark-ignition

The improvements in the hardware isolated near the chamber dump plane are summarized in Figure 2.8. To allow for pressure measurements at the burner-face the interface between

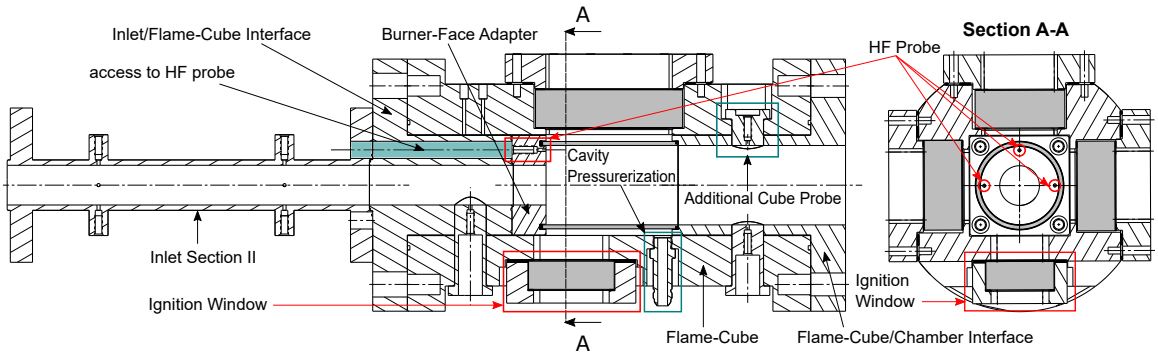

Figure 2.8. Modified FPC hardware with burner face dynamic pressure ports

Inlet sections and Flame-Cube was redesigned and separated into two parts. The Burner-Face Adapter features three HF probe ports clocked by 90° about the combustor axis. The intention for these measurements was to spatially resolve the high frequency transverse and azimuthal modes that were observed in the FPC configuration. The Adapter is mounted on an interface plate and the probes and flow path are sealed with a combination of two metal o-rings. The interface between probe and Adapter is sealed with copper gaskets, which is the usual seal used for HF instrumentation throughout the system. The cooling water tubing and instrumentation cables are fed through three access ports in the redesigned interface flange and modified Inlet section. Cables and tubing are protected from the combustor surfaces through a heat-shielding sleeve that extents from the probe through the access ports.

An Ignition Window was added to utilize all three windows for imaging purposes and laser sheet access to the flame zone. Due to this addition the cavity pressurization port needed to be modified and was included in the Flame-Cube, instead of a blank insert that occupied the Ignition Window pocket in the TPC hardware. Pressure is equalized between the flame tube cavity and chamber center (1L chamber mode node) in the FPC hardware, to avoid cavity contamination with mixture from the inlet duct.To increase the spatial pressure resolution at the chamber head-end a second HF probe insert was included directly opposed of the original insert, to allow for the detection of transverse modes in the flame zone.

The remaining components of the FPC hardware are identical to those used in the TPC experiments, which are detailed in section 2.1. Table 2.5 along with Figure 2.6 and 2.9 provide geometry information to replicated the system for low order models and simulation purposes.

Table 2.5. Design Requirements for VIPER-S FPC

Geometry	Dimension
Inlet Duct Length	720 mm
Premixer Duct Diameter	40 mm
Combustion Chamber Diameter	80 mm
Combustion Chamber Length	1200 mm

2.2.2 Instrumentation and Diagnostics

Pressure and Temperature Measurements

All instrumentation utilized in the FPC combustor is indicated as colored markers in Figure 2.9. An array of high frequency piezoresistive pressure transducers (Kulite WCT-312M-10/35BARA;0.1% FSO), is installed throughout the combustor (indicated in blue) and sampled at the standard facility rate of 180 kHz (DSPCon DataFlex-1000). Table 2.6 specifies the axial location relative to the dump-plane and their respective azimuthal position as indicated in Figure 2.9. A high-frequency transducer installed in the External-Premixer is monitored to ensure isolation of the premixed reactant supply from the combustor dynamics. Low frequency pressure transducers (GE Sensing UNIK50E6) with an accuracy of 0.04% FSO (indicated in green), and Omega K-type thermocouples (indicated in red) are sampled at 100 Hz (1 kHz in ZL8) and located at multiple axial locations throughout the combustor and in the fluid supply system. These measurements are used for condition monitoring during test operation.

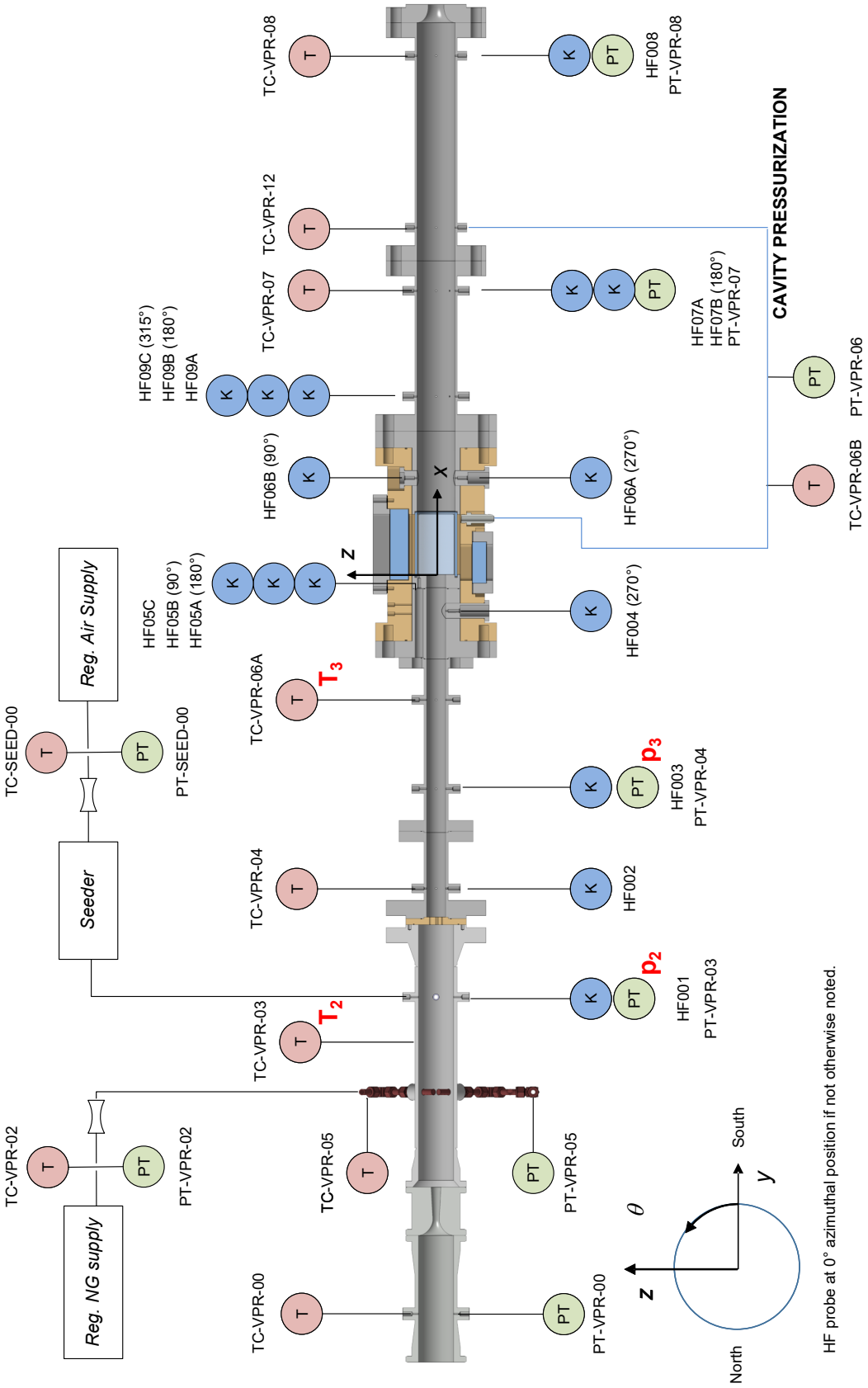

Figure 2.9. Instrumentation of VIPER-S FPC

Table 2.6. VIPER-S FPC HF probe locations

HF Probe	002	003	004	05A	05B	05C	06A
x (cm)	-66	-45	-7.5	0	0	0	20
θ (°)	0	0	0	180	90	0	0
HF Probe	06B	07A	07B	008	09A	09B	09C
x (cm)	20	68	68	104.5	54	54	54
θ (°)	180	0	180	0	0	180	315

OH* Chemiluminescence Imaging

Chemiluminescence (CL) emission images, from electronically excited hydroxyl radicals are recorded at 50 kHz in the optical section of the combustion chamber. A UV filter, centered at 320 nm with 40 nm bandwidth (Semrock 320/40 Brightline Bandpass), isolates the signal from background luminosity. The light is collected by a 98 mm focal-length, f/2.8 objective lens (Cerco Sodern Type-2178), then amplified by a Lambert HiCATT 25 intensifier with 1:1 relay lens, and recorded with a Phantom v2512 high speed CMOS camera with a spatial resolution of 0.197 mm/pixel. The CL imaging configuration is shown in Figure 2.10.

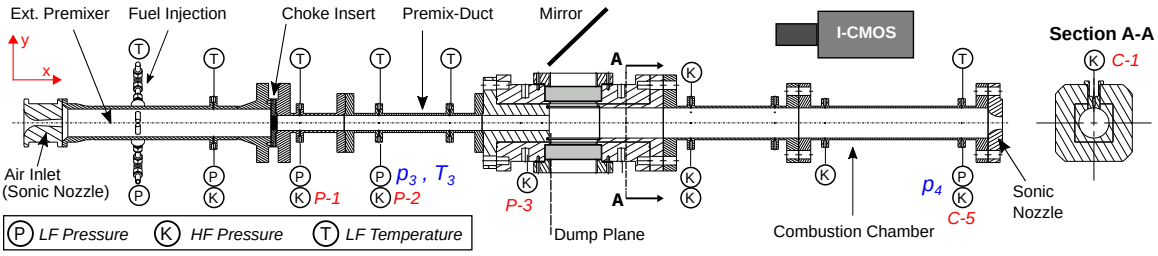

Figure 2.10. CL imaging configuration for the VIPER-S FPC combustor

Particle Image Velocimetry

The PIV configuration for velocimetry measurements in the FPC hardware is identical to the TPC setup. Please refer to subsection 2.1.2. Seed particle were injected in the external premixer to ensure proper mixing of fluid and particles and avoid any affect of the combustor dynamics through the particle injection as shown in Figure 2.9.

3. TECHNICALLY-PREMIXED CONFIGURATION

The multi-scale nature of combustion dynamics and their coupling mechanisms makes the experimental investigation of the phenomena challenging. High thermal power density flames present in gas turbine combustors are naturally unstable, due to the high turbulence levels required to promote sufficient heat and mass transport for flame stabilization. Properly phased interactions between flame dynamics and resonant modes of the combustor can couple and lead to the amplification of pressure perturbations in the system with potentially destructive results. The majority of work focused on vortex-flame interactions has been performed in atmospheric pressure laboratory scale burners, where the acoustics are forced externally using speakers or sirens. While these studies provided valuable fundamental insight, a different set of spatial and temporal scales participate in coupling processes in high power density environments [3]. Thus discriminating cases of combustion dynamics need to be studied in adequately scaled experiments, which are able to generate self-excited dynamics at relevant engine conditions. Such studies aid both, further understanding of the problem as well as the development of predictive capabilities for combustion instabilities through detailed and low-order computational models.

For this purpose, an experiment was developed to accurately represent the nature of thermo-acoustic instabilities in a model combustor operated at elevated pressure with a Siemens Energy, Inc. natural gas injector. The installation of the injector provided technically premixed reactants to the combustion chamber as detailed in 2.1. A parametric survey of operating conditions (T_3 and ϕ) was performed for three distinct injector locations in the premixing duct of the combustor. For the baseline configuration, two test cases that present discriminating instability behavior are analyzed in detail using OH*-chemiluminescence and acoustic measurements. Phase conditioned analysis of deconvoluted chemiluminescence images, a Rayleigh index analysis and dynamic mode decomposition (DMD) are

performed to study the global heat release modes and their relationship with the acoustic field in the combustor to identify possible active coupling mechanisms in this system.

3.1 Parametric Survey

Three TPC configurations were studied where the fuel injection location with respect to the dump plane was changed. A baseline configuration yields a nondimensionalized time lag $\tau = t_{conv} * f_{1L}$ in a range of 1.1 to 1.3, where t_{conv} describes the convection time of fluid from the injection point to the dump plane. Configurations 2 and 3 (schematics shown in Figure 3.1) relocate the fuel injection in the premixer duct, allowing to shift the time lag range by $\approx \pm 0.1$ in respect to the baseline condition.

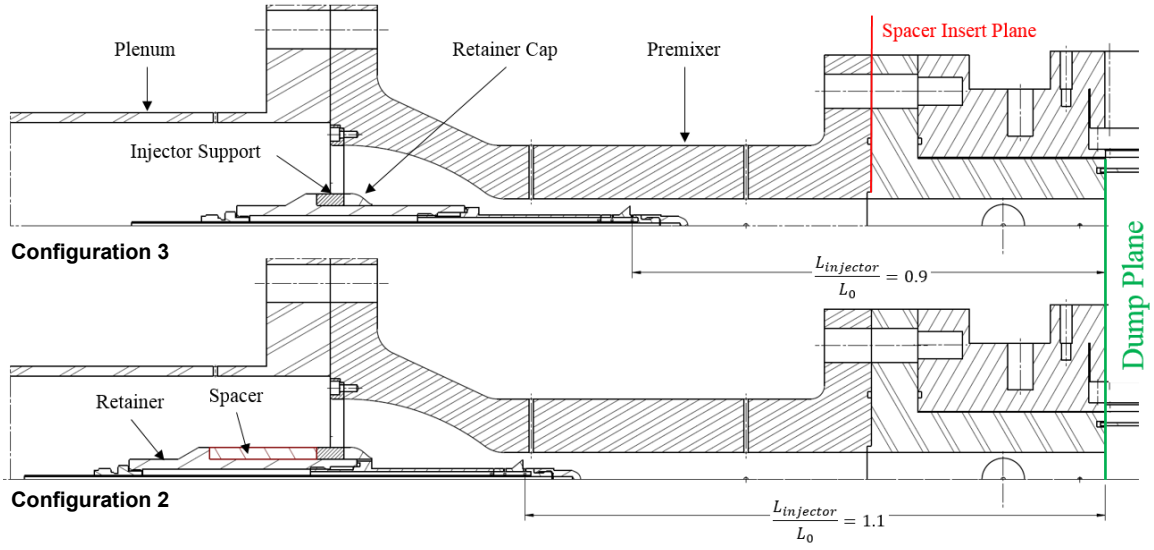

Figure 3.1. Cross-Sections of configurations 3 & 2 of TPC

A flow parameter (FP) target range was defined to $FP = 1.5 - 2$, which was defined by Siemens and corresponds to the typical GT operating range for terrestrial power generation systems and is defined as:

$$FP = \frac{\dot{m}_{air} * \sqrt{T_3}}{p_3} \tag{3.1}$$

where $\dot{m}_{air}$ is the air mass flow rate in kg/s, T_3 the plenum air temperature in K and p_3 the plenum air pressure in bar, defining FP in units of $msK^{0.5}$.

For a constant exit nozzle area, pressure and mass flow rate are directly proportional and thus would not affect the flow parameter. In addition the system pressure would decrease/increase with decreasing/increasing air mass flow rate and miss the target plenum pressure. Thus the air mass flow rate is unsuitable to adjust FP during a test operation day. To achieve the desired sweep through the target range of FP with a constant air mass flow rate and nozzle exit area, the equivalence ratio ϕ and air plenum temperature T_3 are varied. The change in plenum air temperature T_3 directly impacts the flow parameter, whereas ϕ indirectly influences FP, since it alters the adiabatic flame temperature T_{ad} and thus the overall system pressure.

Figure 3.2 summarizes the results of this experimental campaign, where FP as a function of τ is presented and the color code refers to the averaged p'/p_{CH} of the particular test. From Figure 3.2 it can be observed that the 1L mode dynamics show a maximum in the range of $\tau \approx 1.15 - 1.25$. High amplitude dynamics are especially generated for configurations 1 and 3, whereas configuration 2 maintains lower amplitude dynamics throughout FP space.

Two major coupling mechanisms can be identified for the TPC combustor:

1. Equivalence ratio fluctuations

2. Flame-Vortex interactions

The injector orifices are not choked, which is usually the case for industrial systems due to the additional cost associated with additional pressure budget, and thus respond to the dynamic pressure field in the premixer duct. The coupled mode shape corresponding to the chamber 1L frequency, a COMSOL® computation is shown in Figure 2.2. Resulting fuel flow rate modulations generate equivalence ratio fluctuations (ϕ') that are convected downstream towards the flame front. GIM computations for this combustor utilizing a $n-\tau$ model revealed that nondimensionalized time lags in the region of $\tau = [0 - 0.25, 0.75 - 1]$ lead to an amplification of the 1L mode.

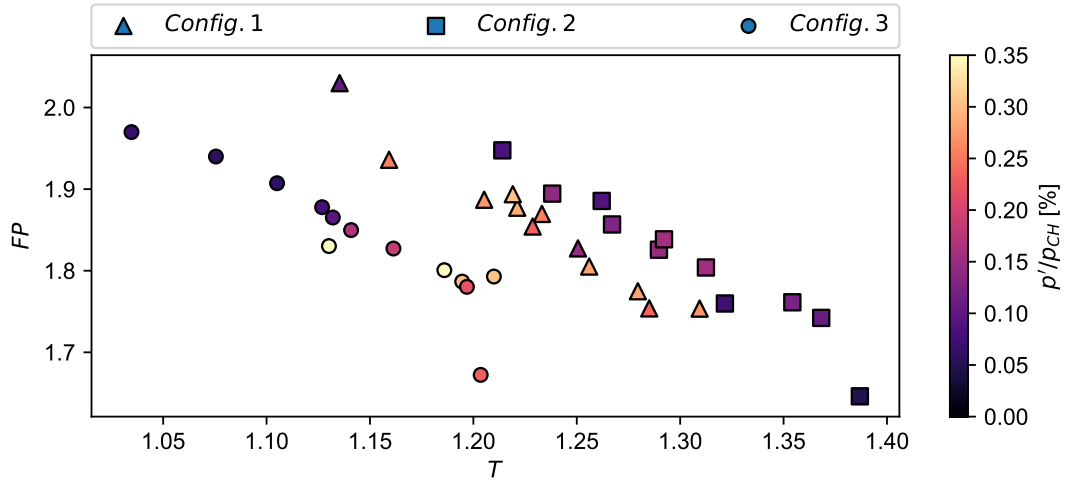

Figure 3.2. Stability map for technically-premixed combustor configurations

For configurations 1 and 3 the injector is located in phase-synchronized pressure field region compared to the flame zone. The positive ϕ' pockets generated at the injection location are convected into the flame zone and arrive during the compression phase of the acoustic cycle at the chamber head end, thus adding energy into the acoustic field to augment the compression process. For configuration 2 the injector is located in a phase-opposed pressure field region and the positive ϕ' pockets arrive during the expansion phase in the flame zone. The resulting phase mismatch of p' and q' lead to an increased dampening of the 1L mode. In configuration 3, the injector is located closer to the the pressure anti-node location at the premixer duct exit, resulting in stronger ϕ' compared to configuration 1 and the potential for higher 1L pressure fluctuations.

Flame-vortex interactions are also identified to augment the chamber dynamics through modulation of the reaction zone. Pressure oscillations at the chamber head end modulate the pressure drop over the combustor dump plane, leading to a pulsation of the jet velocity at the 1L frequency. Periodically shed large scale vortices with length scales in the order of step height H are formed that transport hot products from the recirculation zone towards the reaction zone and promote ignition. During this process the flame surface is increased

leading to an increase in heat release in the domain and an augmentation of the 1L dynamics. During the expansion phase of the acoustic cycle, the jet recovers and flame surface modulations are decreased. These flame-flow interactions are highly nonlinear processes that contribute to the high amplitude instability modes observed in this combustor.

3.2 Particle Image Velocimetry

PIV measurements were attempted in the TPC configuration to understand the flow-flame interactions in the chamber near the dump plane. The introduction of the laser sheet through the curved optical access resulted in glare that limited the effective field of view. Figure 3.3 presents a phase conditioned analysis for a 0.5 s sample of case C1_032 obtained in the red marked region included in Figure 2.4. The phase-conditioned scalar fields represent the mean velocity fields (averaged over 350 vector fields) during the phase angles indicated in the pressure trace for the chamber head-end. Singular Spectrum Analysis (SSA) is used to obtain the velocity and pressure signals presented in Figure 3.3, where modes corresponding to a frequency range of 340-380 Hz have been extracted from the original signals. Jet pulsing as a response to the system pressure field can be observed, leading to u' values as high as 22 m/s. Recirculation zone dynamics are resolved in $\phi = [90, 135, 270, 317]$, where the axial u' component in the recirculation zone region seem to lead the jet response to the acoustic field at the chamber head-end.

Although jet dynamics are clearly resolved, the recirculation zone could not be fully captured due to high glare regions in the outer shear layer that decrease the signal to noise ratio drastically. The glare issues originate in the chamber flame tube which creates high intensity reflections if the incoming laser sheet is not perfectly aligned with the tube axis. Unfortunately careful alignment and glare minimization during test preparations do not guarantee high quality measurements, as the tube can move out of alignment due to thermal expansion of the experiment during the warm-up period. These high glare regions (observed in Figure 3.3) locally saturate the detector and eliminate any signal originating

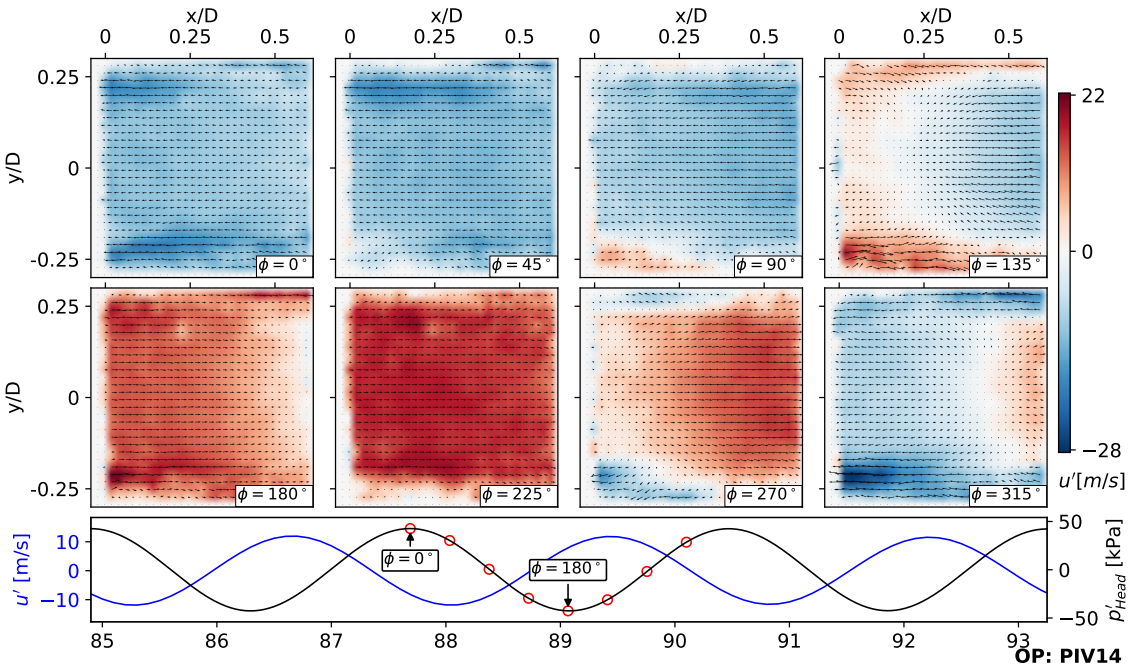

Figure 3.3. 1L chamber mode conditioned axial plane PIV data for case C1_032 (TPC)

from particles in the particular imaging areas. Design and diagnostic modifications are underway to reduce the glare issued from the flame tube.

3.3 Case Discussion

Two distinct operation conditions have been chosen for this analysis, Flame A and B (Table 3.1). Figure 3.4 summarizes the pressure data at the aft-end of the chamber, just upstream of the exit nozzle for both flames. Figure 3.4 a) presents the raw pressure time series for the test periods. An initial pressure spike at $t = 0$s indicates the ignition event followed by the increase of overall system pressure until a limit cycle is reached. A 1 s pressure sample, free of transient processes, is obtained during the 2 s test duration, as indicated in Figure 3.4 a). From the raw pressure histories it can be observed that Flame A reaches limit cycle behavior approximately 100 ms earlier compared to Flame B.

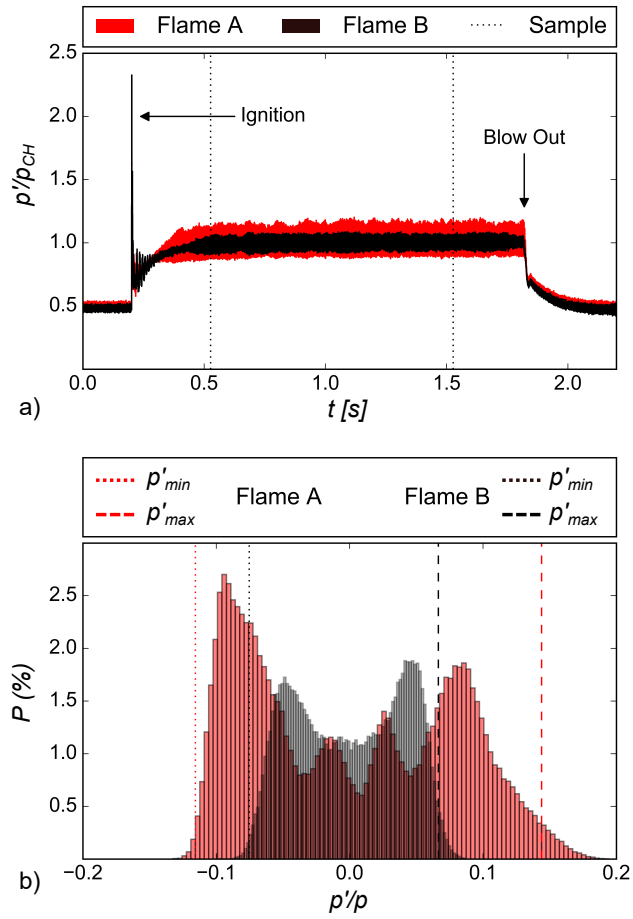

Figure 3.4. a) Pressure time history and b) histogram for Flame A & B

Table 3.1. OPERATION CONDITION SUMMARY

Flame	$\dot{m}_{air}$	ϕ	p_3	T_3	T_{ad}	St_{1L}	$\frac{p\prime}{p_c}$
A	0.55	0.86	8.27	719	2335	0.128	26
B	0.53	1.01	7.59	693	2448	0.125	14
	kg/s	-	bar	K	K	-	%

Figure 3.4 b) depicts the pressure sample histograms as well as the 1% and 99% cumulative percentage locations, defining the minimum and maximum fluctuation magnitude, for both flames. Flame B shows a bimodal distribution, typical of a sinusoidal os-

cillation superimposed with noise, indicating a dominant frequency in the chamber. In contrast to that, Flame A presents a multimodal distribution with two distinct peak pairs, which suggests two major dynamic processes of different amplitudes modulating the pressure fluctuation in the chamber. In addition, the distribution of Flame A is noticeably right-skewed ($skewness = 0.21$), whereas Flame B depicts a more-symmetric distribution ($skewness = -0.05$). This behavior suggests that the compression and expansion phase of the oscillation cycle of Flame A are asymmetric, with a higher sample count in the expansion phase indicative of a more triangular temporal wave structure.

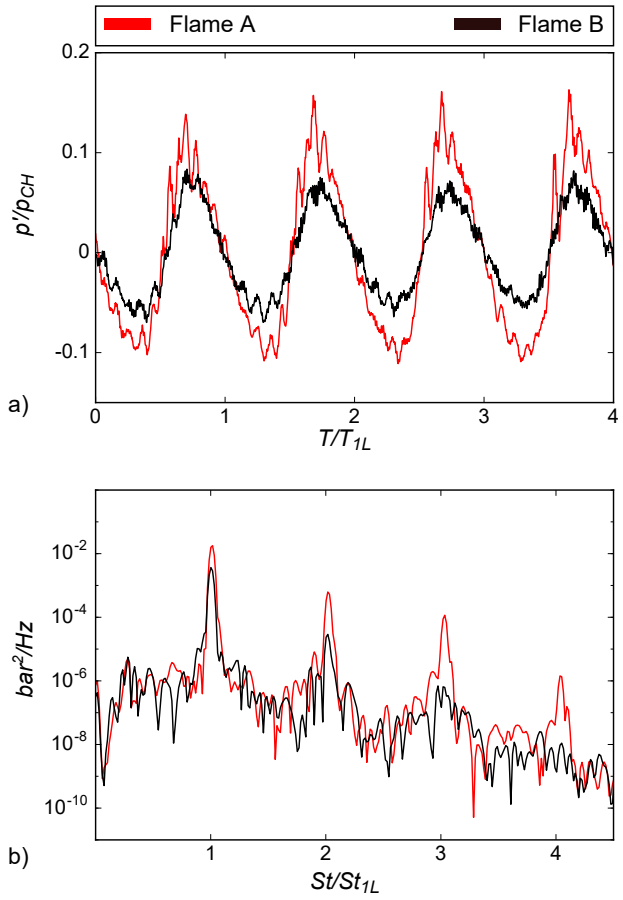

Figure 3.5. a) High-Pass filtered pressure trace and b) PSD for Flame A & B

Pressure fluctuation amplitudes of 23% of the mean chamber pressure are observed within the limit cycle over the 1 s sample period for Flame A in contrast to 12% for Flame

B. Figure 3.5 a) presents a high-pass filtered pressure time history for both flames, in which the clear sinusoidal nature of the pressure fluctuations for Flame B are observable, as suggested by the sample distribution. The dominant modulating frequency is overlaid with low amplitude high frequency dynamics (HFD) throughout the acoustic cycle. Flame A in comparison generates higher amplitude HFD which is superimposed on the first longitudinal mode frequency of the pressure oscillation, responsible for the multimodal character of the sample distribution. In addition, Flame A shows steep-fronted compression waves compared to a more sinusoidal behavior in the expansion phase of the acoustic cycle, leading to the right-skewed distribution observed in Figure 3.4 b).

Figure 3.5B depicts the pressure time series PSD (over 40 1L cycles) for both flames. For Flame A, the strongest mode in the combustor occurs at a Strouhal number of $St_{1L} = 0.128$ which corresponds to the first longitudinal mode in the chamber. Distinct harmonics of this mode are present and neither the amplitude nor the frequencies of these modes are seen to shift throughout the duration of the test. Thus it can be noted that the flame thermal power is high enough that the transient heat loss does not significantly affect the flow temperature and thus the frequencies observed. The 1L mode for Flame B is characterized by a Strouhal number of $St_{1L} = 0.125$ which dominates the spectrum followed by the first and second harmonics. Higher harmonics are present with a lower energy content compared to Flame A.

The phase shift between the transducer signals is analyzed using a band-pass filter at the 1L frequency $\pm$ 1% for the pressure data collected in the chamber at three locations (indicated in Figure). Using this data the mode shape for both flames can be reconstructed and is shown in Figure 3.6. The data points represent the averaged instantaneous pressure magnitude during the maximum of the compression phase at the aft-end of the chamber. A least-square fit of a sinusoidal half wave is performed on both data sets, while enforcing an anti-node at the exit nozzle plane ($dp'/dx = 0$). The position of the chamber head-end anti-node is estimated as $x/L = 0.062$ for Flame A, whereas Flame B generates the anti-node close to the dump plane $x/L = 0$. These aspects are considered and further explored

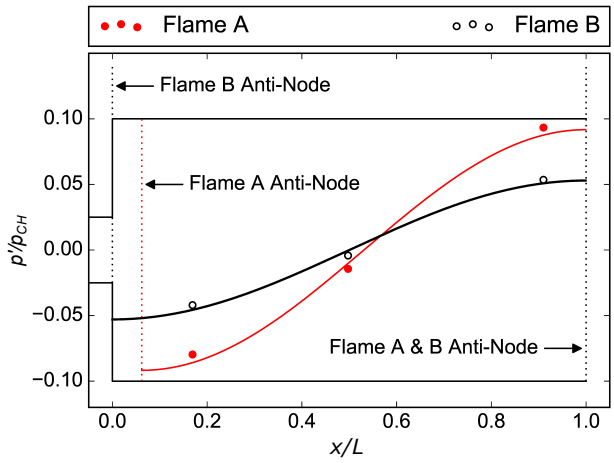

Figure 3.6. 1L mode shape reconstruction

using a phase conditioned analysis of the OH*-chemiluminescence data in the subsequent section.

3.3.1 Phase-Conditioned Analysis

The OH* chemiluminescence data was analyzed over 100 acoustic cycles of the 1L mode, during the limit cycle period to provide a sufficiently large sample to achieve statistical convergence of first and second order central moments throughout the field [46, 47]. Figure and 3.6 illustrate that the head-end pressure transducer, located immediately downstream of the optical access, is situated close to a pressure anti-node, and the transducer at the chamber center at a node with associated low p'. The phase angles are defined using the chamber aft-end pressure transducer in the absence of a measurement location at the flame location. The distances between the aft-end probe to the nozzle exit plane lies within the length of the optical access ($0.11L$) and can thus be utilized for the flame pressure field quantization. The maximum pressure at the flame corresponds to the minimum pressure at the chamber aft-end, defined as a phase angle of 90°. Similarly, the minimum pressure at the flame is defined as 270° and the nodes as 0° and 180° respectively.

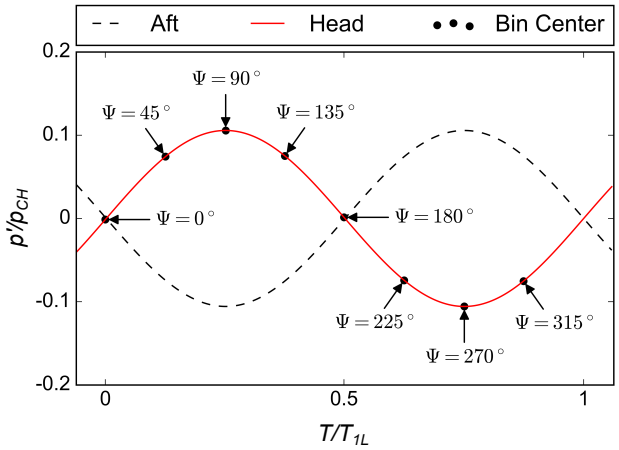

Figure 3.7. Band-Pass filtered pressure for Flame A indicating assigned phase angles

These phase angles and the 45° midpoints represent the center locations of the eight bins utilized for image sorting in the phase conditioned OH* CL analysis. Figure 3.7 indicates the bin center points in the band-pass filtered pressure signal. The intensity of the phase conditioned images is normalized by the time-averaged intensity field for the respective flame condition over the entire sample. A three-point Abel deconvolution algorithm is applied to the upper half of the phase conditioned emission fields to estimate a spatially resolved emission distribution from the line-of-sight integrated chemiluminescence images of the axisymmetric flame [45,48]. Although both flames extend downstream of the optical access, the general behavior of the two flames can be assessed through the analysis.

Figures 3.8 and 3.9 summarize the phase-conditioned deconvoluted emission fields for the eight phase angles corresponding to the 1L mode pressure cycle of Flame A and Flame B respectively. A general comparison of the emission intensity indicates that the heat release is concentrated closer to the dump plane for Flame A than for Flame B. Flame B also appears more stretched, with a strong intensity modulation zone extending past the optical access. For Flame A, starting from $\psi = 0°$, the pressure increases to the cycle maximum at $\psi = 90°$, corresponding to an increase in emission intensity throughout the whole reaction zone length. In addition, the flame moves towards the dump plane, corresponding to a compression of the chamber head-end gases and deceleration of the incoming reactants. The

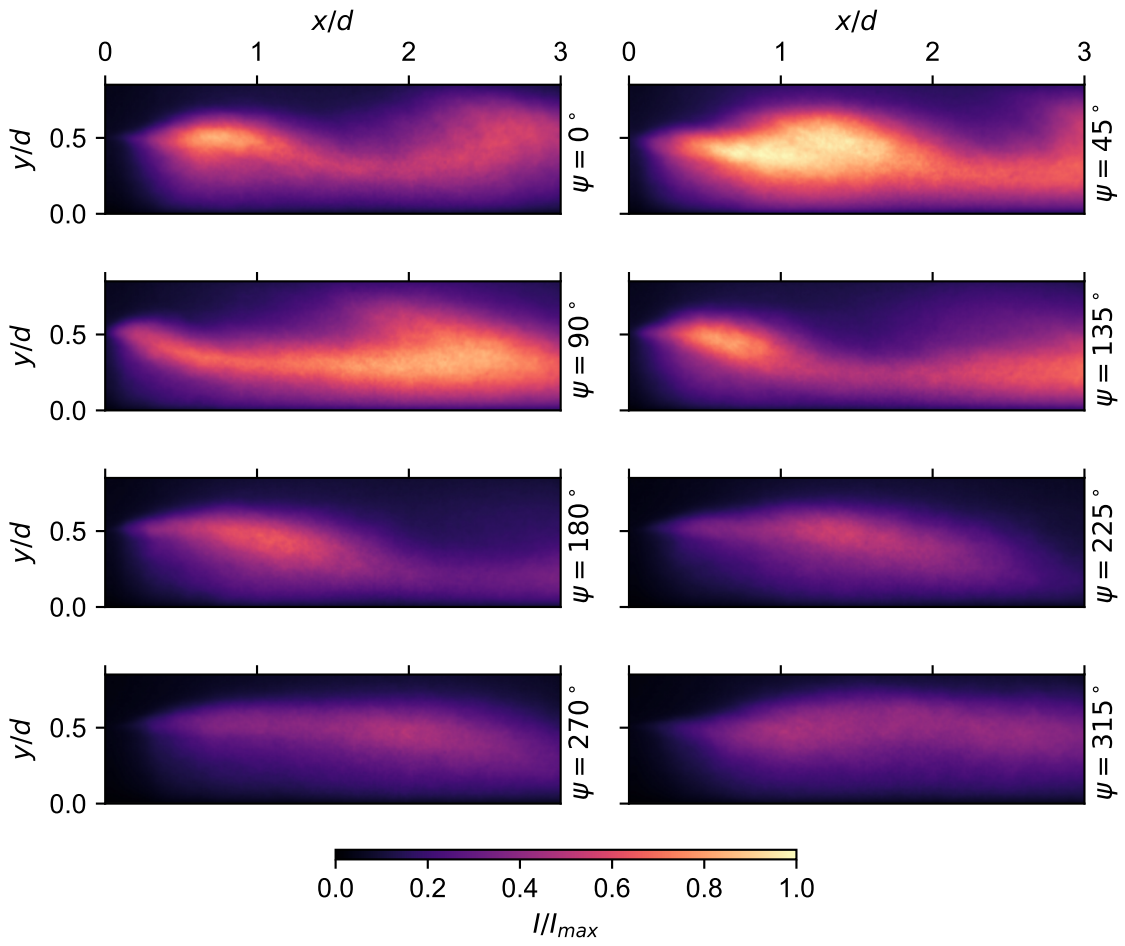

Figure 3.8. OH* chemiluminescence phase conditioned images for Flame A

curved structure of the reaction zone and high intensity elliptical patterns in the emission field indicate strong interactions between vortices originating from the dump plane and the compressed flame. These interactions enhance mixing of combustion products and fresh reactants, which generates an increase in heat release.

In the expansion phase of the cycle ($\psi = 90 - 270°$) the increasing pressure differential and corresponding acceleration of the incoming reactants translates the flame farther downstream of the dump plane, where it anchors in the shear layer of the jet. The flame structure stretches axially and reaction zone modulations through vortices are reduced, leading to

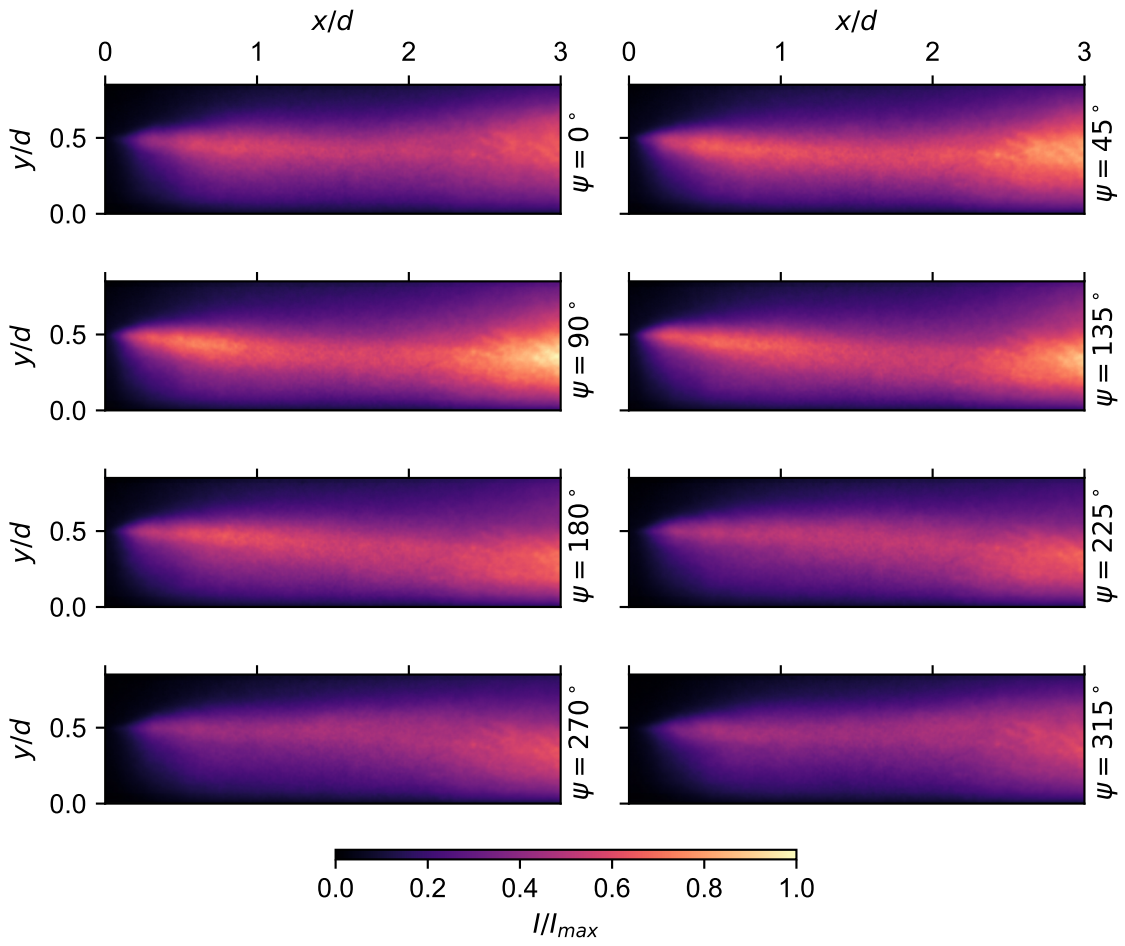

Figure 3.9. OH* chemiluminescence phase conditioned images for Flame B

a more uniform emission field and a heat release reduction. Stepping back into the compression phase of the instability cycle $\psi = 270 - 90°$, the premixed reactant jet decelerates due to the decreased pressure differential and the reaction zone translates back towards the dump plane. An increase in emission intensity is observed in the shear layer zone, indicative of an increase in vorticity and thus mixing. From phase angles $\psi = 0$ to 45°, the re-intensified high level of flame-vortex interactions in the shear layer lead to strong coherent heat release, due to the enhanced mixing of fresh reactants and combustion products originating in the outer recirculation zone.

Flame B shows a significantly different behavior. With increasing pressure in the instability cycle from $\psi = 0 - 90^{\circ}$, the major reaction zone moves upstream due to the decelerating mixture jet. A thin reaction zone is located in the shear layer of the mixture jet during this second half of the compression cycle. A high intensity elliptical pattern in the emission field can be observed 1.5 chamber diameters downstream of the dump plane, indicative of flame surface modulation by large vortex structures. The flame roll-up at this location in the chamber is indicative of a delayed interaction of large vortex structures and jet break down with the reaction zone, locally enhancing mixing and promoting heat release.

During the expansion phase of the instability cycle ($\psi = 90 - 270^{\circ}$) the thin reaction zone in the jet shear layer translates farther downstream, due to bulk flow acceleration. While the accelerated bulk flow decreases the flame-vortex interactions, the thin reaction zone in the jet shear layer anchors 0.75 jet diameters downstream of the dump plane. With the start of the compression phase of the cycle ($\psi = 270 - 45^{\circ}$) the mixture jet decelerates and the reaction zone translates upstream towards the dump plane. The decelerated flow field allows for intensified shear layer burning and flame-vortex interactions ($x/D = 1.5D$), which lead to an increase in heat release due to augmented flame surface modulations. The comparison of the two flames suggests that the reaction zone for Flame B can stabilize in a higher velocity region of the shear layer, where the flow field lacks larger coherent vortex structures, and is thus less modulated throughout the acoustic cycle. In contrast to that, the reaction zone of Flame A needs to reside in lower velocity regions of the shear layer where the effect of the outer recirculation zone is more pronounced and larger vortex structures are located. These structures result in strong modulation of the reaction zone throughout the acoustic cycle for Flame A.

Figure 3.10 compares the fluctuating pressure and OH* emission intensity fluctuation normalized by their mean over the sample period for both flames. Not only are the intensity fluctuations larger for Flame A compared to Flame B, the heat release leads the pressure oscillations whereas for Flame B it is approximately in phase during the phase angles $\Psi = 0 - 180^{\circ}$. In addition Flame A shows a steep increase in emission intensity between $\Psi = 0 - 90^{\circ}$ whereas Flame B maintains a sinusoidal oscillation over the whole acoustic cycle.

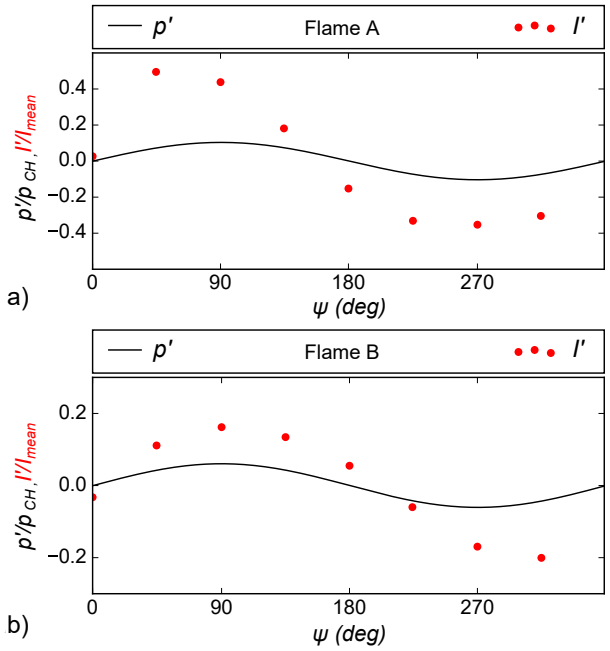

Figure 3.10. Comparison of phase conditioned OH* emission fluctuations for a) Flame A and b) Flame B

These emission modulations for Flame A result of the increased flame surface area during the compression phase in which strong flame-vortex interactions take place close to the dump plane in contrast to the more uniform reaction behavior of Flame B. During the phase angles $\Psi = 180 - 360°$ of the acoustic cycle, the emissions lag the pressure fluctuations for Flame B whereas Flame A shows the opposite behavior. Thus, Flame A promotes the gain of pressure oscillations due to properly modulated heat release fluctuations, whereas Flame B generates more uniform heat release fluctuations which maintain the pressure oscillation but lack the higher energy influx provided by Flame A to the system.

3.3.2 Rayleigh Index Analysis

To compute a Rayleigh index distribution the fluctuating emission intensity is calculated from the instantaneous images and multiplied with the corresponding pressure amplitude obtained from the band-pass filtered data. 100 instantaneous Rayleigh index maps are then

averaged over each phase bin and normalized by the product of the maximum fluctuating quantities, as defined in equation 3.2. Analogous to the phase conditioned data, reasonable axisymmetry of the spatial distribution allows for a reduction of the analysis to the upper half of both flames, shown in Figures 3.11 and 3.12. Per definition of the Rayleigh Index positive and negative regions correspond to driving and damping flame features respectively.

$$RI_{\Psi} = \overline{p'_{\Psi}(i) * I'_{\Psi}(x,y,i)} \tag{3.2}$$

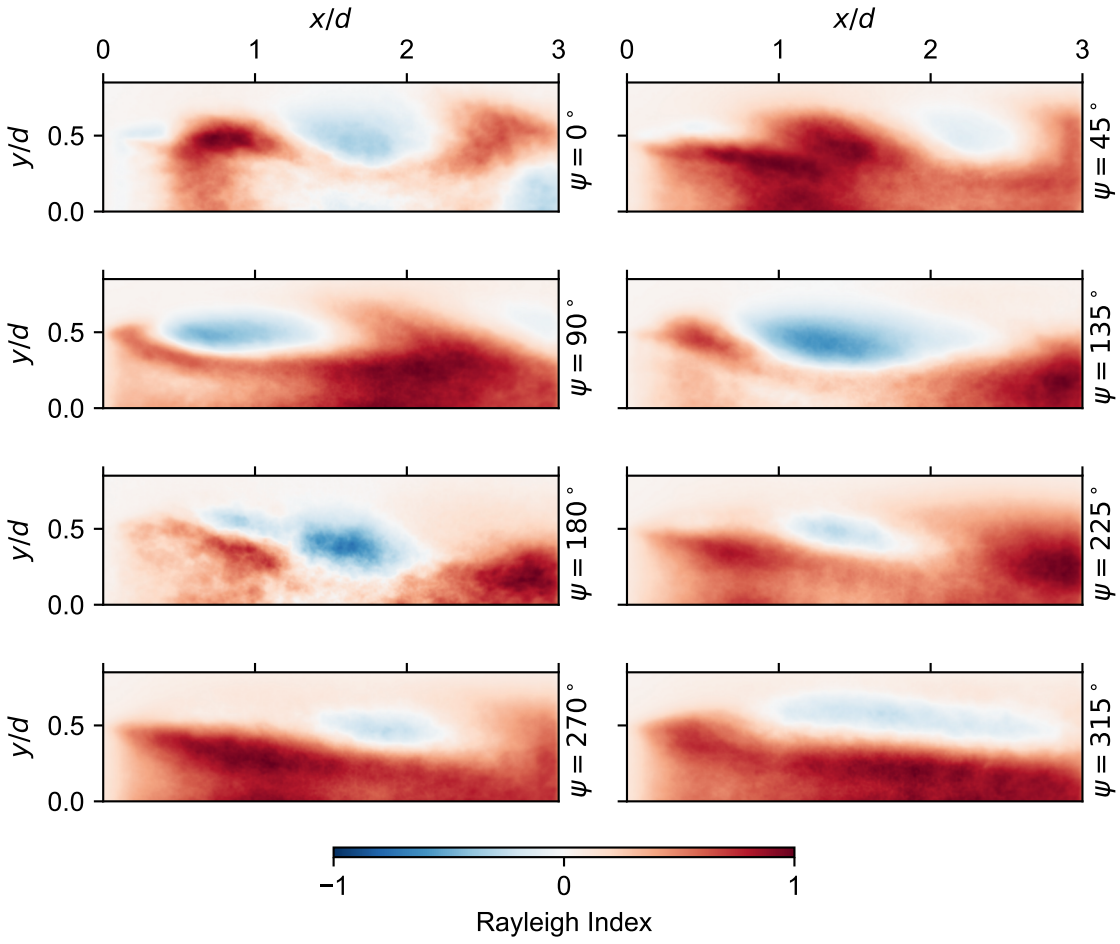

Figure 3.11. Phase conditioned Rayleigh index distribution for Flame A

Corresponding to the pressure nodes, the magnitude of the Rayleigh index for the phase angles $\Psi = 0^\circ, 180^\circ$ is concentrated around zero indicating a neutral behavior of the flame towards the system dynamics. During the compression phase of the acoustic cycle of Flame A ($\Psi = 270 - 90^\circ$), strong flame modulation results in positive heat release fluctuations that promote high instability amplitudes. Coherent elliptical damping regions surrounded by driving features indicate strong flame-vortex interactions, where highly reactive gas zones wrap around less reactive gas pockets indicative of the flame pinching process. The damping regions represent entrained product gases, originating from the outer recirculation zone, transporting heat towards the reaction zone and enhancing heat release in their surroundings. During the expansion phase ($\Psi = 90 - 270^\circ$) these flame-vortex interactions decrease in intensity and the damping regions now correspond to positive heat release fluctuations, driven by vortices in the outer shear layer which transport hot gases towards the reaction zone. The deceleration and acceleration of the mixture jet throughout the acoustic cycle leads to an axial pulsing and pinching of the flame, resulting in strong global heat release rate modulations, which are superimposed onto the local flame-vortex interactions.

Flame B lacks strong flame modulations in the field of view in contrast to Flame A and the reaction zone is less affected by larger vortex structures. The damping regions in the compression phase of the cycle located in the shear layer indicate convecting vortices, which cause an enhancement of the turbulent shear layer burning rather than flame wrapping observed in Flame A. These vortices continue to enhance the reaction in the expansion phase, where the damping regions indicate increased heat release caused by locally intensified heat and mass transfer between the outer recirculation zone and mixture jet. The flame modulations centered at $RI(1.5D, 0)$ can be observed as driving and damping regions for phase angles $\Psi = 90^\circ$ and 225° respectively. To investigate the relationship between the flame-vortex interactions and the dominant 1L mode in the combustion chamber, DMD was applied to the time series of the fluctuating OH* emission fields.

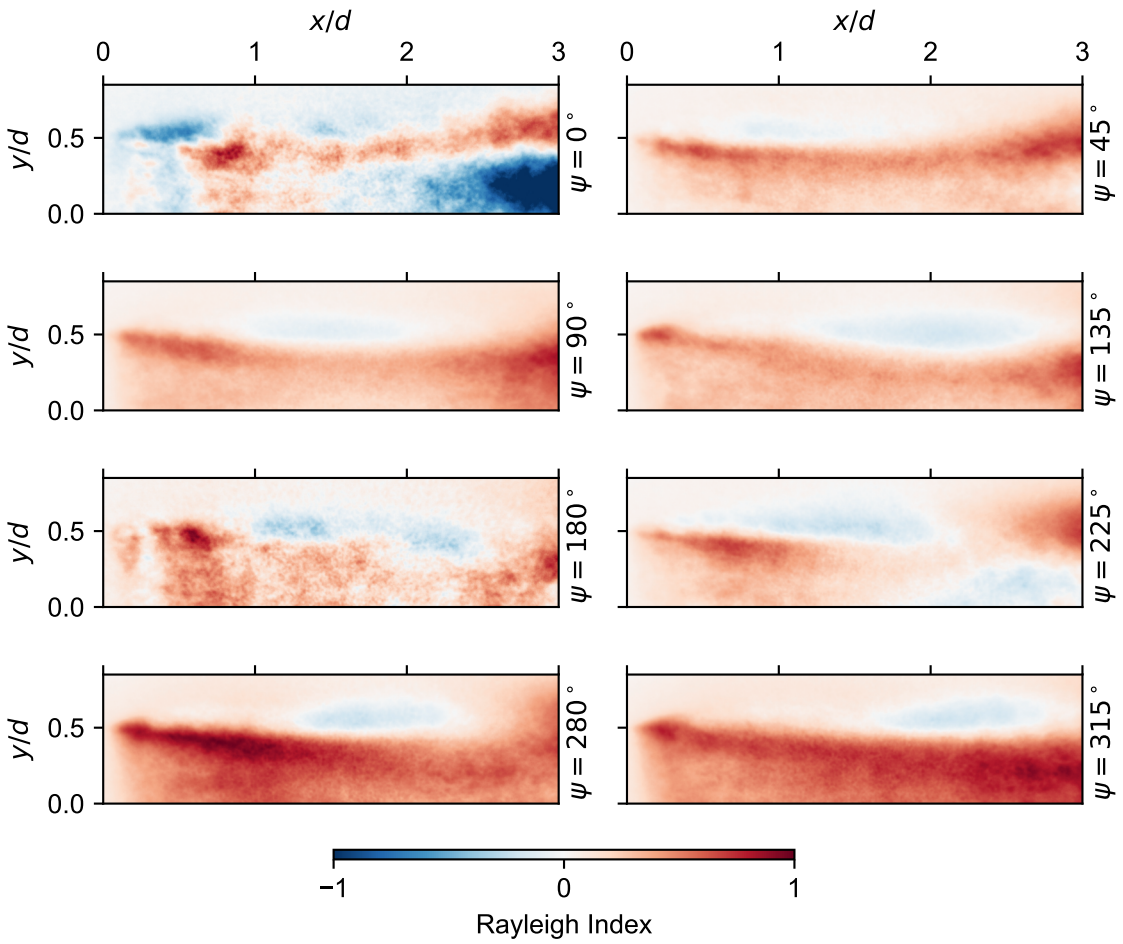

Figure 3.12. Phase conditioned Rayleigh index distribution for Flame B

3.3.3 Dynamic Mode Decomposition

Dynamic mode decomposition (DMD) is a fast method of calculating a subset of the Koopman modes that give dynamic information from a time series of spatially resolved flow data [49]. DMD has been applied to experimental data of unstable reacting flows [50, 51] and has been shown to be advantageous compared to proper orthogonal decomposition (POD) for signals with strong, coherent dynamics [52].

The intensity fluctuations from the OH* chemiluminescence images are calculated over 37 cycles of the 1L acoustic mode for each flame, which provides a sufficient sample size

and limits computation time. The decomposition results in modes corresponding to single frequencies of the heat release fluctuations, which can be reconstructed both spatially and temporally. This approach further elucidates the differences in the flame dynamics between the two cases. Figure 3.13 a) and 3.13 b) present snapshots of the reconstructed OH* intensity fluctuation fields for the first three modes located at $St/St_{1L} = [1,2,3]$ respectively in the DMD spectrum of Flame A and B, shown in Figure 3.14.

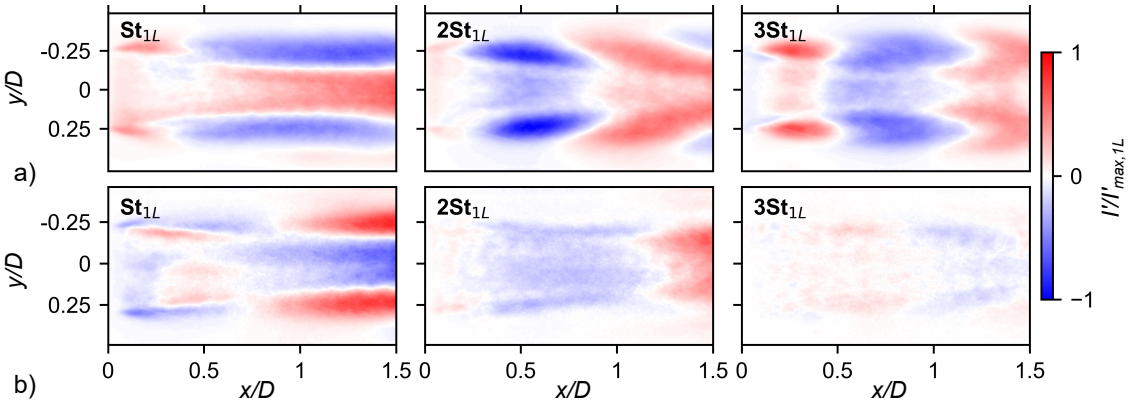

Figure 3.13. DMD reconstructed mode snapshots for a) Flame A and b) Flame B

The path-integrated OH* emission field for Flame A contains intensity fluctuations at frequencies closely corresponding to the 1L instability mode and its temporal harmonics, where the first mode at $St/St_{1L} = 1$ dominates the emission field. The mode spectrum for Flame B in contrast shows strong energy content at the frequency of the 1L instability and the first temporal harmonic only, with the mode at $St/St_{1L} = 1$ being the dominant mode in the emission field. All mode snapshots in Figure 3.13 have been normalized by their respective maximum amplitude for the $St/St_{1L} = 1$ mode. The first mode depicts the intensity fluctuation pattern captured in the OH* emission field, fluctuating at the $St/St_{1L} = 1$ frequency. For both flames this mode shows the fundamental response of the global flame to the 1L mode in the chamber, where the flame is oscillating axially and is compressed between the phase angles $\psi = 270 - 90^{\circ}$ and stretched during the expansion phase between

$\psi = 90 - 270^{\circ}$ of the acoustic cycle. The second and third modes for both flames are located at the frequencies $St/St_{1L} = 2$ and 3.

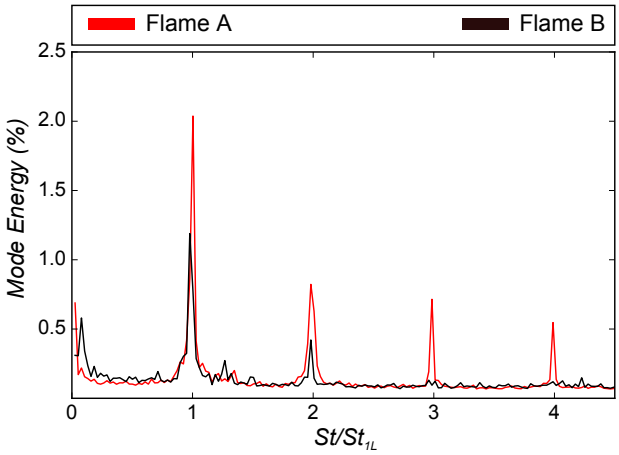

Figure 3.14. DMD mode spectrum for Flame A&B

For Flame A, high intensity elliptical patterns located in the outer shear layer of the mixture jet indicate strong flame-vortex interactions at these frequencies. Flame B, in contrast, shows less prominent structures at both frequencies, indicating that the reaction zone close to the dump plane is not affected by strong vortex interactions. It is rather enhanced in the shear layer by the larger vortex structures present in the outer shear layer zone, transporting hot products into the reaction zone. The intensity fluctuation magnitude indicates that this reaction enhancement for Flame B results in a weaker augmentation of the heat release compared to the high level flame-vortex interactions for Flame A at the frequencies $St/St_{1L} = 2$ and 3.

This analysis supports the phase averaged OH* chemiluminescence observations, where the broader reaction zone of Flame A is engaging in strong flame-vortex interactions close to the dump plane during the compression phase of the 1L acoustic cycle, resulting in a strong heat release augmentation close to the pressure anti-node, enhancing the fundamental 1L mode in the chamber. Flame B in comparison forms a narrower reaction zone, which is less altered by large vortex structures close to the dump plane and only interacts with large scale structures farther downstream during the compression phase of the 1L acoustic

cycle. This behavior leads to a phase shift between the heat release and 1L pressure mode observed in Figure 3.10, resulting in a phase relationship that generates a lower gain of the fundamental 1L instability.

3.3.4 Conclusions

Self-excited combustion instabilities in the TPC of a natural gas fueled high pressure gas turbine combustor were investigated using high frequency pressure measurements and OH*- chemiluminescence. Two conditions with discriminating chamber dynamics, Flame A (23%) and Flame B (12%), showed distinct longitudinal mode dynamics, with the dominant oscillation being the 1L mode. Lower amplitude pressure oscillations were observed for Flame B along with a lower energy content in the temporal harmonics compared to Flame A.

The phase conditioned chemiluminescence data analysis revealed significant differences in the global heat release distribution over the acoustic cycle, where Flame A showed strong flame vortex-interactions close to the dump plane. Flame B in contrast shows more uniform combustion in the shear layer and jet breakdown only occurs $1.5D$ downstream of the dump plane. The deconvoluted emission field suggests that the reaction zone of Flame A is stabilized in the outer shear layer and thus strongly interacts with large vortex structures shed from the backward-facing step during the compression phase of the acoustic cycle. Flame B in comparison develops a narrow reaction zone in the shear layer close to the dump plane and grows in width in the axial direction where vortex alterations take place. The Rayleigh Index analysis further supports these observations. Elliptical structures identified for Flame A, strongly correlate with flame modulations caused by coherent vortex structures.

The DMD analysis revealed that the OH* emission field for both flames is comprised of three dominant spatial modes, corresponding to frequencies close to the fundamental 1L pressure mode at $St/St_{1L} = 1$ and two modes at $St/St_{1L} = 2$ and 3. The first DMD spatial mode corresponds to the flame pulsing in response to the fundamental 1L pressure

mode in the chamber. The two higher DMD spatial modes represent flame interactions with vortex structures in the shear layer of the reactant jet, which are stronger for Flame A compared to Flame B. The resulting increased heat release for Flame A during the compression augments the fundamental 1L mode in the chamber. Flame B generates a more uniform reaction zone and is less affected by these flame-vortex interactions in the field of view examined here. The more sinusoidal heat release fluctuations and their phase relationship with the pressure field for Flame B leads to a smaller amplification of the fundamental 1L mode compared to Flame A, resulting in a lower instability magnitude.

4. FULLY-PREMIXED CONFIGURATION

The dynamics encountered in the technically-premixed configuration suggested that flame-vortex interactions amplify the ϕ' based feedback loop leading to high amplitude 1L limit-cycles. The fully-premixed configuration (FPC) was designed to replicate the frequency of dynamics observed in the TPC with the elimination of potential equivalence ratio fluctuations in the injection system. The simplified premixed injection scheme with premixed reactants helped study the flame-hydrodynamic interactions in the presence of the chamber acoustics in a canonical jet-stabilized flame at operating conditions and a confinement typical of a practical gas turbine combustor. A parametric survey of inlet mixture temperature, equivalence ratio, and premixing duct length highlighted a large variation in pressure fluctuation amplitudes observed in the chamber, even in the absence of equivalence ratio fluctuations. In addition to longitudinal modes, self-excitation of the transverse mode in the chamber at $\sim 5kHz$ was observed. Self-excited transverse instabilities in a single element air-breathing combustor operating at high pressure have not been widely studied to the best of our knowledge. Following a discussion of the parametric survey, a detailed discussion of two representative test conditions is summarized in this chapter: Flame 1 (F1) that presents longitudinal mode dynamics $(p'/p_c = 3\%)$ and Flame 2 (F2) that presents high amplitude transverse instabilities $(p'/p_c = 15\%)$.

4.1 Parametric Survey

The sensitivity of self-excited instability regimes observed in the experiment to a range of flame conditions such as mixture temperature T_3 and global equivalence ratio ϕ were assessed through a parametric survey. Flame parameters are varied in a engine relevant envelope, with T_3 and ϕ ranging between 600 and 800 K and 0.6 and 0.85 respectively. A wide range of different dynamics have been observed throughout 33 test cases, ranging

from high amplitude 1L dynamics over 1T dominated pressure spectra to spinning wave instabilities. Two Inlet duct configurations were tested, a half- ($l_{IN} = 72$ cm, FPC) and a quarter- ($l_{IN} = 36$ cm, FPCS) wave configuration.

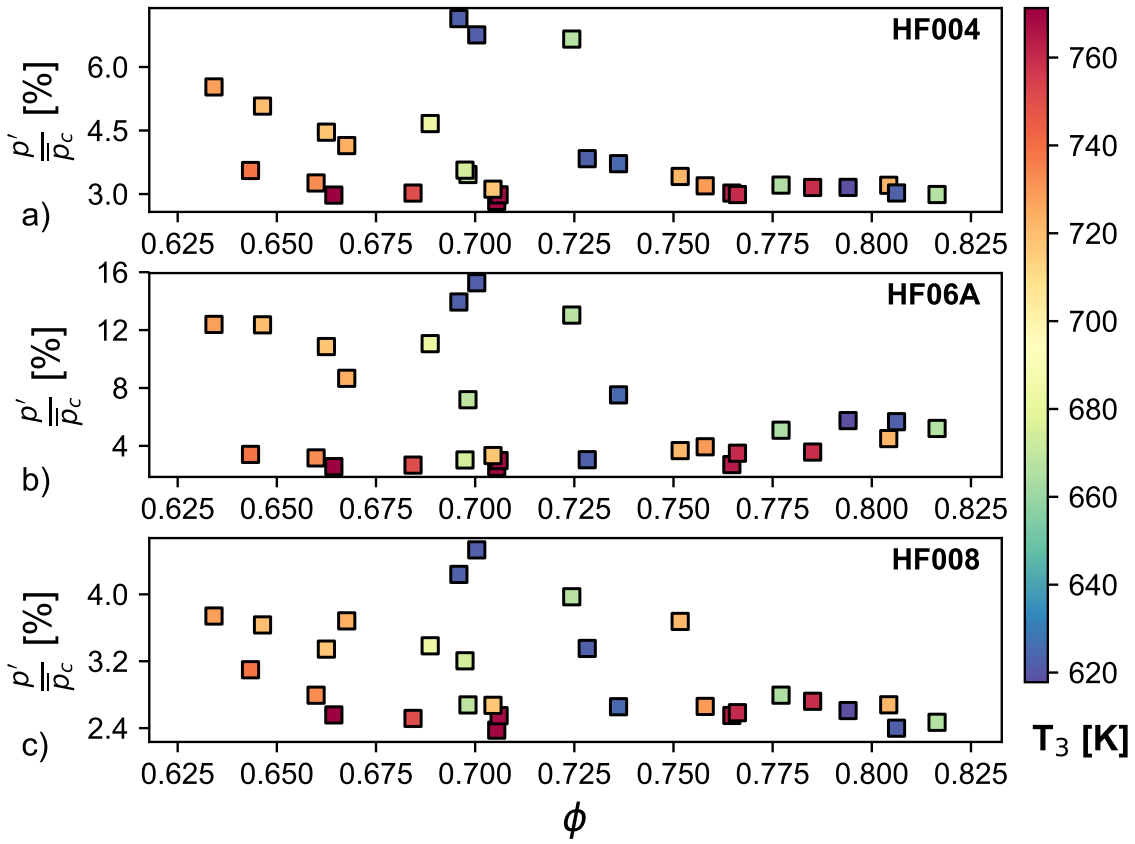

Figure 4.1. Total instability amplitude of FPC vs. ϕ for probe a) HF004, b) HF06A and c) HF008. Note different y-scales.

Figure 4.1 shows the pressure fluctuation amplitude at the aft-end of the premixed duct, chamber head- and aft-end (HF004, HF06A, HF008) of the combustor as a function of equivalence ratio ϕ. The data points are colored based on the mixture temperature T_3. From Figure 4.1 a-b) an increase in p' can be observed as a function of ϕ at the inlet aft-end and chamber head-end. The onset of this increase is a function of T_3 and transfers towards leaner conditions with an increase in T_3. Figure 4.1 c) shows that the aft-end

exhibits a similar behavior, however the magnitudes are significantly decreased compared to the head-end.

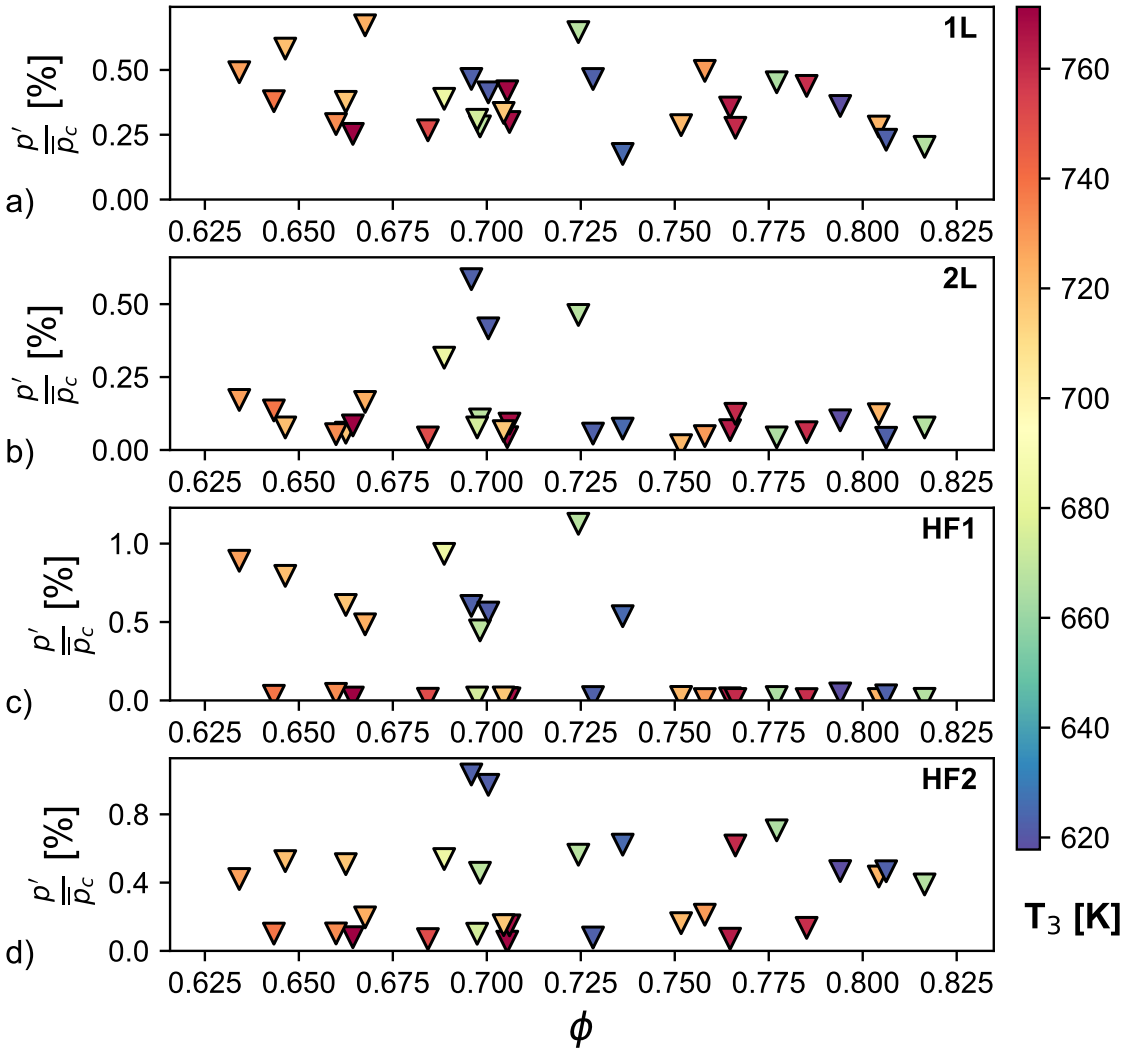

Figure 4.2. Mode amplitudes of FPC vs. ϕ for probe *HF06A*: a) 1L, b) 2L, c) HF1 and d) HF2 mode contributions. Note different y-scales.

These trends can be deconvoluted by decomposing the instability magnitude in the single mode contributions as shown in Figure 4.2. The fundamental longitudinal mode (1L) for a specific T_3 group shows a weak dependency on ϕ, as observed in Figure 4.2 a). A different behavior is observed for the 2L mode, where an amplitude increase occurs at a T_3

specific ϕ threshold, which transfers towards leaner conditions with increasing T_3. Below this threshold the 2L amplitude reaches magnitudes similar to the 1L mode or even exceeds its amplitude (see Figure 4.2 b)). Higher frequency modes are responsible for the strong increase in total instability amplitude at the chamber head-end. Two modes (HF1 and HF2) show elevated magnitudes as high as twice the longitudinal mode amplitudes. The HF1 mode closely corresponds to the fundamental transverse mode frequency ($f_{HF1} = 5 - 5.4$ kHz), whereas mode HF2 is found to reside in the frequency range of $f_{HF2} = 5.6 - 6.3$ kHz. The onset of these dynamics is closely correlated to the 2L dynamics and shifts towards leaner conditions with an increase in T_3. Similar dynamics are observed at the inlet aft-end (HF004).

The chamber aft-end dynamics are decomposed in Figure 4.3. A direct comparison between head- and aft-end longitudinal dynamics show a similar behavior (see a) and b)), however due to the proximity of the aft-end probe to the longitudinal mode anti-node the amplitudes are increased compared to the head-end probe. The higher frequency mode onset is detected at the chamber aft-end as observed in Figure 4.3 c-d), although the mode magnitudes are significantly decreased due to mode cut-off.

4.2 Effect of Inlet Length

A total of 10 tests were conducted with the quarter-wave duct configuration of the fully-premixed hardware (FPCS). Figure 4.4 shows the total instability amplitude at the inlet aft-end, chamber head- and aft-end (HF004, HF06A, HF008) of the combustor vs. equivalence ratio ϕ, where the data points are color-coded based on T_3. From Figure 4.4 an increase in p' can be observed as a function of ϕ at all probe locations. In addition, two cases generated a strong chamber instability in the highest T_3 group at a particular rich condition ($\phi \approx 0.81$), not encountered in the half-wave configuration. Excluding these two cases from the discussion, trends similar to the half-wave configuration are observed, where an increase of instability magnitude occurs at a T_3 specific ϕ.

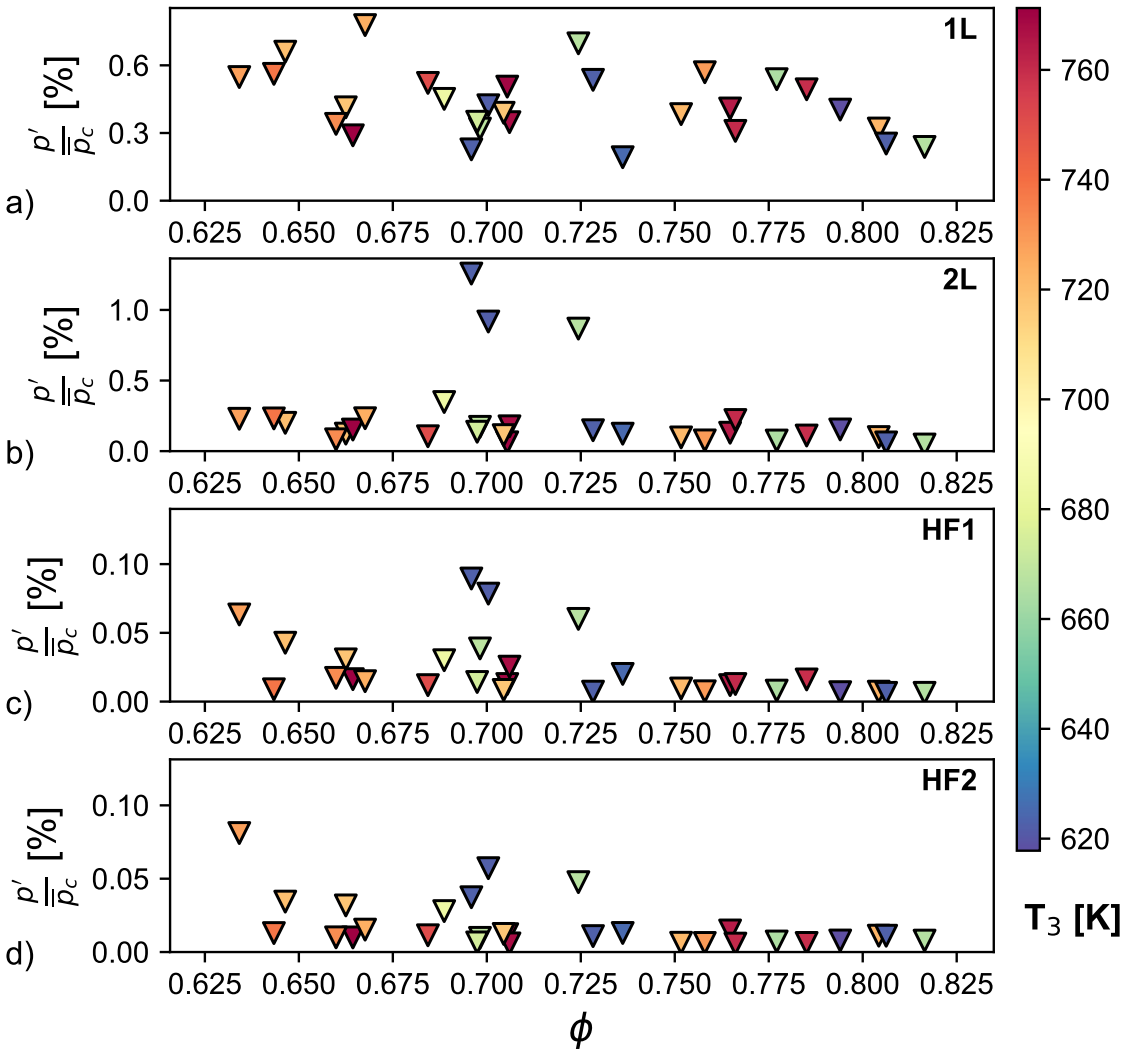

Figure 4.3. Mode amplitudes of FPC vs. ϕ for probe *HF008*: a) 1L, b) 2L, c) HF1 and d) HF2 mode contributions. Note different y-scales.

Figure 4.5 presents the mode specific instability amplitudes for the chamber head-end probe for the quarter-wave configuration. Similar to the FPC, the fundamental longitudinal mode (1L) for a specific T_3 group shows an independence of ϕ, as observed in Figure 4.5 a). The most unstable cases in the FPCS campaign are clearly dominated by the 1L chamber mode (FPCS_001/2), exhibiting $p'/\bar{p} \approx 20\%$ pressure fluctuations. Excluding these two cases from the discussion, all mode specific amplitudes show only a weak dependence on

ϕ. Two cases were encountered for which high frequency dynamics dominated the chamber pressure spectrum. Case FPC_009 with a $\phi = 0.69$ and $T_3 = 670$K exhibits strong pressure oscillations at the HF1 mode, whereas case FPC_005 with a $\phi = 0.65$ and $T_3 = 725$K is dominated by HF2 mode oscillations. Here the HF1 mode corresponds to the fundamental transverse mode at the chamber head-end, however the chemiluminescence imaging clearly correlates a spinning instability (wave motion) with the HF2 mode instability. Thus the second higher frequency mode (HF2) cannot be connected with a combined chamber mode such as a 1T1L or 1T2L mode.

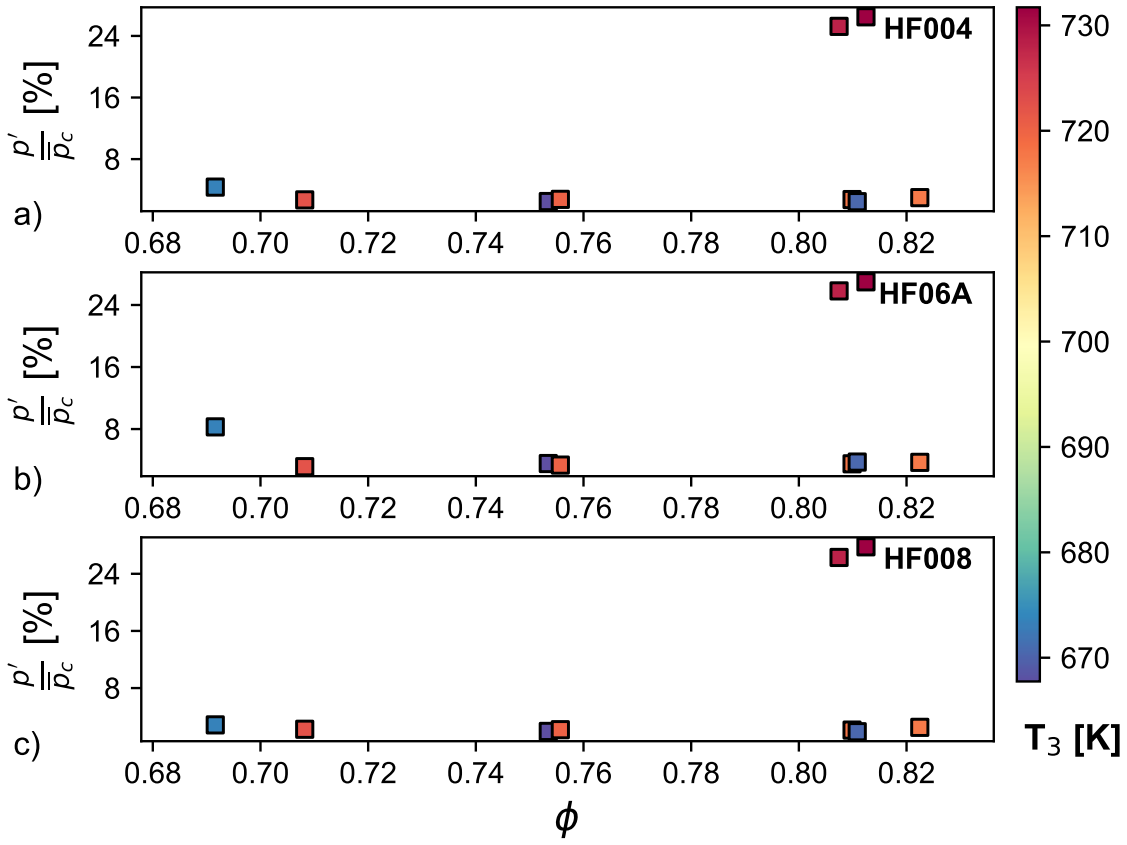

Figure 4.4. Total instability amplitude of FPCS vs. ϕ for probe a) HF004, b) HF06A and c) HF008. Note different y-scales.

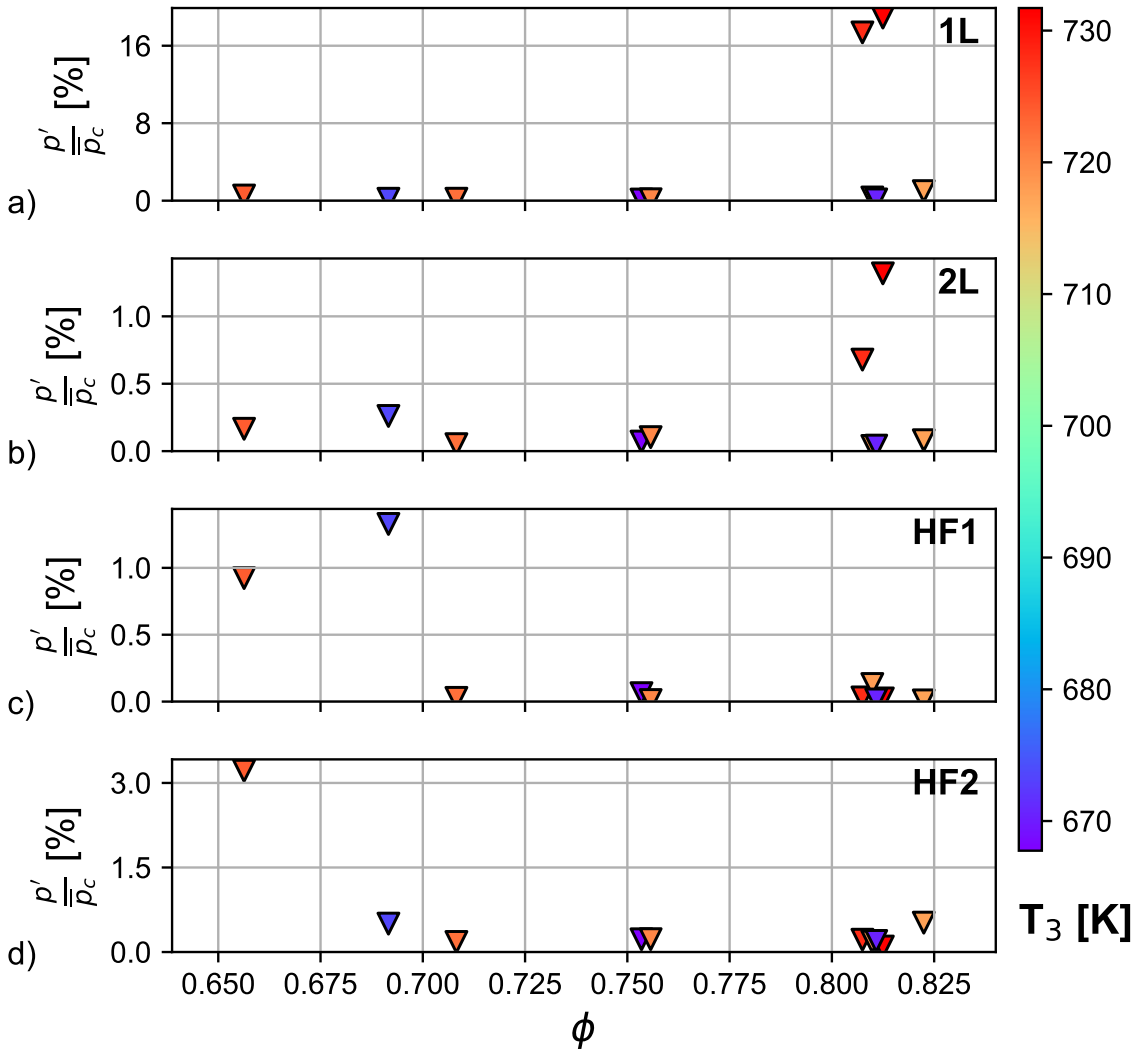

Figure 4.5. Mode amplitudes of FPCS vs. ϕ for probe *HF06A*: a) 1L, b) 2L, c) HF1 and d) HF2 mode contributions. Note different y-scales.

To highlight the different instability regimes observed in the FPCS operation, three cases will be described in more detail for which the operation conditions are documented in Table 4.1.

Figure 4.6 shows a pressure sample and the corresponding power spectrum for the case FPCS_001 at three probe locations. The power spectrum for all probes indicate strong longitudinal dynamics at the fundamental frequency of 400 Hz followed by up to five har-

Table 4.1. Selected operation conditions from phase 3 test survey (FPCS): pressure amplitudes based on HF06A probe

Case	$\dot{m}_{air}$	ϕ	T_3	p_3	$p'/\bar{p}$	p'_{1L}	p'_{HF_1}	p'_{HF_2}
001	0.53	0.81	730	8.10	27.0	18.9	0.02	0.10
005	0.53	0.66	724	7.20	26.7	0.53	0.92	3.22
009	0.52	0.69	673	7.05	8.3	0.20	1.33	0.50
	kg/s	-	K	bar	%	%	%	%

monics at the inlet probe location. All FPCS cases show an elevated 1L mode frequency of $\approx$ 400 Hz, due to the shorter overall system length. No HF1/2 modes are present at a relevant magnitude for this case. The chamber probes however show evidence of other higher frequency modes at 2, 2.4 and 2.8 kHz, which are a multiple of the fundamental 1L

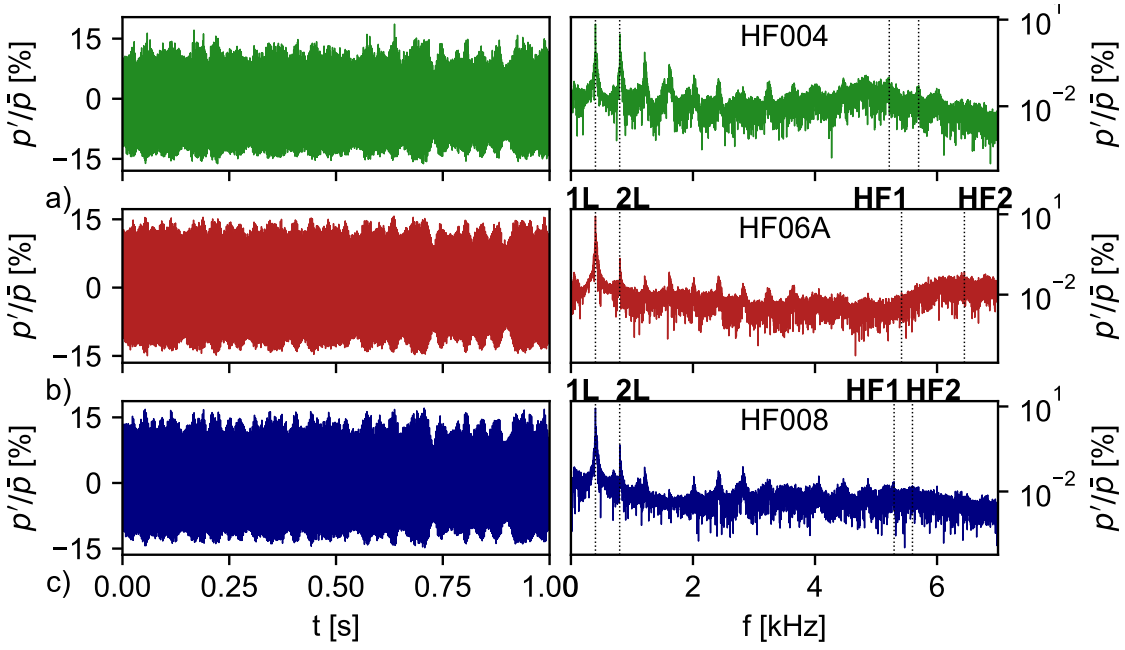

Figure 4.6. Pressure time series and power spectrum for FPCS_001 for probe a) HF004, b) HF06A and c) HF008. Note different y-scales.

mode frequency, however these frequencies may also be related to jet hydrodynamics and need to be analyzed in more detail.

Figure 4.7 shows a pressure sample and the corresponding power spectrum for the case FPCS_005. This flame condition generates strong dynamics at the HF2 frequency of 5.93 kHz, clearly observable at the chamber head-end and Inlet aft-end. The chamber aft-end probe also shows evidence of this mode with a frequency of 5.89 kHz and reaches a magnitude similar to the 1L chamber mode at 410 Hz. The HF1 mode is present at the Inlet aft-end probe at 5.21 kHz and reaches amplitude levels comparable to the HF2 mode. The chemiluminescence images clearly indicate a traveling wave circumscribing the burner-face. The short time periods showing drastic amplitude decrease at $t \approx 0.125$s and 0.49 s correlates to flame dynamic changes, where the traveling wave instability transitions into dynamics comparable to transverse instability cases. Comparing this flame condition with the previous (FPCS_001) one it is worth noting that only a change in equivalence ratio

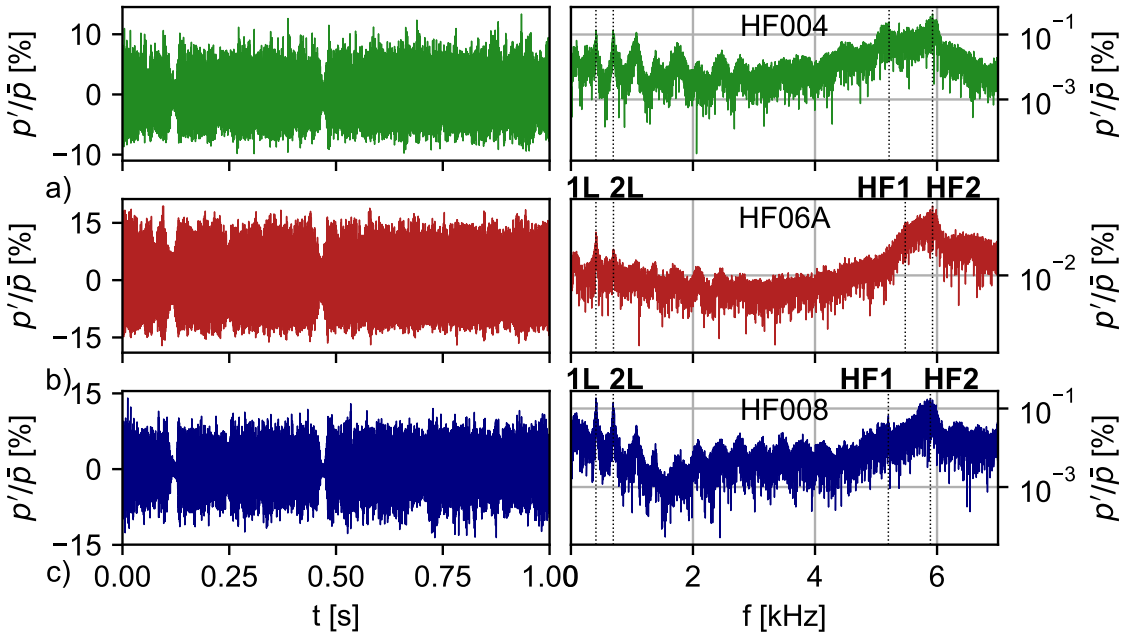

Figure 4.7. Pressure time series and power spectrum for FPCS_005 for probe a) HF004, b) HF06A and c) HF008. Note different y-scales.

leads to a complete change in dynamics (1L vs. 1A), with both cases generating similar total instability amplitudes of ≈ 27 % of the mean chamber pressure.

Figure 4.8 shows a pressure sample and the corresponding power spectrum for the case FPCS_005. This flame condition is dominated by the HF1 mode at the head-end of the chamber at 5.25 kHz. The chamber aft-end pressure field is dominated by the 1L mode at 388 Hz, no significant HF mode contribution is detected due to frequency cut-off (Figure 4.8 c)). The Inlet aft-end probe clearly detects the HF1 mode transmitted from the chamber head-end (Figure 4.8 a)), whereas the HF2 mode, present at the chamber head-end probe at a similar magnitude compared to the HF1 mode (Figure 4.8 b)), does not transmit effectively into the Inlet duct.

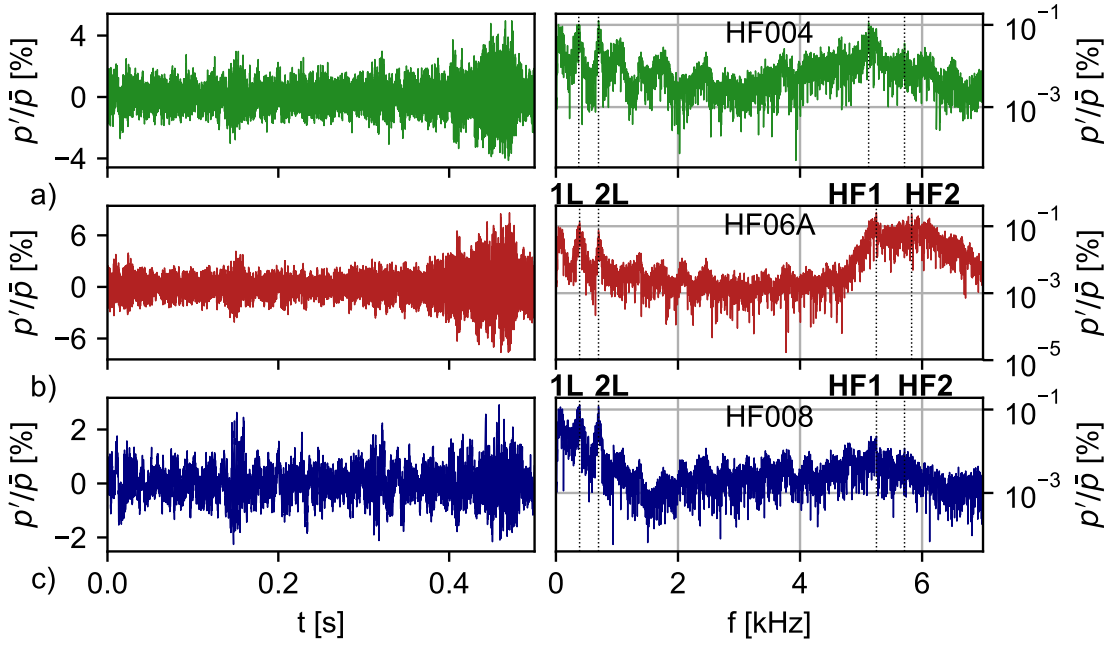

Figure 4.8. Pressure time series and power spectrum for FPCS_009 for probe a) HF004, b) HF06A and c) HF008. Note different y-scales.

4.3 Case Discussion

The following analysis is focused on two cases, Flame 1 (F1 - FPC_026) and Flame 2 (F2 - FPC_025), tabulated in Table 4.2, which have been extracted from the parametric survey discussed above.

Table 4.2. Summary of operating conditions: pressure amplitudes based on HF06A probe

Flame	$\dot{m}_{air}$	ϕ	p_3	T_3	T_{ad}	$p'/\bar{p}$
	[kg/s]	[-]	[bar]	[K]	[K]	[%]
1	0.54	0.72	7.2	625	2116	3
2	0.54	0.69	6.9	625	2071	15

Figure 4.9 a) presents the pressure time history for tests F1 and F2 along with representative time slices showing pressure fluctuations at the combustion chamber head- and aft-end (locations marked in Figure 2.10). For test case F2, pressure fluctuation amplitudes of $p'/p_c = 15\%$ are observed at the head-end (C-1) of the chamber. In Figure 4.9b) the pressure-time history shows intermittent amplitude growth and decay of high frequency pressure oscillations superimposed with a 360 Hz 1L mode. In contrast, F1 dynamics are dominated by the chamber 1L mode at a relatively lower amplitude of $p'/p_c = 3\%$. The pressure fluctuations at the 1L frequency persist at the aft-end measurement location (C-5) for both tests (Figure 4.9 c)), but the high-frequency oscillations are significantly damped.

The amplitude of the high-frequency pressure fluctuations superimposed on the 1L oscillations at location C-1 and subsequent decay of the high-frequency mode at location C-5 are reinforced by the power spectral density (PSD) plots in Figure 4.10 b-c). For test case F1, strong axial mode dynamics at 360 Hz frequency are observed at similar amplitudes at C-1 and C-5 locations, consistent with a fundamental standing longitudinal mode in the CC. Location P-3, also at a pressure anti-node in the PD, shows strong pressure fluctuations at this frequency. In contrast to F1, while axial mode dynamics are still present for test case F2, the power spectrum is dominated by high-frequency pressure fluctuations at

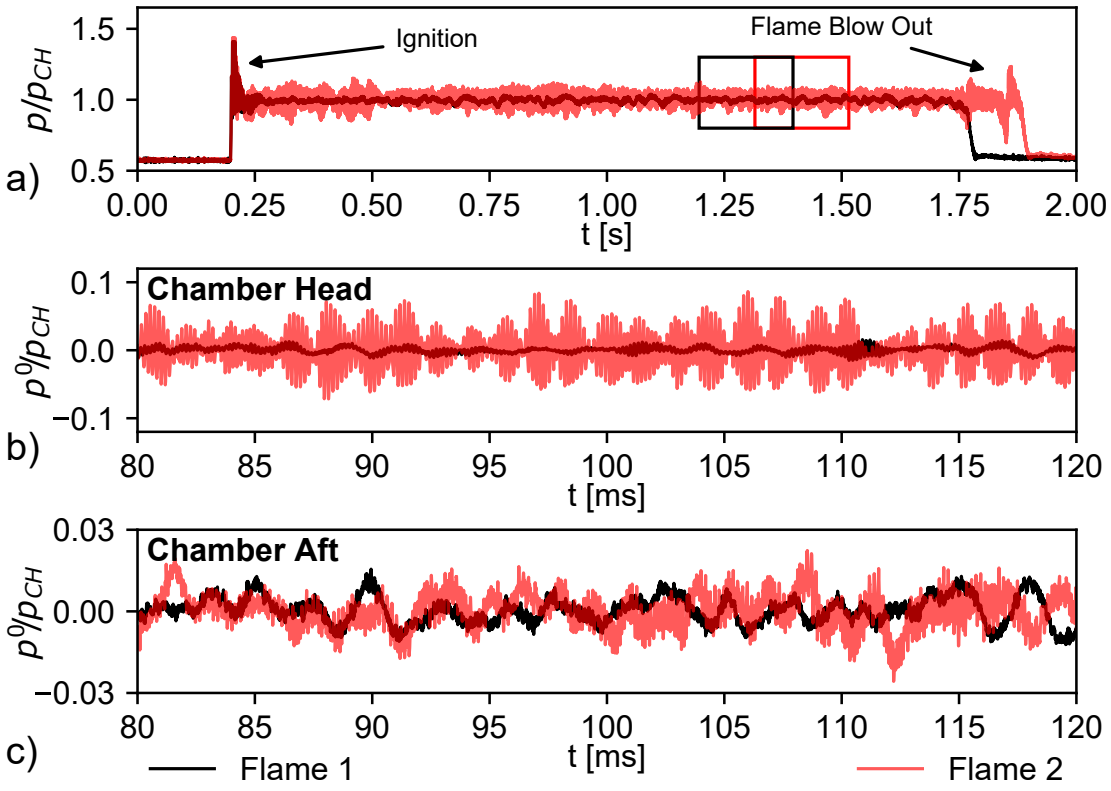

Figure 4.9. a) Pressure time history b-c) high-pass filtered pressure at the chamber-head and -aft end respectively for cases F1 & F2

4.8-6.5 kHz, especially at C-1 and P-3 locations. The fundamental transverse mode (1T) frequency, estimated by the GIM analysis, falls within this range. However these modes are significantly damped at C-5, corresponding to the expected damping of the high frequency dynamics towards the combustor outlet. In addition, for test case F2 a 2L mode at 680 Hz is present in the PD as seen in the spectrum at P-3. The presence of both low- and high-frequency modes observed in the PD are expected to generate periodic vortex shedding patterns that can amplify flame-vortex interactions in the chamber [20]. To highlight the distinct transverse mode instabilities in the combustor, the discussion of results hereafter is focused on F2.

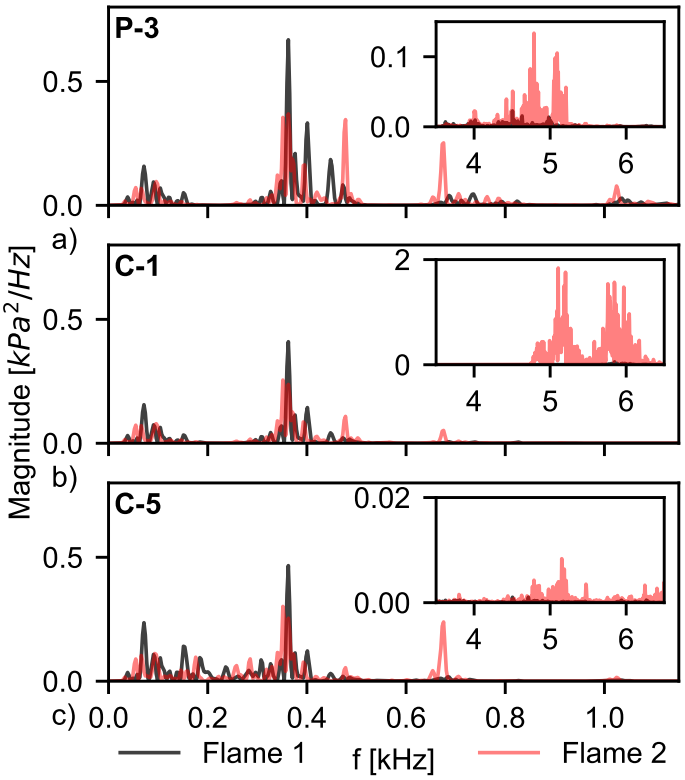

Figure 4.10. Power spectral density for F1 and F2 at the a) PD exit (P-3), b) chamber head-end (C-1) and c) aft-end (C-5) location (Inset graph scales are consistent with major graphs)

4.3.1 Flame Emission Analysis

Figure 4.11 shows a typical time series of instantaneous OH* chemiluminescence snapshots over two time slices for F2. As previously described, the 1T pressure fluctuations at the chamber head-end are modulated in amplitude at a lower frequency for this test case. The sequence of images at the top corresponds to a period of low p' amplitude measured at the C-1 location (probe is orientated normal to FOV, refer to Figure 2.10). These images are characterized by a strong variation in overall intensity in the transverse direction (y-direction, see boxed areas) coupled with asymmetric vortex shedding off the dump-plane about the chamber axis (x-direction). This asymmetric vortex roll-up, representative of helical vortices, is consistent with observations for transverse instabilities made by Rogers

and Marble [25]. Conversely, the images in the bottom row correspond to a period of maximum p' amplitude at C-1. Here, the flame emission is both symmetric about the chamber axis and uniform over the field-of-view (FOV), depicting a more stochastic flame structure.

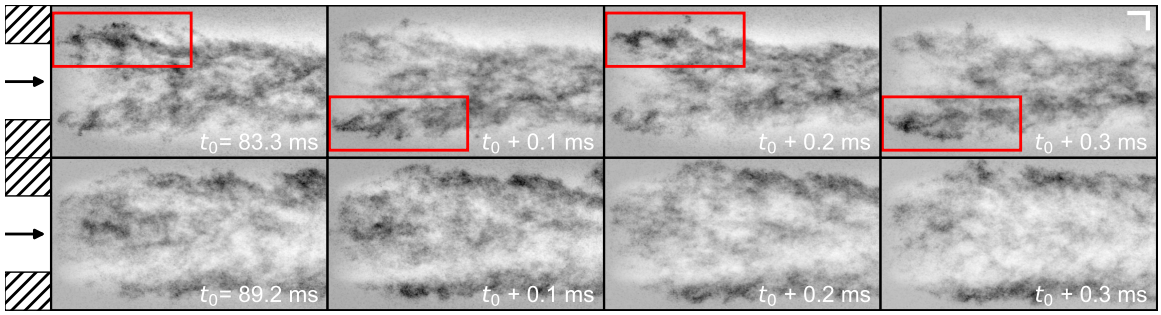

Figure 4.11. Instantaneous chemiluminescence for F2 (Scale is 0.1D; see white markers in top right frame)

Dynamic Mode Decomposition (DMD) [49,51] is applied to the OH*-chemiluminescence data to further analyze the periodic flame behavior. For this analysis 10000 images recorded within the limit-cycle period (see boxed time sections in Figure 4.9 a)) are used to represent a statistically-significant number of cycles of both low- (110-680 Hz) and high-frequency modes (5-10 kHz). The extracted intensity fluctuations from this analysis are qualitatively correlated to heat release oscillations in the FOV based on the super equilibrium concentration of OH* in the reaction zone [44, 45]. Figure 3.13 presents the DMD energy spectrum for F2 combined with spatial modes at the dominant frequencies in the spectrum (see mark-up in Figure 4.12 a)).

Along with a high energy peak at 110 Hz, the DMD energy spectrum for F2 in Figure 4.12 features two broad band peaks located at 4.8-5.5 kHz and 10-10.5 kHz. The 4.8-5.5 kHz region contains modes that are spatially similar in structure to the 5115 Hz mode, which contains the highest energy in this band. The 1T spatial mode shows fluctuations in the y-direction, with alternating regions of high and low intensity either side of the chamber axis. This is overlaid with axial variation in intensity, representative of convective transport

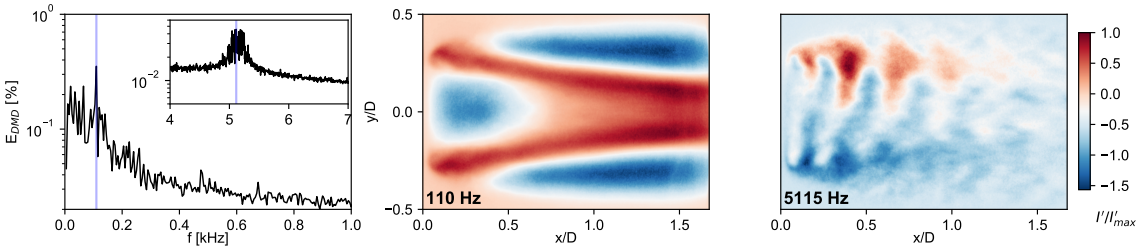

Figure 4.12. a) DMD energy spectrum and spatial modes for F2 at b) 110 Hz and c) 5115 Hz

of the flow structures shed off the combustor dump-plane. As observed in Figure 4.11, the asymmetry in the vortex shedding pattern is seen in the strong inclination of the intensity variation about the y-direction, representing helical vortices. The mode at 10.3 kHz shows smaller scale intensity fluctuations that originate at the dump-plane and pulse in the y-direction as they are convected downstream. However, the mode structure is not conclusive and cannot be assigned to a particular mode in the pressure spectrum.

To temporally correlate the heat release fluctuations in the combustion zone with concurrent pressure measurements at C-1, multiple interrogation windows are defined, indicated in Figure 4.13, throughout which time series of local emission intensity fluctuations were obtained. The first window pair (W1) is located in the vicinity of the dump-plane edge (solid lines) and is centered on the initial flame roll-up location seen in the mean subtracted instantaneous emission field in Figure 4.13 a). A second pair of windows (W2) is located in the upper and lower half of the FOV, capturing the reaction zone in the shear-layer (dashed lines). Representative time slices of the intensity fluctuations and power density spectra for the upper window signals for W1 and W2 are presented in Figure 4.13 c-d). Both signal pairs of W1 and W2 show a principal oscillation at 5.1 kHz which is amplitude modulated at 110 Hz, corresponding to the major modes found in the PSDs (4.13 b)). At periods of high amplitude oscillations (i.e. Figure 4.13 c-d) t=94-95 ms) the upper and lower half signal, especially in W1, show a 180° phase shift, indicating an asymmetric heat-release distribution for the respective window pairs and ultimately about the chamber axis. W1

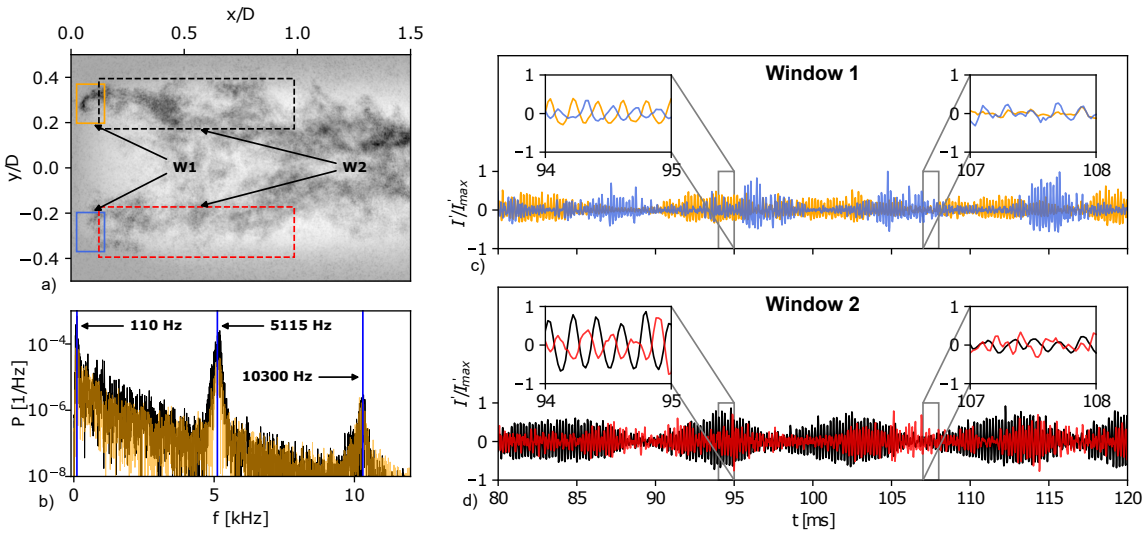

Figure 4.13. a) Instantaneous I' field and interrogation window declaration, b) PSD of upper W1 and W2 window signals and c-d) summed I' signals of window pairs W1 and W2 respectively

captures the initial flame roll-up and is correlated to the vortex-shedding process, which is estimated at 5.1 kHz based on this analysis. The asymmetry in the heat-release signal indicates asymmetric vortex-shedding during time periods of high amplitude oscillations in W1 and W2. In low amplitude periods (i.e. Figure 4.13 c-d) t=107-108 ms), upper and lower window signals have a more stochastic intensity distribution in the FOV. This flame behavior is consistent with the presence of a slowly rotating 5.1 kHz 1T mode at the Burner-Face. It is pointed out that the 10.3 kHz mode found in the DMD analysis can be located in both intensity spectra, the nature of this flame-affecting mode however can not be determined based on this analysis.

4.3.2 Singular Spectrum Analysis

Singular Spectrum Analysis (SSA) is used to further investigate the nature of the high frequency flame modulations. SSA provides a means of data-adaptive pattern recognition in a time series, by generating a delay-coordinate phase space from which augmented

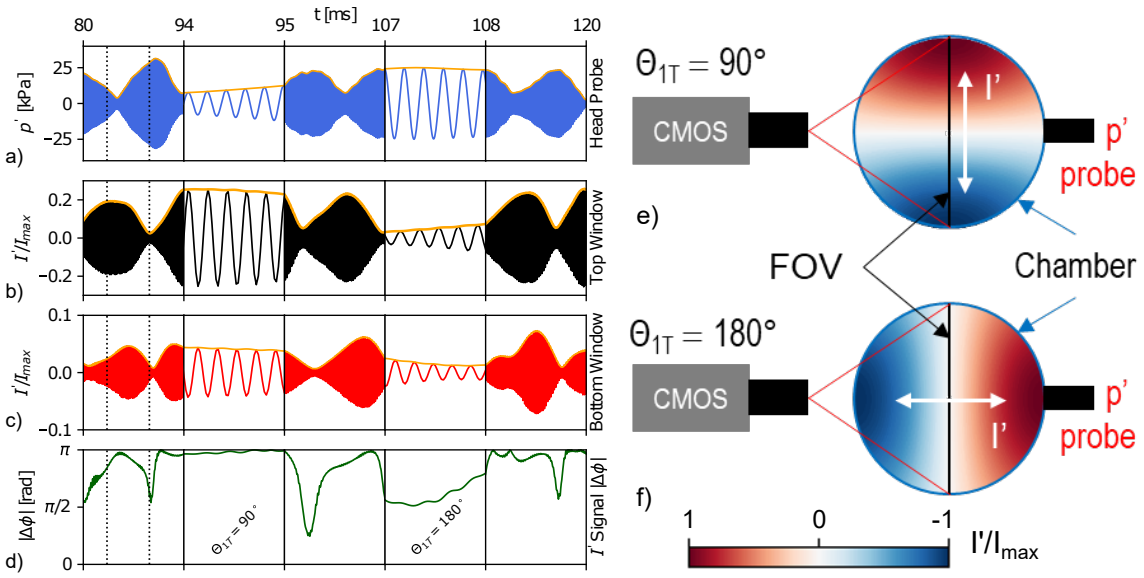

Figure 4.14. Flame 2 SSA reconstructed signals for a) C-1 pressure, b-c) upper and lower W2 I' signal, d) phase difference between upper and lower W2 signals and e-f) 1T mode schematics. Black dotted lines represent the two time slices at which instantaneous snapshots are provided in Figure 4.11.

principal vectors are extracted, corresponding to the dominant modes in the original time series. SSA is capable of extracting highly non-linear patterns, which can be amplitude and/or phase modulated and are thus advantageous over classical frequency based linear methods [53, 54].

Figure 4.14 a-c) presents the SSA processed C-1 pressure and W2 intensity signals respectively, for which modes in the frequency range of 4950-5250 Hz were summed. All three signals are characterized by a 110 Hz amplitude modulation, where the chamber-head pressure modulations are 180° out of phase with the intensity signal modulation. The phase difference between the upper and lower intensity-time history for W2 shown in Figure 4.14 d) is calculated from the difference of the respective Hilbert transform arguments and is a heat-release symmetry indicator about the x-axis of the FOV.

Periods of increased emission intensity fluctuation amplitude correlate with a $\phi = 180°$ phase shift between the two signals (W1 & W2), and agrees with a 1T pressure field at the chamber head-end, for which the anti-node axis is oriented parallel ($\Theta_{1T} = 90°$) to the field-of-view (FOV), as illustrated in Figure 4.14 e). The pressure signal, measured at a location normal to the FOV (refer to C-1 in Figure 2.10), has a reduced amplitude in these time periods, corresponding to the 1T pressure node centered on the transducer axis. For time periods in which the pressure signal has an increased amplitude (i.e. $\Theta_{1T} = 180°$), the intensity signal amplitudes are reduced and the phase difference decays significantly, correlating to stochastic heat release fluctuations distributed evenly across the FOV. A 1T mode oriented normal to the FOV, schematically shown in Figure 4.14 f), corresponds to this behavior. Here the anti-node axis is oriented parallel to the pressure transducer axis, leading to a maximum pressure amplitude during these periods. Heat release intensity modulation at the 1T frequency is thus occurring in the plane perpendicular to the FOV, and cannot be captured by line-of-sight integrated chemiluminescence measurements. These two processes are illustrated over two separate cycles of the 1T mode in Figure 4.11 highlighted by dotted lines at 83 and 89 ms in 4.14. The top row of snapshots corresponds to $\Theta_{1T} = 90°$ and the bottom-row corresponds to $\Theta_{1T} = 180°$.

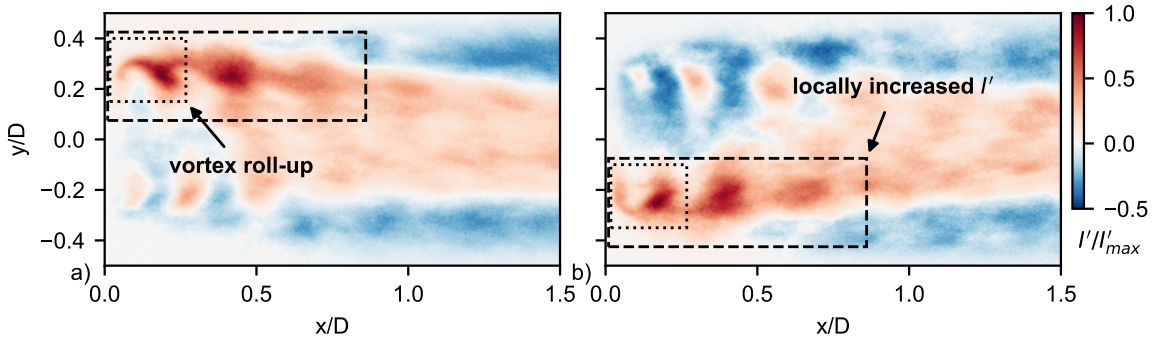

Figure 4.15. Phase conditioned OH* chemiluminescence images at heat-release maximum on a) upper and b) lower combustor half, indicating the flame response to the 1T mode pressure field orientated at $\Theta_{1T} = 90°$

The SSA reconstructed W2 signals can be used to phase-condition the chemiluminescence images during time periods for which the 1T mode is oriented parallel to the FOV (i.e. $\Theta_{1T} = 90^{\circ}$). Hereby time instances for which the phase difference $|\Delta\phi| > 175^{\circ}$ and the signal amplitude $I'/I'_{max} > 0.25$ are identified for the upper and lower window and spatially averaged. Figure 4.15 shows the resulting phase-averaged emission fields (≈ 110 images each) for which Figure 4.15a) and b) represent emission fields for time periods of maximum I' in the upper and lower half of the combustor respectively. Both mean fields clearly indicate the asymmetry in the I' field about the combustor axis (dashed mark-up), indicating higher local levels of heat release. In addition the asymmetric vortex shedding can be observed in these spatially averaged images (dotted mark-up), which can be connected to a 1T pressure field at the Burner-Face oriented parallel to the FOV (i.e. $\Theta_{1T} = 90^{\circ}$). Based on this analysis it is hypothesized that a non-stationary 1T mode is present in the chamber for Flame 2, that circumscribes the Burner-Face at 55 Hz. This rate of rotation corresponds to the DMD spatial mode at 110 Hz, shown in Figure 3.13a), as well as the amplitude modulation observed in the chamber pressure and chemiluminescence emission intensity. Such a mode rotation rate would result in intensity signals for which the spatial heat release fluctuation maximum varies temporally from the outer-recirculation zone ($\Theta_{1T} = 90^{\circ}$) towards the chamber axis ($\Theta_{1T} = 180^{\circ}$).

4.3.3 Conclusions

Self-excited combustion instabilities in a high pressure (p_c =7 bar) backward-facing step combustor were investigated using high frequency pressure measurements and OH*-chemiluminescence. The combustor was found to present both low- and high-frequency instabilities at 1L (360 Hz) and 1T (5.1 kHz) chamber modes. Two representative test conditions that show discriminating flame behavior, F1 and F2 were investigated.

A higher equivalence ratio (ϕ = 0.72) test case Flame 1 presented mainly longitudinal mode dynamics of a lower amplitude ($p'/p_c = 3\%$) and the pressure spectrum was dominated by a standing 1L mode in the combustor. The OH*-chemiluminescence images

for this case were characterized by axisymmetric vortex shedding representative of ring vortices and consequent axial flame-vortex interactions.

The leaner test case (ϕ = 0.69) Flame 2 was characterized by high amplitude ($p'/p_c =$ 15%) high-frequency modes that have been seldom observed in single-element self-excited combustors. A dominant fundamental transverse mode was observed in both the chamber head-end pressure measurement as well as the OH*-chemiluminescence images. DMD analysis of the images indicated the presence of asymmetric vortex shedding of the backward-facing step, representative of helical vortices, at the 1T (5.1 kHz) frequency resulting in an high amplitude transverse instability in the combustor. SSA of the spatially averaged intensity fluctuations and the chamber head-end pressure signal indicated amplitude modulation of both the pressure and heat release fluctuations at 110 Hz. The pressure and intensity fluctuation modulations are out of phase with each other indicating a non-stationary 1T mode that rotates at a frequency of 55 Hz about the chamber axis.

5. HIGH FREQUENCY DYNAMICS IN THE FULLY-PREMIXED CONFIGURATION COMBUSTOR

The premixed duct lengths for both, technically- and fully-premixed configurations were designed to promote positive pressure coupling at the dump plane of the combustor. With the same geometric configuration, a wide range of instabilities- mode, amplitude, and frequency- were observed over a parametric sweep of operating conditions. For the technically premixed configuration, the longitudinal modes were typically stronger, with higher amplitudes at lower equivalence ratios. By decoupling potential equivalence ratio fluctuations in the fully-premixed configuration, the instabilities were seen to transition from longitudinal to transverse modes at a lean subset of the operational envelope.

In this chapter, a discussion of experiments where specific parameters that affect flame structure and jet instabilities, namely the jet Mach number, chamber pressure, and dump-plane geometry is provided. The primary focus is to understand the underlying physical mechanisms that drive the range of combustor instability regimes. In particular, the role of near-field jet instabilities formed in the shear layer on overall flame stability. On the other hand large scale structures that develop further downstream in the shear layer are observed to differ from the waves that are formed initially due to vortex merging [55]. Different regions of the axial shear alters the local reaction layer across different spatial modes and rates resulting in a complex spatial coupling of the heat release and flow field.

In order to test the hypothesis that hydrodynamics are responsible for the major coupling mechanism leading to instability regime changes, the sensitivity of transverse and longitudinal mode dynamics on the power level and geometric configuration are studied. In particular the inlet duct velocity $\bar{u}_{IN}$, mean chamber pressure $\bar{p}_4$, and the protrusion of the inlet duct into the combustion chamber are discretely varied from the baseline configuration discussed in Chapter 4.

Changes in system pressure ($\bar{p}_4 \approx 7$ bar) and inlet velocity ($\bar{u}_{IN} \approx 120$ m/s) alter the flame power level, which affects the temporal and spatial scales involved in the coupling mechanisms generating self-excited combustion instabilities. The range of turbulent length scales in the flow field vary as a function of the Reynolds number $Re = \rho \bar{u}_{IN} d/\mu$ and directly affected by the pressure, and temperature of the flow field as well as the jet velocity. Chemical scales such as ignition delay, kinetic rates, and turbulent flame speed are functions of gas composition and properties and affect the location of the reaction layer within the jet shear layer. The thermal flame power is estimated from the chemical energy stored in the supplied fuel such that:

$$P_{therm} = \dot{m}_f \cdot HV = \rho_f \cdot u_{IN} \cdot A_{IN} \cdot HV \tag{5.1}$$

where HV is the heating value of the fuel in J/kg. The jet diameter d is held constant for these tests, thus the jet velocity and/or system pressure (fuel density) variation lead to changes in thermal flame power.

5.1 Pressure Sensitivity

In order to study the effect of system pressure on the combustor dynamics the mass flow rate is adjusted while keeping the exit nozzle area constant. System pressure affects the Reynolds number and thus turbulent scales present in the flow field. Additionally, pressure affects the chemical kinetics and thus reaction parameters that alter the reaction layer response to flow perturbations. Target pressures are 10 and 4 bar, whereas the baseline chamber pressure is ≈ 7 bar. The experiment operation envelope is documented in Table 5.1.

The chamber pressure p_c is directly proportional to $\dot{m}_{tot}$ if A_e is unchanged. This leads to the following flame properties that need to be considered when analyzing the pressure sensitivity study results:

- Flame thermal power is directly proportional to system pressure and total mass flow rate

$$P_{th} \propto \dot{m}_{tot} \propto p_c \tag{5.2}$$

Table 5.1. Operation envelope for pressure sensitivity study

$\dot{m}_{air}$	$\bar{p}_c$	$\bar{u}_{IN}$	ϕ	T_3	D_E
0.32	4	120	0.61-0.78	650-760	3.322
0.75	10				
kg/s	bar	m/s	-	K	cm

- Volumetric fuel flow rate, inlet velocity and system pressure are linear dependent on mass flow rate

$$\dot{q}_f, v_{IN} \propto \frac{\dot{m}_{tot}}{p_c} \approx const. \tag{5.3}$$

- Flame length (and volume) is a function of the volumetric fuel flow rate

$$L_f, V_f \propto \dot{q}_f \approx const. \tag{5.4}$$

- The flame thermal power density is a function of p_c

$$P = \frac{P_{th}}{V_f} \propto p_c \tag{5.5}$$

- The jet Reynolds number is a function of p_c

$$Re_{jet} = \frac{\rho \cdot u_{IN} \cdot d}{\mu} \propto p_c \tag{5.6}$$

These relationships are shown in Figure 5.1 for the pressure sensitivity study. Figure 5.1 a) shows the linear relationship between thermal power and chamber pressure, which needs to be considered for the comparison between different system pressure tests. Figure 5.1 c) shows the linear relationship between Re_{jet} and p_c, which leads to a drastic change in spatiotemporal scales available for flame interaction in the flow field. However as stated above $\dot{q}_f$ and thus the flame length/volume is approximately constant, which leads to a linear relationship between the thermal power density P and p_c.

Figure 5.2 summarizes the effect of chamber pressure $\bar{p}_c$ on the total instability amplitude $p'/\bar{p}_c$, in which the data is color-coded based on T_{ad}. Probes HF004/06A/008 all

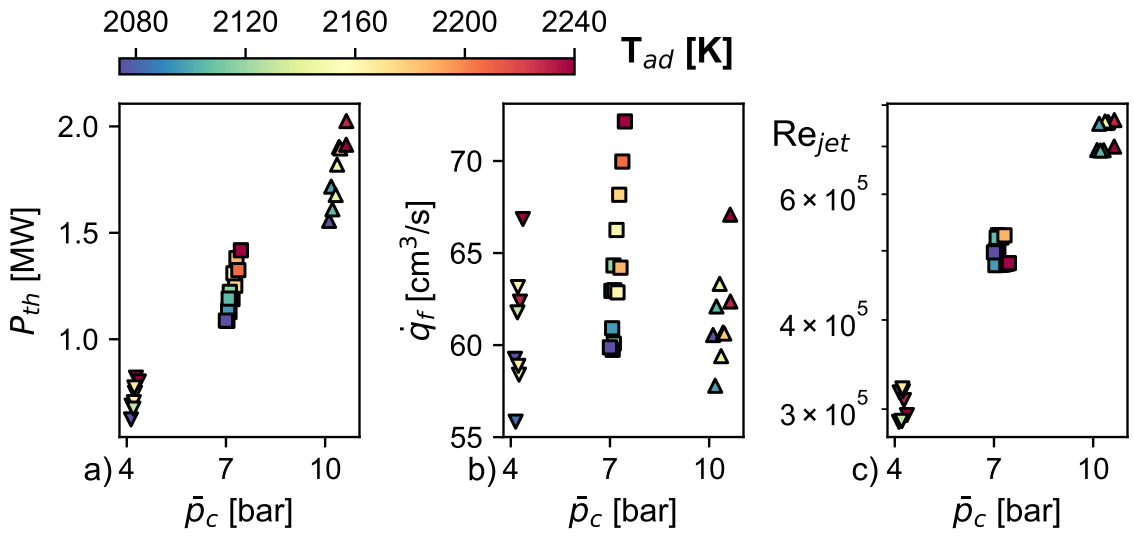

Figure 5.1. a) P_{th} and b) $\dot{q}_f$ and c) Re_{jet} vs. $\dot{m}$ as a function of the mean chamber pressure

indicate that the total magnitude of pressure fluctuations decreases with $\bar{p}_c$. In addition the variance of $p'/\bar{p}_c$ decreases with $\bar{p}_c$ which indicates that the p' amplitudes decrease with $\bar{p}_c$. The contrary is observed at the chamber head-end (HF05C), where $p'/\bar{p}_c$ increases with $\bar{p}_c$.

Figure 5.3 shows the pressure amplitudes specific to the 1L, 2L, HF1(1T) and HF2 mode as a function of $\bar{p}_c$. As the probes HF004/06A/008 are primarily exposed to longitudinal dynamics, it can be inferred that the energy contained within the longitudinal dynamics saturate and do not gain energy from increased $\bar{p}_c$ as observed in Figure 5.3, where the 1L and 2L mode contributions decrease with $\bar{p}_c$. The fact that the variance of $p'/\bar{p}_c$ decreases for the longitudinal mode amplitudes with $\bar{p}_c$ may be correlated to the increases of Re_{jet}. With an increased number of spatiotemporal scales available for the flame and thus heat release to interact with, the longitudinal dynamics that primarily couple with larger flow structures (larger time scales) can decrease as more energy is distributed across smaller spatiotemporal scales. This is further supported by the increase of the HF1 mode contributions with $\bar{p}_c$ for probe HF05C as observed in Figure 5.3, which results in the opposite trend seen in Figure 5.2 compared to the remaining probes.

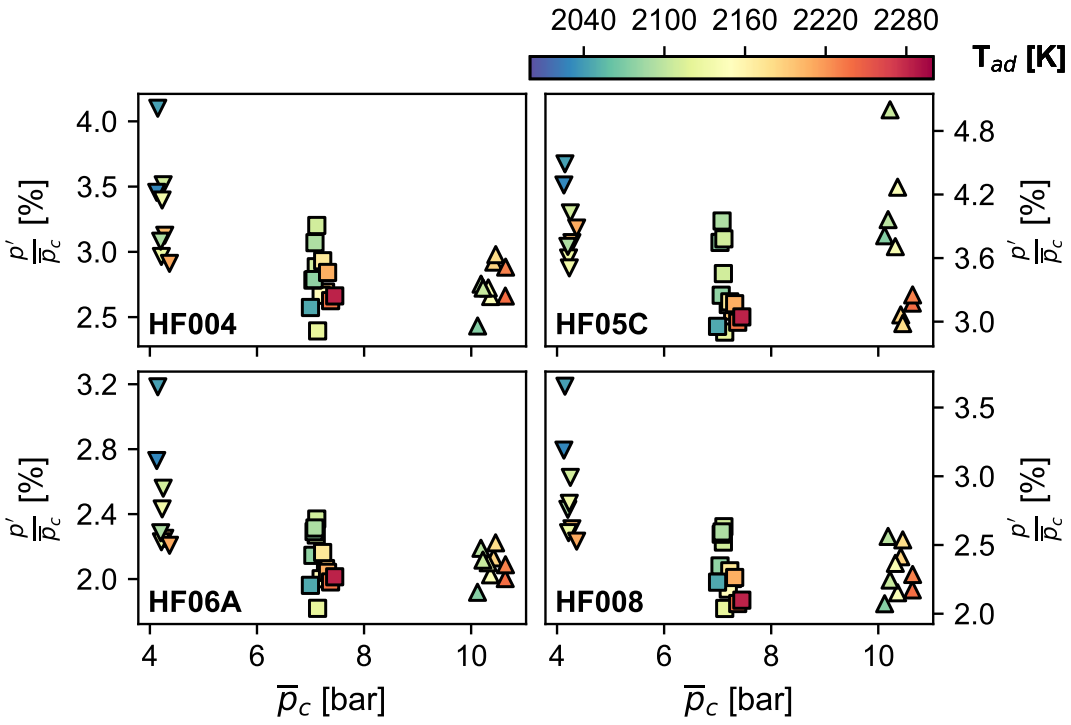

Figure 5.2. $p'/\bar{p}_c$ vs. ϕ of pressure sensitivity study at selected probes. Note different y-scales.

Table 5.2. Selected operation conditions from the pressure sensitivity study: pressure amplitudes based on HF05C probe

Case	$\dot{m}_{air}$	ϕ	T_3	p_3	$\frac{p'}{\bar{p}}$	p'_{1L}	p'_{HF_1}	p'_{HF_2}
113	0.32	0.66	660	4.3	4.5	0.73	0.1	0.1
126	0.75			10.2	57.4	0.85	8.8	0.9
	kg/s	-	K	bar	%	%	%	%

Two representative cases, one at 4 bar and the other at 10 bar which show distinct changes in dynamics with a change in $\bar{p}_c$ are documented in Table 5.2. Case FPC_113 is dominated by longitudinal modes at 354 Hz and 686 Hz (1L and 2L chamber mode), as observed in the power spectra for probe locations HF004/05C/008 in Figure 5.4 a-c).

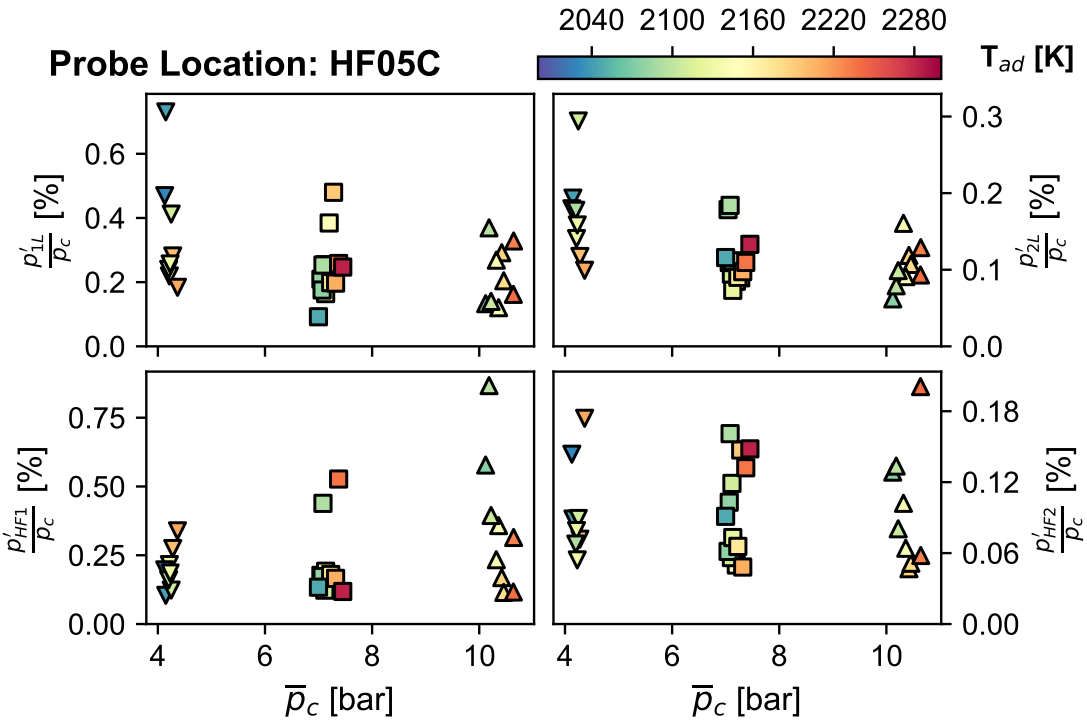

Figure 5.3. Mode contributions to $p'/\bar{p}_c$ vs. ϕ of pressure sensitivity study at selected probes. Note different y-scales.

Higher frequency modes are present at the chamber head-end at 5.12 kHz (HF1) and 5.64 kHz (HF2) and superimposed on the dominant 1L pressure oscillations.

Case FPC_126 in contrast is dominated by a strong HF1 mode at 5.2 kHz observed in the power spectra shown in Figure 5.5. At the burner-face probe the HF1 mode reaches amplitudes that are an order of magnitude higher than the 1L mode. The dynamics at the aft of the chamber are still dominated by 1L mode.

5.2 Injection Velocity Sensitivity

The injection velocity ($\bar{u}_{IN}$) is changed by adjusting the reactant mixture mass flow rate $\dot{m}_{tot}$ and exit nozzle area A_{ex} in order to maintain the baseline mean chamber pressure of $\bar{p}_c = 7bar$. The change in $\bar{u}_{IN}$ alters the Re_{jet} which affects both the turbulent sales present

in the flow field as well as the instability characteristics of the jet shear layer. Target velocities are 90 and 150 m/s, whereas the baseline velocity is $\bar{u}_{IN} \approx 120$ m/s. The experiment operational envelope has been summarized in Table 5.3.

Table 5.3. Operation envelope for the inlet velocity sensitivity study

$\dot{m}_{air}$	$\bar{p}_c$	$\bar{u}_{IN}$	ϕ	T_3	D_E
0.40	7	90	0.63-0.77	660-780	2.827
0.66		150			3.649
kg/s	bar	m/s	-	K	cm

The flame power P_{th} is directly proportional to $\dot{m}_{tot}$ and $\bar{u}_{IN}$. The following flame properties need to be considered when interpreting the results from the velocity sensitivity study:

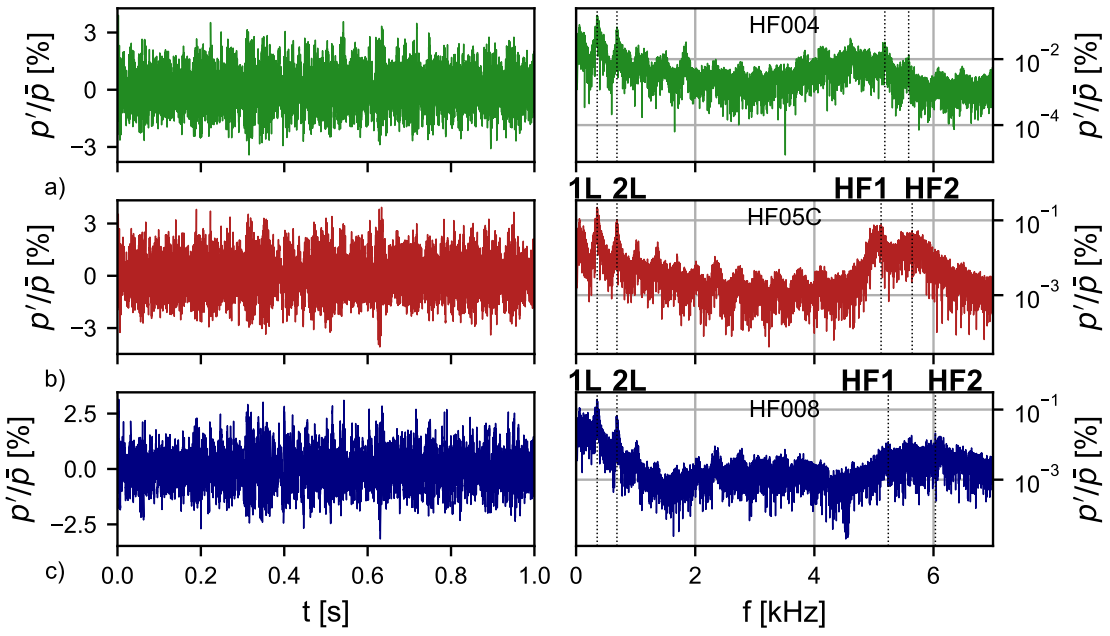

Figure 5.4. Pressure time series and power spectrum for FPC_113 for probe a) HF004, b) HF05C and c) HF008. Note different y-scales.

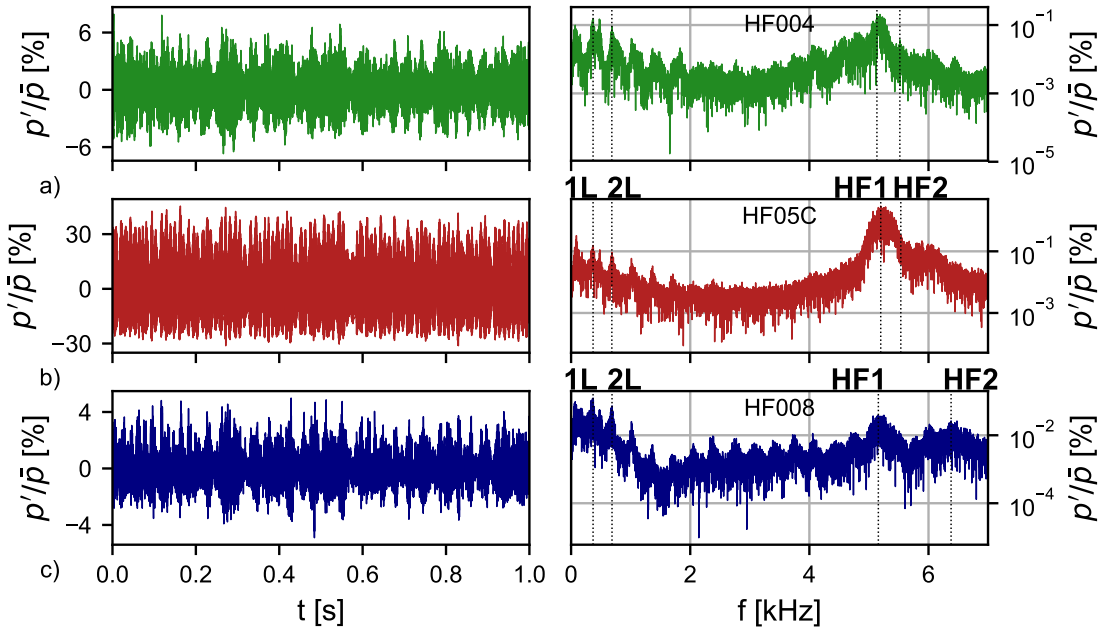

Figure 5.5. Pressure time series and power spectrum for FPC_126 for probe a) HF004, b) HF05C and c) HF008. Note different y-scales.

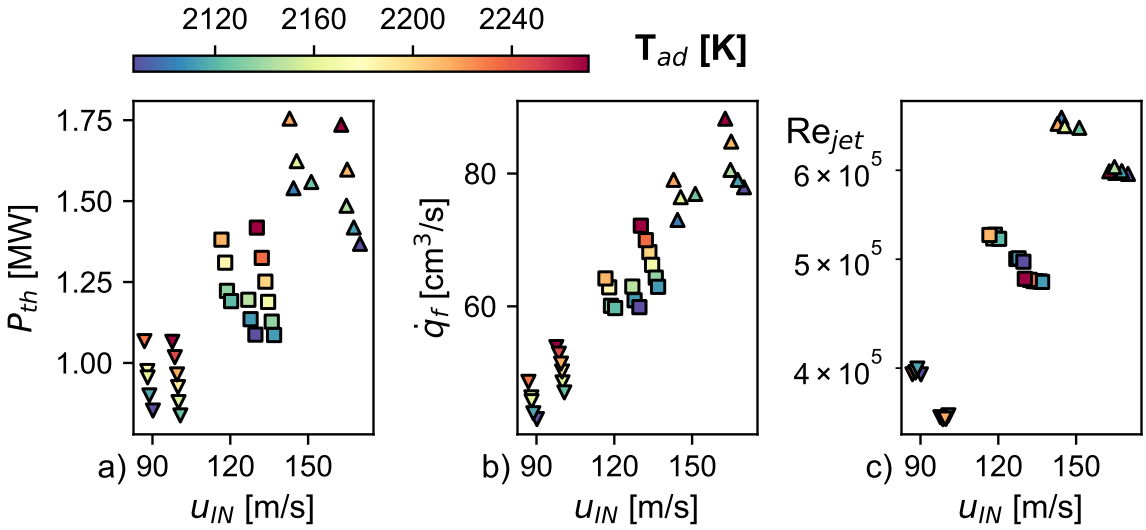

Figure 5.6. a) Flame power and b) volumetric fuel flow rate for velocity sensitivity tests

- Flame thermal power is directly proportional to u_{IN} for a constant chamber pressure $\bar{p}_c$

$$P_{th} \propto \dot{m}_{tot} \propto u_{IN} \tag{5.7}$$

- Volumetric fuel flow rate and inlet velocity are a function of total mass flow rate at constant system pressure

$$\dot{q}_f, v_{IN} \propto \dot{m}_{tot} \tag{5.8}$$

- Flame length (and volume) is a function of the volumetric fuel flow rate

$$L_f, V_f \propto \dot{q}_f, \dot{m}_{tot} \tag{5.9}$$

- The flame thermal power density is not a strong function of $\bar{u}_{IN}$

$$P = \frac{P_{th}}{V_f} \propto \frac{\dot{m}_{tot}}{\dot{m}_{tot}} \approx const. \tag{5.10}$$

- The jet Reynolds number is a function of u_{IN}

$$Re_{jet} = \frac{\rho \cdot u_{IN} \cdot d}{\mu} \propto \bar{u}_{IN} \tag{5.11}$$

Figure 5.6 a) shows the linear relationship between thermal power and inlet velocity, which needs to be considered for the comparison between different system pressure tests. Figure 5.6 c) shows the linear relationship between Re_{jet} and $\bar{u}_{IN}$, which leads to a drastic change in spatiotemporal scales available for flame interaction in the flow field. However as stated above $\dot{q}_f$ is a function of $\bar{u}_{IN}$ for a constant $\bar{p}_c$ as shown in Figure 5.6 b), resulting in a weak relationship between flame power density P and the varying parameter $\bar{u}_{IN}$ for these tests in contrast to the pressure sensitivity study.

Figure 5.7 summarizes the results of the velocity sensitivity study and presents the total instability amplitude $p'/\bar{p}_c$ as a function of $\bar{u}_{IN}$, in which the data is color-coded based on T_{ad}. All probes indicate that the total magnitude of pressure fluctuations increases with $\bar{u}_{IN}$. These trends are most likely correlated to the increase of P_{th} with $\bar{u}_{IN}$ as the turbulence level increases with $\bar{u}_{IN}$. The variance of $p'/\bar{p}_c$ measured at HF05C is observed to increase with $\bar{u}_{IN}$, which is correlated to an increased magnitude of modes HF1 and HF2.

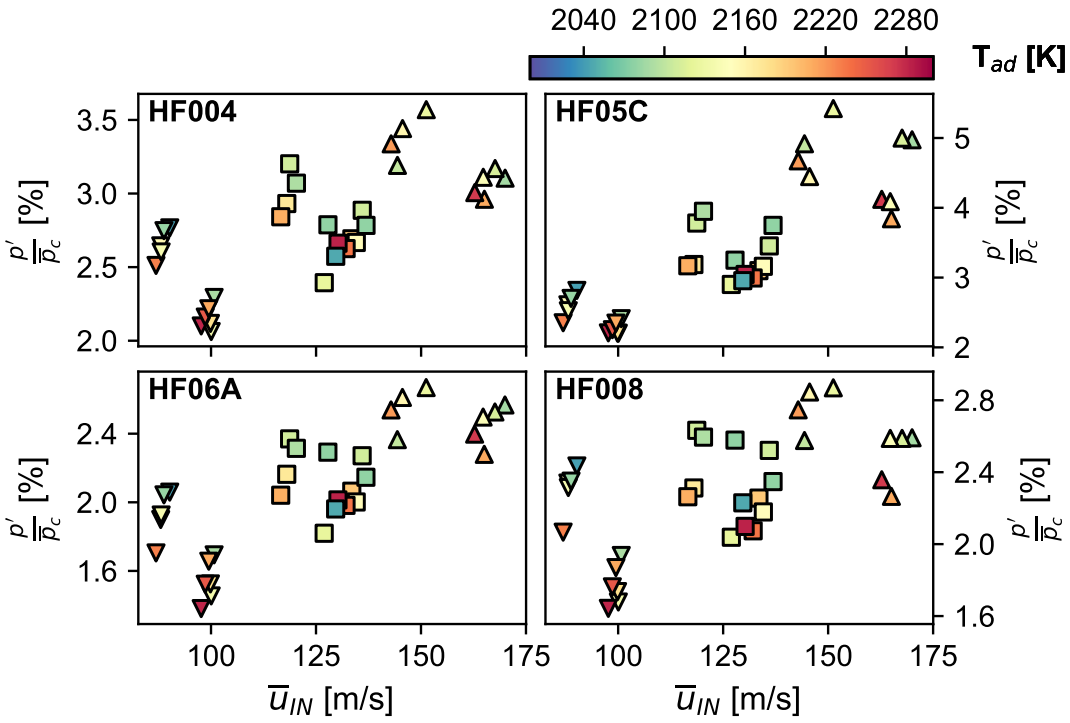

Figure 5.7. $p'/\bar{p}_c$ vs. ϕ of velocity sensitivity study at selected probes. Note different y-scales.

Figure 5.8 shows the pressure amplitudes specific to the 1L, 2L, HF1(1T) and HF2 mode as a function of $\bar{u}_{IN}$. The longitudinal modes show an independence of $\bar{u}_{IN}$, except for a small velocity band ranging from 100 to 130 m/s, which corresponds to the baseline velocity range, where the magnitude of these modes drop. Longitudinal mode amplitudes for $\bar{u}_{IN} < 100$ and $\bar{u}_{IN} > 130$ m/s are comparable when normalized by P_{th} or $\dot{m}_{tot}$. The drop of the longitudinal dynamics is correlated with an increased HF1 magnitude measured at the burner-face, which points to a coupling of the shear layer instability modes and chamber 1T resonance frequency. The HF2 magnitude is found to be invariant with $\bar{u}_{IN}$, except for two narrow velocity bands centered around 100 and 165 m/s.

To investigate the influence of shear layer instabilities on the combustion instability regime Strouhal numbers (St) for the 1L, 2L and HF1 mode amplitudes are computed.

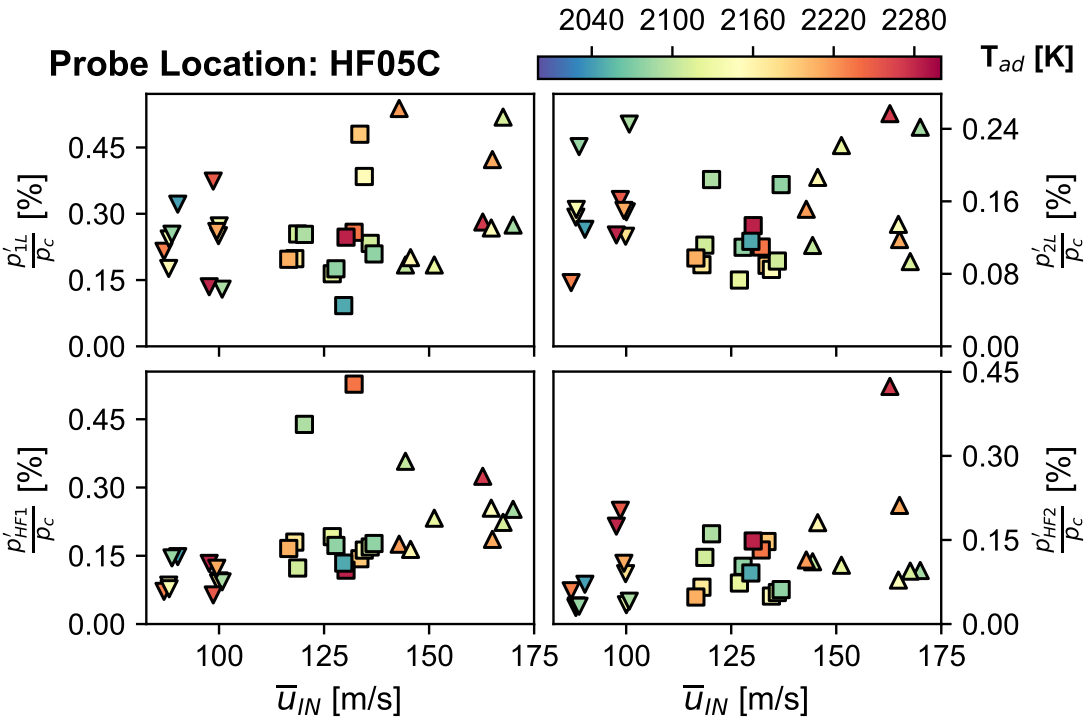

Figure 5.8. Mode contributions to $p'/\bar{p}_c$ vs. ϕ of velocity sensitivity study at selected probes. Note different y-scales.

Figure 5.9 shows the velocity sensitivity data as well as the phase 3 FPC data (no burner-face probes installed) which serves as the baseline for this analysis. The amplitudes are normalized by their respective maximum value in each mode subset, i.e. for the 1L mode amplitudes:

$$p'_{max} = max(p'_{1L}|_{90m/s}, p'_{1L}|_{120m/s}, p'_{1L}|_{150m/s}) \tag{5.12}$$

Colored bands mark the resonance frequency regions in terms of St for each inlet duct velocity group. The 1L and 2L modes are strongest in the baseline configuration ($\bar{u}_{IN} =$ 120m/s). Especially the 2L mode reaches maximum amplitudes at a $St \approx 0.23$ and $\phi \approx 0.68 - 0.72$, which is a common frequency for axisymmetric vortex-shedding modes associated with the shear layer Kelvin-Helmholtz instability [28].

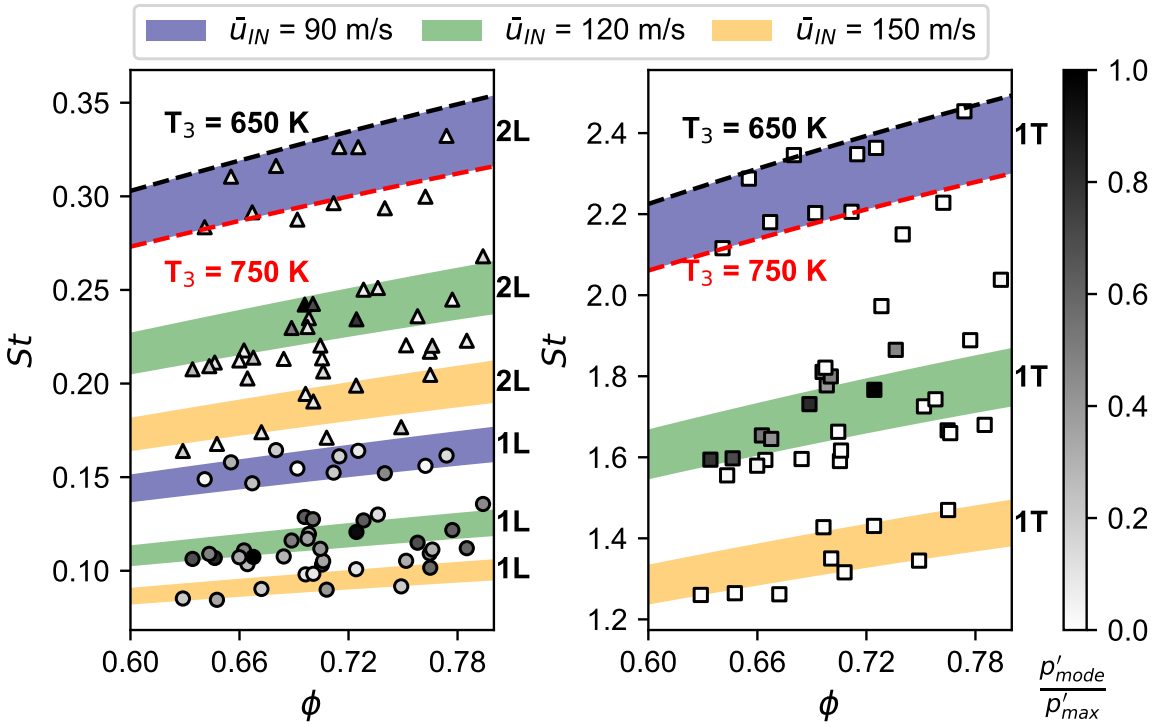

Figure 5.9. Three combustor mode frequency groups for selected $\bar{u}_{IN}$ in terms of Strouhal number (St) based on the jet diameter d

The HF1 dynamics are observed to be most prominent in the baseline configuration as well. Especially the region $St \approx 1.6-1.7$ for $\phi < 0.72$ promotes high amplitude 1T dynamics at the chamber head-end. The inlet duct velocities $\bar{u}_{IN} = 90$ and 150 m/s alter the shear layer dynamics and shift these out of the 1T resonant mode frequency regions, resulting in overall low magnitudes compared to the baseline configuration. This study proves that the shear layer resonant modes need to couple with the acoustic resonant modes in order to develop 1T mode limit cycles in the combustion chamber.

5.3 Influence of Burner-Face Probes on HFD

The obtain correlated pressure and chemiluminescence data at the location of flame stabilization, pressure transducers were installed on the backward-facing step of the com-

bustor. The transducers were installed in recessed cavities, similar to ones used in all other pressure measurements. However, these burner-face transducer cavities were found to influence the onset of high amplitude transverse and azimuthal dynamics in the experiment. To discuss this effect two conditions summarized in Table 5.4 are dicussed here.

Table 5.4. Operation conditions for burner-face Probe effect analysis

Case	$\dot{m}_{air}$	ϕ	T_3	p_3	$p'/\bar{p}$	p'_{1L}	p'_{HF_1}	p'_{HF_2}
091	0.53	0.60	730	7.1	11.4	0.40	0.34	0.25
099		0.59			3.9	2.14	0.05	0.07
	kg/s	-	K	bar	%	%	%	%

The mean operating conditions for the two cases are identical within experimental measurement uncertainty and the only variance is the installation of the three burner-face probes HF05A, HF05B, and HF05C. For case FPC_091 the FPC configuration in which no burner-face probes are installed (similar to all results discussed in Chapter 4) was used, whereas for case FPC_099 the experiment was equipped with three transducers using the modified interface and burner-face adapter plate. By comparing the pressure time series and power spectra for both cases in Figure 5.10 and 5.11 a distinct change in the instability regime is observed. Both cases, as most of the FPC tests do show amplitude modulations for the participating modes throughout the test duration, thus these cases do not fully develop typical limit-cycle dynamics.

Case FPC_091 exhibits high amplitude pressure oscillations at the chamber head-end of $p'/\bar{p}_c = 11.4\%$ and is dominated by the HF1 and HF2 modes. The 1L mode is present at a similar magnitude compared to the HF2 mode, however the high frequency dynamics dominate the chamber head-end.

Case FPC_099 in contrast is dominated by low amplitude 1L oscillations in the chamber. Twice the magnitude of case FPC_091 is reached, whereas the higher frequency modes are significantly reduced by an order of magnitude and are effectively not participating. There are time periods (i.e. t = 0.04-0.05) in which the 1L oscillations decrease in amplitude

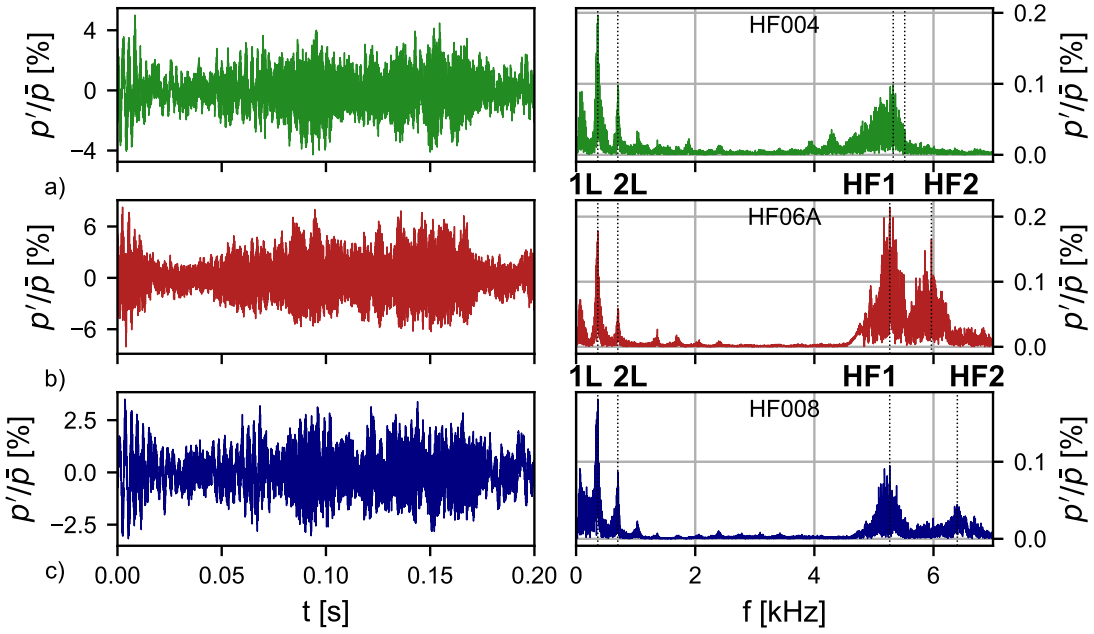

Figure 5.10. Pressure time series and power spectrum for FPC_091 for probe a) HF004, b) HF06A and c) HF008. Note different y-scales.

and the HFD are more prominent, however the 1L mode is dominant in the combustion chamber.

These changes in instability regimes may be result of an initial damping effect of the recessed burner-face probes on the HFD modes, which are placed at locations close to the anti-node location of the 1T chamber mode. ONce the flow-field recovers from the initial ignition spike, and within the initial development phase of the jet shear layer, these cavities may provide enough damping to a developing 1T mode such that the planar 1L mode, unaffected by these sensors, will succeed where the 1T mode does not. This theory is supported by the fact that the 1L oscillations reach twice the magnitude in case FPC_099 compared to FPC_091, in which both modes coexist, thus the 1L mode extracts energy that would otherwise be used to maintain the transverse dynamics at the head-end. Therefore the altering effect of the burner-face probes needs to be considered in the pressure and velocity sensitivity study results.

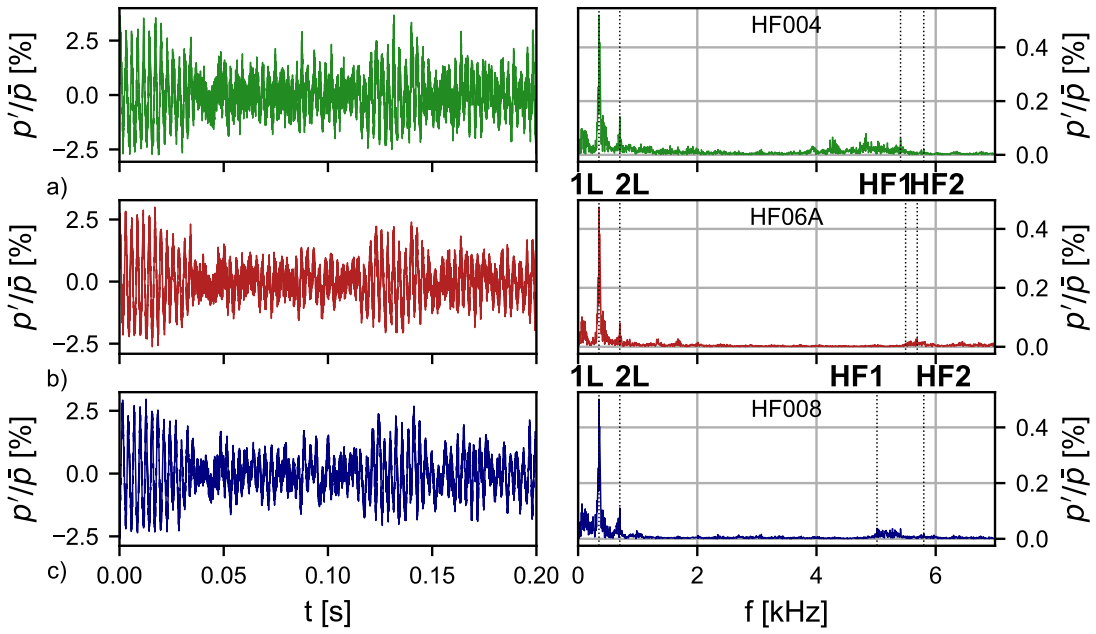

Figure 5.11. Pressure time series and power spectrum for FPC_099 for probe a) HF004, b) HF06A and c) HF008. Note different y-scales.

5.4 Protrusion Study

The protrusion study aimed to investigate the effect of inlet duct immersion into the combustion chamber. As a result of this duct modification the flame is located further downstream of the 1L anti-node at the chamber head-end compared to the baseline configuration. The spatial offset of pressure and heat release fluctuations may affect the longitudinal dynamics, granted that the chamber spatial modes are not affected by the duct modification. The protrusion has a wall thickness of 1.5 mm and extends 40 mm into the combustion chamber, as shown in Figure 5.12 and the test operation envelope is summarized in Table 5.5.

Figure 5.13 summarizes the protrusion configuration, FPC phase 3 and phase 5 data for probes HF06A and HF008, as these probes are available in all data sets. The chamber head-end instability trends for the protrusion hardware are comparable to the FPC phase 3 data set, however larger total instability magnitudes are reached in the protrusion hardware

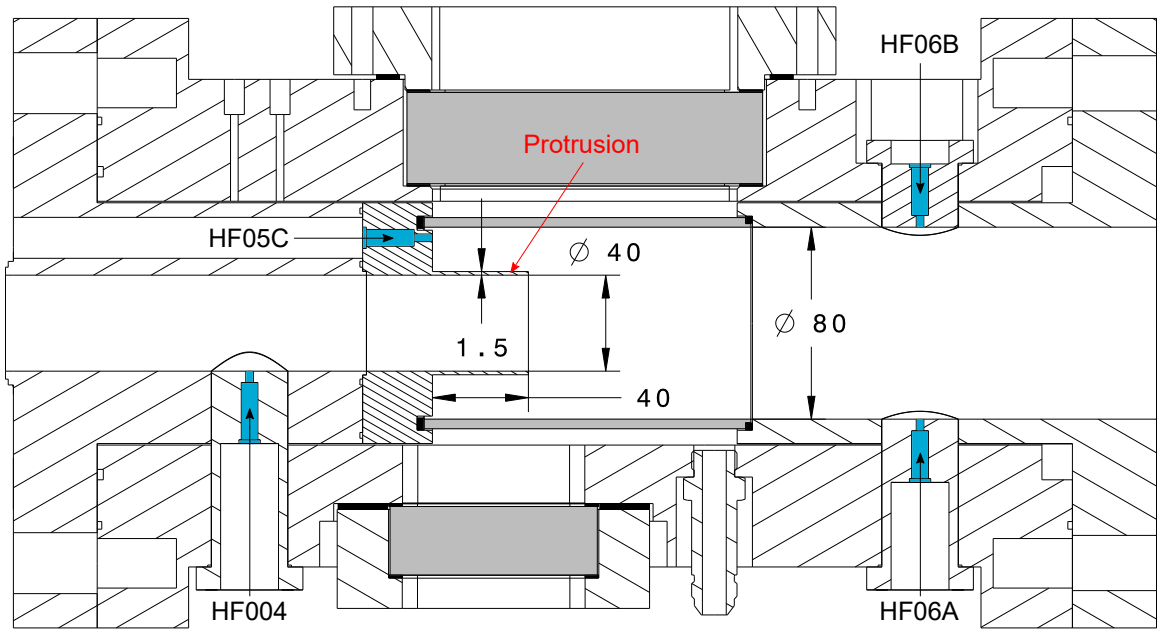

Figure 5.12. Protrusion geometry and referenced probe locations at the combustion chamber head-end. All dimensions in mm.

for $\phi < 0.7$. There exists a threshold ϕ at which the head-end dynamics increase drastically and this value shifts towards leaner conditions with an increase in T_3. Comparison of the phase 5 baseline (burner-face probe installed) with the protrusion and phase 3 data shows that the $p'/\bar{p}_c$ at the chamber head-end (HF06A) are significantly reduced and no clear trends can be observed.

In contrast to that, the protrusion chamber aft-end data is comparable in magnitude with the phase 3 and phase 5 data, where $p'/\bar{p}_c$ increases with decreasing ϕ (right column in Figure 5.13). This is a general chamber aft-end trend for which lower T_3 conditions promote higher $p'/\bar{p}_c$ for the same ϕ. The phase 3 FPC data will serve as baseline for the following analysis, as the amplitudes are comparable.

The increased instability magnitude at the chamber head-end is due to the onset of the 1L, HF1 and HF2 mode as observed in Figure 5.14. For the baseline configuration the 1L mode remains unaffected by ϕ changes, whereas for the protrusion hardware an increase in amplitude for leaner conditions is observed ($\phi < 0.68$). The 2L mode in the protrusion data

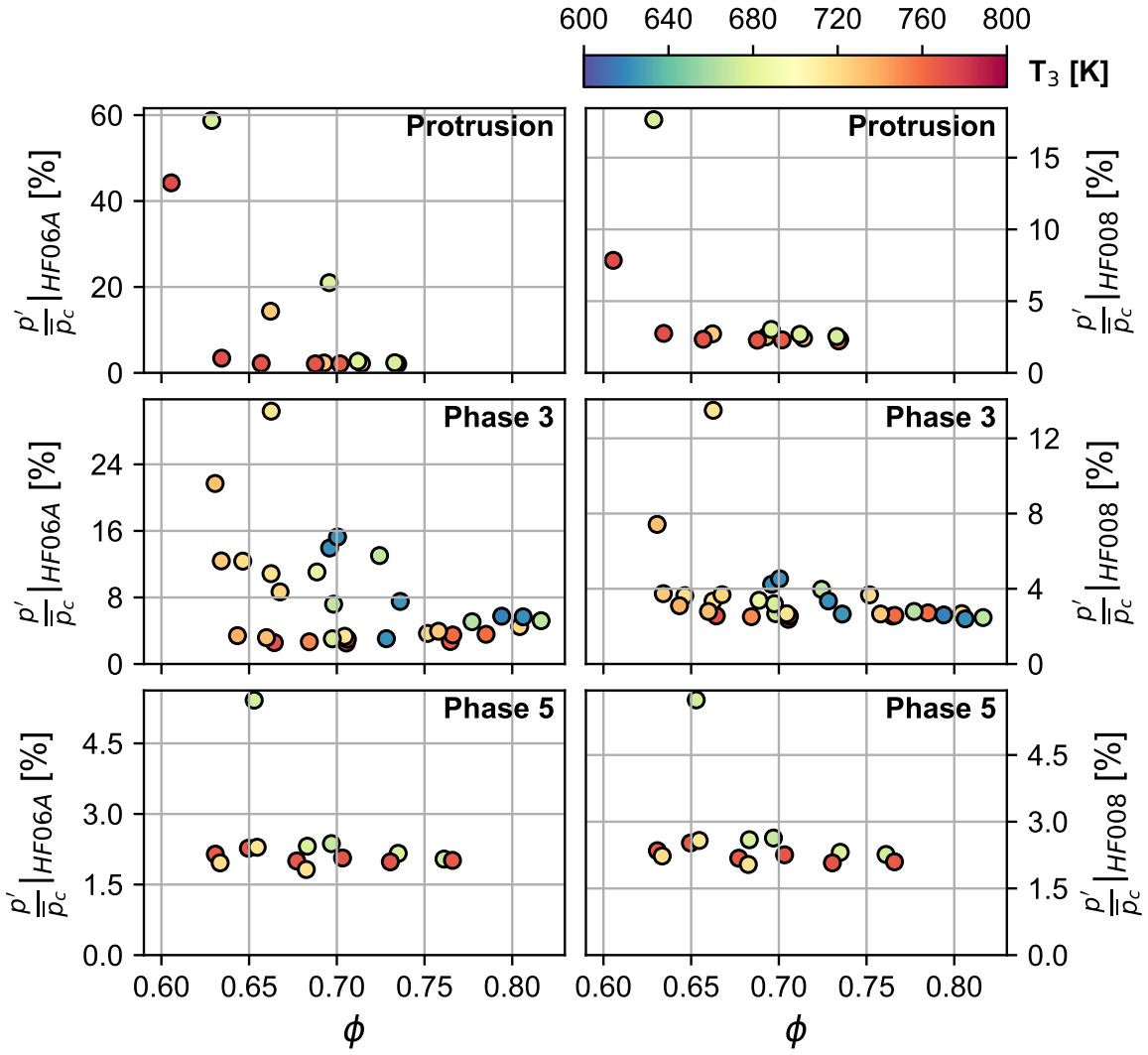

Figure 5.13. $p'/\bar{p}_c$ for protrusion configuration, FPC phase 3 and phase 5 at probes HF06A and HF008. Note different y-scales.

follows the 1L mode trend, which is in contrast to the baseline data, in which the 2L mode increases in magnitude for $\phi < 0.75$. The HF1 and HF2 mode amplitudes increase sharply for a ϕ threshold value, which moves towards leaner conditions with increasing T_3. The HF1 mode is more dominant for lower T_3 conditions, whereas the HF2 mode dominates at high T_3 operation.

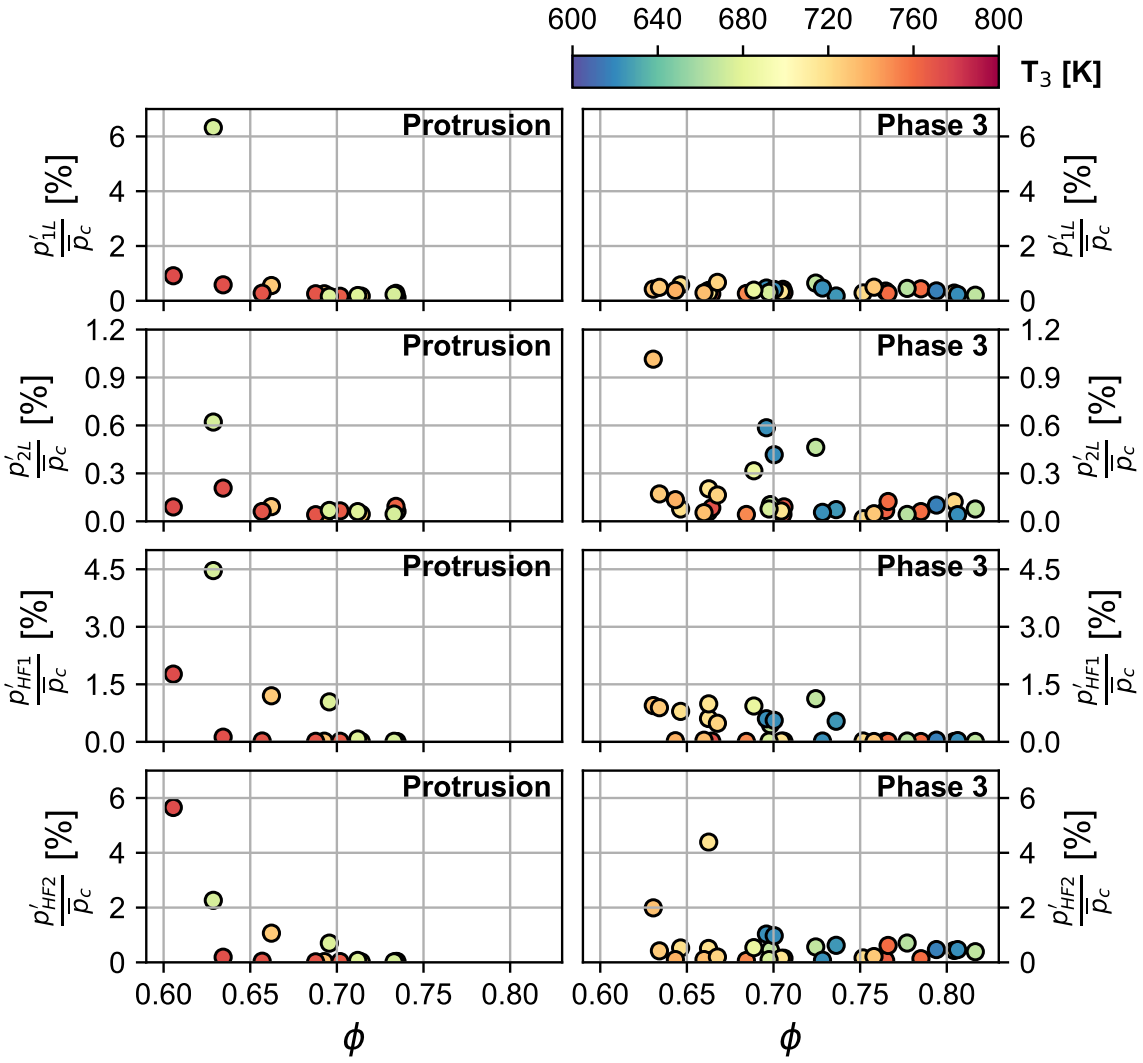

Figure 5.14. $p'_{mode}/\bar{p}_c$ for protrusion configuration and FPC baseline (phase 3) at HF06A. Note different y-scales for plot rows.

The longitudinal frequencies are not affected by the protrusion hardware and are located at $\approx 340-360$ Hz and $\approx 700-740$ Hz for the 1L and 2L mode respectively. In contrast to that, the frequency separation between modes HF1 and HF2 decrease and most conditions produce a single broadband mode located at $\approx 5.5-6$ kHz, similar to the HF3 instability regime in the baseline data. The main results of this study include:

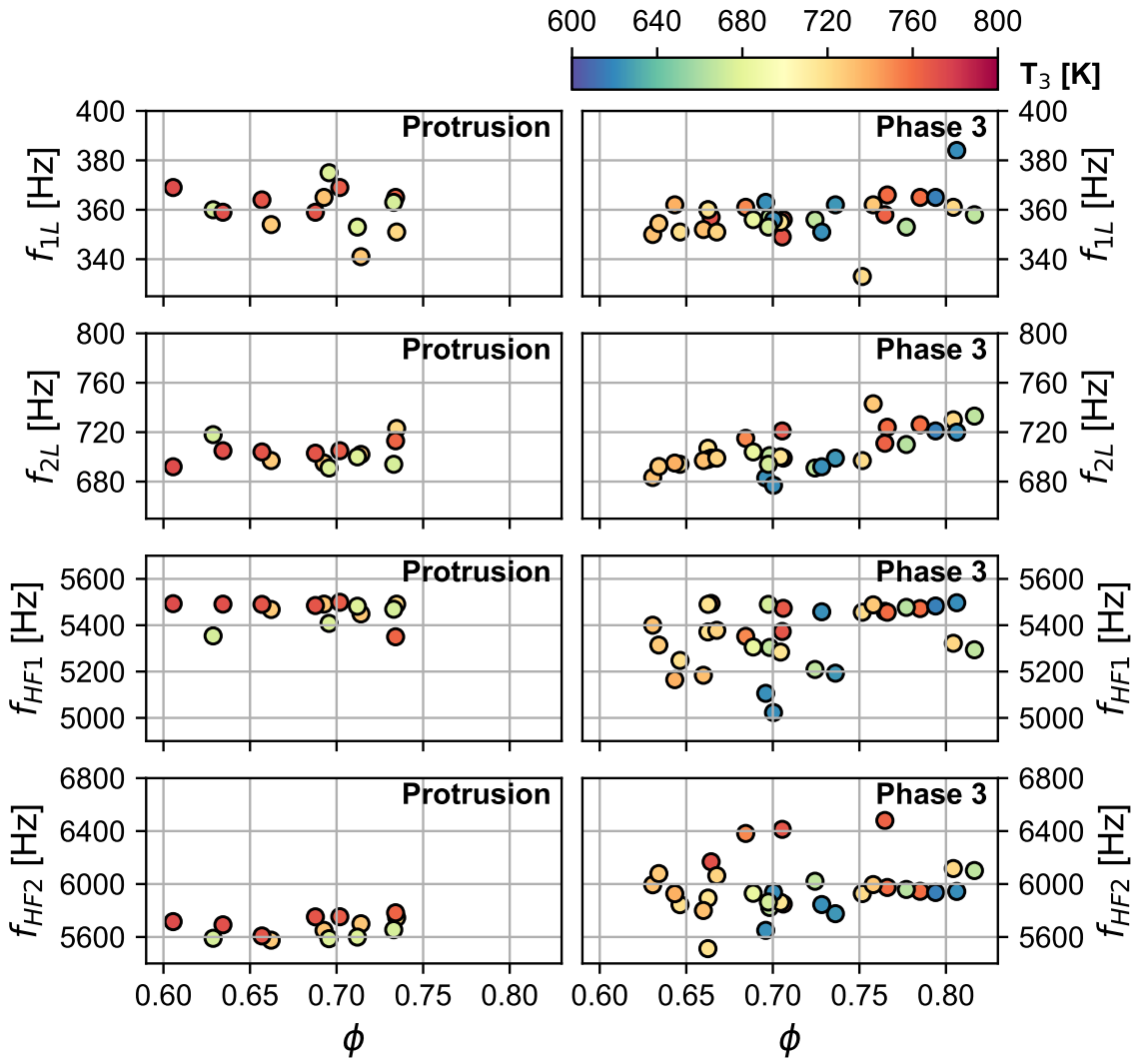

Figure 5.15. Mode frequencies for protrusion configuration and FPC baseline (phase 3) at HF06A. Note different y-scales for plot rows.

- The immersion of the inlet duct into the chamber does not alter the longitudinal chamber mode frequencies. The 1L mode shows a ϕ dependency and increases for leaner conditions, where lower T_3 conditions result in larger amplitudes for the same ϕ. This is in contrast to the baseline data, where the 1L mode is unaffected by changes in ϕ. The 2L mode follows the 1L trend, however in contrast to the baseline

data, the 2L amplitudes are decreased for the region $0.65 < \phi < 0.75$, in which the baseline configuration shows larger magnitudes.

- The HF1 and HF2 mode amplitudes are not affected by the inlet duct immersion and show similar trends compared to the baseline data. The frequency separation between the two modes however is affected and a dynamics separation into two modes becomes questionable based on FFT methods.

- The burner-face probe installed for the protrusion tests does not affect the chamber dynamics. The protrusion hardware shows the same potential for high amplitude transverse and azimuthal modes as observed in the FPC hardware with no burner-face probes installed. As the inlet duct is immersed, any disruption provided by the probe cavity will have dissipated by the time it is convected through the recirculation zone and reaches the nozzle near field. In addition the chamber head-end flow field with the inlet protrusion may feature two recirculation zone, where an additional one is located in the annulus created by the protrusion and flame tube. Thus the nozzle near field is composed of an axisymmetric flow. This is in contrast to the baseline configuration, where the probe cavities create an asymmetry and may provide enough damping in the initial transverse/azimuthal development phase of the instability to suppress its growth.

Table 5.5. Operation envelope for protrusion study

$\dot{m}_{air}$	$\bar{p}_c$	$\bar{u}_{IN}$	ϕ	T_3	D_E
0.53	7	120	0.6-0.74	670-770	3.322
kg/s	bar	m/s	-	K	cm

5.5 Instability Damping with Resonators

A resonator study was conducted as an attempt to dampen the high amplitude 1T mode (HF1) observed in the protrusion study. Two resonator inserts were installed in two of the burner-face adapter probe holes, which result in two Helmholtz-type resonators as shown in Figure 5.16.

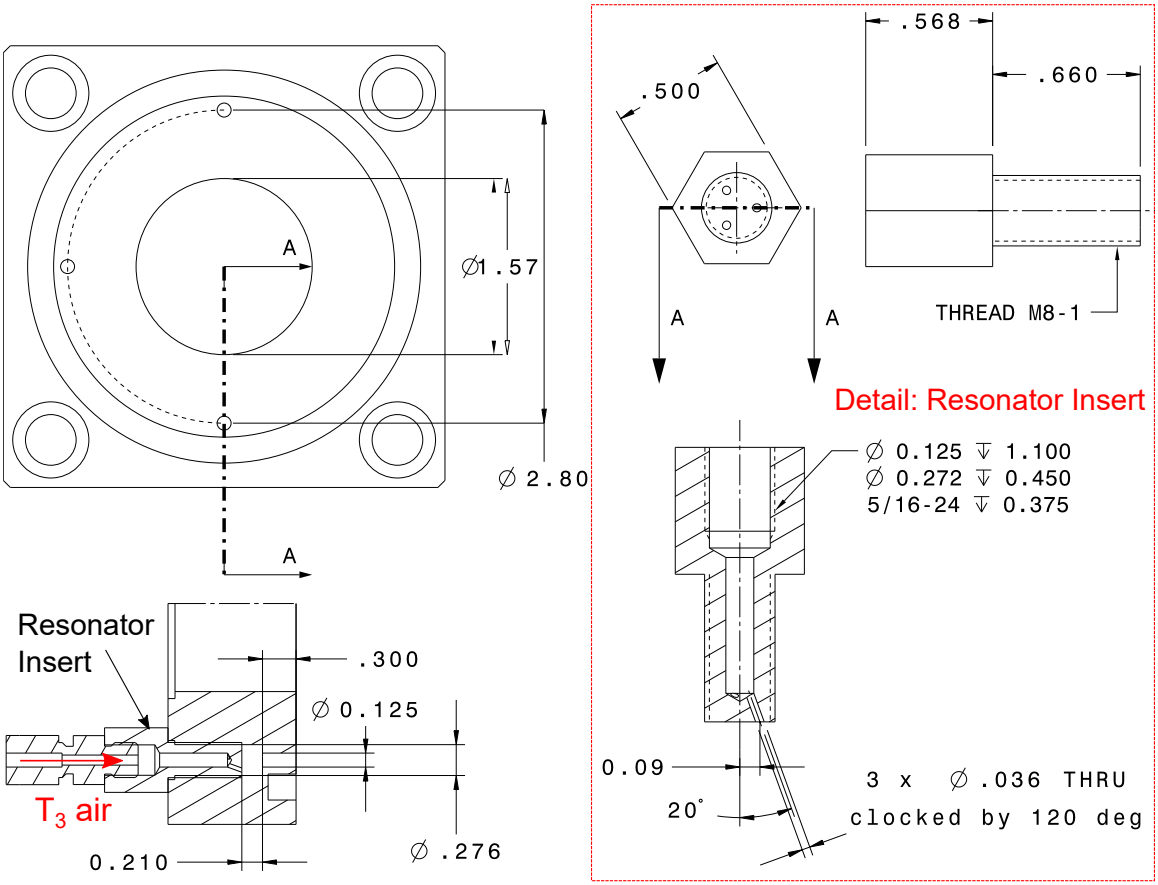

Figure 5.16. Resonator design and installation within burner-face adapter plate. Dimension are in inches.

The two resonators are purged with air at T_3 extracted from the main air supply prior injection into the External-Premixer. The purge flow is metered via a CFVN and is routed to the resonator insert port. The purge air is then injected into the resonator cavity through three 0.914 mm orifices, which are angled by 20° to avoid jet impingement on the resonator

Table 5.6. Operation envelope for resonator study

$\dot{m}_{air}$	$\bar{p}_c$	$\bar{u}_{IN}$	ϕ	T_3	$\dot{m}_{purge}$	$\bar{u}_{res}$	$\bar{u}_{neck}$	D_E
0.53	7	120	0.6-0.74	670-770	0.7	70	12	3.322
kg/s	bar	m/s	-	K	g/s	m/s	m/s	cm

neck. The operation envelope including the combined resonator purge mass flow rates (for two resonators) and injection velocities are documented in Table 5.6, where $\bar{u}_{res}$ and $\bar{u}_{neck}$ are the purge velocities into the resonator cavity and out of the resonator neck respectively.

The resonators show a successful reduction in total instability amplitudes at all chamber locations as shown in Figure 5.17 for the range of conditions tested. $p'/\bar{p}_c$ reduction of up to 72% and 67% at HF06A and HF05C can be achieved (see $\phi < 0.64$ for $T_3 = 770$ K group). The resonators influence especially the targeted high frequency modes HF1 and HF2 as shown in Figure 5.18. A reduction in mode amplitude for HF2 is observed for $\phi < 0.67$ for all T_3 groups at location HF05C and HF06A. As already mentioned in the protrusion study, the distinct two modes are significantly closer spaced compared to the FPC baseline and develops a broadband mode in the HF2 band (peak at ≈ 5.6 kHz). The resonators do not affect the frequency of the HFD modes and perform well, considering that only two resonators were installed.

The main results of this study include:

- The resonators successfully reduce total instability magnitudes in the protrusion hardware, reductions of up 72% were measured.

- The HF1 and HF2 mode amplitudes are significantly reduced for $\phi < 0.67$.

- Considering the significant effect of the resonators on the high frequency mode amplitudes, the influence of the burner-face probe cavities on HFD in the baseline FPC hardware is plausible and should be considered when working with the project phase 4 and 5 data sets.

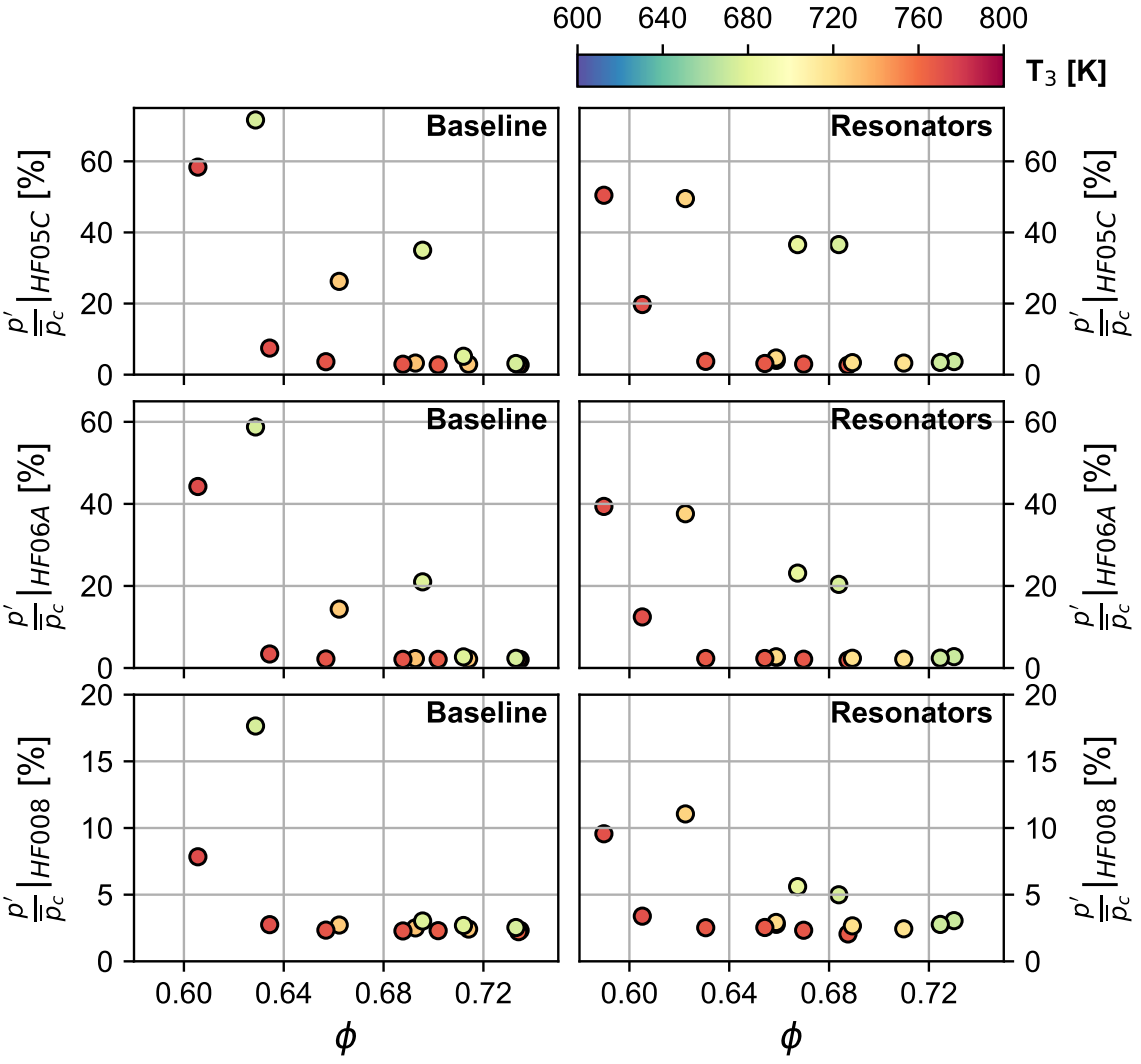

Figure 5.17. $p'/\bar{p}_c$ for resonator equipped and baseline protrusion configuration at probes HF05C, HF06A and HF008. Note different y-scales for plot rows.

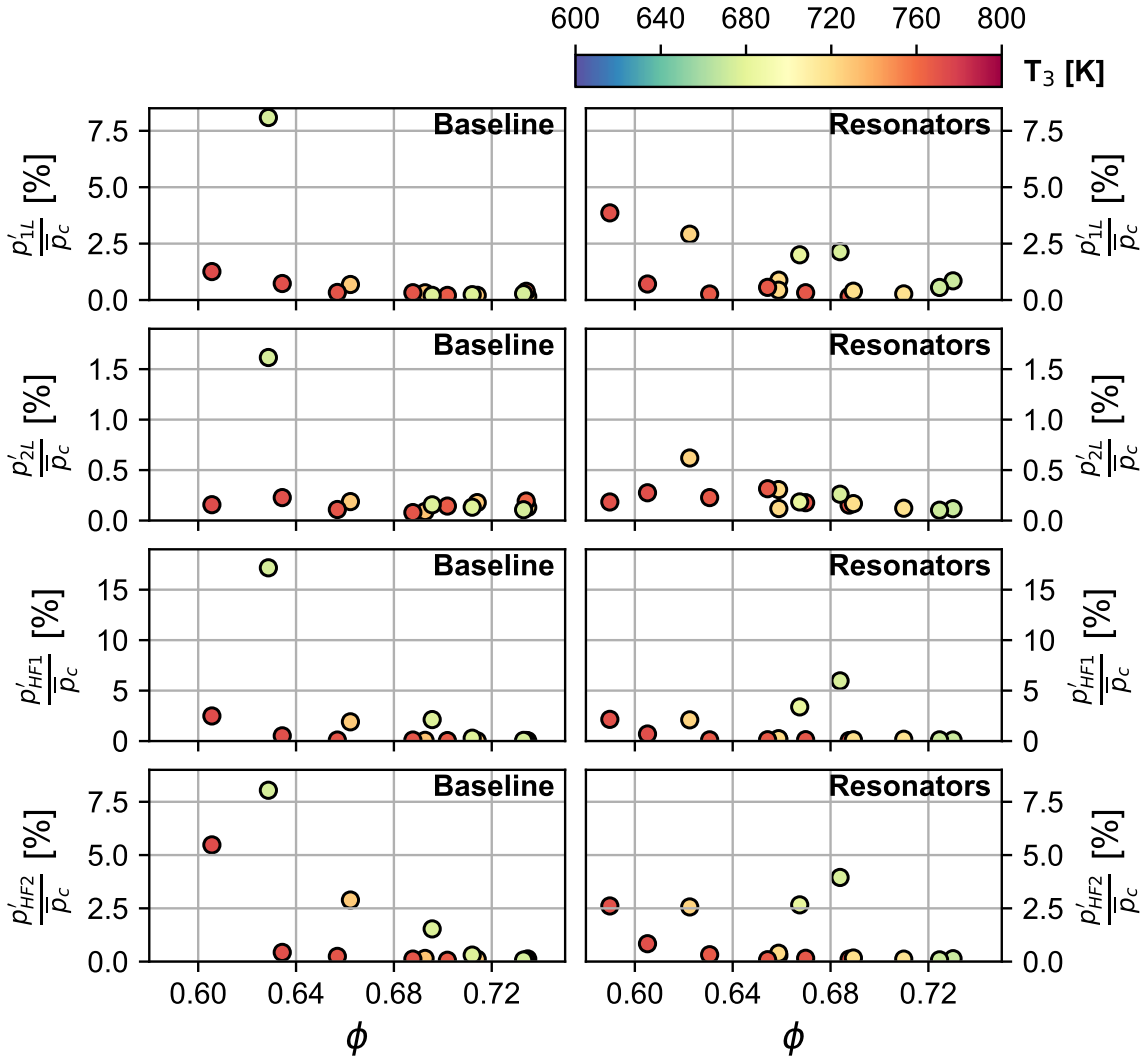

Figure 5.18. Mode frequencies for resonator equipped and baseline protrusion configuration at probe HF05C. Note different y-scales for plot rows.

6. LINEAR STABILITY ANALYSIS

Hydrodynamic instabilities within these complex flow fields are a fundamental link between pressure and heat release perturbations, as velocity perturbations interact with the reaction layer and can induce local fluctuations in energy release through flame surface alteration. As a major part of the reaction zone is located in the shear layer that forms between the recirculating region and the jet potential core, the flame is subject to the inherent instabilities of the confined jet flow. Eddies and subsequent larger coherent structures forming in the shear layer downstream of the sudden expansion, modulate the transport of heat, mass, and momentum within the reaction zone and lead to fluctuations in the flame heat release [56]. The interaction between these turbulent flame processes and the resonant acoustic field are often linked through hydrodynamic characteristics of the flow, which are strong functions of velocity, temperature, and density. Local pressure oscillations in turn influence the gas properties which closes the complex feedback loop leading to the natural propensity to unstable behavior of turbulent flames. An asymmetry in the flow field promotes spatial asymmetries in the distribution of local heat release, which has the potential to drive transverse instability modes.

Spatiotemporal linear stability analysis (LSA) has been successfully applied to determine the stability characteristics of complex flow fields. The presence of multiple instability regimes and their dependence on hydrodynamic features amplified at acoustic frequencies motivated the use of the analysis for the fully premixed configuration of the experiment. In this chapter the governing equations for this analysis are formulated and validated against analytical solution for linear duct acoustics. Subsequently the base flow reconstruction is formulated and different methods to model the temperature and density field in the experiment are discussed. The effect of the reaction layer thickness and the shear layer structure on the solution of the generalized eigenvalue problem is then assessed and the final model form justified.

6.1 Model Formulation

The combustor geometry is cylindrical, thus the cylindrical coordinate system is chosen, where the coordinates are x, r and θ with corresponding velocity components u, v and w. The following assumptions are made for this problem: The flow field is

1. compressible and the gas state variables are governed by the ideal gas law.
2. is adiabatic.
3. is inviscid, justified by the inertia dominated flow at Reynolds numbers $Re_{d_{IN}} > 5 \cdot 10^5$.
4. is not acted upon by body forces.
5. is parallel, i.e. the local base flow is only a function of r.
6. time invariant.

Based on these assumptions, the conservation equations for mass, momentum and energy can be presented by the compressible Euler equations:

$$\frac{\partial \rho}{\partial t} + \frac{\partial}{\partial x}(\rho u) + \frac{1}{r}\left(\frac{\partial}{\partial r}(r\rho v) + \frac{\partial}{\partial \theta}(\rho w)\right) = 0 \tag{6.1}$$

$$\rho\left(\frac{\partial u}{\partial t} + u\frac{\partial u}{\partial x} + v\frac{\partial u}{\partial r} + \frac{w}{r}\frac{\partial u}{\partial \theta}\right) = -\frac{\partial p}{\partial x} \tag{6.2}$$

$$\rho\left(\frac{\partial v}{\partial t} + u\frac{\partial v}{\partial x} + v\frac{\partial v}{\partial r} + \frac{w}{r}\frac{\partial v}{\partial \theta} - \frac{w^2}{r}\right) = -\frac{\partial p}{\partial r} \tag{6.3}$$

$$\rho\left(\frac{\partial w}{\partial t} + u\frac{\partial w}{\partial x} + v\frac{\partial w}{\partial r} + \frac{w}{r}\frac{\partial w}{\partial \theta} + \frac{vw}{r}\right) = -\frac{1}{r}\frac{\partial w}{\partial r} \tag{6.4}$$

$$c_p\rho\left(\frac{\partial T}{\partial t} + u\frac{\partial T}{\partial x} + v\frac{\partial T}{\partial r} + \frac{w}{r}\frac{\partial T}{\partial \theta}\right) = \frac{\partial p}{\partial t} + u\frac{\partial p}{\partial x} + v\frac{\partial p}{\partial r} + \frac{w}{r}\frac{\partial p}{\partial \theta} \tag{6.5}$$

Assuming that each flow variable is composed of a time invariant mean and time dependent perturbation component, the Reynold's decomposition is utilized, i.e. for the static pressure $p(\mathbf{x},t) = p_0(\mathbf{x}) + p'(\mathbf{x},t)$ where $\mathbf{x} = [u,v,w]^T$. The decomposed variables are substituted into equations 6.1-6.5 and the equations for the mean quantities are subtracted.

The resulting set of equation is linearized by neglecting higher order terms, products of perturbations and their derivative, i.e. u'^2, $u'v'$ and $v'\frac{\partial u'}{\partial r}$. This results in the following set of linearized perturbation equations:

$$\frac{1}{\rho_0}\frac{\partial \rho'}{\partial t}+\frac{u_0}{\rho_0}\frac{\partial \rho'}{\partial x}+\frac{1}{r}\frac{\partial u'}{\partial x}+v'\left(\frac{1}{r}+\frac{1}{\rho_0}\frac{\partial \rho_0}{\partial r}\right)+\frac{\partial v'}{\partial r}+\frac{1}{r}\frac{\partial w'}{\partial \theta}=0 \tag{6.6}$$

$$\frac{\partial u'}{\partial t}+u_0\frac{\partial u'}{\partial x}+v'\frac{\partial u_0}{\partial r}=-\frac{1}{\rho_0}\frac{\partial p'}{\partial x} \tag{6.7}$$

$$\frac{\partial v'}{\partial t}+u_0\frac{\partial v'}{\partial x}=-\frac{1}{\rho_0}\frac{\partial p'}{\partial r} \tag{6.8}$$

$$\frac{\partial w'}{\partial t}+u_0\frac{\partial w'}{\partial x}=-\frac{1}{r\rho_0}\frac{\partial p'}{\partial \theta} \tag{6.9}$$

$$c_p\rho_0\left(\frac{\partial T'}{\partial t}+u_0\frac{\partial T'}{\partial x}+v'\frac{\partial T_0}{\partial r}\right)=\frac{\partial p'}{\partial t}+u_0\frac{\partial p'}{\partial x} \tag{6.10}$$

representing conservation of mass, momentum and energy respectively. Using the linearized equation of state,

$$p'=R_s(T_0\rho'+\rho_0T') \tag{6.11}$$

ρ' is eliminated from the mass conservation equation.

$$\begin{aligned}&\frac{1}{R_sT_0\rho_0}\frac{\partial p'}{\partial t}-\frac{1}{T_0}\frac{\partial T'}{\partial t}+\frac{u_0}{R_sT_0\rho_0}\frac{\partial p'}{\partial x}-\frac{u_0}{T_0}\frac{\partial T'}{\partial x}\\&+\frac{1}{r}\frac{\partial u'}{\partial x}+v'\left(\frac{1}{r}+\frac{1}{\rho_0}\frac{\partial \rho_0}{\partial r}\right)+\frac{\partial v'}{\partial r}+\frac{1}{r}\frac{\partial w'}{\partial \theta}=0\end{aligned} \tag{6.12}$$

This reduces the system of equations to the set of perturbation variables of interest $q'=[p',u',v',w',T']$, where R_s and c_p are the specific gas constant and the heat capacity at constant pressure. The gas medium in the domain is assumed to be air at a constant base flow pressure of p_3 with $R_s=287$ J/kg-K. c_p is calculated for air at the given $T_0(r)$ using the thermophysical property library CoolProp [57]. In order to investigate the stability characteristics of the flow field a modal Ansatz of the form

$$q'(r,t)=\hat{q}(r)e^{j(\alpha x+m\theta-\omega t)} \tag{6.13}$$

is employed, where $\hat{\boldsymbol{q}}=[\hat{p},\hat{u},\hat{v},\hat{w},\hat{T}]^T$. The axial and temporal wave numbers $\alpha=\alpha_r+j\alpha_i$ and $\omega=\omega_r+j\omega_i$ are complex values, where the imaginary part describes the growth rate

in space and time respectively. ω_r is the angular frequency of the oscillation in time. α_r is the axial wave length of the instability, where $\alpha_r = 2\pi/\lambda_x$ and λ_x is the physical wave length in meters. The azimuthal wave number m is an integer, that describes the periodicity in the azimuthal direction, θ and is positive or negative, describing instabilities travelling in opposite angular directions. Using the Ansatz in equations 6.7-6.12 and casting the system into a discrete formulation yields,

$$\begin{aligned}\frac{\alpha u_0}{\rho_0 R_s T_0}\hat{p} + \alpha\hat{u} - j\left(\frac{1}{r} + \frac{1}{\rho_0}\frac{d\rho_0}{dr} + \frac{d}{dr}\right)\hat{v} \\ + \frac{m}{r}\hat{w} - \frac{\alpha u_0}{T_0}\hat{T} = \omega\left(\frac{1}{\rho_0 R_s T_0}\hat{p} - \frac{1}{T_0}\hat{T}\right)\end{aligned} \tag{6.14}$$

$$\frac{\alpha u_0}{\rho_0}\hat{p} + \alpha u_0\hat{u} - j\frac{du_0}{dr}\hat{v} = \omega\hat{u} \tag{6.15}$$

$$-\frac{j}{\rho_0}\frac{d\hat{p}}{dr} + \alpha u_0\hat{v} = \omega\hat{v} \tag{6.16}$$

$$\frac{m}{r\rho_0}\hat{p} + \alpha u_0\hat{w} = \omega\hat{w} \tag{6.17}$$

$$-\alpha u_0\hat{p} - jc_p\rho_0\frac{dT_0}{dr}\hat{v} + \alpha c_p\rho_0 u_0\hat{T} = \omega\left(-\hat{p} + c_p\rho_0\hat{T}\right) \tag{6.18}$$

A generalized eigenvalue problem can now be formulated for the given system of equations as

$$\boldsymbol{A}\hat{\boldsymbol{q}} = \omega\boldsymbol{B}\hat{\boldsymbol{q}} \tag{6.19}$$

which is solved with the Python based *SciPy* linear algebra package using the function *eig* [58].

The computational domain is bounded by the combustor wall at $r = r_{CC} = d_{IN}$, where the boundary condition $v'(r_{CC}) = 0$ is enforced. The domain is discretized with a staggered grid, for which p', u', w' and T' are evaluated at the center of N segments and the radial velocity perturbations v' at the $N+1$ segment boundaries. A schematic of the continuous and discretized domain is shown in Figure 6.1.

Compact schemes are utilized to improve the computational efficiency [59, 60] of the solver. This approach mimics spectral methods, as the entire domain is evaluated by formulating implicit operators. If a staggered grid arrangement is used, the quantities defined on

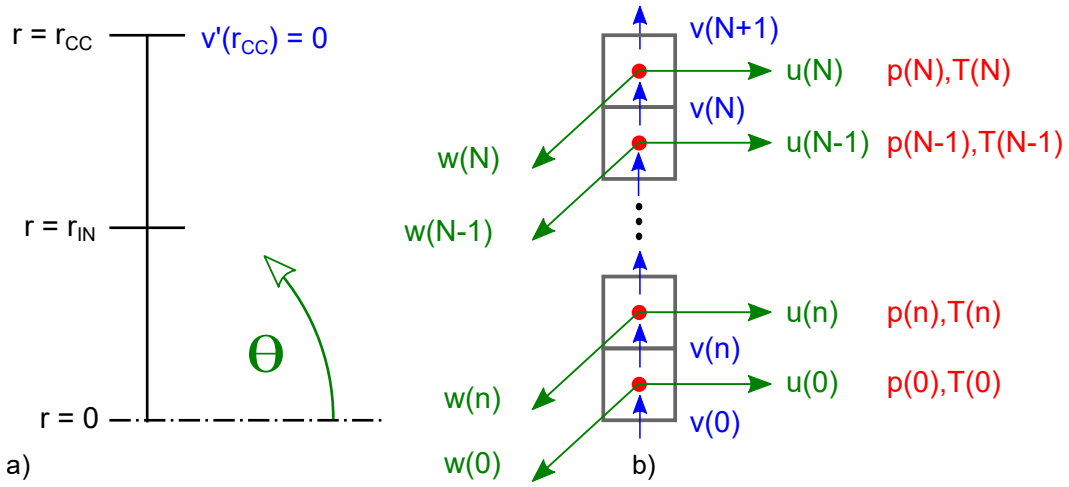

Figure 6.1. a) Continuous computational domain and b) discretized representation of the employed staggered grid

the separate grids can be linked through compact schemes as well. The basic idea is to use the leading terms of a Taylor series expansion at a given point on the grid to approximate the quantity of interest as in

$$\mathbf{A}\phi(i) = \mathbf{B}\psi(j) \tag{6.20}$$

where ϕ is the quantity of interest and ψ the quantity available to describe ϕ. If i and j are identical, collocated quantities are sought i.e. $\phi = \frac{\partial u}{\partial r}$ and $\psi = u$, whereas if i and j are shifted by a constant, staggered quantities are related. ϕ and ψ in the above equation are linked through a linear combination which is represented by the matrices $\mathbf{A}$ and $\mathbf{B}$. Thus the solution to ϕ is found by inverting the matrix $\mathbf{A}$ yielding

$$\phi(i) = \mathbf{A}^{-1}\mathbf{B}\psi(j) \tag{6.21}$$

The coefficients of $\mathbf{A}$ and $\mathbf{B}$ depend on the number of terms that are employed from the Taylor Expansion to describe the linear combination. Therefore lower order schemes need to be used adjacent to the domain boundaries. As the pressure is only described at internal points, this quantity and its derivative at the domain origin $r = 0$ are evaluated through a polynomial formulation that is based on the first three pressure values $p(0,1,2)$. Sixth-

order schemes are employed for the internal points of the grid, whereas boundary adjacent and boundary values are described by fourth and third-order schemes respectively.

6.2 Model Validation

The formulated model framework is tested against analytical solutions for cylindrical duct acoustics, which have been documented extensively, e.g. in [61–63].

Following Rienstra [63], harmonic modal solutions of the acoustic field in a hard-walled circular duct can be formulated by solving the inviscid wave equation, where the mass conservation equation reduces to a form of Bessel's equation if the sound speed is constant and a cylindrical coordinate system is employed. This equation reads:

$$p'' + \frac{1}{r}p' + \left(\omega^2 - k^2 - \frac{m^2}{r^2}\right)p = 0 \tag{6.22}$$

where ω, k and m are the temporal, axial and azimuthal wave numbers respectively. The acoustic velocity normal to the wall ($r = R$) need to vanish, thus the boundary condition

$$\frac{\partial p}{\partial r}(r = R) = 0 \tag{6.23}$$

is employed. Solutions to the pressure field are then described by Bessel functions in the form:

$$p(r) = J_m(\alpha_{\mu m} r) \tag{6.24}$$

where J_m is the Bessel function of the first kind of order m and $\alpha_{\mu m}$ are radial wave numbers which are determined by the roots of J'_m which follows from the boundary condition at the wall. These roots are tabulated in table 6.1 and the solutions to the pressure field are then constructed by:

$$p_{\mu m}(r) = N_{\mu m} J_m\left(\alpha_{\mu m}\frac{r}{R}\right)e^{-jm\theta} \tag{6.25}$$

The axial part of the solution is dropped, as the solution in the cross-sectional plane is of priary interest. The solution is normalized using the factor,

$$N_{\mu m} = \frac{\sqrt{2}}{J_m(\alpha_{\mu m})\sqrt{1 - \frac{m^2}{\alpha_{\mu m}^2}}} \tag{6.26}$$

Table 6.1. $\alpha_{\mu m}$: roots of J'_m for the three leading radial and azimuthal wave number combinations [63]

μ / m	0	1	2	3
0	0	1.8412	3.0542	4.2012
1	3.8317	5.3314	6.7061	8.0152
2	7.0156	8.5363	9.9695	11.3459
3	10.1735	11.7060	13.1704	14.5859

with the exception of $N_{10} = \sqrt{2}$.

The corresponding solutions to v and w are found from the radial and azimuthal momentum conservation equations, which simplify here to

$$v = -\frac{j}{\rho_0}\frac{\partial p}{\partial r} \tag{6.27}$$

$$w = -\frac{m}{\rho_0 r}p \tag{6.28}$$

where ρ_0 and R are the gas density and the duct radius. Figure 6.2 summarizes the solutions for three radial and two azimuthal wave number combinations for air at $T_0 = 1425$ K and $p_0 = 7.2$ bar and a duct radius of $R = 0.04$ m. The resulting pressure mode shapes show wall-concentric nodal lines for a given radial wave number, whereas the azimuthal wavenumber determines the periodicity in θ, leading to nodal lines that intersect the domain origin, as observed for $m = 1, 2$. The resulting velocity field is driven by the pressure potential, resulting in velocity components normal to the nodal lines of the pressure field. There are only wall-concentric nodal lines for pure radial modes, leading to radial velocity perturbations and a non-existent azimuthal velocity field. Introducing origin intersecting nodal lines for $m > 0$, the azimuthal velocity field corresponds to the pressure gradients in the azimuthal direction. 2D reconstructions for these modes are given in Appendix A.

The model formulated in chapter 6.1 was tested against the analytical solutions described above for different grid resolutions by varying the azimuthal wave number m and the number of segments N. For a given m the radial mode solutions naturally arise of

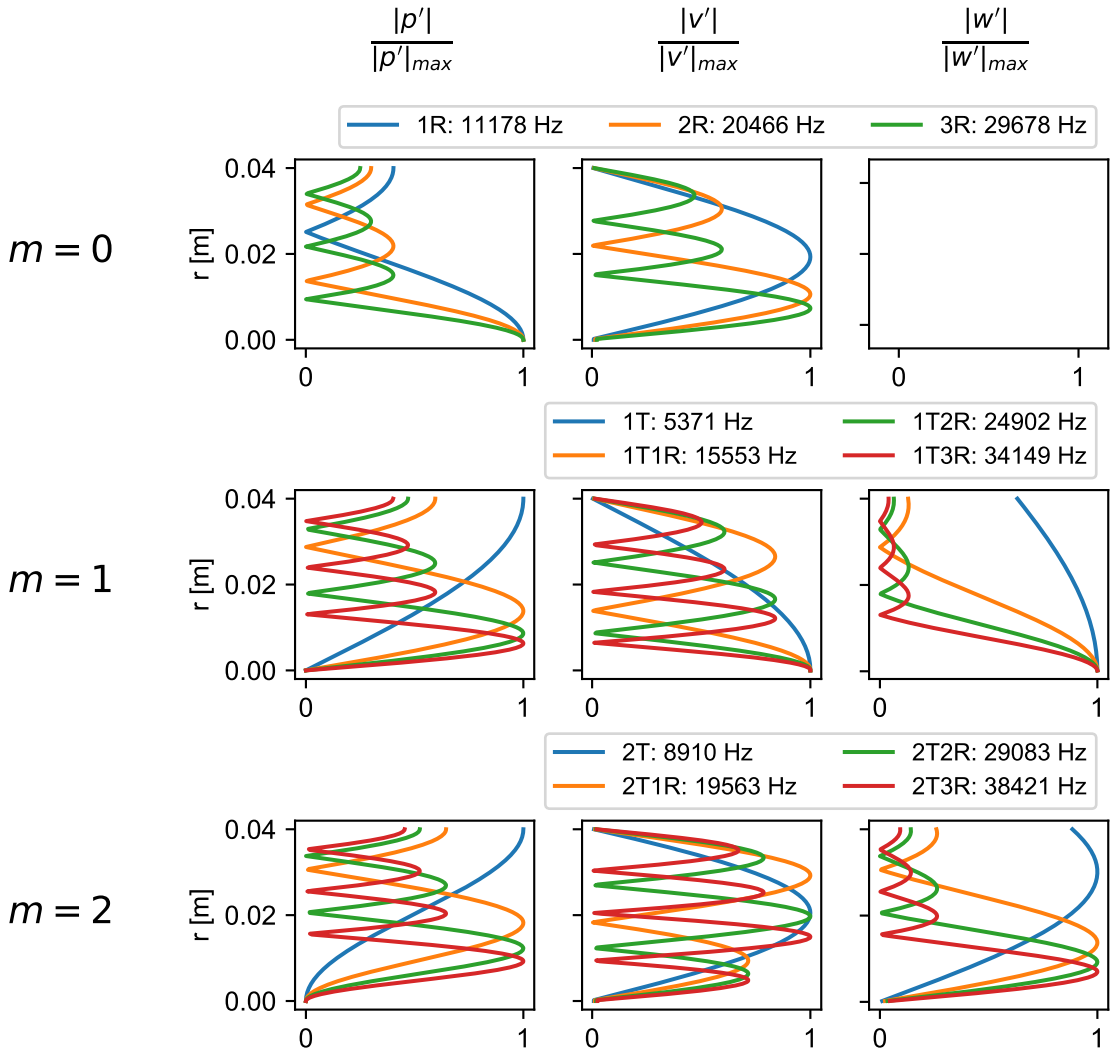

Figure 6.2. Analytical duct mode solutions for air at $T_0 = 1425$ K and $p_0 = 7.2$ bar and a duct radius of $R = 0.04$ m

the generalized eigenvalue problem for which the equation system derived in chapter 6.1 simplifies to

$$-j\left(\frac{1}{r}+\frac{d}{dr}\right)\hat{v}+\frac{m}{r}\hat{w}=\omega\left(\frac{1}{\rho_0 R_s T_0}\hat{p}-\frac{1}{T_0}\hat{T}\right) \tag{6.29}$$

$$-\frac{j}{\rho_0}\frac{d\hat{p}}{dr}=\omega\hat{v} \tag{6.30}$$

$$\frac{m}{r\rho_0}\hat{p}=\omega\hat{w} \tag{6.31}$$

$$0 = \omega\left(-\hat{p} + c_p \rho_0 \hat{T} \right) \tag{6.32}$$

comprised of the mass, the radial and azimuthal momentum and energy equation. The cross-sectional modal solutions for a homogeneous constant density quiescent gas are sought. Consequently, gradients in the base flow and the axial wave number terms have been omitted, resulting in an axial independence of the solution. The computed frequencies are compared to the analytical solution and the error between the solutions is determined using

$$E(N) = \frac{|f_{analytic} - f_{LSA}|}{f_{analytic}} \tag{6.33}$$

Good agreement is achieved with the analytical solutions for as low as 10 segments ($E < 8\%$) and for $N = 50$ the error lies below 0.01% for all modal wave number combinations, as shown in Figure 6.3. The analytical modes have been computed with an accuracy of four decimals for the Bessel function roots, thus limiting this comparison apparent in the inflection of the error for the azimuthal wave numbers $m = 0, 1$.

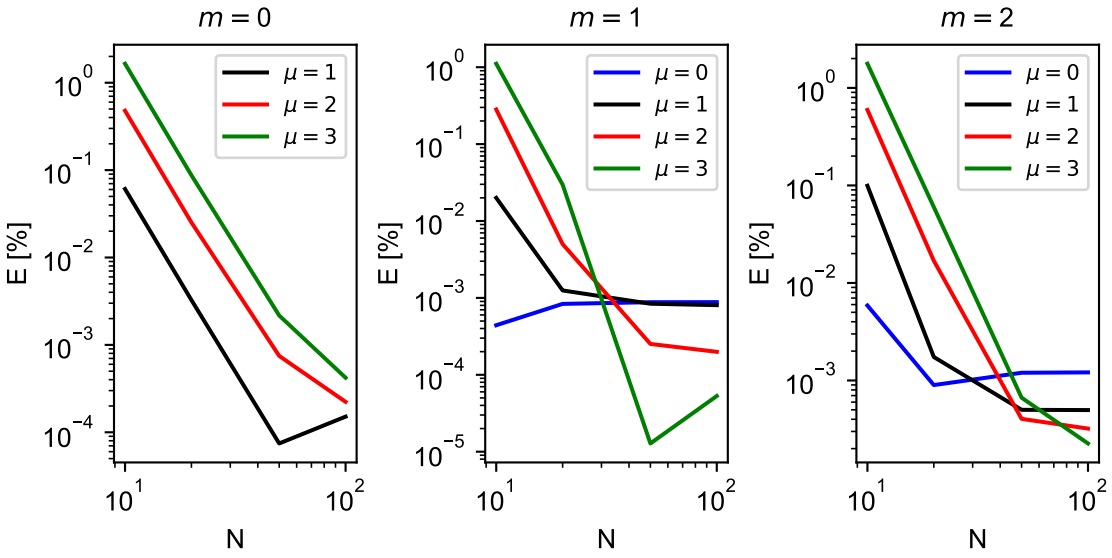

Figure 6.3. Frequency error between model and analytical predictions as a function of segments N for the first three leading azimuthal and radial wave number combinations

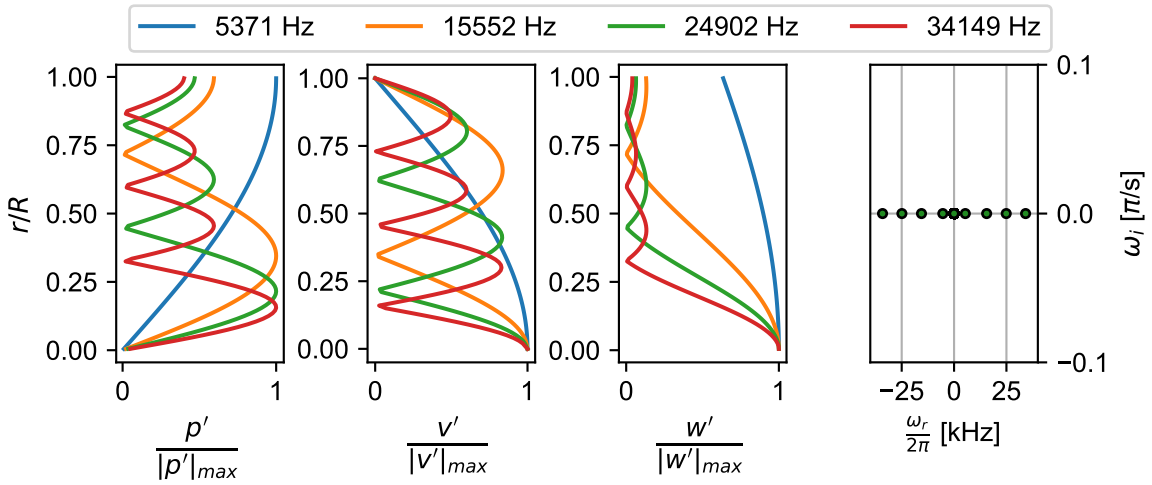

Figure 6.4. Frequency error between model and analytical predictions as a function of segments N for the first three leading azimuthal and radial wave number combinations

Figure 6.4 presents the computed eigenvectors for p, v and w along with the eigenspectrum of the eigenvalue problem with $m = 1$. The spectrum is clipped to show the first three leading modes, the 1T, 1T1R, 1T2R and 1T3R at 5.4, 15.6, 24.9 and 34.1 kHz. The solutions for these modes with a positive and negative real part of the temporal frequency indicate counter-clockwise and clockwise rotating waves. A superposition of the positive and negative solution results in standing wave patterns, representing the acoustic duct modes. A direct comparison between the analytical solutions to the radial profiles for the perturbation quantities and the eigenvectors found by the model indicate excellent agreement. 2D reconstructions of the duct modes computed by the model are also given in Appendix A.

6.3 Base Flow Formulation

The circular cross-section in combination with the small expansion-ratio of the combustor makes velocity measurements challenging, as outlined in the section 3.2, in Chapter 3. In addition the lack of cooling and resulting brief combustion periods do not allow for point based measurements such as LDV. Therefore analytical formulations are employed

to estimate the flow field in the flame zone of the combustor for a temporal linear stability analysis performed in chapter 7.4. The base flow is assumed to be locally parallel and inviscid. Axial velocity u_0, fluid temperature T_0 and density ρ_0 are described by local profiles in cylindrical coordinates in order to investigate the stability of the flow at a given axial position x in the flow field. A hyperbolic tangent based formulation is employed for the axial velocity profile and defined by:

$$u_0(x,r) = u_c(x)\left[\frac{1-\beta(x)}{2} + \frac{\beta(x)+1}{2}\tanh\left(\frac{1}{\delta(x)}(r_{IN}+r_s-r)\right)\right] \tag{6.34}$$

where u_c is the local center line velocity and β the back flow ratio defined by $\beta(x) = u_{0,min}(x)/u_c(x)$ [28, 37]. The width of the transition region in the profile is controlled by δ and models the shear layer width, which is assumed to increase linearly with the classical result for the round jet spread rate of $S = 0.094$ [64].

$$\delta(x \leq x_s) = \delta_{min} + \frac{r_{IN}-\delta_{min}}{x_s}x \tag{6.35}$$

$$\delta(x > x_s) = r_{IN} \tag{6.36}$$

where an initial shear layer thickness of $\delta_{min} = 4.9L_{IN}Re_x^{-0.5} = 0.026d_{IN}$ is assumed based on Blasius' solution to the zero-pressure gradient boundary layer thickness for pipe flow [64]. The resulting shear layer development length is $x_s = 5.4d_{IN}$. The centerline of the shear layer is defined by the variable r_s where,

$$r_s(x < x_{s,c}) = \frac{r_{IN}}{x_{s,c}}x \tag{6.37}$$

$x_{s,c} = 12.5d_{IN}$ is the distance for the shear layer center to reach the wall of the combustion chamber. This estimate is computed using the slope of a two-dimensional mixing layer reported by Champagne as $\frac{dy_{0.5}}{dx} = 0.04$ [65].

The back flow ratio β determines the velocity magnitude at the wall and is negative in the recirculation zone for $x < x_r$ and positive downstream of x_r as the mean profile slowly assumes that of a fully developed pipe flow. Experimental data from Stevenson [66] and Pitz [67] suggest a maximum recirculation velocity magnitude of 22% of the center line velocity u_c, that occurs at $x_\beta = 1.5d_{IN}$, and a shortened recirculation zone length of

$x_r = 3.5d_{IN}$ compared to a non-reacting flow field. Two polynomials are formulated to describe the back-flow ratio in the recirculation zone and in the developing region as:

$$\beta(x \leq x_r) = \frac{\beta_{max}}{x_\beta^2 - x_r x_\beta}\left(x^2 - x_r x\right) \tag{6.38}$$

$$\beta(x > x_r) = \frac{\beta_{min}}{(x_r - x_d)^2}\left((x_r - x_d)^2 - x_d^2 + 2x_d x - x^2\right) \tag{6.39}$$

with $\beta_{max} = 0.22$ and $\beta_{min} = -0.05$ and $x_d = 7d_{IN}$ as the length of the analysis domain. Stevenson showed that the center line velocity u_c is observed to decay farther downstream compared to a non-reacting flow field and is estimated as:

$$u_c(x) = u_{in} + \frac{u_d - u_{IN}}{(x_d - x_p)^2}\left(x_p^2 + x^2 - 2x_p x\right) \tag{6.40}$$

where $x_p = 3.5d_{IN}$ is the jet potential core length and $u_d = 0.88u_{IN}$ the center line velocity at the end of the domain [66]. The radial derivative of the axial velocity is defined as

$$\frac{du_0}{dr}(x,r) = u_c(x)\left[\frac{\beta(x)+1}{2\delta(x)}\cosh^{-2}\left(\frac{1}{\delta(x)}(r_{IN} - r)\right)\right] \tag{6.41}$$

Temperature and density fields are linearly related by the ideal gas law. The base flow temperature and density field formulation follows that of Ghoniem and Manoharan [35,37] and are defined by

$$T_0(x,r) = T_4\left[\frac{1+TR}{2} + \frac{1-TR}{2}\tanh\left(\frac{r - r_f(x)}{\delta_f}\right)\right] \tag{6.42}$$

$$\rho_0(x,r) = \rho_4\left[\frac{1+DR}{2} + \frac{1-DR}{2}\tanh\left(\frac{r - r_f(x)}{\delta_f}\right)\right] \tag{6.43}$$

The temperature and density ratio are $TR = T_3/T_4$ and $DR = \rho_3/\rho_4$, where T_3 is a measured quantity and T_4 is calculated from the choked nozzle equation [68]

$$T_4 = \left(\frac{\dot{m}_{tot}}{A_e p_4 \gamma}\right)^{-2} \frac{1}{R_s \gamma}\left(\frac{2}{\gamma+1}\right)^{\frac{\gamma+1}{\gamma-1}} \tag{6.44}$$

given the total mass flow rate $\dot{m}_{tot} = \dot{m}_{air} + \dot{m}_{fuel}$ and the product gas properties calculated using NASA CEA [69] for a specific flame condition. ρ_3 and ρ_4 are then calculated using the ideal gas law with the measured static system pressure and $R_s = 287$ J/kg/K, assuming

air properties for the entire domain. δ_f controls the transition region width and models the preheat and reaction zone, which is estimated with the Blint thickness [70] $\delta_L^0 \approx \delta_L(T_4 - T3)^{0.7}$ where the laminar flame thickness is $\delta_L \approx 0.001 d_{IN}$. r_f defines the inflection point in the scalar profiles and thus describes the reaction layer location relative to the center line. With a given flame length L_f and assuming a conical flame shape the reaction layer position is a linear function of x and defined by

$$r_f(x) = r_{IN} - \frac{r_{IN}}{L_f} x \tag{6.45}$$

The radial derivatives of the density and temperature fields are given as

$$\frac{dT_0}{dr}(x,r) = T_4 \left[\frac{1-TR}{2\delta_f} \cosh^{-2}\left(\frac{r - r_f(x)}{\delta_f} \right) \right] \tag{6.46}$$

$$\frac{d\rho_0}{dr}(x,r) = \rho_4 \left[\frac{1-DR}{2\delta_f} \cosh^{-2}\left(\frac{r - r_f(x)}{\delta_f} \right) \right] \tag{6.47}$$

As an alternative to the definition of r_f and d_f given above, the mean OH^* intensity distribution can also be obtained from chemiluminescence imaging. This can be employed to estimate the location of the inflection point and thickness of the transition region in the temperature and density profile. Even though that the line-of-sight integrated intensity distribution is not a quantitative measure of the flame envelope, the mean reaction zone location can be readily identified from this measurement.

Figure 6.5 a) shows the top half of the mean image of a representative flame based on 1000 frames, which is the result of a spatial average of the upper and lower half of the complete image. Figure 6.5 b) shows extracted radial intensity profiles from the image in Figure 6.5 a), for which the axial extraction locations are color marked. For each axial location a running average is computed based on a window length of 15 pixels in the r-direction. For each profile a maximum is identified (dashed line) which, for a large enough sample will closely correspond to the radial location of highest heat release and is thus assumed to be a fair approximation of the radial position of the temperature and density profile inflection point r_f.

The thickness of the T_0 and ρ_0 transition zone is approximated with the difference between the radial location of I_{max} and I_{99}, which is determined by the radial location for

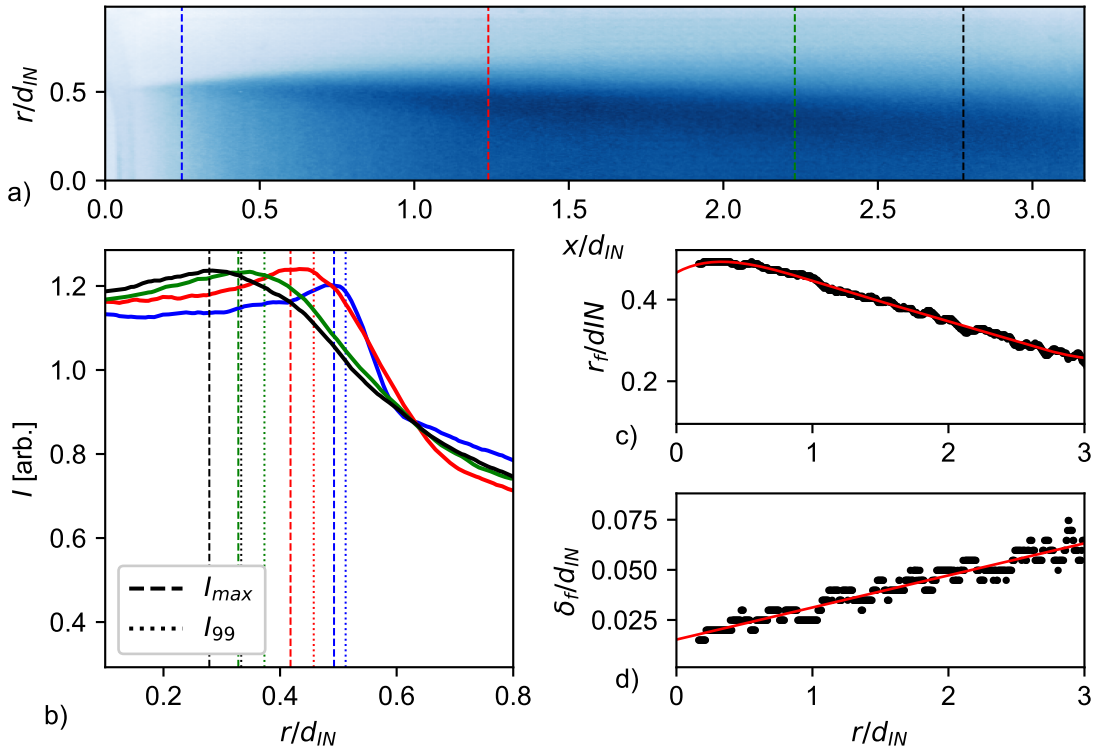

Figure 6.5. a) half mean image of a representative flame, b) radial intensity profiles with marked positions of I_{max} and I_{99}, c) radial location of I_{max} and polynomial curve-fit representing r_f, d) difference $r(I_{99}) - r(I_{max})$ and linear curve-fit representing δ_f

which the intensity profile decreased to $I(r) = 0.99 I_{max}$. As the shear layer growth with axial distance from the sudden-expansion and the potential mixture jet core area decreases, the local ratio of burned to unburned gas increases, leading to larger conductive heat transfer into the cold mixture jet core and thus to an increase in the preheat zone width. Both quantities are shown in Figure 6.5 c-d), as well as the polynomials fitted to the samples. For the inflection point center r_f a polynomial of degree 5 is used, whereas a linear curve-fit is used for the transition half-width δ_f.

The resulting base flow formulations for a given operating condition are summarized in Figure 6.6. Changes in flame length in case of the conical reaction zone lead to different levels of interaction between the reaction and shear layer, as the temperature/density derivative location relative to the axial velocity derivative is altered. The chemiluminescence

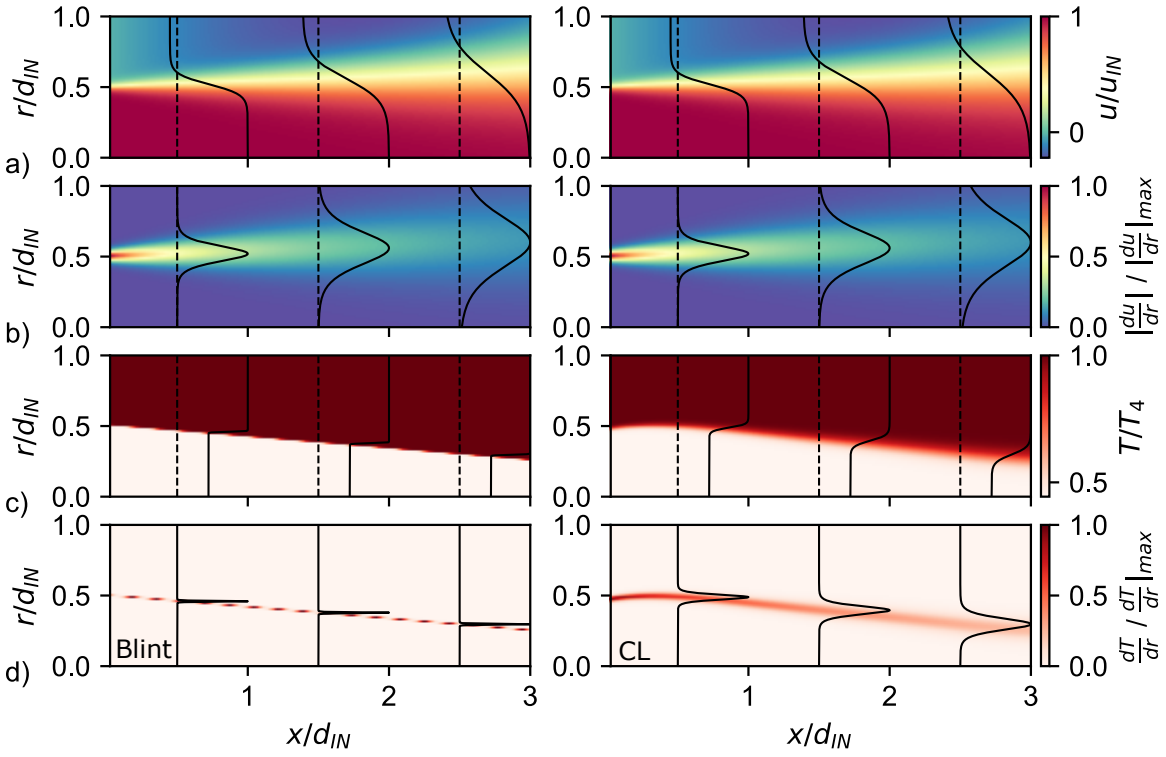

Figure 6.6. Reconstructed base flow field for linear stability analysis: a) axial velocity u normalized by u_{IN}, b) magnitude of axial velocity gradient $|\frac{du}{dr}|$ normalized by $|\frac{du}{dr}|_{max}$, c) local temperature T normalized by T_4 and d) temperature gradient $\frac{dT}{dr}$ normalized by $\frac{dT}{dr}|_{max}$. Superimposed profiles are normalized by their respective maximum. Left column shows temperature field with $\delta_f = \delta_L^0$ and a conical flame shape. Right column shows chemiluminescence derived d_f and r_f temperature field.

derived reaction zone additionally considers the equivalence ratio effect, where leaner mixtures lead to lower flame speeds and thus a transition of the reaction layer into lower velocity regions towards the recirculation zone. Velocity, temperature and density derivatives also vary drastically for the different operation conditions, leading to a complex interaction between the different instability source terms which will be shown to affect the shear layer stability and possible resonant modes inherent in the flow field.

6.4 Influence of Reaction Layer Thickness and Shape on LSA

To evaluate the different base flow reaction layer options defined in chapter 6.3 the model is used to compute the solution for a test flame condition tabulated in Table 6.2. The axial location $x/d_{IN} = 1$ corresponding to 40 mm downstream of the sudden expansion is considered. For these test the spatial wave number is set to $\alpha = 200$, related to an axial wave length of $\lambda_x = 2\pi/\alpha = 0.03$ m, and the azimuthal wave number is set to $m = 0$, which restricts the model to axisymmetric perturbation modes. All cases discussed in this section are computed with $N = 500$, leading to a grid resolution of $d_{IN}/N = 80$ μm. The chemiluminescence and analytically derived values for r_f and δ_f are documented in Table 6.3.

Table 6.2. Base flow test operation condition

p_3	ϕ	T_3	T_4	u_{IN}	L_f/d_{IN}	z_3	z_4	I_{max}	I_{99}	$f(L_f)$	δ_L^0
[bar]	[-]	[K]	[K]	[m/s]	[-]	$\frac{kg}{m^2 s}$	$\frac{kg}{m^2 s}$	[mm]	[mm]	[mm]	[mm]
7.2	0.76	765	1720	134	4.46	1797	1171	18	1.2	15.5	0.14

Two modes are found, for which the velocity perturbations are concentrated either in the cold mixture jet or the warm wake or recirculation region of the domain, as observed in the axial velocity profiles in 6.7. The axial velocity profile inflection location is marked in each sub-figure with r_s, which indicates the maximum of $\frac{\partial u}{\partial r}$ and thus presents the location of maximum shear stress in the domain. At $x/d_{IN} = 1$, r_s is located on a larger radii compared to reaction zone center r_f.

The Jet Mode corresponds to a mixture jet concentrated mode as observed in the axial velocity perturbations. The radial offset in the profiles between the base options $r_f = f(L_f)$ and $r_f = I_{max}$ results from the different reaction layer inflection point location relative to the domain center line. The chemiluminescence extracted location lies on a larger radii compared to the linear function based on L_f, effectively altering the domain span as the reaction layer transition presents a local change in specific acoustic impedance $z = \rho a$ (see Table 6.2). The transition region width δ_f affects the offset of the profile alteration caused

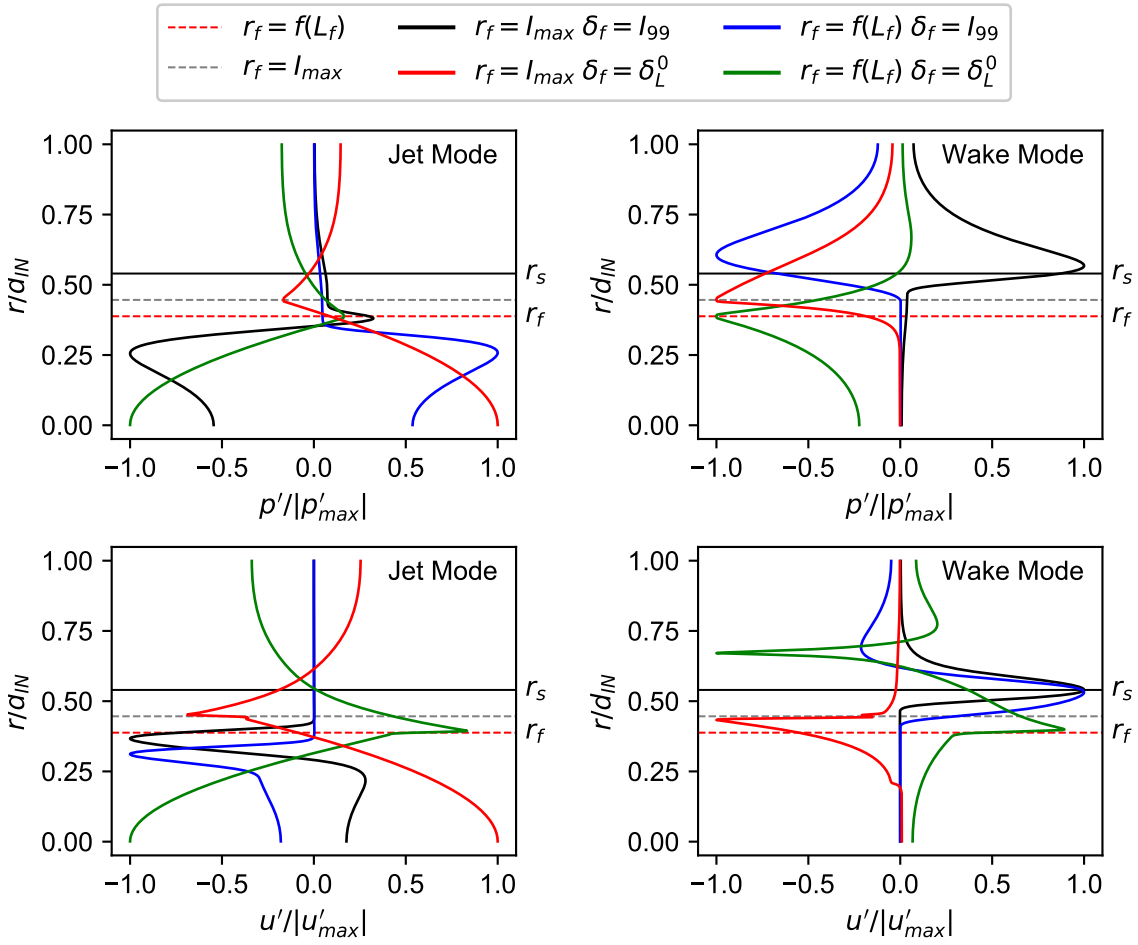

Figure 6.7. p' and u' for Mode 1 and 2 for several base flow reaction layer options

by the change in density and temperature. In general the smaller width transition region $\delta_f = \delta_L^0$ acts like a hard wall, the pressure profiles for these cases show a finite magnitude at the interface between the two fluid domains. In contrast to that, the larger transition region width $\delta_f = l_{99}$ generates an interface that acts more similar to a pressure release boundary, for which the profiles show low amplitudes of pressure at the fluid boundary. The corresponding velocity profiles behave according to the pressure potential and are restricted to their fluid domain for the thicker transition region $\delta_f = l_{99}$, whereas the thinner interface region generates velocity perturbations that develop in the entire domain, with noticeable jumps in the profiles at the location of r_f.

Table 6.3. Frequency and growth rate comparison between different base flow reaction layer options

Base	r_f=I_{max} d_f=I_{99}		r_f=$f(L_f)$ d_f=I_{99}		r_f=I_{max} d_f=δ_L^0		r_f=$f(L_f)$ d_f=δ_L^0	
Flow	Jet	Wake	Jet	Wake	Jet	Wake	Jet	Wake
f [Hz]	4169	659	4230	1327	22349	4249	22531	-262
ω_i [π/s]	332	3672	119	3815	10141	5.5	6501	181

The mode frequencies corresponding to the presented profiles in Figure 6.7 are presented in Table 6.3, where the frequency of the modes are listed as $f = \omega_r/2\pi$. Frequency and growth rate of the Jet Mode is less affected by the change in r_f for the cases with $\delta_f = I_{99}$, whereas the Wake Mode shows a significant increase in frequency for $r_f = f(L_f)$ compared to the chemiluminescence derived location I_{max}. The Wake Mode is a shear layer associated mode, determined by the correlation of the perturbation extrema radial location with r_s, and thus gains energy by the axial velocity gradient. An increase between the extrema of velocity and temperature/density gradients, i.e. $r_f = f(L_f)$ places the location of maximum shear in a higher temperature region compared to $r_f = I_{max}$ for a constant δ_f, thus leading to a higher frequency of the mode. The Jet Mode is intrinsic to the mixture jet domain, gaining energy from the temperature and density gradients induced by the reaction layer. The radial wave length of this mode is affected by the position of r_f, observed in the decreased frequency for $r_f = I_{max}$ as the spatial domain for this mode is increased compared to $r_f = f(L_f)$ for a constant δ_f.

The frequencies and growth rates for the base flow configuration for which the transition region thickness is set to the Blint thickness, $\delta_f = \delta_L^0$, vary drastically compared to the $\delta_f = I_{99}$ option. Both LSA modes are dominated by the influence of the extreme density and temperature gradients due to the decreased transition region width, leading to non-physical frequencies and growth rates.

Given these results and the fact that the transition region width in the temperature and density profile is significantly underestimated with the Blint thickness, the chemilumines-

cence derived thickness $\delta_f(x) = I_{99}(x)$ is selected. In addition, the effect of the global equivalence ratio ϕ on the reaction layer position within the flow field is not considered by restricting the r_f to $f(L_f)$. The comparison above for a constant $\delta_f = I_{99}$ showed that the distance between the velocity and gas state gradients has an impact on the perturbation modes, therefore the location of the reaction layer inflection point will also be assigned based on the chemiluminescence derived value $r_f(x) = I_{99}(x)$. This approach will allow for a flame specific analysis, reflecting the distinct changes in the operation parameters T_3, T_4 and ϕ.

6.5 Grid Sensitivity Study

A grid sensitivity study was performed for the chosen base flow configuration of chapter 6.4 with $r_f(x) = I_{99}(x)$ and $\delta_f(x) = I_{99}(x)$ at the identical flame condition. Two axial locations are studied $x/d_{IN} = 0, 1$, for which the base flow gradients are strongest for $x/d_{IN} = 0$. The segment number is varied from 50 to 500 elements in increments of 50 segments. Figures 6.8 and 6.9 present the mode frequencies and growth rates for $x/d_{IN} = 0, 1$ respectively. The associated error of the solution is defined by

$$E(N) = \frac{|\omega(N-50) - \omega(N)|}{\omega(N-50)} \tag{6.48}$$

where the real and imaginary part of the temporal wave number is evaluated separately. For both axial positions in the base flow the frequencies and growth rates converge to integer accuracy or errors $< 10^{-3}$ for $N = 250$. This choice for the segment number allows for efficient computation which reasonable accuracy for the objective of this model.

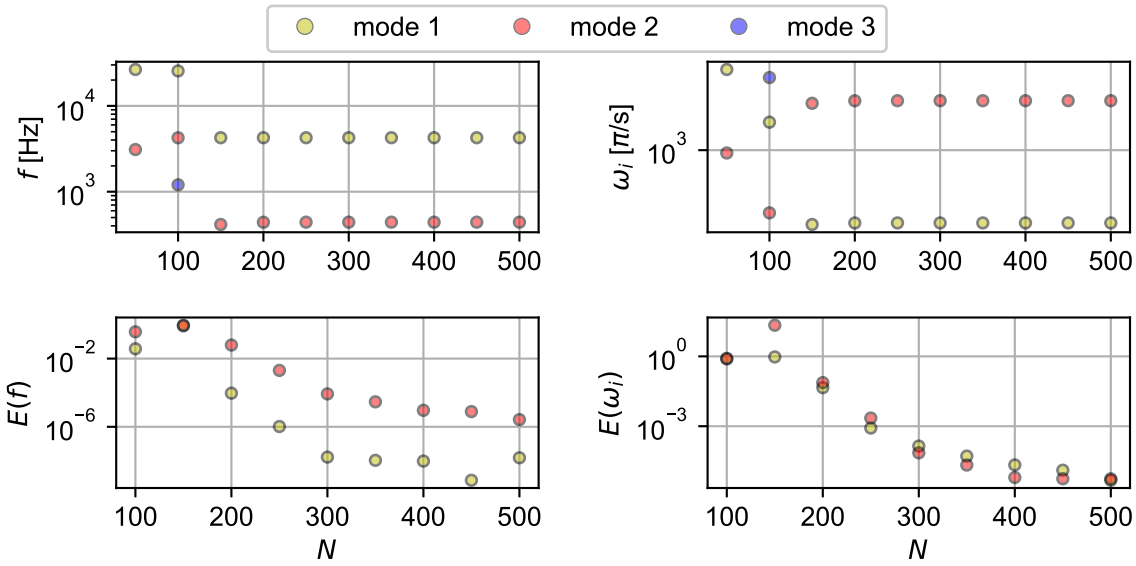

Figure 6.8. $f = \omega_r/2\pi$ and ω_i with associated errors for axial location $x/d_{IN} = 0$ for segments $N = [50, 500]$

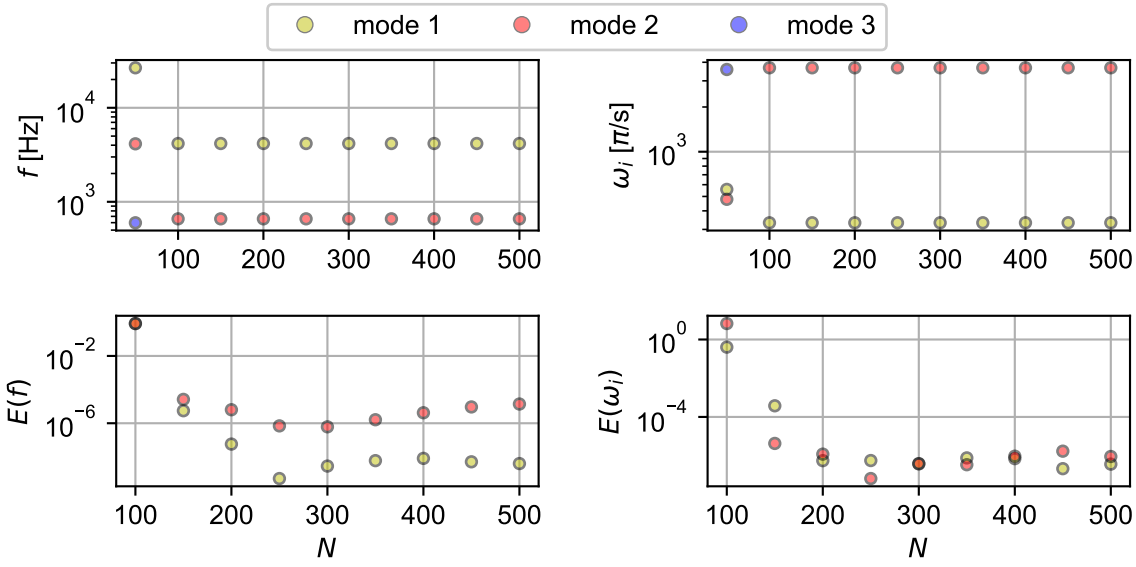

Figure 6.9. $f = \omega_r/2\pi$ and ω_i with associated errors for axial location $x/d_{IN} = 1$ for segments $N = [50, 500]$

7. INSTABILITY REGIMES OF A CONFINED JET FLAME

The objective of this chapter is to classify different modes of self-excited instabilities observed in the FPC combustor with discrete changes in operating conditions, all at a mean chamber pressure of ≈7 bar and flame thermal power of 1.3 MW. An instability regime map for this configuration is established, which highlights the sensitivity of system dynamics to operation parameters. Pressure and OH* chemiluminescence is analyzed for representative cases in order to delineate the different characteristics of each class. A linear stability analysis of an analytically reconstructed base flow for FPC is performed at discrete axial positions for which a parallel flow assumptions hold. The discretized linearized compressible Euler equations are solved and the most unstable modes in each flame condition are compared with the experimental data.

Table 7.1. Summary of operating conditions for Chapter 7

Case	ϕ	p_3	T_3	T_{ad}	u_{jet}	$p\prime/p_4$	$f_{1L,th}$	$f_{1T,th}$	L_f/d_{IN}
	[-]	[bar]	[K]	[K]	[m/s]	[%]	[Hz]	[kHz]	[-]
F1	0.76	7.2	764	2280	134	2.7	380	5.4-6.8	4.46
F2	0.65	6.7	720	2070	134	12.4	365	5.2-6.4	6.14
F3	0.70	6.9	623	2073	115	13.9	365	5.0-6.4	6.41
F4	0.79	7.1	617	2217	110	5.7	380	5.0-6.7	5.44
F5	0.66	6.8	718	2092	132	30.4	370	5.2-6.5	5.97

The sensitivity of different instability classes on the flame parameters mixture temperature T_3 and global equivalence ratio ϕ was assessed through a parametric survey. The flame condition was systematically varied in an application-relevant envelope, ranging between 600 and 800 K and 0.6 and 0.85 for T_3 and ϕ respectively. A wide range of different dynamics have been observed throughout this survey, ranging from high amplitude 1L dynamics

over 1T dominated pressure spectra to spinning wave instabilities. Five flame conditions, tabulated in Table 7.1, have been selected to highlight the different instability regimes.

The location of the pressure probes as well as the OH^* chemiluminescence field of view (FOV) utilized for the analysis presented in this chapter are marked in the schematic provided in Figure 7.1.

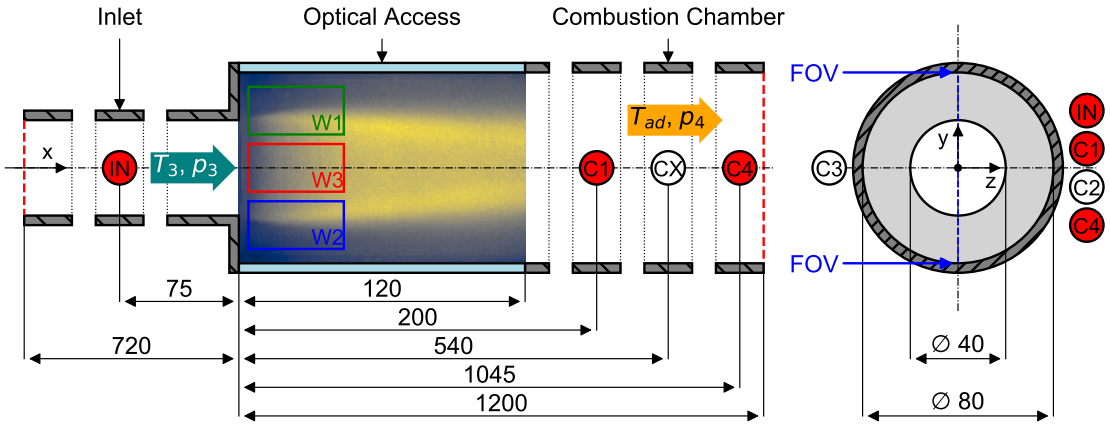

Figure 7.1. Schematic of VIPER-S combustor. (- - -) are sonic/choked boundaries, system inlet and exit planes respectively. C2 and C3 axial probe locations at CX marker position. All dimensions in mm.

7.1 System Acoustics

An expansion area ratio $\varepsilon = 4$ between the combustion chamber and the premixed duct results in a high aspect ratio flame, that establishes in the shear layer of the reactant jet and surrounding recirculation zone. Figure 7.2 a) schematically presents this flow field, in which the fluid forming the jet core is at the unburned reactant temperature T_3 and the surrounding volume is mostly comprised of recirculated products at temperature T_4, which is approximated by T_{ad}. To estimate the mean flame length for a given operating condition the laminar flame speed is computed using CANTERA [71], where the reactant mixture is estimated with CH_4-Air and the gas state by the inlet properties p_3 and T_3. The turbulent flame speed S_t is then computed with the correlation formulated by Kobayashi [72] using $u'_{rms} \approx 0.1 \cdot \overline{u}_{jet}$ and p_3. Assuming a conical mean flame shape and the global reactant con-

sumption speed formulation by Driscoll [73] $S_t = \dot{m}/(\overline{A}_f \rho_u)$ a representative mean flame length, based on the five flame conditions tabulated in Table 7.1, $L_f/d_{in} \approx 5.7$ is computed. As a result an inhomogeneous temperature field is established, that needs to be considered in the following analysis.

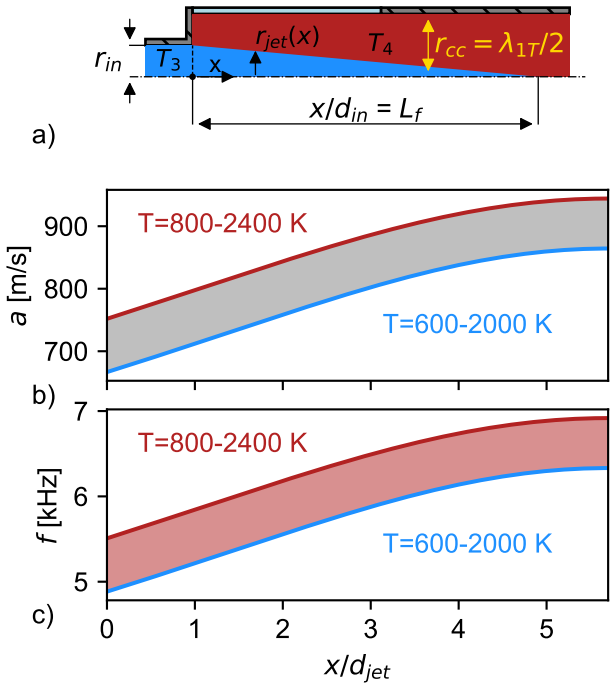

Figure 7.2. a) Schematic of flame zone, b) sound speed envelope as axial function and c) resulting axial dependence of the fundamental transverse mode frequency

The jet-stabilized flame can be defined as acoustically compact when considering axial dynamics, as the mean flame length $L_f \approx 5.7 d_{in} = 0.23$ m is relatively small compared to the longitudinal wavelengths of interest ($L_f/\lambda_{1L,system} = 0.12$). Here the wave propagation is parallel to the mean flow direction and duct axis, thus a uniform temperature distribution over the combustion chamber domain is assumed, as the jet potential core volume is small compared to the chamber volume. Transverse dynamics in contrast are observed normal to the direction of mean-flow direction and encounter the inhomogeneous temperature field in the flame zone. Considering transverse dynamics the flame diameter is of the order of

the wavelengths of interest and the spatial heat-release distribution of the flame cannot be neglected as the flame is non-compact in this tier of dynamics. In order to estimate the variation of sound speed in the flame zone, an axial sound speed function is defined as:

$$a(x) = \frac{a_3 \rho_3 A_{jet}(x) + a_4 \rho_4 A_{rec}(x)}{\rho_3 A_{jet}(x) + \rho_4 A_{rec}(x)} \tag{7.1}$$

This area/density weighted sound speed calculation estimates the lumped sound speed a in a given cross-sectional area in the flame zone. The resulting a envelope for the parametric survey is shown in Figure 7.2 b), from which a significant variance ($\sim 20\%$) of the speed of sound over the flame length is observed. The cutoff frequencies of the fundamental modes of interest are estimated by:

$$f_{\ell mn} = \frac{a}{2\pi} \sqrt{\left(\frac{\eta_{mn}}{r_{cc}}\right)^2 + \left(\frac{\ell \pi}{L_{cc}}\right)^2} \tag{7.2}$$

where η_{mn} is 1.8412 for the fundamental transverse chamber mode (1T) and ℓ is the integer defining the longitudinal mode number [74]. The resulting 1T frequency envelope spans over 2 kHz in the flame zone and is shown in Figure 7.2 c). This drastic change over the flame length represents a large interaction potential with hydrodynamic processes over a wide frequency range that originate in the shear layer. Mode frequency estimates of the cases analyzed in the following are included in 7.1. The 1L mode estimate is computed using T_{ad}, whereas for the 1T mode a frequency range needs to be considered that is based on the extrema of $a(x)$.

7.2 Pressure Dynamics

7.2.1 Flame 1

Figure 7.3a-c) provides an overview of the instability characteristics of case F1 based on the pressure signal at probe location C1. Longitudinal dynamics describe this flame condition, where the fundamental longitudinal mode (1L) and the 2L mode dominate the pressure spectrum at 360 and 720 Hz respectively. Eight additional temporal harmonics are present of which the 5L, 7L and 11L at 1.79, 2.5, 4 kHz show elevated pressure amplitudes.

A broad-band higher frequency mode is observed at 6.4 kHz, which lies in the theoretical 1T range for this operation point. The power spectrum of this condition pre-combustion indicates the presence of a hydrodynamic periodic process at 4.9 kHz. In order to investigate the nature of the higher frequency dynamics and gain resolution in time, a complex Morlet wavelet transform is computed in the frequency spectrum of interest, spanning 100 to 1000 Hz and 4 to 8 kHz respectively. The higher frequency mode found in the Welch's estimation (5 windows with 5400 samples each with 50% overlap) of the power spectrum in Figure 7.3b) is observed to be non-stationary in the scalogram shown in Figure 7.3c). Multiple time periods of elevated amplitude level are detected at $t = 20 - 40$ ms and $t = 60 - 65$ ms at ≈ 6.5 kHz, where a mode frequency modulation to a lower frequency band at ≈ 6 kHz leads to a reduction of the mode amplitude by a factor of two.

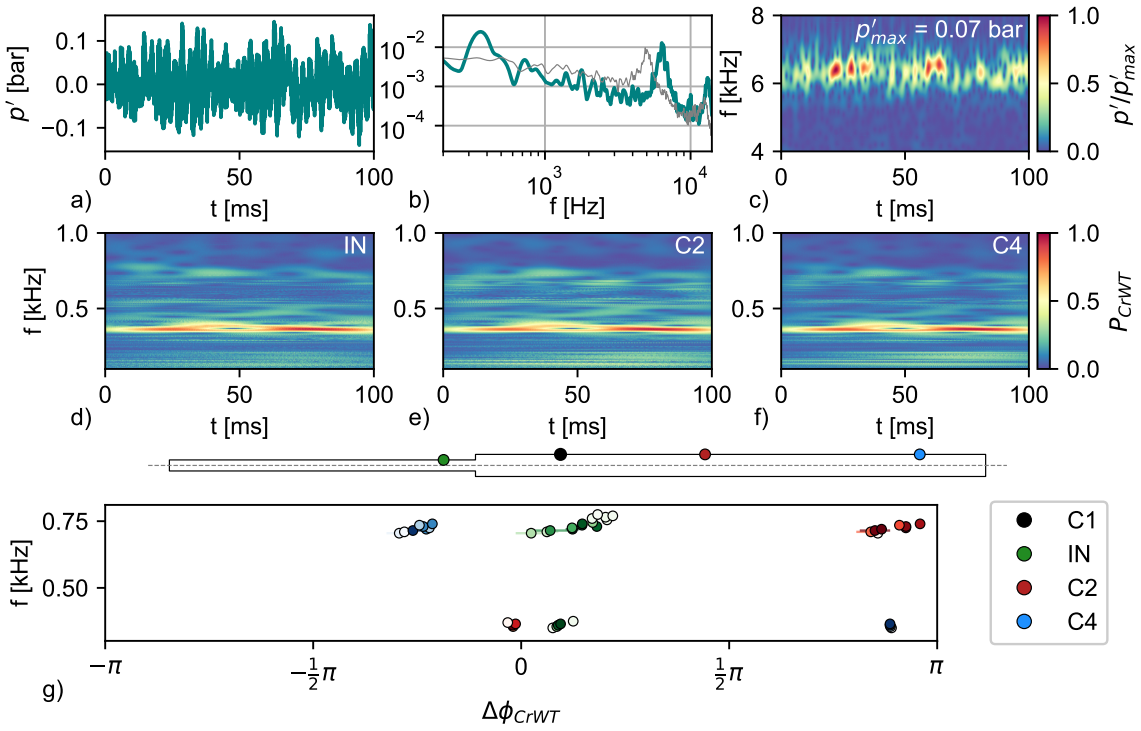

Figure 7.3. Flame 1: a) High-pass filtered pressure signal at C1, b) Welch's power spectrum estimate for signal in a) and pre-combustion (grey). c) Amplitude based Wavelet scalogram for probe C1. d-e) CrWT magnitude based scalograms for probes IN, C2 and C4 g) CrWT based phase difference of IN, C2 and C4 relative to C1 at frequencies of common power.

To determine the phase and amplitude relationship of the dynamics observed at probe C1 with other locations in the proximity of the flame, a Cross-Wavelet transform (CrWT) is utilized. This analysis allows determination of regions in the wavelet space, for which the C1 probe show common power and may correspond to the same physical process. To ensure that the CrWT at a given time instance and frequency is a valid sample for a phase relationship analysis a selection threshold is defined. Only regions in the CrWT space that show a squared CrWT modulus $\sqrt{|CrWT|}$ of $P_{CrWT} = \sqrt{|CrWT|}/\sqrt{|CrWT|}_{max} > 0.75$ are extracted and used to calculate statistical measures. The phase difference $\Delta\phi_{CrWT}$ and frequency of common power of valid samples are calculated and a amplitude weighted the circular mean and variance of $\Delta\phi_{CrWT}$ at a given frequency is computed.

A chaotic power distribution is observed in the frequency range 4-8 kHz in the CrWT space for probes IN and C2-3 (not shown), although the high amplitude periods at 6.5 kHz mentioned above are detected at the respective probe locations. From the incoherent nature of the dynamics centered at 6.4 kHz however can be inferred that the chamber head-end globally does not engage in sustained transverse dynamics. The CrWT scalograms shown in Figure 7.3d-f) display the dominant 1L and 2L modes present at all system probe locations. The 1L mode shows a weak amplitude modulation and the amplitude ratio between 1L and 2L modes is ≈ 2. The phase relationship for these two modes is presented in Figure 7.3g) where the markers and horizontal lines locate the weighted circular mean and variation of $\Delta\phi_{CrWT}$ for a given frequency. The IN and C1 probes display a $\Delta\phi_{CrWT} \approx 0 - \pi/8$ whereas the chamber aft-end probe C4 is located at $\Delta\phi_{CrWT} \approx \pi$ for the 1L mode frequency, thus representing a standing half-wave mode pattern. A small circular variance for these phase calculations ($\overline{Var}_{\phi} \approx 0$) reflect the phase-locked dynamics in time.

The phase dependencies flip for the probes C2 and C4 in case of the 2L mode as the additional pressure anti-node centered about the chamber length is established. These dynamics result in a relatively low magnitude of $p'/p = 2.7\%$ and is representative of the flame conditions that are comprised of a superposition of multiple modes at low amplitude levels.

7.2.2 Flame 2

Flame 2 is characterized by high amplitude, high frequency dynamics resulting in an overall $p'/p = 12.4\%$ shown in Figure 7.4a). The power spectrum estimate in Figure 7.4b) depicts a dominant broadband mode centered at 5.36 kHz and a secondary mode is present at 5.85 kHz at a reduced amplitude. A harmonic is present at 10.6 kHz corresponding to the dominant mode in the spectrum. The 1L and 2L modes are identified at 360 Hz and 710 Hz with amplitudes ranging an order of magnitude lower than the high frequency content in the spectrum. Multiple harmonics of the 1L mode can be identified in the spectrum at lower amplitudes. 5.1 kHz and 12.4 kHz modes are observed in the pre-combustion spectrum that are not associated with an acoustic mode and may correspond to hydrodynamic processes. The WT scalogram in Figure 7.4c) reveals a $\approx$ 120 Hz amplitude modulation of the 5.36 kHz mode. The broadband display of both HF modes in the power spectrum estimate is caused by a significant frequency modulation in time, which becomes apparent in Wavelet space. The second HF mode follows the frequency modulation seen for the dominant mode, whereas a periodic amplitude modulation is not observed and in contrast periods of a constant low amplitude and absence are observed. The CrWT scalograms in Figure 7.4d-f) reveal that the dominant mode transmits into the inlet and is present at both remaining chamber probes C2-3. The secondary HF mode in contrast is only detected downstream of C1 at probes C2-3 and is not found at the probe IN, suggesting that the secondary mode originates downstream of C1 whereas the dominant mode manifests itself in the entire flame zone. Both of the high frequency modes lie in the theoretical 1T mode range, where the axial sound speed distribution may result in different realizations of transverse dynamics in the flame-root and -tip zone.

The phase relationship between the remaining flame zone and C1 probe are shown in Figure 7.4g) for the first HF mode. The circular mean phase marker color depth represents the magnitude of common power at the respective frequency. Probes C2-3 follow the same frequency-phase trajectory relative to probe C1, suggesting that the dynamics at that axial location are phase-locked at $\Delta\phi_{CrWT} \approx 0.35\pi$ and $\approx 0.73\pi$. At that phase the amplitudes

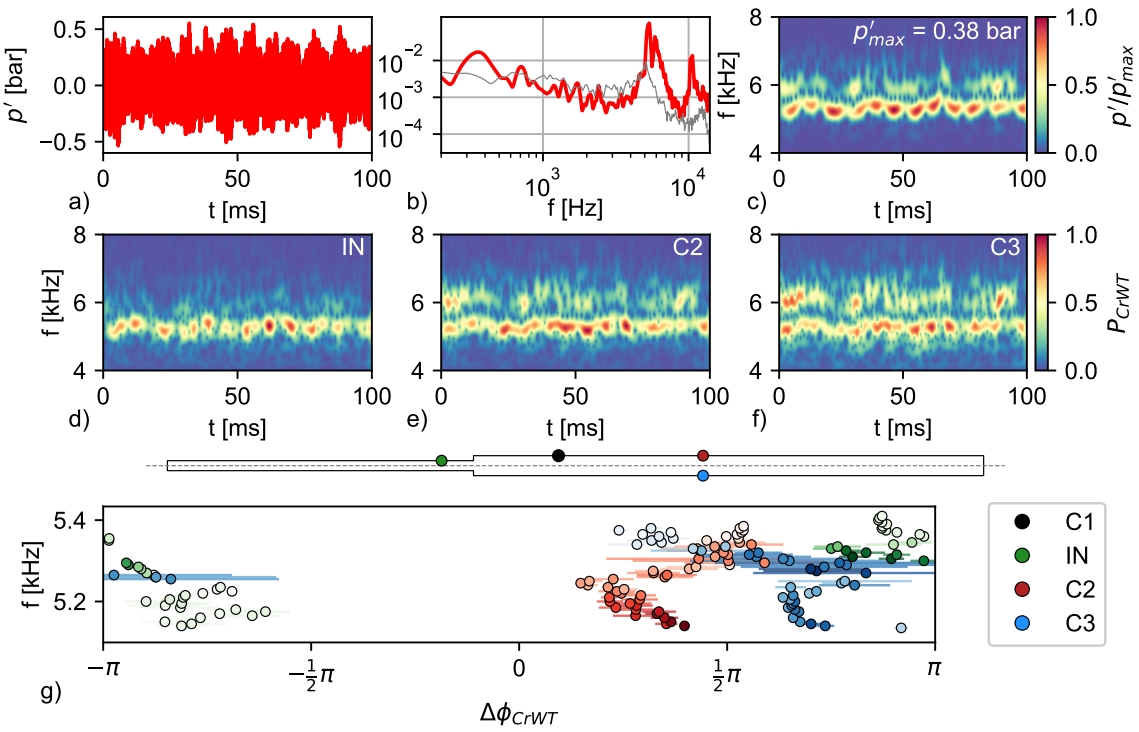

Figure 7.4. Flame 2: a) High-pass filtered pressure signal at C1, b) Power spectrum estimate for signal in a) and pre-combustion (grey). c) Amplitude based Wavelet scalogram for probe C1. d-e) CrWT magnitude based scalograms for probes IN, C2 and C3 g) CrWT based phase difference of IN, C2 and C3 relative to C1 at frequencies of common power.

reach a maximum between 5.1-5.2 kHz accompanied with a minimum in $\overline{Var}_\phi$. In contrast the inlet probe shares common power at a higher frequency tier centered about 5.3 kHz and shows a phase difference of $\Delta\phi_{CrWT} \approx \pm\pi$. The relative high values of $\overline{Var}_\phi = 0.06 - 0.17$ result of the nonstationary nature of the first HF mode, especially as the exponential decay of the transverse dynamics reduce the measured amplitude to 60 mbar in contrast to 380 mbar at C1. The phase relationship at C1-2 suggests that no coherent 1T acoustic mode exists at $x/d_{jet} = 13.5$ that can be attributed to the axial decay of the 1T mode and the axial increase in sound speed, leading to a distortion of the pressure signal and an inconsistency of the phase relationship when compared to a standing 1T mode.

7.2.3 Flame 3

The C1 signal of Flame 3 is shown in Figure 7.5a) and pressure oscillations of $p'/p = 13.9\%$ are observed. Two high frequency modes centered at 5.1 and 5.8 kHz characterize this condition, whereas in contrast to Flame 2 the second HF mode is dominant over the first at probe location C1 as identified in Figure 7.5b). In comparison with Flame 1& 2 the 2L mode at 680 Hz contains more energy than the 1L mode at 360 Hz. In the pre-combustion spectrum two broadband modes centered at 4.7 and 12 kHz are observed that do not correspond to a resonant eigenmode of the combustor. The scalogram of the C1 signal in Figure 7.5c) reveals that both HF modes are highly nonstationary in frequency and show significant amplitude modulation at ≈ 120 Hz, with HF mode 2 generating twice the amplitude of HF mode 1. In contrast to Flame 2 the lower amplitude HF mode is present throughout the sample and the amplitude modulation of both modes is in phase. The CrWTs presented in Figure 7.5d-f) indicate common power for HF mode 2 at the probe locations C2-3, downstream of C1, whereas the inlet probe does show a stronger response to HF mode 1, which is also observed in Flame 2.

The phase relationship of the flame zone probes relative to C1 presented in Figure 7.5g) reveal that common dynamics found between the flame zone probes are situated within a 500 Hz wide frequency band. The probes C2-3 display a relative phase difference of $\Delta\phi_{CrWT} \approx \pi$ centered at a frequency of 5.55 kHz with a maximum in common power. Var_ϕ is at a minimum for these probes in the frequency-phase space indicating phase-locked dynamics that are consistent with a 1T acoustic field as C2 and C3 are located at the same axial position but orientated azimuthally opposed. A phase difference of $\Delta\phi_{CrWT} \approx 0$ between C1 and IN is observed. The phase relationship for HF mode 1 is similar to what is observed in Flame 2 where the relative phase between C2 and C3 is $\approx 0.35\pi$.

7.2.4 Flame 4

Figure 7.6a) shows a representative pressure signal of Flame 4 that generates pressure oscillations of $p'/p = 5.7\%$. A single high frequency mode centered at 5.8 kHz dominates

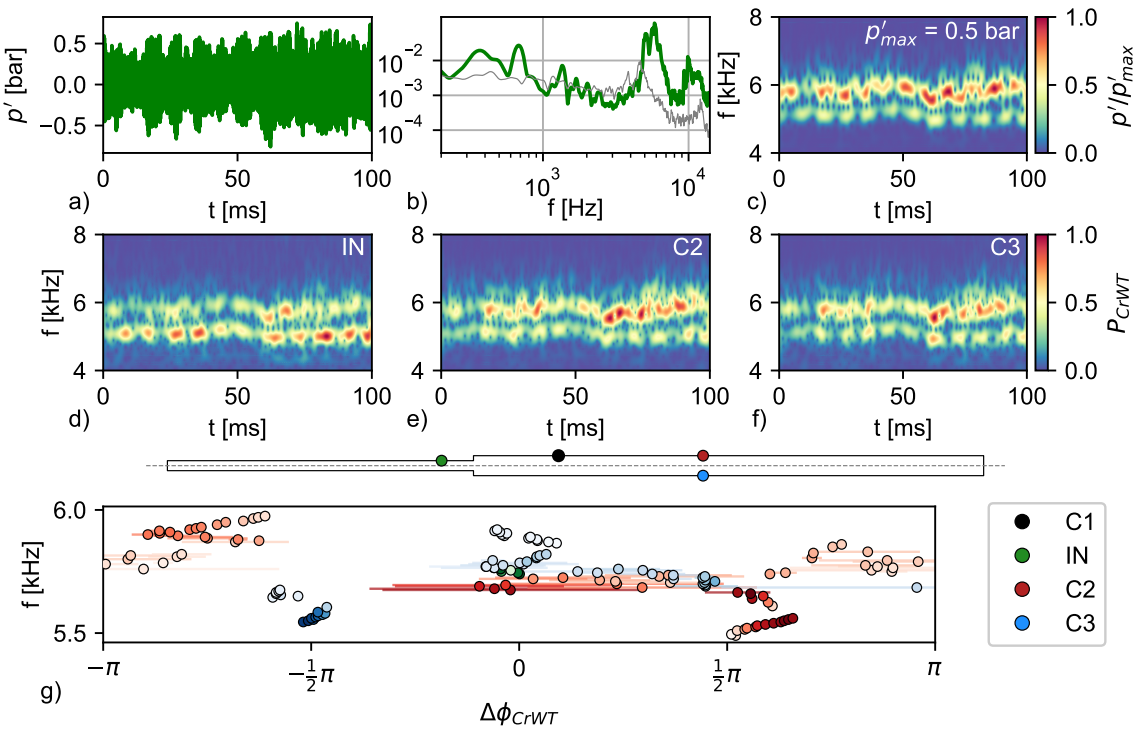

Figure 7.5. Flame 3: a) High-pass filtered pressure signal at C1, b) Welch's power spectrum estimate for signal in a) and pre-combustion (grey). c) Amplitude based Wavelet scalogram for probe C1. d-e) CrWT magnitude based scalograms for probes IN, C2 and C3 g) CrWT based phase difference of IN, C2 and C3 relative to C1 at frequencies of common power.

the pressure spectrum at C1. A harmonic of that mode is evident at 11.6 kHz which is also present in the pre-combustion spectrum next to a mode centered at 4.5 kHz. The 1L and 2L modes are observed at 360 Hz and 720 Hz respectively, where the ratio of the HF to 1L mode amplitude is 2. As in the previous flame condition, multiple harmonics of the 1L mode are observed in the pressure spectrum. The WT scalogram in Figure 7.6c) demonstrates the coherent nature of the HF mode, no periodic frequency or amplitude modulations can be observed, rather stochastic changes occur. The 1L mode is affected by amplitude modulations that stand out clearly in the WT scalogram (not shown here) but can be inferred from the pressure signal in Figure 7.6a), where the period centered about 50 ms shows decreased 1L activity.

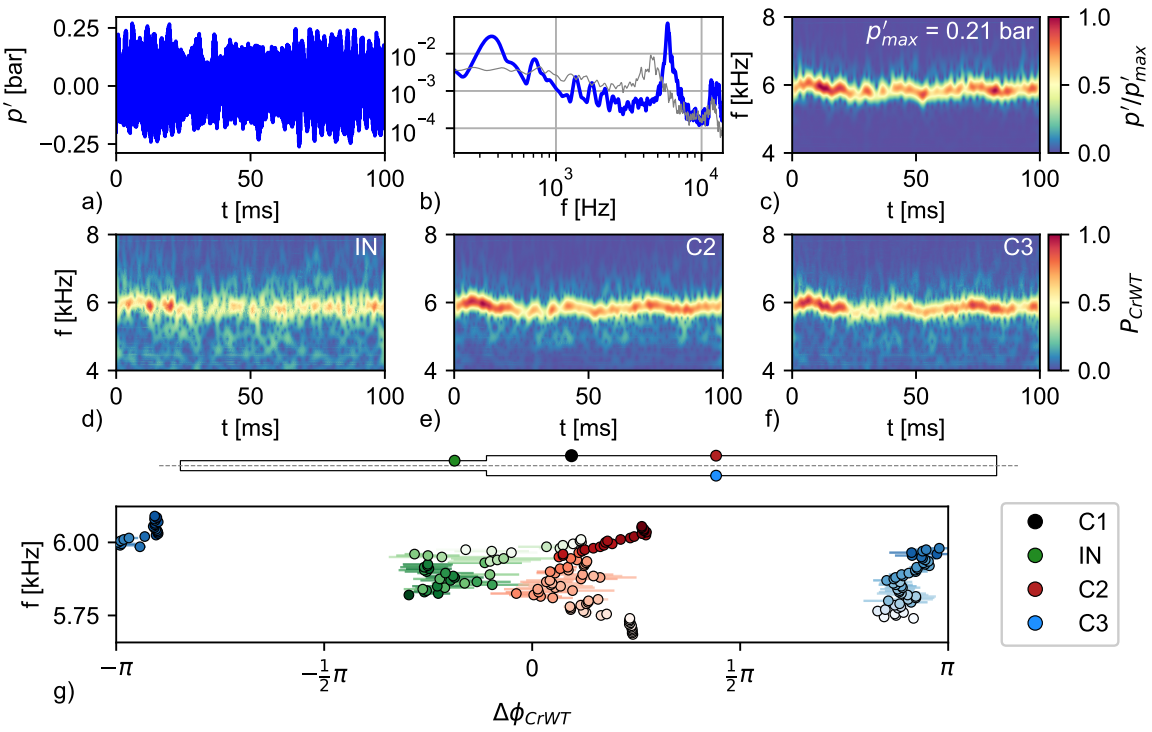

Figure 7.6. Flame 4: a) High-pass filtered pressure signal at C1, b) Welch's power spectrum estimate for signal in a) and pre-combustion (grey). c) Amplitude based Wavelet scalogram for probe C1. d-e) CrWT magnitude based scalograms for probes IN, C2 and C3 g) CrWT based phase difference of IN, C2 and C3 relative to C1 at frequencies of common power.

The CrWT scalograms shown in Figure 7.6d-f) indicate that the HF mode is detected at the remaining flame zone probes and the inlet, however a more coherent coupling is observed for probes C2-3. As the mode resides at higher frequencies the common power of C1 with the probes C2&3 increases, indicating a more favorable relationship between the resonant acoustic mode and the driving mechanisms. The resulting phase relationships are included in Figure 7.6g) and a relative phase difference between the probes C2-3 of $\approx \pi$ and a $\Delta\phi_{CrWT}$ of 0 and $|\pi|$ for C2 and C3 relative to C1 respectively reveal a 1T mode pressure field. The correlated frequency-phase trajectories of C2-3 indicate the phase-locked dynamics as the 1T mode adjusts to changes in sound speed throughout the test duration. The absence of periodic amplitude modulations for this flame condition suggest that the 1T

mode pressure nodal-line is relatively stationary compared to Flame 3. A $\Delta\phi_{CrWT} \approx 0$ for the inlet probe supports the presence of a fundamental transverse mode in the chamber.

7.2.5 Flame 5

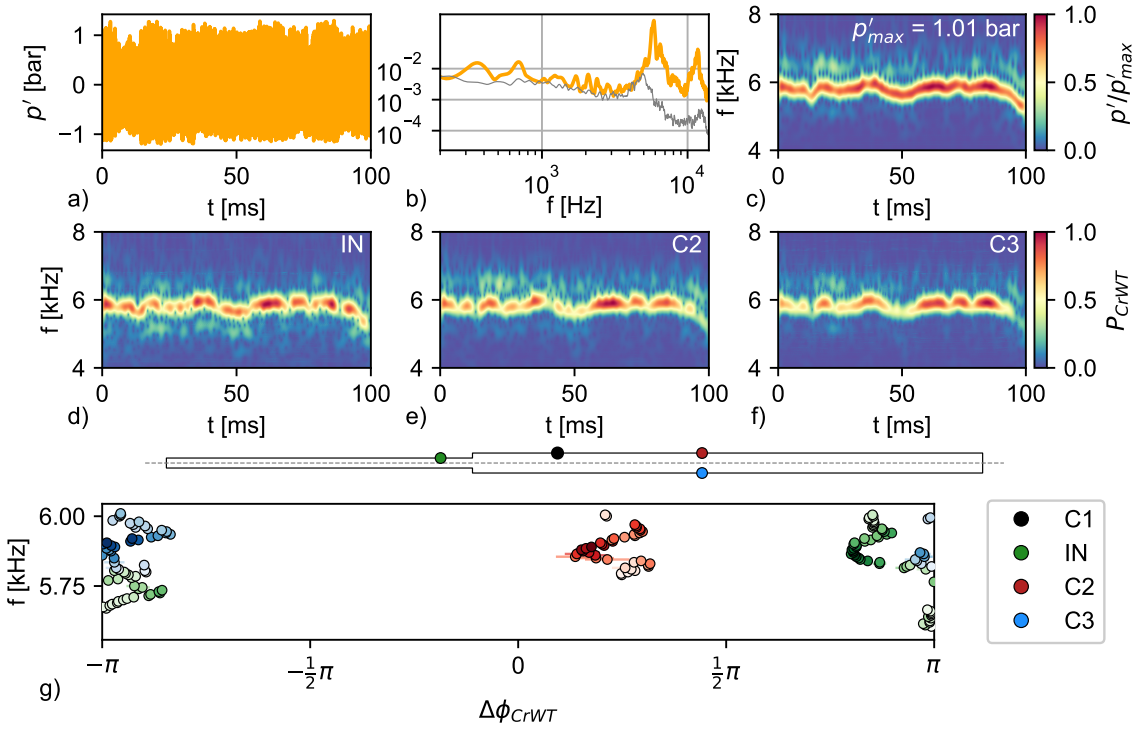

Figure 7.7. Flame 5: a) High-pass filtered pressure signal at C1, b) Welch's power spectrum estimate for signal in a) and pre-combustion (grey). c) Amplitude based Wavelet scalogram for probe C1. d-e) CrWT magnitude based scalograms for probes IN, C2 and C3 g) CrWT based phase difference of IN, C2 and C3 relative to C1 at frequencies of common power.

Figure 7.7a) presents the pressure signal for Flame 5, which is seen to transition into a spin mode from the transverse instability regime similar to Flame 2, hence this case has similar operation parameters (see Table 7.1). The power spectrum in Figure 7.7b) is dominated by a 5.85 kHz mode and the corresponding harmonic at 11.7 kHz. The pre-combustion spectrum indicates the presence of a 5 kHz and 12.5 kHz mode. The 1L and 2L modes are located at 360 Hz and 690 Hz and generate comparable amplitudes and the

superposition results in pressure oscillations of $p'/p = 30.4\%$ at the probe location C1. The WT scalogram in Figure 7.7c) reveals coherent dynamics centered about 5.85 kHz. Frequency modulations of this mode can be observed within a 500 Hz band, for which the amplitude develops a maximum at the center frequency. The CrWT scalograms presented in Figure 7.7d-f) show that the dominant mode is established throughout the flame zone and transmits into the inlet. Amplitude modulations seen at these probe locations correspond to the maximum amplitude periods observed in the WT scalogram for probe C1.

A relative phase difference of $\approx \pi$ between the probes C2-3 indicate a transverse pressure field similar to Flame 4. In contrast to Flame 4 the inlet probe shows a $\Delta\phi_{CrWT} \approx |\pi|$ indicating an asymmetry in the transverse pressure field. All probe frequency-phase trajectories correlate and a low $\overline{Var}_\phi$ indicate phase-locked dynamics.

7.2.6 Instability Class Map

The analysis discussed in the previous section can be extended to the entire operation envelope of the combustor to demonstrate the instability regime dependence on the flame operating condition. For that purpose the pressure signal at probe location C1 is analyzed for its spectral content in the frequency range of interest. As two higher frequency modes are observed a selective mode extraction is performed, for which the spectrum in the range of 4.5-6.5 kHz is considered. If two modes are observed as in Flame 2 &3, the lower frequency mode is defined as mode $HF1$ and the higher frequency mode as $HF2$. In the case that only one mode occurs, as in Flame 4 & 5, the mode is assigned to the $HF2$ group, as these single modes are found in the higher frequency tier ranging from 5.5-6 kHz, whereas the $HF1$ mode is found in the 4.9-5.4 kHz band.

Figure 7.8 summarizes this analysis and provides an overview of the instability mode amplitudes as a function of the flame operation conditions u_{jet} and T_{ad}. As the total mass flow rate $\dot{m}_{tot} \approx const$ a change in T_3 alters the jet velocity by $u_{jet} \propto 1/T_3$ as the inlet pressure $p_3 \approx const$. The adiabatic temperature is computed from the global equivalence ratio ϕ and mixture temperature T_3 for each particular condition. Thus these two parameters

reflect the influence of the hydrodynamics and chemical kinetics in the flow field on the instability mode selection.

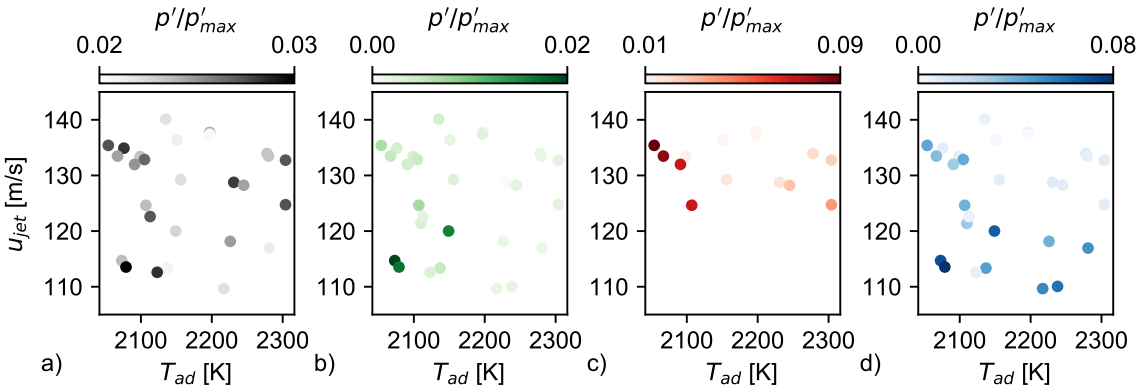

Figure 7.8. Amplitude levels for modes a) 1L, b) 2L, c) $HF1$ and d) $HF2$ as a function of flame operation parameters u_{jet} and T_{ad} based on Welch power spectrum estimates of the C1 pressure signal for each survey condition.

No clear dependence of the 1L mode on the flame operation condition is observed in Figure 7.8a), however three clusters of higher mode magnitudes are identified, of which two are centered about 135 m/s and 115 m/s at lower flame temperatures of $T_{ad} < 2150$ K and one is located at 130 m/s for $T_{ad} > 2200$ K. The 2L mode maintains a relatively low amplitude throughout the operation envelope compared to the remaining modes as shown in Figure 7.8b). The 2L amplitudes are slightly increasing towards lower T_{ad} and a magnitude maximum region is centered at ≈ 115 m/s and flame temperatures lower than $T_{ad} < 2200$. The $HF1$ mode only occurs in the upper half of the operation envelope for $u_{jet} > 120$ m/s and a magnitude increase is observed towards the left and right bounds of that operation space as shown in Figure 7.8c). A maximum amplitude region for $HF1$ is located in the upper left bound of the operations space for $T_{ad} < 2150$. A comparison with the 1L amplitude map reveals a correlation with the elevated $HF1$ amplitude regions. The $HF2$ mode is found in the entire operation envelope but develops elevated magnitude levels in the lower half of the operation space for $u_{jet} < 120$ m/s, except for the region in which

the $HF1$ mode shows a maximum as shown in Figure 7.8d). A $HF2$ maximum is located at $u_{jet} \approx 115$ m/s and $T_{ad} < 2200$, which coincides with the maximum 2L amplitude region.

The mode dependence on u_{jet} in combination with T_{ad} indicates the importance of accessing the underlying flow field hydrodynamics. Although shear layer instabilities are known as a major coupling mechanism between heat-release and pressure oscillations in a given combustor configuration, the onset of this linkage and the underlying physics are yet to be determined. Based on the mapping in Figure 7.8 a connection between the jet operation conditions and thus the shear layer state is made, which is determined by the underlying mean velocity and density profiles. Velocity perturbation modes/waves in the shear layer are maintained by the mean flow velocity gradient and can be significantly altered by the presence of a density gradient.

7.3 Flame Dynamics

To determine the level of flame coupling with the above described dynamics the intensity fluctuations from the OH* chemiluminescence emission in the FOV are extracted. Hereby the spectral content of a spatial mean series of 5000 images

$$I' = \frac{1}{mn} \sum_{x,y}^{m,n} I'_{x,y} \tag{7.3}$$

is considered first, representing the global flame emissions in a 100 ms period that is correlated with the analyzed pressure samples in section 7.2. The resulting power spectra for each flame is shown in Figure 7.9. The I' spectrum of Flame 1 indicates coupling with the 1L and 2L mode at 360 and 720 Hz respectively. The $HF2$ mode detected in the C1 pressure spectrum in Figure 7.3 does not couple with the flame in the FOV, indicating that any pressure field interaction must occur farther downstream. Although longitudinal mode coupling occurs, the I' spectrum for Flame 2 is dominated by oscillations at the $HF1$ mode at 5.3 kHz and the first harmonic at 10.4 kHz, that corresponds to the dominant mode observed in the pressure spectrum in Figure 7.4. The emission spectrum of Flame 3 indicates major coupling at multiple modes, where the highest energy modes are found at

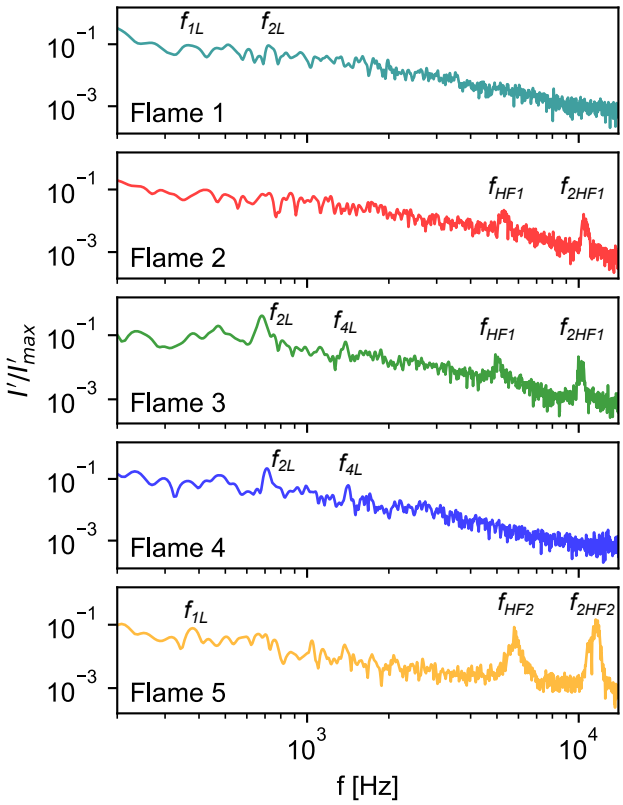

Figure 7.9. Welch power spectra estimates of the OH* chemiluminescence intensity fluctuations I' in the total field-of-view (FOV)

680 Hz and 1390 Hz, corresponding to the 2L and 4L chamber mode found in the pressure spectrum in Figure 7.5. Additionally the $HF1$ mode and its harmonic at 5 kHz and 10 kHz respectively are observed to alter the flame emissions. In contrast to that, the dominant $HF2$ mode in the pressure spectrum for this flame condition does not couple with the flame in the FOV, similar to the observations made for Flame 1. The I' spectrum for Flame 3 indicates no coupling with the $HF2$ mode in the FOV, which was found to dominate the pressure spectrum at C1.

Modes located at 710 Hz and 1420 Hz are found to dominate the flame dynamics, which correspond to the 2L and 4L pressure chamber modes identified in the power spectrum for probe C1 in Figure 7.6. Flame 5 is seen to exhibit significant emission dynamics at 5.8 kHz and 11.6 kHz, which correspond to the $HF2$ mode and the respective harmonics found in

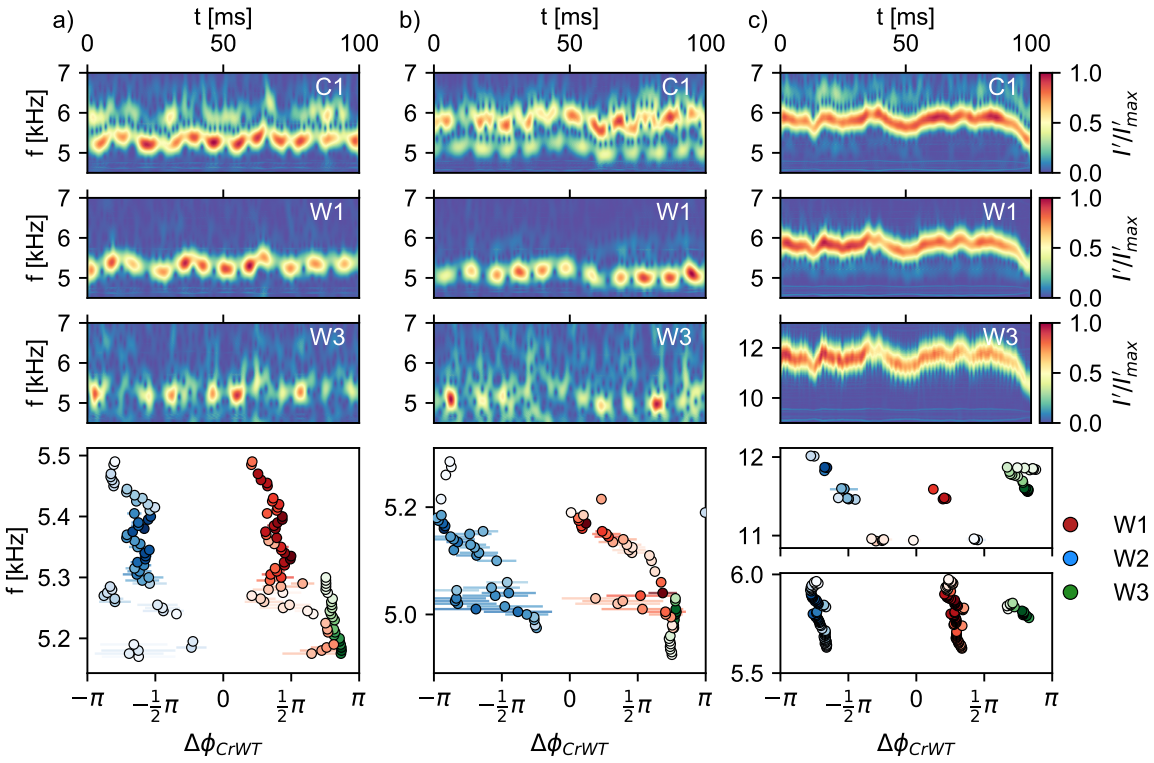

Figure 7.10. First three rows: amplitude based Wavelet scalogram of p' measured at probe C1 and OH* intensity fluctuations in windows W1 and W3. Lower rows: CrWT based phase difference of I' at W1, W2 and W3 relative to p' measured at probe C1 at frequencies of common power for a) Flame 2, b) Flame 3 and c) Flame 5.

the pressure spectrum at C1 in Figure 7.7. Hereby the mode at 11.6 kHz dominates this spectrum and the 5.8 kHz represents a sub-harmonic.

As Flames 2, 3 and 5 indicate coupling with the HF modes identified in the respective pressure analysis, a Wavelet Transform based analysis allows for insight in the spatiotemporal coupling of the flame emission and chamber pressure field. For that purpose the flame emission extraction is spatially limited to the windows W1, W2 and W3, defined in Figure 7.1, and the resulting signals are analyzed in WT space. To directly correlate the intensity signals to the pressure field, the C1 probe signal is down sampled to the imaging frequency of 50 kHz and a Cross-Wavelet Transform based phase relationship between p' and I' is

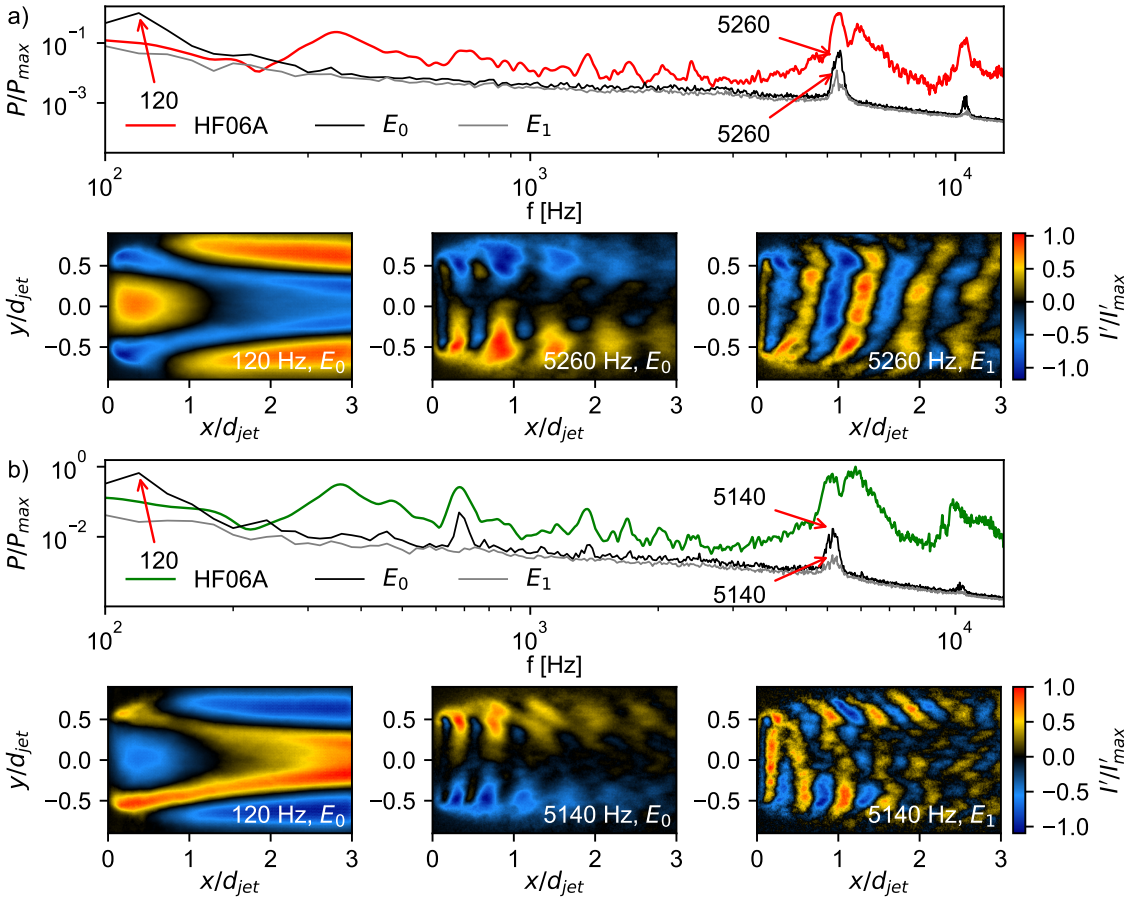

Figure 7.11. First and second SPOD mode spectra and C1 probe pressure spectrum with selected SPOD modes for a) Flame 2, b) Flame 3. The real part of the modes is shown $Re(\Psi_{f,k})$ where k is the SPOD mode number and f the mode frequency.

determined. Similar to the WT pressure analysis, only valid samples from the CrWT are considered for a phase difference calculation, for which $P_{CrWT} > 0.8$.

The WT scalogram of the W1 signal of Flame 2 shown in Figure 7.10 a) indicates strong I' corresponding to the $HF1$ pressure oscillations at C1. An identical amplitude modulation is apparent in the W1 I', but a relative phase difference of $\Delta\phi \approx \pi$ between the p' and I' modulation is identified. The W3 I' in contrast correlates with p' at C1 and high amplitude periods of oscillation are coincident. The W1 and W2 signals are in phase-quadrature ($\Delta\phi_{CrWT} = \pm\pi$) with the pressure signal at C1, which also infers that the I' in

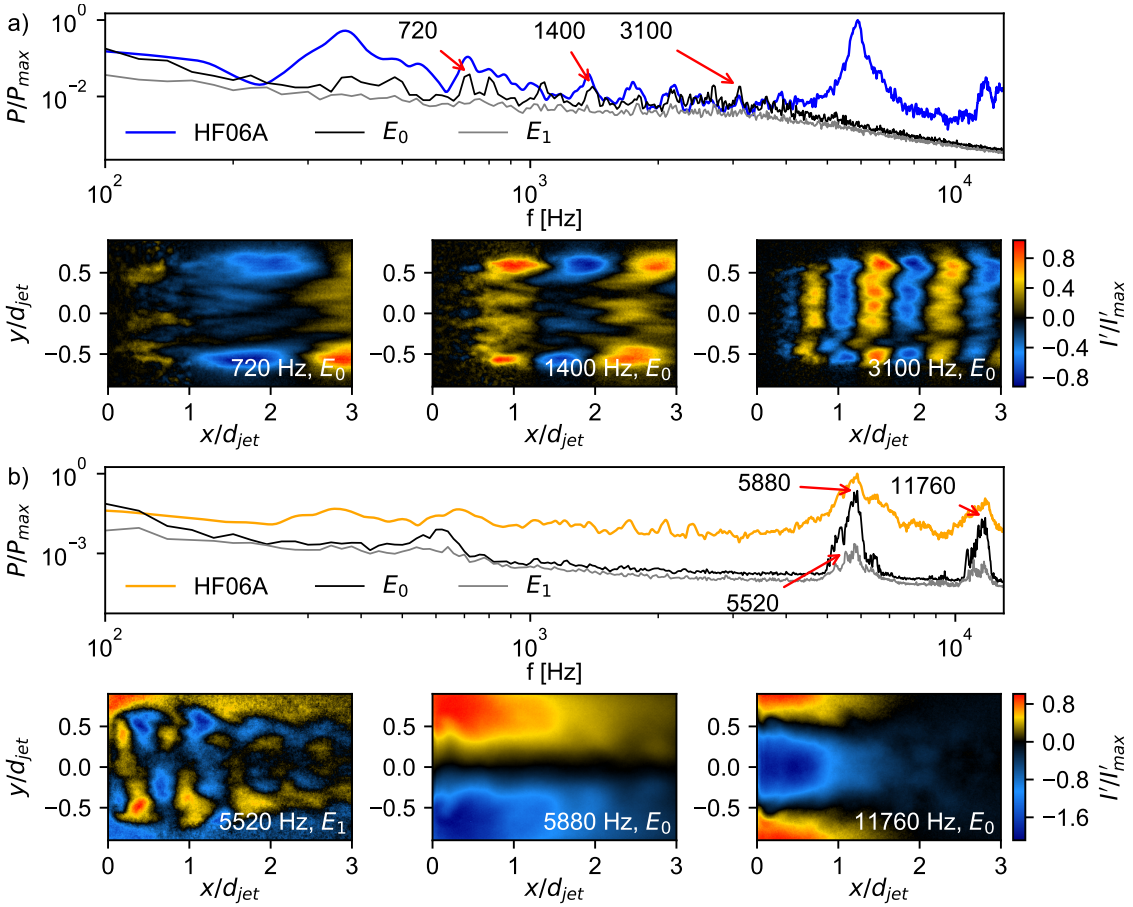

Figure 7.12. First and second SPOD mode spectra and C1 probe pressure spectrum with selected SPOD modes for a) Flame 4, b) Flame 5. The real part of the modes is shown $Re(\Psi_{f,k})$ where k is the SPOD mode number and f the mode frequency.

the upper and lower half of the chamber are phase opposed, as the relative phase difference between W1 and W2 is $\Delta\phi \approx \pi$. The W3 I' in contrast is in phase opposition with p' at C1 as $\Delta\phi_{CrWT} \approx \pi$. These phase relationships are consistent with a nonstationary 1T mode that is established in the flame zone of the combustor, for which the mode nodal-line circumscribes the chamber axis at 60 Hz. This mode behavior has also been described in Chapter 4. As the 1T nodal-line is located normal to the FOV, pressure and velocity fluctuations associated with the mode act parallel to the FOV and the flame response/coupling with the acoustic field is observable as the flame brush undergoes strong transverse dis-

placement and asymmetric shear layer roll-up occurs, yielding high amplitude $I'_{W1,W2}$ at $\Delta\phi_{W1-W2} = \pi$. In these instances the pressure probe C1 and the W3 window is located at the 1T nodal-line, resulting in low amplitude oscillations at the 1T frequency. A nodal-line orientation parallel to the FOV results in a reduction of I' in W1 and W2 and $\Delta\phi_{W1-W2} \approx 0$, as the transverse velocity and pressure oscillations now act normal to the FOV. In these instances the anti-nodes are located in line with the probe C1 and the window W3, leading to high p'_{C1} & I'_{W3} and $\Delta\phi_{CrWT,W3} \approx \pi$, indicating the phase opposition of acoustic pressure and velocity fluctuations at the 1T frequency. The phase quadrature between $I'_{W1,W2}$ and p'_{C1} results from instances where the 1T mode transitions between these two extrema and the angle between FOV and nodal-line approaches 45°.

The pressure spectrum for Flame 3 in Figure 7.10 b) indicates the presence of both modes, $HF1$ and $HF2$, yet only flame coupling with the $HF1$ mode is observed in the FOV yielding a similar behavior as Flame 2. Less coherent phase relationships compared to Flame 2 may be contributed to the increased magnitude of the $HF2$ mode (1T mode in fully developed flow field), leading to a reduced energy contained in the 1T realization close to the nozzle near-field (acoustic energy conservation).

The significant instability level of Flame 5 becomes apparent in the I' scalogram in 7.10 c), as I'_{W1} perfectly correlates with the dynamics of p'_{C1}. The intensity signal extracted from W3 indicates strong oscillations at the harmonic frequency of the $HF2$ mode, exhibiting the same coherent amplitude level observed in the scalograms for I'_{W1} and p'_{C1}. The relative phase relationship between the W1 and W2 signals of $\Delta\phi = \pi$ indicate phase opposition of the flame emissions in the upper and lower chamber-half. The constant amplitude of the p' and I' oscillations in connection with these phase relationships determines the presence of a travelling wave, rather than an acoustic resonant mode.

To further visualize the spatiotemporal p' and I' relationships determined in the foregone analysis, Spectral Proper Orthogonal Decomposition (SPOD) is utilized. The algorithm described by Towne et al is applied for which the published MATLAB suite is applied to decompose the emission field into distinct modes, both in space and time [75]. 10000 mean subtracted images of flame emission are included in the computation spanning 200

ms of the overall test duration, where each emission ensemble includes the 100 ms pressure samples analyzed for each flame condition. This ensemble length is sufficient to study $\approx$ 24 cycles of the amplitude modulation of the I' at the $HF1$ and $HF2$ modes that occurs at $\approx$ 120 Hz and thus represents the lowest frequency of interest. The resulting frequency resolution in the SPOD analysis is 20 Hz based on 5 image blocks (Hamming Window) with 50 % overlap.

Figure 7.11&7.12 include the energy spectra for the first and second SPOD mode ensemble indicated as E_0 and E_1 respectively for Flame 2, 3, 4 and 5. The pressure spectrum at probe location C1 is included for comparison and all spectra are normalized by their respective maximum power. Both SPOD mode spectra for Flame 2 are dominated by two dynamical process, one correlating to the dominant pressure $HF1$ mode and a second to the respective harmonic as observed in Figure 7.11 a). In addition a lower frequency process at 120 Hz is present in the first SPOD spectrum. The real part of the first SPOD modes at 120 Hz and 5360 Hz as well as the second SPOD mode at 5260 Hz clarify the I' dynamics of Flame 2 in the WT based analysis in Figure 7.10 a). As the 1T mode circumscribes the combustor axis in the recirculating region of the flow field (the nozzle near-field), the flame strongly engages with the nonstationary pressure/velocity field. In the 5.36 kHz SPOD mode an asymmetric initial shear layer roll-up is seen to couple with the 1T mode, leading to the high amplitude oscillation periods in the W1&2 emission windows. A concurrent displacement of the flame brush leads to a spatial asymmetry in heat-release in the chamber volume about the chamber axis, supplying energy into the unsteady pressure field. As the 1T mode circumscribes the chamber center axis the emission intensity fluctuates over a longer time scale which is captured in the 120 Hz SPOD mode. As the emission imaging is a line-of-sight integrated measurement, asymmetric intensified light emission about the chamber axis correlate to a nodal-line orientation normal to the FOV, leading to the tapered spatial region originating in the nozzle near field. This period of the 120 Hz cycle corresponds to instances when the 1T nodal-line is orientated normal to the FOV. During the rotation of the 1T mode anti-nodes out of the FOV, the flame broadens as the main interaction path is now inline with the imaging, leading to the wings of the tapered regions and

intensified flame emission about the center axis in the nozzle near-field. These dynamics describe a highly distorted flame shape, where the conical reaction zone is contracted and the flame flattens about the 1T nodal-line.

The second SPOD spectrum indicates an additional dynamic process at 5.36 kHz that underlies the major transverse motion of the flame brush. Inclined bands of high intensity are observed in the second SPOD mode at 5.36 that are convected by the mean flow field. These bands correspond to the asymmetric shear layer roll-up occurring at the 1T frequency, which yields distinct toroidal flow structures (vortex rings) that interact with the reaction layer. The convection velocity of these vortex rings can be estimated based on the 8 instances within the FOV as $u_{conv} = 3d_{jet}f_{HF1}/VN \approx 125$ m/s, where $VN \approx 5$ is the number of intensity bands in the FOV, which corresponds to $\approx u_{jet}$.

Flame 3 shows similar SPOD spectra in Figure 7.11 b) compared to Flame 2 but also indicates strong flame coupling with the 2L chamber mode as indicated by the mode in the first SPOD spectrum at 680 Hz. The SPOD mode corresponding to this frequency indicates strong axial, symmetric flame modulations about the chamber axis (not shown here). The first SPOD modes at 120 Hz and 5.14 kHz correspond to the same processes described for Flame 2. As the $HF2$ mode dominates the pressure spectrum, the $HF1$ mode is less energetic leading to less coherent flame dynamics. The high intensity bands rapidly disintegrate downstream of a $x/d_{jet} \approx 1.5$, indicating a rapid destruction of the vortices into smaller structures compared to Flame 2, for which these structures are present within the whole FOV.

Strong longitudinal mode coupling is observed in the SPOD spectra of Flame 4 in Figure 7.12 a). When compared to the pressure spectrum, the modes at 720, 1400 and 3100 Hz stand out in the first SPOD spectrum, which all display axial modulations in the flame emissions. The 720 Hz mode corresponds to the 2L chamber mode, where axisymmetric patterns indicate periodic intensity fluctuations in the reaction layer that are correlated to the periodic shear layer roll-up and vortex merging, that occurs further downstream in Flame 4 (and 1) compared to Flames 2 and 3. The first SPOD mode at 1.4 kHz is connected to the

third harmonic of the 1L chamber mode whereas the mode at 3.1 kHz isplaying periodic axisymmetric structures that interact with the reaction layer.

Flame 5 displays a completely different flame dynamics indicated by the SPOD spectra and corresponding modes in Figure 7.12 c). Strong coupling of the flame emissions is observed with the $HF2$ pressure mode and its harmonics. As the CrWT analysis in Figure 7.10 c) already established, the flow field is dominated by a single travelling wave circumscribing the potential jet core at 5.88 kHz as observed in the corresponding first SPOD mode. The harmonic mode at 11.76 kHz displays the I' related to the wave passing through the center line of the FOV, resulting in the harmonic mode as both passes are detected. These dynamics dictate a wave speed of $u_{wave} = \pi d_{CC} f_{HF2} = 1480$ m/s, assuming the wave is bounded by the chamber wall, which corresponds to 90% of the Chapman-Jouguet velocity of 1650 m/s for an air-methane mixture at the given operation point (computed with NASA-CEA). The second SPOD mode at 5.52 kHz shows asymmetric roll-up of the underlying reaction layer in the the nozzle near-field, similar to the shedding process observed in Flame 2&3. In contrast to these flames, the emission patterns emerging from this asymmetric roll-up indicate a helical structure is formed around the potential core of the jet that interacts with the inner reaction layer. The observed zigzag pattern results of the line-of-sight integrated image of the flame emissions that are altered by a single helical structure in the shear layer (continuous vortex-tube).

7.4 Linear Stability Analysis of Base Flow

A linear stability analysis of the in chapter 6.3 formulated base flow is performed. Assuming inviscid and locally parallel flow at a specific axial location the compressible Euler equations and energy equation in cylindrical coordinates x, r, θ are linearized. Utilizing the Reynolds decomposition, axial, radial and azimuthal velocities u,v and w and the gas state variables p, T and ρ are decomposed as $q = q_0 + q'$, where q_0 and q' is the unperturbed base state and the superimposed perturbation respectively. The equation system is derived

in chapter 6.1 and only the final set is duplicated here. Assuming harmonic perturbations the linearized mass, momentum and energy equations read:

$$\frac{\alpha u_0}{\rho_0 R_s T_0}\hat{p} + \alpha\hat{u} - j\left(\frac{1}{r} + \frac{1}{\rho_0}\frac{d\rho_0}{dr} + \frac{d}{dr}\right)\hat{v} + \frac{m}{r}\hat{w} - \frac{\alpha u_0}{T_0}\hat{T} = \omega\left(\frac{1}{\rho_0 R_s T_0}\hat{p} - \frac{1}{T_0}\hat{T}\right) \tag{7.4}$$

$$\frac{\alpha u_0}{\rho_0}\hat{p} + \alpha u_0\hat{u} - j\frac{du_0}{dr}\hat{v} = \omega\hat{u} \tag{7.5}$$

$$-\frac{j}{\rho_0}\frac{d\hat{p}}{dr} + \alpha u_0\hat{v} = \omega\hat{v} \tag{7.6}$$

$$\frac{m}{r\rho_0}\hat{p} + \alpha u_0\hat{w} = \omega\hat{w} \tag{7.7}$$

$$-\alpha u_0\hat{p} - jc_p\rho_0\frac{dT_0}{dr}\hat{v} + \alpha c_p\rho_0 u_0\hat{T} = \omega\left(-\hat{p} + c_p\rho_0\hat{T}\right) \tag{7.8}$$

Given that the flow field in this configuration is reasonably parallel compared to flow fields with a mean swirl component, a local LSA is justified. The aim for this analysis is to study the confined jet stability characteristics in the presence of an inhomogeneous density and temperature distribution and its spectral receptivity to acoustic fluctuations within the range of the observed dynamics.

The computational domain is bounded by the combustor wall at $r = r_{CC} = d_{IN}$, where the boundary condition $v'(r_{CC}) = 0$ is enforced. The domain is discretized with a staggered grid approach, for which p', u', w' and T' are evaluated at the center of $N = 250$ segments and the radial velocity perturbations v' at the $N+1$ segment boundaries.

To assess the general stability characteristics of the flow fields for Flames 1-4, a temporal analysis at axial locations of $x/d_{IN} = [0,3]$ in increments of $0.125 d_{IN}$ is conducted. For a given $\alpha \in \mathscr{R}$ the generalized eigenvalue problem is solved and perturbation modes with growth rates of $\omega_i > 1$ are extracted. Figure 7.13 a) shows a representative eigenspectrum. The eigenvalues along the ω_r axis represent the continuous spectrum of the dispersion relation and two discrete modes (marked in red) are observed that are associated with convectively unstable modes. The complex conjugates result from the inviscid formulation of the problem and any eigenmodes with frequencies $\omega_r > 20$ kHz are discarded.

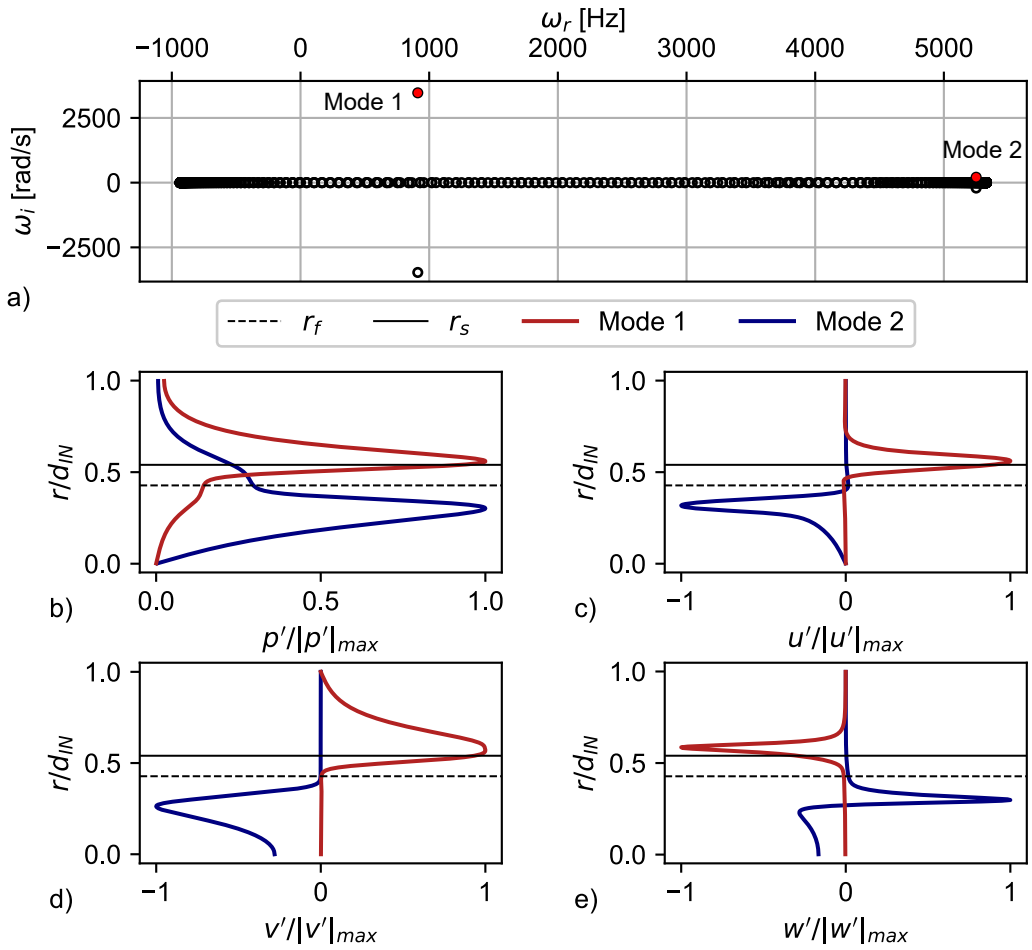

Figure 7.13. a) Eigenvalue spectrum of temporal LSA, b) p', c) u', d) v' and e) w' profiles for Flame 2 with $N = 250$, $\alpha = 250$, $m = 1$, $x/d_{IN} = 1$.

Two modes from the spectrum are identified, which are subsequently referred to as Mode 1 and Mode 2. The associated eigenvectors for the pressure and velocity components are presented in Figure 7.13 b-e). Mode 1 is a shear layer driven mode, identified by the location of the profile extrema located adjacent to the velocity gradient maximum which is marked by the location of r_s. Mode 2 is connected to the mixture jet body, for which all perturbation quantities develop a maximum below the reaction layer. The pressure profiles for both modes indicate interaction between the mixture jet and recirculation zone region, whereas the velocity perturbations are contained within each associated region.

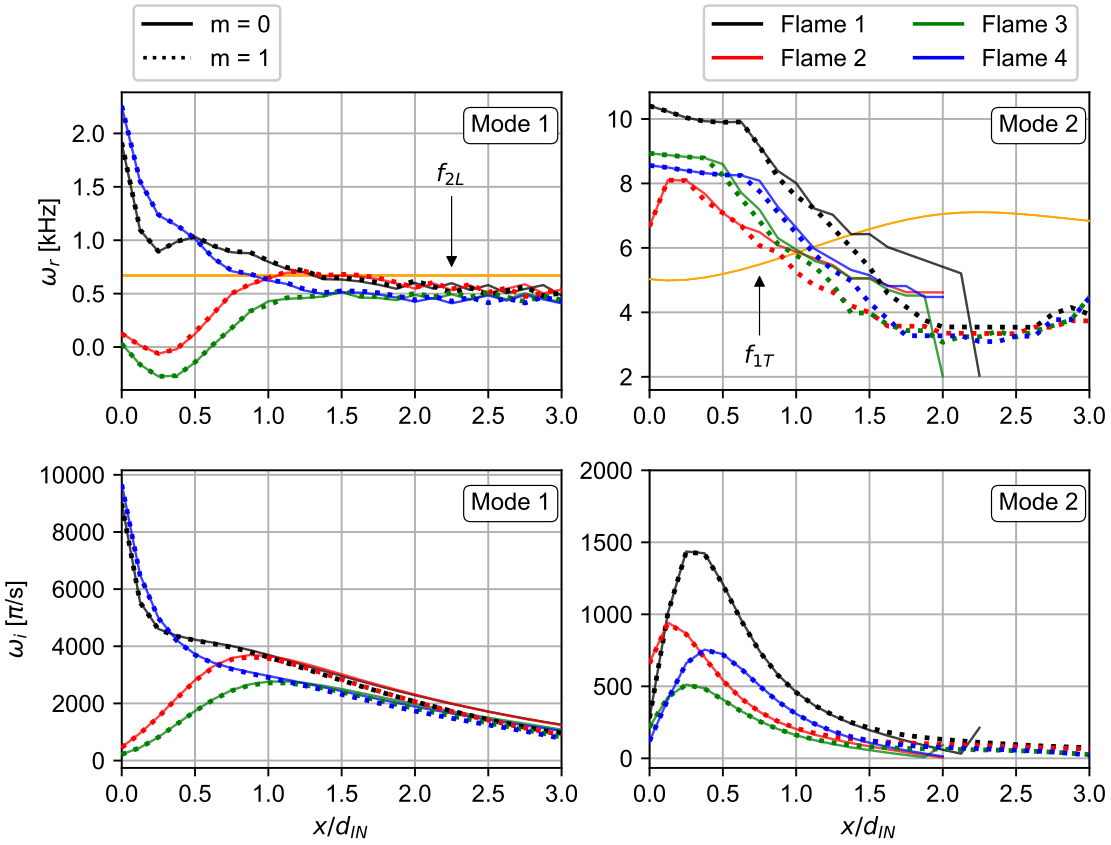

Figure 7.14. Perturbation modes extracted from temporal stability analysis at $x/d_{IN} = 1.5$: a) frequency and b) temporal growth rate ω_i as a function of normalized spatial wavelength λ_x/d_{IN} of convectively unstable modes for Flames 1-5.

Figure 7.14 provides an overview of the stability characteristics for flame condition 1-4 over the analyzed axial span for azimuthal wave numbers $m = [0, 1]$, for which the most unstable modes are plotted. Mode 1 continuously decreases in frequency and growth rate for Flames 1 and 4 within the axial range $x/d_{IN} = 0 - 1.5$. Downstream of that the preferred Mode 1 frequency is observed to stagnate at 500-600 Hz, whereas the growth rate continues to decrease. The reduction in frequency and growth rate is related to the relaxation of the base flow gradients in the axial direction downstream of the sudden expansion. Flame 2 and 3 in contrast develop a negative low frequency region in the axial range $x/d_{IN} = 0 - 1$, indicating a clock-wise rotation direction. The growth rates are significantly lower in the

near field of the sudden expansion compared to Flame 1 and 4 before the mode develops a maximum at $x/d_{IN} \approx 1$. Downstream of that region Mode 1 behaves similarly for all flames. These trends are consistent with both azimuthal wave numbers. The preferred frequency of Mode 1 resides in a frequency band that is compatible with the 2L chamber acoustic eigenmode for all flames. Thus any stochastic process perturbing the shear layer within that frequency band yields a spatially growing disturbance in the downstream direction. This convectively unstable mode has the potential to couple with the combustor acoustic mode through unsteady heat release, that is generated by the interaction of hydrodynamic perturbations and the reaction layer.

Mode 2 is associated with the reactant jet injection region, and resides at higher frequencies compared to Mode 1, which is compatible with the transverse acoustic eigenmodes of the combustor. All flames develop a maximum in temporal growth rate within the axial range $x/d_{IN} = 0 - 0.75$. The frequency hereby decreases towards the level of the 1T acoustic mode of the combustor, indicated by the 1T mode frequency plotted for Flame 2 (computed with LSA for $m = 1$ and $\alpha = 0$). Frequency intersection of the hydrodynamic instability and the acoustic eigenmode is observed in a narrow region centered around $x/d_{IN} = 1$. These trends are consistent with both azimuthal wave numbers within the axial range $x/d_{IN} = 0 - 0.75$, whereas the axisymmetric mode ($m = 0$) deviates from the helical mode. Perturbation modes with $m = 0$ reside at slightly higher frequency for larger axial extent until $x/d_{IN} = 2.25$, where the shear layer is unable to support the axisymmetric modes of type 2. The helical perturbation mode steadily decreases until $x/d_{IN} = 2.25$ where an inflection point is observed, leading to a frequency increase towards the end of the computational domain.

The temporal stability characteristics for Flames 1-4 are compared for the axial location $x/d_{IN} = 1$ in Figure 7.15. The local maximum temporal growth rates for both modes and azimuthal wave numbers are indicated with vertical lines and horizontal lines mark the 2L and 1T acoustic mode frequencies. The maximum growth rate for Mode 2 is reached in a frequency range in close proximity to the local 1T eigenfrequency for Flame 2, 3 and 4, whereas Flame 1 shows a significant offset between the 1T and preferred frequency of

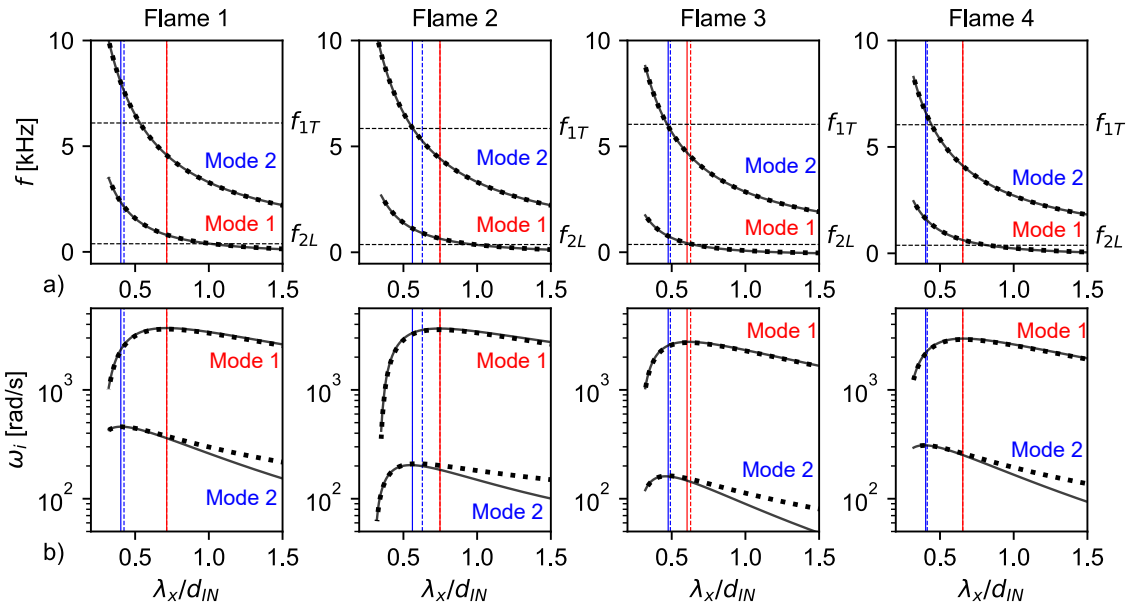

Figure 7.15. Perturbation modes extracted from temporal stability analysis at $x/d_{IN} = 1.5$: a) frequency and b) temporal growth rate ω_i as a function of normalized spatial wavelength λ_x/d_{IN} of convectively unstable modes for Flames 1-4 at $x/d_{IN} = 1$. Vertical (—) and (- - -) lines mark $m = 0$ and $m = 1$ maximum of ω_i. Mode trajectories for $m = 0$: (—), $m = 1$: (▪)

Mode 2. The predicted Mode 2 frequency at $x/d_{IN} = 1$ for Flame 2 is 5.25 kHz with an axial wavelength $\lambda_x/d_{IN} = 0.63$ and is in excellent agreement with the SPOD mode found for this flame at 5.26 kHz. Flame 3 has a preferred Mode 2 frequency of 5.45 and 4.88 kHz at $x/d_{IN} = 1.125$ and 1.25 respectively with the associated axial wave lengths $\lambda_x/d_{IN} = 0.52$ and 0.58, indicating reasonable agreement with the SPOD mode at 5.14 kHz. The computed λ_x/d_{IN} values for both flames show good agreement with the wave pattern inferred from the SPOD modes in Figure 7.11.

Figure 7.16a) shows the reconstructed perturbation quantity fields for Flame 2 with $\alpha = 250$ and $m = 1$ at $x/d_{IN} = 1$, corresponding to the most unstable mode at that axial wave length. The perturbation quantities reach their maximum amplitude in the jet core region. All three velocity components yield the maximum magnitude along the reaction layer imposed boundary, indicating an increase of shear along the reaction layer capable

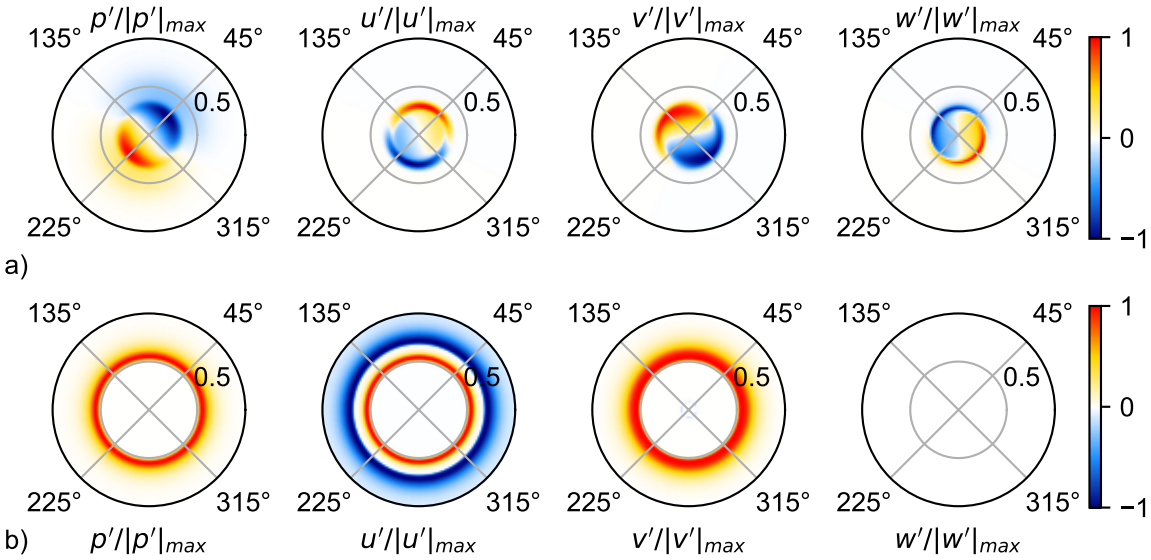

Figure 7.16. Reconstructed perturbation fields for p', u', v' and w' for: a) Mode 2 of Flame 2 at $x/d_{IN} = 1$, $\alpha = 250$ and $m = 1$ b) Mode 1 of Flame 4 at $x/d_{IN} = 0.75$, $\alpha = 320$ and $m = 0$

of flame surface alterations. Helical modes perturbation modes are not restricted to one direction of rotation, especially in a non-swirling jet, for which no rotation direction is preferred. A superposition of the $m = 1$ mode with its $m = -1$ counterpart yields a flapping motion of the jet core which results in asymmetric shear layer roll-up. Given the chemical time scales are compatible with these perturbations, the reaction layer will be altered by the shear layer roll-up, yielding an asymmetry in the flame surface distribution within a cross-section of the flame. The single nodal-line within this distribution is compatible with the 1T acoustic field and thus holds a large potential for self-excitation of the 1T mode in the flame zone. The SPOD modes for Flame 2 and 3 in Figure 7.11 indicate the presence of an underlying helical wave structure that supports this hypothesis. A single helical mode in the shear layer also results in a asymmetric roll-up but in contrast to the flapping mode, no nodal-line within a cross-sectional plane exists, thus the potentially arising heat-release distribution is not compatible with the 1T acoustic field in this configuration.

Preferred frequencies of Mode 1 are found in the region of longitudinal acoustic modes of the combustor. Flame 1 and 4 show good agreement in the measured 2L frequencies with the preferred axisymmetric modes with 730 Hz at $x/d_{IN} = 1.125$ and 710 Hz at $x/d_{IN} = 0.75$ for Flame 1 and 2 respectively. Figure 7.16b) presents the corresponding reconstructed perturbation quantity fields for Flame 4, where the perturbations are located within the recirculation zone adjacent to the shear layer center. Axial velocity fluctuations are centered on the nodal line of the radial velocity perturbations, that lead to an symmetric increase of the axial velocity gradient. This motion is similar to the varicose motion seen leading to a Kelvin-Helmholtz instability that eventually results in shear layer roll-up.

7.5 Conclusions

Combustion instability classes and their sensitivity on operation parameters in a premixed jet-stabilized NG-air combustor at gas turbine relevant conditions have been studied. The single element burner shows distinct changes in dynamics with changes in the global equivalence ratio ϕ and air temperature T_3. Pressure and OH^* chemiluminescence emission data of five flames were analyzed to highlight the three instability classes observed in this burner configuration. Longitudinal, transverse and spinning mode dominated flames were identified, for which a mapping of the classes in the operational space indicated the presence of hydrodynamic processes that determine the combustion instability regime.

The analysis of the pressure and flame dynamics lead to the following hypotheses:

1. Longitudinal modes (1 and 2L) are present throughout the operation envelope for the experiment. The turbulent flow field present in the flame zone provides a wide spectrum of velocity perturbations that lead to heat release oscillations through interaction with the reaction layer. Damping processes in the system limit the resulting interaction and yield a low contribution of these modes to the overall instability level in this configuration.

2. The axial variation of the temperature field in the chamber head-end caused by the non-compact flame leads to a wide frequency range for transverse mode excitation

through feedback with hydrodynamic processes originating in the jet shear layer. Two modes of excitation are present to drive a transverse instability within the chamber. In the nozzle near field the coexistence of counter-rotating helical shear layer instability waves ($m \pm 1$) cause asymmetric interaction between the reaction layer and the velocity fluctuations produced by the shear layer waves. As the temperature and density field within the shear layer changes drastically as result of the reaction, different shear layer partitions provide different orbits of different radii or wave-guides, in which different fluid states prescribe possible harmonic wave solutions.

3. A superposition of two counter-rotating waves results in a standing shear layer instability pattern. A frequency difference between these two modes can lead to a procession of the velocity mode nodal-line within the shear layer at the frequency difference of the two helical waves. The velocity interference between the two waves at the anti-nodal-line causes the shear layer to roll-up, increasing the reaction layer surface locally and generating an asymmetric heat-release distribution about the chamber axis.

4. If the shear layer modes excite perturbations in the range of possible transverse acoustic modes in the flame zone, the flow field will undergo self-excitation and a combustion instability is sustained within the bounds of possible acoustic-coupling, prescribed by the axial variation of sound speed. The 1T mode locks-on to the asymmetry in heat-release and the resulting asymmetric pressure differential about the sudden-expansion favors the shear layer roll-up locally, as the gradient about the inflection point of the axial velocity profile is increased.

5. Due to the presence of the jet potential core a 1T mode established in the nozzle near-field resides at frequencies that are below the 1T cut-off frequency in the fully developed flow with a homogeneous temperature distribution at T_4. The mode is trapped within the combustion zone of the chamber, which results in the observed axial decay of pressure information in the downstream direction.

6. In the fully developed flow field the sound speed is uniform at an elevated level compared to the nozzle near-field leading to increased potential 1T mode frequencies. As described above, the superposition of two helical modes, now at nearly identical frequencies as the temperature field is nearly uniform, results in a flapping (transverse) motion of the jet remnants. This heat-release displacement relative to the chamber center-axis, when occurring at or close to the resonant 1T frequency, couples with the acoustic pressure field and leads to self-excitation of the transverse mode. In this scenario, axisymmetric shear layer modes may be favored in the nozzle near-field, as indicated in the SPOD spectra of Flame 4. Helical modes however may develop further downstream in the reattachment/developing zone of the flow field as potential coupling mechanism between heat-release and acoustic pressure field.

These conclusions are reinforced by a local linear stability analysis of a reconstructed base flow for four flame conditions. The spectrum of possible perturbation modes in the reacting shear layer was examined. The analysis mimics the reaction layer by introducing density and temperature profiles in the base flow. The modelling of heat release was excluded from this analysis, as the inherent shear layer modes are sought. From the axial variation of the preferred mode frequencies and associated growth rates in Figure 7.14 it is concluded that a reduction in ϕ and the corresponding reaction layer transition into lower velocity zones towards the recirculating products leads to a stabilization of shear layer Mode 1. This is supported by the reduced growth rates of Mode 1 for Flame 2 and 3 along with the low frequency for these modes. In contrast to that Flame 1 and 4 show elevated growth rates and frequencies that are compatible with longitudinal acoustic modes of the combustor. The increased offset between reaction and shear layer center, destabilizes Mode 2 for which the preferred mode frequencies are compatible with the 1T chamber mode. Stochastic perturbations inherent in the turbulent flow field trigger Mode 2 for which a superposition of the $m = \pm 1$ shear layer modes lead to a mixture jet flapping. This motion generates an asymmetry in the heat-release distribution with a single nodal-line, that is compatible with the 1T chamber mode. In addition an inflection point in the Mode 2 frequency for $m = 1$ towards the end of the computational domain suggests the existence

of helical waves further downstream, whereas axisymmetric Mode 2 type perturbations are not supported by the flow field beyond $x/d_{IN} > 2.5$.

It was shown that temporal LSA is able to predict convectively unstable shear layer modes, that may undergo coupling with acoustic modes of the combustor. This analysis should be extended into a global analysis, which will allow a further characterization of the two modes found in the local analysis and determine if these modes are absolutely unstable and thus fully determine the instability regime for a given operation condition.

8. SUMMARY AND CONCLUSIONS

The overarching goal of this study was to study the mechanics of self-excited combustion instabilities in a model combustor for power-generation applications. For a confined lean premixed jet stabilized flame, the role of hydrodynamic instabilities on the occurence and amplification of combustion dynamics at multiple thermoacoutic chamber modes was evaluated. To achieve this goal, a single-element natural gas fueled model combustor VIPER-S was designed, capable of operating at chamber pressures up to 22 bar and thermal power levels of 1.5 MW, while providing optical access to the flame zone. At these conditions the wide range of spatiotemporal scales available in the flow field resulted in the self-excitation longitudinal and transverse instabilities. The operating condition determined which of these modes is amplified yielding a sustained limit-cycle of pressure oscillations in the combustor. The canonical experimental configuration of VIPER-S allows for the detailed mapping of the system pressure along with simultaneous flame emission measurements, making the experiment an ideal platform for low- and high-fidelity model validation studies.

Two fuel injection schemes were investigated, a "technically-premixed" configuration (TPC) for which the injector was located within the inlet duct directly upstream of the combustion chamber, simulating the fuel injection in a single element of an terrestrial gas turbine combustor. In this configuration, the injector was exposed to the dynamic pressure field in the combustor, for which the injector stiffness determines the level of interaction between fuel injection rate and system dynamics. In the "fully-premixed" configuration (FPC) the fuel is injected in an external-premixer that is coupled through a choked orifice plate to the combustor inlet, effectively decoupling the system dynamics from the reactant supply and potential equivalence ratio fluctuations.

The sensitivity of the fundamental longitudinal mode (1L) of the combustor on fuel injection location within the inlet duct and flame condition was investigated in TPC. For a constant fuel injection distance to the sudden-expansion, a reduction in the global equiv-

alence ratio (ϕ) lead to an increase of the limit-cycle amplitude. OH^* flame emission measurements showed increased flame-vortex interaction for a reduction of ϕ along with a shift of the time lag between pressure and flame intensity oscillations in the flame zone. For high ϕ flames the intensity and pressure oscillations were in phase, whereas a reduction in ϕ lead to leading intensity fluctuations. The reduced reactant consumption speed for the lower ϕ mixture leads to a higher degree of flame-vortex interactions as the reaction layer adjusts its radial location within the oscillating velocity field. This dynamic process is significantly reduced for higher ϕ flames, leading to a reduced 1L limit-cycle amplitude.

To assess the effect of fuel injection location within the inlet duct on the system 1L mode, the parametric study described above was repeated, for which the injector was shifted by ± 4 cm compared to the baseline location. The baseline injector location is located in a phase-synchronized pressure field region compared to the flame zone, leading to positive ϕ' pockets that are convected into the flame zone prior to the compression phase and thus augmenting $p\prime$. This process amplifies the 1L dynamics in the chamber for normalized convective time lags of $T = 1.15 - 1.25$, which is effectively determined by T_3 for a constant air mass flow rate. Higher pressure fluctuation amplitudes were observed in configuration 3 where the injector was located closer to a pressure anti-node in premixing duct. Here the larger fluctuations in the pressure differential over the injector result in larger ϕ', that reinforce this coupling mechanism. For configuration 2 the injector is located within a phase-opposed pressure field compared to the flame zone. Positive ϕ' pockets arrive during the expansion phase in the flame zone, resulting in an interference of p' and q' and consequently lower limit-cycle amplitudes.

The potential for equivalence ratio fluctuations in response to flame-vortex interactions in the TPC configuration motivated the change to a fully-premixed configuration. In the FPC, an external premixer isolated from the combustor using a choked orifice plate was used to premix the natural gas and air. The acoustic mode-shape of this FPC was tuned to present similar dynamics as the TPC. A parametric survey in mixture temperature T_3 and ϕ revealed that in addition to longitudinal dynamics, transverse, and spin instabilities were excited. The 1L mode dominated the dynamics for rich flame conditions ($\phi > 0.7$),

whereas a reduction of ϕ lead to excitation of the fundamental transverse mode (1T). This ϕ threshold is decreased with an increase in the mixture temperature T_3. Two realizations of the 1T mode are detected within two frequency regions. The first region centered at $\sim$5.2 kHz corresponds to the effective sound speed in the flame zone, which is lower compared to the sound speed in the fully developed flow, due to the presence of the cold mixture jet core. Flame coupling at this frequency is associated with a chamber axis precessing 1T mode. The second realization corresponds to the 1T frequency in the fully developed flow, downstream of the flame zone where the temperature field is homogeneous and the sound speed associated with T_4 determines the higher frequency range at $\sim$6 kHz. Spinning mode instabilities with larger amplitude limit-cycles were observed to onset for $\phi < 0.66$ in combination with $T_3 > 670$ K. Computed azimuthal speeds of these waves were $\sim$ 1480 m/s, which corresponds to $\sim$90% of the Chapman-Jouguet velocity for NG-air at the given flame conditions. Flame emission data indicates different types of flame - shear layer coupling for longitudinal and transverse dominated flames. For longitudinal modes the flame emissions are characterized by axisymmetric patterns indicating shear layer coupling with planar pressure waves in the chamber. A flapping motion of the flame is observed for 1T dominated cases in the frequency region $\sim$5.3 kHz, indicating asymmetric perturbations in the shear layer that alter the reaction layer and couple with the transverse pressure field.

The effect of chamber pressure and inlet velocity on the dynamics in FPC was studied through two additional parametric test campaigns. In the system pressure study, the mean chamber pressure was changed by $\pm$3 bar from the baseline reference pressure of 7 bar, by increasing/decreasing the total mass flow rate through the system. As the exit nozzle area is kept constant, the inlet velocity remains unchanged from the baseline tests at 7 bar. The longitudinal mode amplitudes were observed to be insensitive to the changes in mean chamber pressure and saturate at a certain level. The transverse modes in contrast gain energy from the increased chamber pressure and show elevated amplitudes compared to the baseline tests. This effect may be correlated to the drastic change in Reynolds number of the flow field as the mean chamber pressure is adjusted. With an increase in pressure smaller

turbulent scales become available for flame-flow coupling processes, thus supplying energy to the transverse acoustic modes with compatible wave lengths.

In the inlet velocity study, u_{in} was altered by $\pm$30 m/s from the baseline velocity $\sim$120 m/s, while keeping the mean chamber pressure at the baseline level of 7 bar by adjusting the nozzle exit area of the combustion chamber. The longitudinal modes were found to be insensitive to changes in u_{in} whereas the transverse modes showed highest excitation levels at the baseline velocity. A comparison of the velocity study and baseline data shows that the 1T mode excitation is strongest for a St band of 1.6-1.7 based on the inlet diameter, which corresponds to the baseline u_{in} range.

A protrusion study was conducted to investigate the influence of a duct immersion into the chamber head-end on the chamber dynamics. The longitudinal dynamics were found to be dependent on the global equivalence ratio, where a reduction in ϕ lead to an increase of the 1L amplitude. In addition a reduction in T_3 lead to an increase in the 1L amplitude for the entire ϕ range studied. This is in sharp contrast to the FPC baseline data, where the longitudinal modes were seen to be fairly insensitive to the flame condition. In contrast to that, the transverse modes behaved similarly compared to the FPC baseline data. A resonator study was conducted within the protrusion hardware, to reduce the transverse mode excited in this configuration. Two resonators, purged with T_3 air, were sized to produce a Helmholtz resonance at the measured 1T frequency in the flame zone, i.e. $\sim$5.4 kHz. A parametric sweep in T_3 and ϕ showed a reduction of the transverse mode amplitudes and a significant reduction of the total instability amplitude of up to 70%.

The overarching observation from the fully-premixed configuration indicated a dominant role of shear layer hydrodynamics on the nature of the dominant combustion instability mode for a given operating condition. In order to assess the range of modes the shear layer is able to support, a linear stability model of the base flow in FPC was formulated based on the linearized compressible Navier-Stokes equations. The model was first used to compute the fundamental transverse acoustic mode frequency in the flame zone, which showed a strong dependency on the local cross-sectional temperature distribution. Five operating conditions were studied to characterize the different classes of instabilities observed

in FPC. A wavelet based pressure analysis showed that two realizations of the 1T mode are possible, where the lower frequency mode (HF1) is trapped within the flame zone and the higher frequency 1T mode (HF2) resides in the fully developed flow field, where the frequency is determined by T_4. Flame 2 and 3 were shown to excite a 1T mode within the flame zone, which was identified by a Cross-Wavelet Transform analysis of the pressure and flame emission data. Flame 1 is characterized by longitudinal dynamics, whereas for Flame 4 a 1T mode in the fully developed flow field is observed. A spinning instability is present in Flame 5 leading to a limit-cycle with an amplitude of $\sim$1 bar. A spectral POD (SPOD) analysis of the OH^* flame emission images, showed axisymmetric emission patterns correlated with the longitudinal dynamics for Flame 1 and 4. For Flame 2 and 3 the analysis identified the dominant transverse motion of the flame brush, which corresponds to a flapping motion of the jet. In addition an underlying helical motion was found at the same frequency as the dominant flapping mode. These results indicate the presence of two counter-rotating helical modes that when superimposed result in the dominant flapping motion of the jet that undergoes coupling with the 1T acoustic pressure field in the flame zone.

To test if the shear flow field in FPC allows for these shear layer perturbation modes a temporal linear stability analysis was conducted based on the developed model. The base flow of FPC was reconstructed via analytical profiles, where the density and temperature profile are fitted to the mean OH^* chemiluminescence emission image for each flame and mimic the reaction layer. Two modes are found to be convectively unstable within the domain. Mode 1 is associated with the shear layer and develops velocity perturbations that are located in the outer shear layer or recalculation zone region. Mode 2 is connected to the mixture jet domain, where the perturbation are confined by the reaction layer and develop their maximum towards that bound. Both modes therefore have have the potential to alter the reaction layer and thus the local flame surface area. A sweep over axial wave numbers at a specific axial location within the base flow for each flame allows to identify the locally most unstable or preferred mode. Flame 1 and 4 show Mode 1 frequencies that lie within the range of their 2L acoustic eigenmodes along with a high temporal growth rates within

the axial range of $x/d_{IN} = 0 - 1$. Axial wave length and mode frequencies hereby show good agreement with the pressure and flame dynamics. In contrast to that, Flame 2 and 3 generate Mode 1 frequencies that are not compatible with their longitudinal acoustic eigenmodes. Mode 2 for Flame 2 and 3 shows preferred frequencies compatible to the local 1T eigenmode within the axial range $x/d_{IN} = 0.75 - 1.25$. The computed axial wave length for these modes are in excellent agreement with the pressure and flame dynamics and match the axial wavelength inferred from the associated SPOD modes.

The distinct change between the flame conditions that favor coupling with transverse rather than longitudinal acoustic modes is a complex interplay between u_{IN}, T_3 and ϕ. For Flame 2 and 3, the reaction layer position extracted from the chemiluminescence mean image is located above the shear layer center line in the nozzle near field. The resulting offset between temperature/density and velocity gradient stabilizes the shear layer Mode 1, which favors excitation at low frequencies in the longitudinal acoustic mode range. Mode 2, which is associated with the jet, shows favorable regions of coupling with the local 1T eigenmode for all four flames. Flame 2 and 3 however do not support a longitudinal mode coupling in the initial axial range $x/d_{IN} = 0 - 1$ and thus are more likely to undergo coupling with the 1T acoustic eigenmode. Flame 1 and 4 in contrast show large growth rates and frequencies of Mode 1 in the initial axial range $x/d_{IN} = 0 - 1$, compatible with the longitudinal combustor modes.

The linear stability analysis was able to predict the most unstable modes in the shear layer of the fully-premixed configuration of VIPER-S. A comparison with the preferred modes and local acoustic eigenmodes allows for a physics based analysis of the observed coupling between hydrodynamics and thermoacoustics involved in the excitation of different instability modes. The predictive capability of this tool may be used to generate stability maps as a function of flame operation parameters, when coupled with a turbulent consumption speed model. Such a framework could locate the reaction layer within the analytically derived flow field and determine the stability characteristics for a given flame condition. This procedure could be employed within the early design phase of a new burner system, in order to avoid configurations that likely undergo self-excitation.

REFERENCES

[1] Ben T Zinn and Timothy C Lieuwen. Combustion instabilities: Basic concepts. *Combustion Instabilities in Gas Turbine Engines: Operational Experience, Fundamental Mechanisms, and Modeling*, 210:3–26, 2005.

[2] Sebastian Ducruix, Thierry Schuller, Daniel Durox, and Sebastien Candel. Combustion instability mechanisms in premixed combustors. *Progress in Astronautics and Aeronautics*, 210:179, 2005.

[3] Thierry Poinsot. Prediction and control of combustion instabilities in real engines. *Proceedings of the Combustion Institute*, 36(1):1–28, 2017.

[4] Jacqueline O'Connor, Vishal Acharya, and Timothy Lieuwen. Transverse combustion instabilities: Acoustic, fluid mechanic, and flame processes. *Progress in Energy and Combustion Science*, 49:1–39, 2015.

[5] Tobias Hummel, Frederik Berger, Michael Hertweck, Bruno Schuermans, and Thomas Sattelmayer. High-frequency thermoacoustic modulation mechanisms in swirl-stabilized gas turbine combustors—part ii: Modeling and analysis. *Journal of Engineering for Gas Turbines and Power*, 139(7):071502, 2017.

[6] Frederik M Berger, Tobias Hummel, Michael Hertweck, Jan Kaufmann, Bruno Schuermans, and Thomas Sattelmayer. High-frequency thermoacoustic modulation mechanisms in swirl-stabilized gas turbine combustors—part i: Experimental investigation of local flame response. *Journal of Engineering for Gas Turbines and Power*, 139(7):071501, 2017.

[7] Timo Buschhagen, Rohan Gejji, John Philo, Lucky Tran, J Enrique Portillo Bilbao, and Carson D Slabaugh. Self-excited transverse combustion instabilities in a high pressure lean premixed jet flame. *Proceedings of the Combustion Institute*, 2018.

[8] Yen Ching Yu. *Experimental and analytical investigations of longitudinal combustion instability in a continuously variable resonance combustor (CVRC)*. PhD thesis, Purdue University, 2009.

[9] Yen C Yu, James C Sisco, Stanford Rosen, Ajay Madhav, and William E Anderson. Spontaneous longitudinal combustion instability in a continuously-variable resonance combustor. *Journal of Propulsion and Power*, 28(5):876–887, 2012.

[10] Matthew E Harvazinski, Cheng Huang, Venkateswaran Sankaran, Thomas W Feldman, William E Anderson, Charles L Merkle, and Douglas G Talley. Coupling between hydrodynamics, acoustics, and heat release in a self-excited unstable combustor. *Physics of Fluids*, 27(4):045102, 2015.

[11] Mark Sliphorst, Stefan Gröning, and Michael Oschwald. Theoretical and experimental identification of acoustic spinning mode in a cylindrical combustor. *Journal of Propulsion and Power*, 27(1):182–189, 2011.

[12] Rainer Lückerath, Wolfgang Meier, and Manfred Aigner. Flox® combustion at high pressure with different fuel compositions. *Journal of Engineering for Gas Turbines and Power*, 130(1):011505, 2008.

[13] Oliver Lammel, Harald Schütz, Guido Schmitz, Rainer Lückerath, Michael Stöhr, Berthold Noll, Manfred Aigner, Matthias Hase, and Werner Krebs. Flox® combustion at high power density and high flame temperatures. *Journal of Engineering for Gas Turbines and Power*, 132(12):121503, 2010.

[14] Oliver Lammel, Michael Stöhr, Peter Kutne, Claudiu Dem, Wolfgang Meier, and Manfred Aigner. Experimental analysis of confined jet flames by laser measurement techniques. *Journal of Engineering for Gas Turbines and Power*, 134(4):041506, 2012.

[15] Zhiyao Yin, Patrick Nau, Isaac Boxx, and Wolfgang Meier. Characterization of a single-nozzle flox® model combustor using khz laser diagnostics. In *ASME Turbo Expo*, pages V04BT04A017–V04BT04A017, 2015.

[16] Michael Severin, Oliver Lammel, Holger Ax, Rainer Lückerath, Wolfgang Meier, Manfred Aigner, and Johannes Heinze. High momentum jet flames at elevated pressure: B - detailed investigation of flame stabilization with simultaneous piv and oh-lif. In *ASME Turbo Expo 2017: Turbomachinery Technical Conference and Exposition*, pages V04BT04A028–V04BT04A028. American Society of Mechanical Engineers, 2017.

[17] Oliver Lammel, Michael Severin, Holger Ax, Rainer Lückerath, Andrea Tomasello, Yeshawini Emmi, Berthold Noll, Manfred Aigner, and Lukasz Panek. High momentum jet flames at elevated pressure: A - experimental and numerical investigation for different fuels. In *ASME Turbo Expo 2017: Turbomachinery Technical Conference and Exposition*, pages V04BT04A035–V04BT04A035. American Society of Mechanical Engineers, 2017.

[18] Sebastien Candel. Combustion instability mechanisms in premixed combustors. *Combustion Instabilities in Gas Turbine Engines: Operational Experience, Fundamental Mechanisms, and Modeling*, 2005.

[19] D. A. Smith and E. E. Zukoski. Combustion instability sustained by unsteady vortex combustion. In *21st Joint Propulsion Conference*, page 1248, 1985.

[20] Thierry J Poinsot, Arnaud C Trouve, Denis P Veynante, Sebastien M Candel, and Emile J Esposito. Vortex-driven acoustically coupled combustion instabilities. *Journal of fluid mechanics*, 177:265–292, 1987.

[21] KK Venkataraman, LH Preston, DW Simons, BJ Lee, JG Lee, and D Santavicca. Mechanism of combustion instability in a lean premixed dump combustor. *Journal of Propulsion and Power*, 15(6):909–918, 1999.

[22] Michael Stöhr, Rajesh Sadanandan, and Wolfgang Meier. Experimental study of unsteady flame structures of an oscillating swirl flame in a gas turbine model combustor. *Proceedings of the Combustion Institute*, 32(2):2925–2932, 2009.

[23] Ramgopal Sampath and Satyanarayanan R Chakravarthy. Investigation of intermittent oscillations in a premixed dump combustor using time-resolved particle image velocimetry. *Combustion and Flame*, 172:309–325, 2016.

[24] Seunghyuck Hong, Raymond L Speth, Santosh J Shanbhogue, and Ahmed F Ghoniem. Examining flow-flame interaction and the characteristic stretch rate in vortex-driven combustion dynamics using piv and numerical simulation. *Combustion and Flame*, 160(8):1381–1397, 2013.

[25] Don E Rogers and Frank E Marble. A mechanism for high frequency oscillations in ramjet combustors and afterburners. *Jet Propulsion*, 26(1):456–462, 1956.

[26] Ionut Danaila and BJ Boersma. Mode interaction in a forced homogeneous jet at low reynolds numbers. In *Proceedings of the summer program*, pages 141–158, 1998.

[27] Nicholas A Worth, Dhiren Mistry, Tim Berk, and James R Dawson. Vortex dynamics of a jet at the pressure node in a standing wave. *Journal of Fluid Mechanics*, 882, 2020.

[28] Alfons Michalke. Survey on jet instability theory. *Progress in Aerospace Sciences*, 21:159–199, 1984.

[29] E Villermaux and EJ Hopfinger. Self-sustained oscillations of a confined jet: a case study for the non-linear delayed saturation model. *Physica D: Nonlinear Phenomena*, 72(3):230–243, 1994.

[30] Patrick Huerre and Peter A Monkewitz. Absolute and convective instabilities in free shear layers. *Journal of Fluid Mechanics*, 159:151–168, 1985.

[31] Patrick Huerre and Peter A Monkewitz. Local and global instabilities in spatially developing flows. *Annual review of fluid mechanics*, 22(1):473–537, 1990.

[32] Matthew P Juniper and Sebastien M Candel. The stability of ducted compound flows and consequences for the geometry of coaxial injectors. *Journal of Fluid Mechanics*, 482:257–269, 2003.

[33] Matthew P Juniper. The full impulse response of two-dimensional jet/wake flows and implications for confinement. *Journal of Fluid Mechanics*, 590:163–185, 2007.

[34] Matthew P Juniper. The effect of confinement on the stability of non-swirling round jet/wake flows. *Journal of Fluid Mechanics*, 605:227–252, 2008.

[35] Ahmed F Ghoniem, Anuradha Annaswamy, Daehyun Wee, Tongxun Yi, and Sungbae Park. Shear flow-driven combustion instability: Evidence, simulation, and modeling. *Proceedings of the Combustion Institute*, 29(1):53–60, 2002.

[36] Matthew P Juniper. Absolute and convective instability in gas turbine fuel injectors. In *ASME Turbo Expo 2012: Turbine Technical Conference and Exposition*, pages 189–198. American Society of Mechanical Engineers, 2012.

[37] Kiran Manoharan and Santosh Hemchandra. Absolute/convective instability transition in a backward facing step combustor: Fundamental mechanism and influence of density gradient. *Journal of Engineering for Gas Turbines and Power*, 137(2):021501, 2015.

[38] Kilian Oberleithner, Michael Stöhr, Seong Ho Im, Christoph M Arndt, and Adam M Steinberg. Formation and flame-induced suppression of the precessing vortex core in a swirl combustor: experiments and linear stability analysis. *Combustion and Flame*, 162(8):3100–3114, 2015.

[39] Pedro Paredes, Steffen Terhaar, Kilian Oberleithner, Vassilis Theofilis, and Christian Oliver Paschereit. Global and local hydrodynamic stability analysis as a tool for combustor dynamics modeling. *Journal of Engineering for Gas Turbines and Power*, 138(2), 2016.

[40] Scott E Meyer, Stephen D Heister, Carson Slabaugh, Robert P Lucht, Andrew Pratt, Rohan M Gejji, Michael Bedard, and Aaron Lemcherfi. Design and development of the high pressure combustion laboratory at purdue university. In *53rd AIAA/SAE/ASEE Joint Propulsion Conference, 2017*, page 4965, 2017.

[41] G Campa and SM Camporeale. A novel fem method for predicting thermoacoustic combustion instability. In *European COMSOL Conference*, 2009.

[42] Giovanni Campa and Sergio Mario Camporeale. Prediction of the thermoacoustic combustion instabilities in practical annular combustors. *Journal of Engineering for Gas Turbines and Power*, 136(9):091504, 2014.

[43] SM Camporeale, B Fortunato, and G Campa. A finite element method for three-dimensional analysis of thermo-acoustic combustion instability. *Journal of Engineering for Gas Turbines and Power*, 133(1):011506, 2011.

[44] Yukio Mizutani, Kazuyoshi Nakabe, Yasushi Matsumoto, Takatoshi Saeki, and Tohru Matsui. Processing of luminescent radical images for flame diagnostics. *JSME international journal. Ser. 2, Fluids engineering, heat transfer, power, combustion, thermophysical properties*, 32(3):455–463, 1989.

[45] CJ Lawn. Distributions of instantaneous heat release by the cross-correlation of chemiluminescent emissions. *Combustion and Flame*, 123(1):227–240, 2000.

[46] James D Gounder, Isaac Boxx, Peter Kutne, Stefan Wysocki, and Fernando Biagioli. Phase resolved analysis of flame structure in lean premixed swirl flames of a fuel staged gas turbine model combustor. *Combustion Science and Technology*, 186(4-5):421–434, 2014.

[47] Michael Stöhr, Isaac Boxx, Campbell D Carter, and Wolfgang Meier. Experimental study of vortex-flame interaction in a gas turbine model combustor. *Combustion and Flame*, 159(8):2636–2649, 2012.

[48] Cameron J Dasch. One-dimensional tomography: a comparison of abel, onion-peeling, and filtered backprojection methods. *Applied optics*, 31(8):1146–1152, 1992.

[49] Peter J Schmid. Dynamic mode decomposition of numerical and experimental data. *Journal of fluid mechanics*, 656:5–28, 2010.

[50] Cheng Huang, William E Anderson, Matthew E Harvazinski, and Venkateswaran Sankaran. Analysis of self-excited combustion instabilities using decomposition techniques. In *51st AIAA Aerospace Sciences Meeting*, pages 1–18, 2013.

[51] Cheng Huang, William E Anderson, Matthew E Harvazinski, and Venkateswaran Sankaran. Analysis of self-excited combustion instabilities using decomposition techniques. *AIAA Journal*, 2016.

[52] Sukesh Roy, Jia-Chen Hua, Will Barnhill, Gemunu H Gunaratne, and James R Gord. Deconvolution of reacting-flow dynamics using proper orthogonal and dynamic mode decompositions. *Physical review E*, 91(1):013001, 2015.

[53] Robert Vautard, Pascal Yiou, and Michael Ghil. Singular-spectrum analysis: A toolkit for short, noisy chaotic signals. *Physica D: Nonlinear Phenomena*, 58(1):95–126, 1992.

[54] Andrew C. Noble, Galen B. King, Normand M. Laurendeau, James R. Gord, and Sukesh Roy. Nonlinear thermoacoustic instability dynamics in a rijke tube. *Combustion Science and Technology*, 184(3):293–322, 2012.

[55] KC Schadow and E Gutmark. Combustion instability related to vortex shedding in dump combustors and their passive control. *Progress in Energy and Combustion Science*, 18(2):117–132, 1992.

[56] Robert Zhang, Isaac Boxx, Wolfgang Meier, and Carson D Slabaugh. Coupled interactions of a helical precessing vortex core and the central recirculation bubble in a swirl flame at elevated power density. *Combustion and Flame*, 202:119–131, 2019.

[57] Ian H. Bell, Jorrit Wronski, Sylvain Quoilin, and Vincent Lemort. Pure and pseudo-pure fluid thermophysical property evaluation and the open-source thermophysical property library coolprop. *Industrial & Engineering Chemistry Research*, 53(6):2498–2508, 2014.

[58] Pauli Virtanen, Ralf Gommers, Travis E. Oliphant, Matt Haberland, Tyler Reddy, David Cournapeau, Evgeni Burovski, Pearu Peterson, Warren Weckesser, Jonathan Bright, Stéfan J. van der Walt, Matthew Brett, Joshua Wilson, K. Jarrod Millman, Nikolay Mayorov, Andrew R. J. Nelson, Eric Jones, Robert Kern, Eric Larson, CJ Carey, İlhan Polat, Yu Feng, Eric W. Moore, Jake Vand erPlas, Denis Laxalde, Josef Perktold, Robert Cimrman, Ian Henriksen, E. A. Quintero, Charles R Harris, Anne M. Archibald, Antônio H. Ribeiro, Fabian Pedregosa, Paul van Mulbregt, and SciPy 1. 0 Contributors. SciPy 1.0–Fundamental Algorithms for Scientific Computing in Python. *arXiv e-prints*, page arXiv:1907.10121, Jul 2019.

[59] Sanjiva K Lele. Compact finite difference schemes with spectral-like resolution. *Journal of computational physics*, 103(1):16–42, 1992.

[60] Kenn KQ Zhang, Babak Shotorban, WJ Minkowycz, and Farzad Mashayek. A compact finite difference method on staggered grid for navier–stokes flows. *International journal for numerical methods in fluids*, 52(8):867–881, 2006.

[61] Lawrence E Kinsler, Austin R Frey, Alan B Coppens, and James V Sanders. Fundamentals of acoustics. *Fundamentals of Acoustics, 4th Edition, by Lawrence E. Kinsler, Austin R. Frey, Alan B. Coppens, James V. Sanders, pp. 560. ISBN 0-471-84789-5. Wiley-VCH, December 1999.*, page 560, 1999.

[62] Finn Jacobsen. Propagation of sound waves in ducts. *Lecture note–Advanced Acoustics, Acoustic Technology, Ørsted DTU*, 2005.

[63] Sjoerd W Rienstra. Fundamentals of duct acoustics. *Von Karman Institute Lecture Notes*, 2015.

[64] Stephen B Pope. Turbulent flows, 2001.

[65] FH Champagne, YH Pao, and Israel J Wygnanski. On the two-dimensional mixing region. *Journal of Fluid Mechanics*, 74(2):209–250, 1976.

[66] Warren H Stevenson, H Doyle Thompson, and RD Gould. Laser velocimeter measurements and analysis in turbulent flows with combustion. part 2. Technical report, PURDUE UNIV LAFAYETTE IN SCHOOL OF MECHANICAL ENGINEERING, 1983.

[67] Robert W Pitz and John W Daily. Combustion in a turbulent mixing layer formed at a rearward-facing step. *AIAA journal*, 21(11):1565–1570, 1983.

[68] George P Sutton and Oscar Biblarz. *Rocket propulsion elements*. John Wiley & Sons, 2016.

[69] Bonnie J McBride. *NASA Glenn coefficients for calculating thermodynamic properties of individual species*. National Aeronautics and Space Administration, John H. Glenn Research Center . . . , 2002.

[70] Thierry Poinsot and Denis Veynante. *Theoretical and numerical combustion*. RT Edwards, Inc., 2005.

[71] David G. Goodwin, Raymond L. Speth, Harry K. Moffat, and Bryan W. Weber. Cantera: An object-oriented software toolkit for chemical kinetics, thermodynamics, and transport processes, 2018. Version 2.4.0.

[72] Hideaki Kobayashi. Experimental study of high-pressure turbulent premixed flames. *Experimental thermal and fluid science*, 26(2-4):375–387, 2002.

[73] James F Driscoll. Turbulent premixed combustion: Flamelet structure and its effect on turbulent burning velocities. *Progress in energy and Combustion Science*, 34(1):91–134, 2008.

[74] E Laudien, R Pongratz, R Pierro, and D Preclik. Experimental procedures aiding the design of acoustic cavities. *Liquid Rocket Engine Combustion Instability*, 169:377–399, 1995.

[75] Aaron Towne, Oliver T Schmidt, and Tim Colonius. Spectral proper orthogonal decomposition and its relationship to dynamic mode decomposition and resolvent analysis. *Journal of Fluid Mechanics*, 847:821–867, 2018.

A. SOLUTIONS TO CIRCULAR DUCT MODES

The figures below show 2D reconstructions of the analytical duct mode solutions given in chapter 6.2.

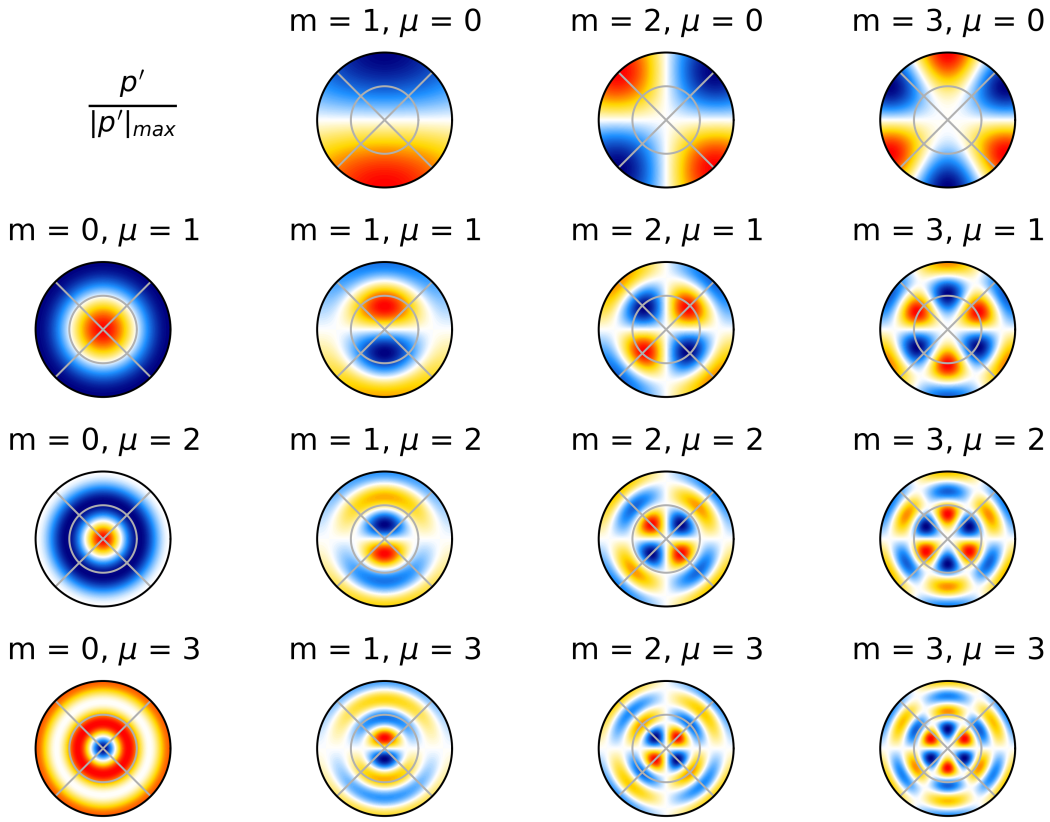

Figure A.1. Analytical duct mode solutions for p in air at $T_0 = 1425$ K and $p_0 = 7.2$ bar and a duct radius of $R = 0.04$ m

The figures below show 2D reconstructions of the linear stability model solutions given in chapter 6.2.

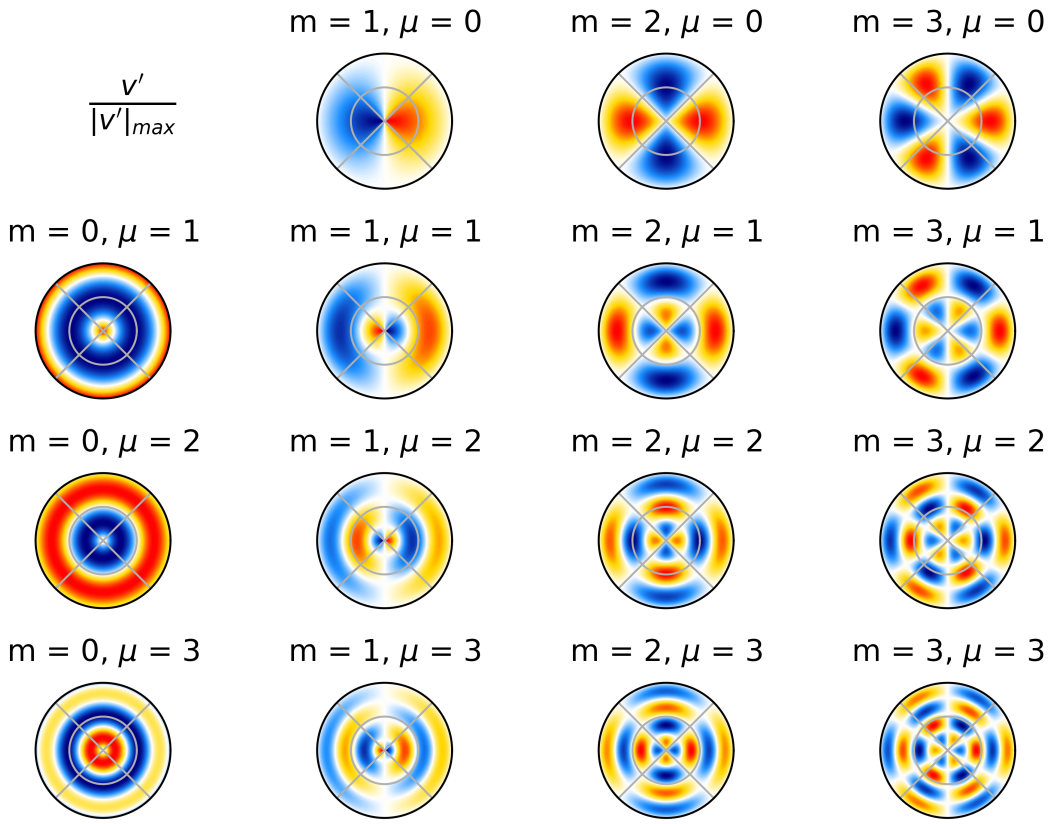

Figure A.2. Analytical duct mode solutions for v in air at $T_0 = 1425$ K and $p_0 = 7.2$ bar and a duct radius of $R = 0.04$ m

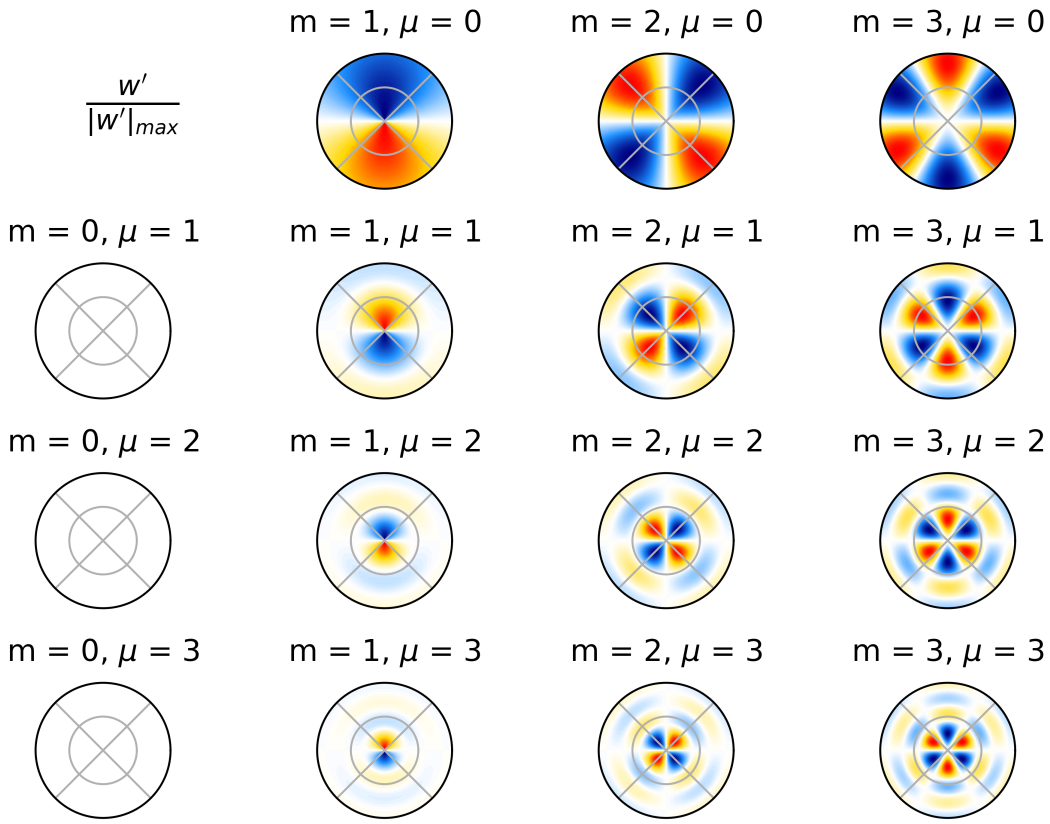

Figure A.3. Analytical duct mode solutions for w in air at $T_0 = 1425$ K and $p_0 = 7.2$ bar and a duct radius of $R = 0.04$ m

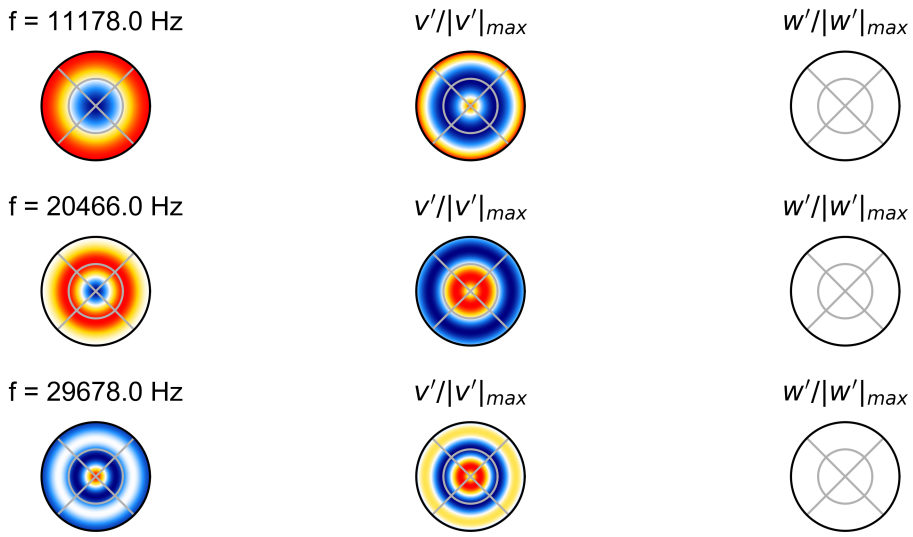

Figure A.4. LSA computed duct mode solutions for $m = 0$ in air at $T_0 = 1425$ K and $p_0 = 7.2$ bar and a duct radius of $R = 0.04$ m

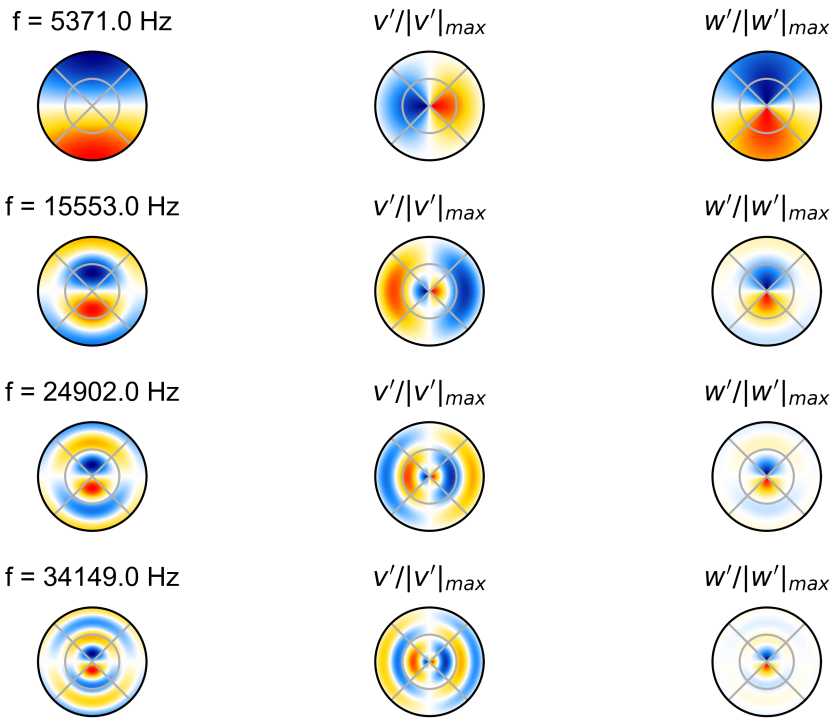

Figure A.5. LSA computed duct mode solutions for $m = 1$ in air at $T_0 = 1425$ K and $p_0 = 7.2$ bar and a duct radius of $R = 0.04$ m

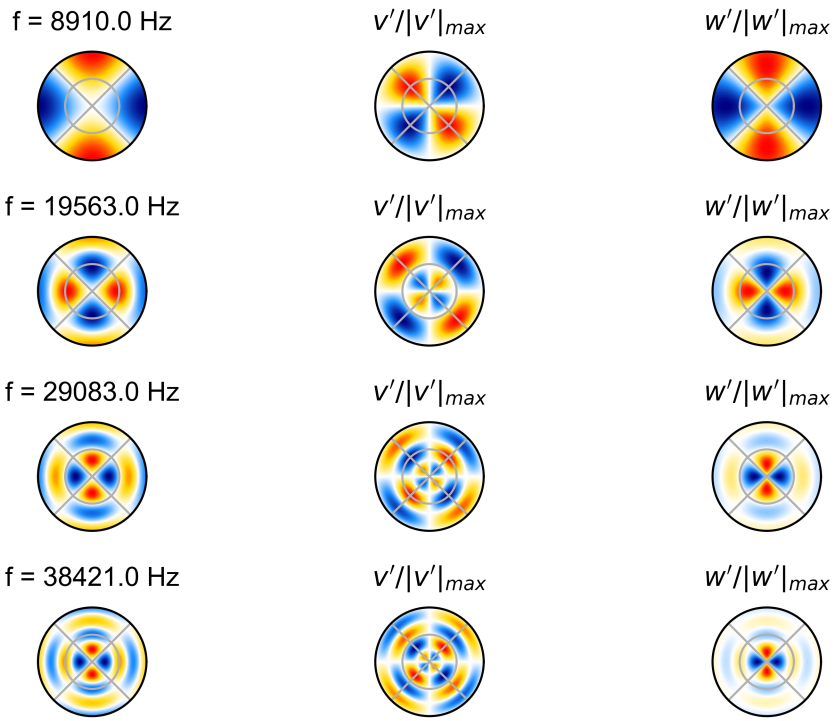

Figure A.6. LSA computed duct mode solutions for $m = 2$ in air at $T_0 = 1425$ K and $p_0 = 7.2$ bar and a duct radius of $R = 0.04$ m

VITA

Timo Buschhagen was born on May 1st, 1989 to Petra and Uwe Buschhagen in Stadthagen, Germany. He concluded a vocational training as Technical Product Designer in 2011 and obtained a Bachelor of Engineering in Mechanical Engineering at the Ostfalia - University of Applied Sciences in Wolfenbüttel, Germany in 2012. In 2013 he recieved a Fulbright Masters Program scholarship and attended Purdue University from 2013 to 2015 concluding with a Master of Science in Aeronautics & Astronautics under Prof. Heister and Sullivan. Following that he started his PhD program in the School of Aeronautics & Astronautics at Purdue University under Prof. Slabaugh focusing on combustion dynamics in gas turbine type combustors.